Universitat Politècnica de Catalunya

Departament de Física Aplicada

# On the growth of nearshore sand bars as instability processes of equilibrium beach states

Memòria presentada per

**Francesca Ribas Prats**

per optar al grau de Doctora en Ciències.

Director:

**Albert Falqués Serra**

Barcelona, Novembre del 2003

A tots els meus mestres,
i entre ells,
i molt especialment,
als meus pares i als meus avis,
per haver-me despertat
el desig d'aprendre

Terra de rius per on camino:
t'obres a cada pas, et dónes,
flueix la saba sota els peus,
la pedra es torna font...

I amb tot, per més que bec
la set no em dóna treva.


De *Liebeslied*, Lala Blay

# Contents

# Chapter 1

# General introduction

Flameja el sol ponent l'estol de veles
en el llunyà confí del cel i l'aigua.
La mar, inquieta, com un pit sospira
en la platja reclosa i solitària.
D'on pot venir la inquietud de l'ona?
Ni un núvol en el cel... ni un alè d'aire...
D'on pot venir la inquietud de l'ona?
Misteri de la mar! L'hora és ben dolça.
Flameja el sol ponent l'estol de veles.

De *Seguit de vistes al mar (III)*, Joan Maragall

## 1.1 The beach, an intriguing physical system

The beach is one of the most visited natural environments of the Earth. Many people enjoy staying at this place of meeting of water and land, attracted by the combination of sun, peace and ever-changing waves. Due to the strong development suffered by this narrow strip of the world surface in the last fifty years, coastal engineers have been strongly involved in trying to overcome the generated problems. But any engineering tool should be based on a strong knowledge of the physics governing the corresponding dynamical system. Consequently, the scientific study of beach systems has turned out to be crucial for the well-being of this natural environment.

Furthermore, the beach is much more than an accumulation of sand where people build houses and sunbathe. The beauty, power and mystery of this natural environment have attracted the attention of artists and scientists since a long time ago. From the point of view of a physicist, very intriguing processes occur in the region of the beaches that is
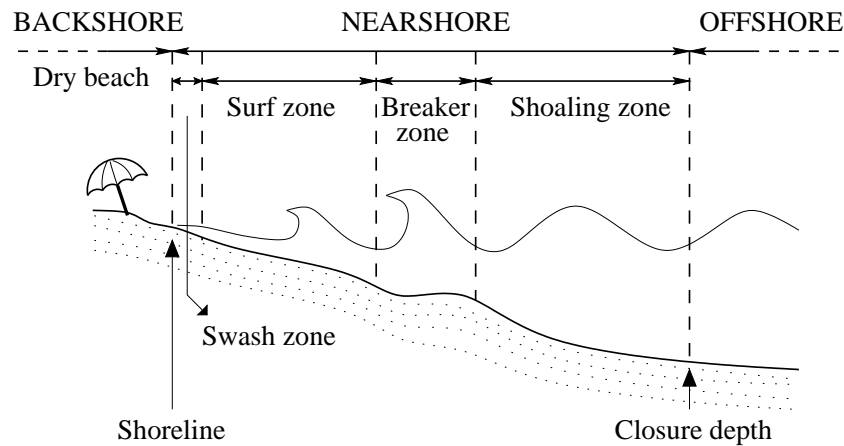
Figure 1.1.1: Terminology used to describe the cross-shore profile of the nearshore. The dynamical system object of this thesis, called nearshore zone, lies from the closure depth to the oscillating shoreline and consists of the shoaling, breaker, surf and swash zones.

permanently underwater, where waves, currents and sediment motion reign magnificently. Its highly complex non-linear behaviour provides an exciting and virgin territory for the exploration of old and new ideas about dynamical systems. This intrinsic scientific interest is the main motivation of this thesis.

In this chapter we first present the beach regions and the main physical processes involved. Then, section 1.2 shows some introductory examples of existing field observations about the geophysical phenomena observed in the nearshore system. Section 1.3 gives a draft overview of the existing theories that explain these geophysical phenomena. The chapter ends up explaining the aim, the approach and the outline of the thesis (section 1.4).

## 1.1.1   Definitions and terminology

There is no clear definition of beach within the geophysical literature and the terminology used to describe its regions varies widely among the different books. The names and definitions presented in this chapter have been taken from Komar (1998) and Short (1999). Figure 1.1.1 shows the cross-shore section of a beach, with its main regions. Looking at the large differences between the governing physical processes, a first division into offshore, nearshore and backshore zones can be done. The system studied in this thesis is the *nearshore zone*, the dynamics of which is dominated by waves, currents and sediment transport. Its seaward boundary is the *closure depth*, which can be defined as the depth below which waves do not feel the bottom sufficiently to produce detectable changes in the topography. Its landward limit is the *shoreline*, defined as the oscillating line of demarcation between the dry beach and the underwater portion.
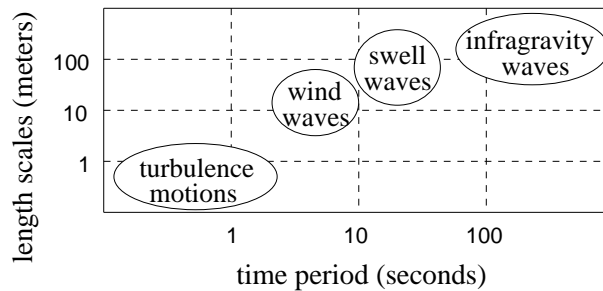
Figure 1.1.2: Length and time scales of the different hydrodynamical periodic motions that can act simultaneously in the beach.

On the basis of the difference between wave processes, the nearshore zone can be divided into four regions. The *shoaling zone* lies between the closure depth and the breaker zone. At its seaward limit, waves begin to interact with the sand in the bottom. As a consequence, wave height increases and wave number decreases across all this region, a phenomenon called *shoaling*. The *breaker zone* is the portion of the nearshore region in which waves become unstable and break. In case of uniform waves (i.e. all of them arriving with the same wave height) it becomes a single breaking line. The *surf zone* is situated shoreward of the breaker zone, where most of the waves are already broken. It is the area where most of the wave energy is transformed into other types of energy. Finally, the shoreline oscillates following the wave cycle and this defines a (smaller) fourth region called *swash zone*, which is alternately covered by water during the up-run and exposed during the backwash.

## 1.1.2   A complex mixture of length and time scales

A striking characteristic of the nearshore environment is the large number of phenomena that compete at different length and time scales. The first process that probably attracts the attention of an observer is wave breaking, due to its incredible variability. A large amount of energy can be generated in storms far away from beaches, mainly due to wind stress. This energy, accumulated over a large area of the sea, is then transported across the ocean by surface waves and it is finally released to the beach. Due to the breaking process, this wave energy is partly dissipated through bottom friction and high-frequency turbulent motions and partly transferred to other hydrodynamical processes, such as 'mean' currents and an elevation of the 'mean' sea water level.

These different hydrodynamical processes give a first set of time and length scales. Figure 1.1.2 shows these scales for some of the hydrodynamical processes, from information found in Horikawa (1988), Komar (1998) and Short (1999). Turbulent eddies (small vortices induced by breaking waves) can be found with time scales of the order of seconds and lengths below the meter. The period of the incident *high-frequency waves* (also called surface gravity waves) ranges from 3 to 10 seconds in case of *wind waves* and from 10 to 20 seconds in case of *swell waves*. Their wave length can vary from 5 to 200 meters. Surface *low-frequency*
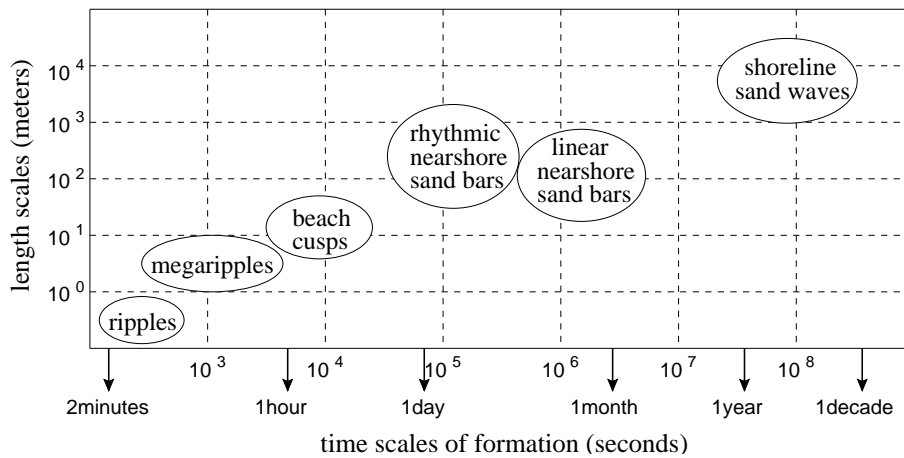
Figure 1.1.3: Length and time scales of the different topographic patterns that can be found in the beach.

*or infragravity waves* are large-scale oscillations of the 'mean' free surface elevation, which can be either progressive or standing. Depending on their shape and dynamics they are classified as *bound long waves*, *leaky waves* or *edge waves*. Another type of low-frequency motion is produced by the *shear waves*, fluctuations of the longshore current velocity that arise form a shear instability of the current. All these low-frequency motions can be found in the nearshore with periods of the order of minutes and length scales of the order of hundreds of meters. Finally, the main components of the *tidal waves* (which are not shown in Fig. 1.1.2) have periods of 12 and 24 hours and length scales of many kilometers.

In the nearshore, the water is flowing over a sandy bottom and this induces shear stresses that are able to mobilise the sediment. Thus, the final consequence of wave energy arriving to the sandy beach is the generation of strong sand transport processes, which in turn modify the aspect of the topography and the shoreline. Toographic changes are usually much slower than the variations of waves and currents. But in geological terms, the nearshore topography is one of the fastest-changing parts of the surface of the Earth. As an example, a winter storm can destroy a beach within a single day.

In spite of the complex behaviour in space and time of nearshore hydrodynamics, relatively regular patterns of different length scales emerge sometimes on the topography of the beach, due to the coupling between bottom evolution and hydrodynamical forcing. Studying the shape, growth and dynamics of these sand patterns is one of the competences of the interdisciplinary research field called *nearshore morphodynamics*. The typical approach used in this field is considering the topography of the beach as the superposition of a long-term averaged configuration plus different morphological patterns, which are generated and destroyed at a wide range of time scales (giving a second scaling in the nearshore, see Dean (1977) and Bowen (1980)). Figure 1.1.3 shows a classification of such type of topographic patterns, from information partially found in Horikawa (1988), Komar (1998) and Short (1999). A certain correlation between spatial and temporal scales of these different observed

geophysical features has been widely recognised but the precise values for the growth times are still a matter of discussion.

The *sea ripples* are small undulations that occur very often on the sandy bottom of the beach. They have wave lengths of the order of several centimeters and growth times of several minutes. The *sea megaripples* and *dunes* are rather larger features, which wave lengths range up to some few meters. Their typical growth rates range from minutes to 1 hour (Engelund & Fredsoe, 1982; Allen, 1984; Sleath, 1984; Blondeaux, 1990; Vittori & Blondeaux, 1990). The *beach cusps* are small undulations of the shoreline with a wave length of several meters and growth times of several hours. They are related with the swash zone dynamics (Kuenen, 1948; Russell & McIntire, 1965; Guza & Bowen, 1975; Inman & Guza, 1982; Werner & Fink, 1993; Coco *et al.*, 2000).

The *nearshore sand bars* are larger and typically elongated shoals of sand that can modify the topography of the entire nearshore zone under certain circumstances. Sometimes they display an *oblique or transverse* orientation with respect to the shoreline. This latter type of bars can be attached to the coast leading to shoreline undulations (normally called *megacusps*) and sometimes systems of several bars with a relatively regular spacing have been reported in the literature. A second type of nearshore bar systems that are also alongshore rhythmic are the so-called *'crescentic longshore bars'*. They can be defined as systems of bumps and holes located periodically along the breaker region. The alongshore wave lengths of the rhythmic systems of nearshore bars presented so far range from tens of meters to about 1 kilometer with a growth time varying from a few hours to a few days (Evans, 1938; Guilcher *et al.*, 1952; Bowen & Inman, 1971; Hino, 1974; Hunter *et al.*, 1979; Holman & Bowen, 1982; Wright & Short, 1984; Lippmann & Holman, 1990; Deigaard *et al.*, 1999; Caballeria *et al.*, 2002; Wijnberg & Kroon, 2002; Lafon *et al.*, 2002). Another type of nearshore sand bars, which do not show any kind of alongshore inhomogeneity, are called *alongshore uniform or shore-parallel sand bars.* One of these elongated bars is found very often near the breaker zone of natural beaches and two or more bars located at different positions of the cross-shore profile sometimes coexist. Either the spacing between them or the width of the surf zone (in case of a single bar) can be taken as their length scale, ranging from tens to hundreds of meters. Their time of formation is still controversial but it has been recognised to range from a few days to about 1 month (King & Williams, 1949; Dyhr-Nielsen & Sorensen, 1970; Winant *et al.*, 1975; Bowen, 1980; Mei, 1985; Roelvink & Stive, 1989; Lippmann & Holman, 1990; Aagaard *et al.*, 1998; Wijnberg & Kroon, 2002).

Finally, very large-scale undulations of the shoreline, named *shoreline sand waves*, also stem sometimes with length scales of several kilometers and time scales of the order of several years (Bakker, 1968; Verhagen, 1989; Inman *et al.*, 1992; Ashton *et al.*, 2001; Falqués & Calvete, 2003). In some cases, examples of shoreline sand waves reported in the literature are clearly related to rhythmic nearshore sand bars (Evans, 1938; Bruun, 1954; Thevenot & Kraus, 1995; Michel & Howa, 1999; Guillen *et al.*, 1999). For instance, the shore-attachments of oblique and shore-parallel sand bars (megacusps) can be sometimes regarded as small shoreline sand waves of length scales of the order of hundreds of meters. A nice example of these kind of systems can be seen in Fig. 1.1.4. The open coast of Sylt Island, in the North of Germany, very often displays a system of rhythmic oblique/transverse sand bars and the corresponding megacusps or small shoreline waves with length scales of hundreds of meters (Yoyoki *et al.*, 2002).

Figure 1.1.4: Photography of a beach of Sylt Island in the North coast of Germany. A system of rhythmic oblique sand bars is visible during low tide in this dynamical system (Yoyoki *et al.*, 2002). The corresponding induced undulations in the shoreline (megacusps or small shoreline sand waves) are also noticeable. The spacing is quite regular, with length scales of hundreds of meters

This thesis is focused on describing the hydro- and morphodynamical processes in the nearshore that display time scales from hours to months and length scales from tens to hundreds of meters. The topographic features found in this range of scales are then the so-called nearshore sand bars, both alongshore uniform and alongshore rhythmic.

## 1.2 Field observations in the nearshore environment

### 1.2.1 Acquisition of field data in the nearshore

*'Remember, when discoursing about water, to induce first experience, then reason'*
- Leonardo da Vinci

Fluid dynamics is not always intuitive, nor is nearshore morphodynamics. Before starting to tackle these subjects theoretically, one should look carefully to nature in order to infer some empirical laws. One can then imagine and build physical principles to explain the observed behaviour. Lastly, the final test of any reliable scientific knowledge is again the experiment.

The traditional way of measuring in the nearshore consists of setting instruments at different locations, which can give values for the wave height, period and direction, the current velocities, the sediment concentrations, etc. Obtaining beach topography is more challenging but several methods have been developed so far (the most modern ones use submersible vehicles). Some examples of long-term beach topography surveys are cited several times throughout this thesis. Many of them have been performed in the Field Research Facility (FRF) in the Duck beach, in North Carolina, U.S.A. (undoubtedly the most studied beach in the world, see for instance Thornton & Humiston (1996) and Birkemeier & Holland (2001)). A second widely measured location is the Dutch coast (JARKUS project, see Ruessink & Kroon (1994) and Wijnberg & Terwindt (1995)). Such topographic measurements have been very valuable to increase our knowledge of the nearshore morphodynamics. The main problem is that they can not be performed often because they are complicated and expensive. As a result, the time periods that would be useful to observe the dynamics of nearshore sand bars (days to months) are hardly ever covered by such traditional methods. Either they resolve well the fast temporal scales of bar growth (days) but they do not last enough to see their long term evolution or they are long enough to capture the inter-annual variations but they can not resolve the daily motions (this is the case in most of the surveys reported in the literature). Another drawback of these methods is that very important morphological changes are induced by storm conditions, under which the measurements in situ are difficult (if not impossible).

In order to overcome these problems, a very useful and cheap *'remote sensing'* technique was developed in the Field Research Facility, in the Duck beach (in the framework of the well-known *'ARGUS project'*, see Lippmann & Holman (1989)). The physics behind this technique is the existing correlation between the white foam produced by breaking waves and the underlying topographic features (due to the fact that waves break in the shallower

Figure 1.2.1: Oblique time exposure image of two shore-parallel sand bars in the surf zone of the Noordwijk beach, in The Netherlands, on $19^{th}$ November 2000. Wave breaking over two submerged shore-parallel sand bars produces white foam that appears as two white bands in this 10-minute time exposure image.

areas). Very enlightening pictures of the nearshore can then be obtained from a simple film taken by an ordinary camera. In order to filter the instantaneous variations of the foam, 10-minute time exposure images are used. Figure 1.2.1 shows an example of an oblique time exposure image obtained from a camera installed in a hotel roof in the Noordwijk beach, in The Netherlands.

In general, several cameras are installed in order to film a beach domain as large as possible. Then several oblique images, such as the one displayed in Fig. 1.2.1, are usually available covering different directions. Rectifying these oblique images to obtain a planview and adding them to a single picture give a complete planview of the studied beach (see Fig. 1.2.2). The rectified images are obtained using standard techniques to transform the original coordinates of the oblique image to the coordinates of a real planview. These ‘AR-GUS images’ show the real shape and orientation of the topographic features. Nowadays, tens of beaches are being monitored and studied all around the world in the framework of the ‘ARGUS project’. In spite of its limitations (the precise value of the water depth is lacking), this project has opened a new universe in the study of nearshore sand bars. In the present chapter, many ‘ARGUS images’ are used to show examples of the studied topographic features.
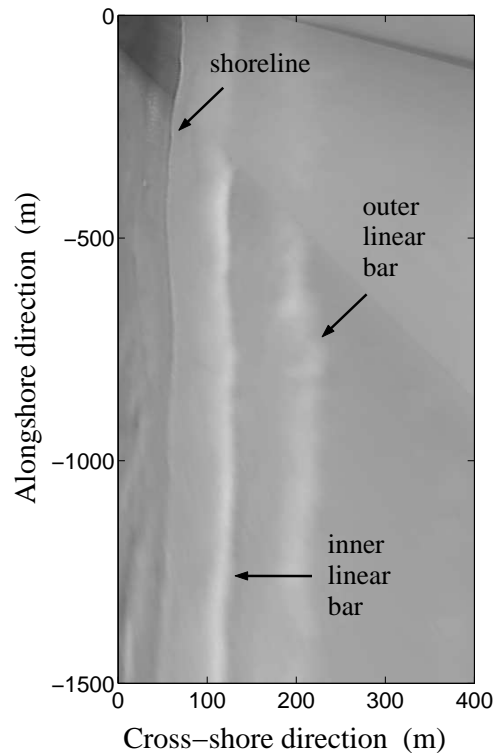
Figure 1.2.2: Planview time exposure image of the two shore-parallel sand bars in the Noordwijk beach, in The Netherlands, on $19^{th}$ November 2000. This image has been obtained through a rectification of the oblique image shown in Fig. 1.2.1. Standard techniques to transform the original coordinates of the oblique image to the coordinates of a real planview are used.

## 1.2.2 Examples of alongshore uniform equilibrium beach profiles

The most evident attribute of the topography of a beach is an overall deepening from the coastline to the offshore direction. And indeed, from time to time the profiles are relatively alongshore uniform and monotonous, with the water depth increasing quite lineally with the cross-shore coordinate. These simple profiles seem to be independent of the hydrodynamic areas described in section 1.1.1. However, much more often a large spatial and temporal variability is found in the bottom of natural beaches, even in the same geographical location. The apparent uniformity is often broken both in the cross-shore and in the alongshore directions by the growth of nearshore sand bars (see section 1.1.2). Very often, even without losing the alongshore uniformity, the deepening in the cross-shore direction is not monotonous but it displays terraces and shore-parallel troughs and bars (the latter pattern has already been introduced in Fig. 1.1.3). Many field observations of alongshore uniform equilibrium profiles worldwide can be found in the literature (Dean, 1977; Wright *et al.*, 1979; Bowen, 1980; Wright & Short, 1984; Stive, 1986; Dean, 1991; Roelvink & Broker, 1993; Kit & Pelinovski, 1998; Komar, 1998; Short, 1999; Plant *et al.*, 2001*b*).
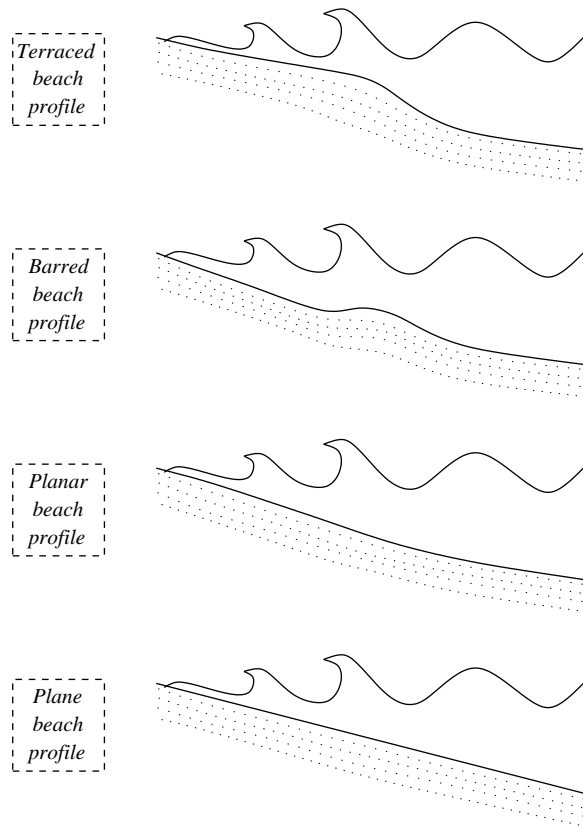
Figure 1.2.3: Scheme of the four types of alongshore uniform cross-shore profiles used in this thesis. See the text for explanation.

The name *'terraced beach profile'* is used in this thesis to refer to profiles showing a relatively constant and gently sloping bottom in the surf zone (called terrace) and a much larger slope in the breaker region that diminishes again in the shoaling zone, with the typical concave-up shape. On the contrary, our concept of *'barred beach profile'* indicates alongshore uniform profiles that display a clear trough followed by a shore-parallel bar as one moves seaward. The crucial difference between these two profile types is that in the former case the gradient of the water depth in the offshore direction is always positive, while in the latter case it becomes negative in some regions. On the other hand, the name *'planar beach profile'* refers to profiles that show similar slopes along the surf and breaker zones (so without any terrace, bar or trough). The slope can diminish along the shoaling zone showing the typical concave-up shape. Finally, in case of dealing with an exactly constant sloping beach (so that the slope is constant along all the profile), we use the name *'plane or constant sloping beach profile'*. Figure 1.2.3 shows a scheme of the four types of beach profiles used in this thesis. When we need to refer to profiles that have not any bar or trough, we use the name *'non-barred beach profile'* (which includes terraced, planar and plane profiles).
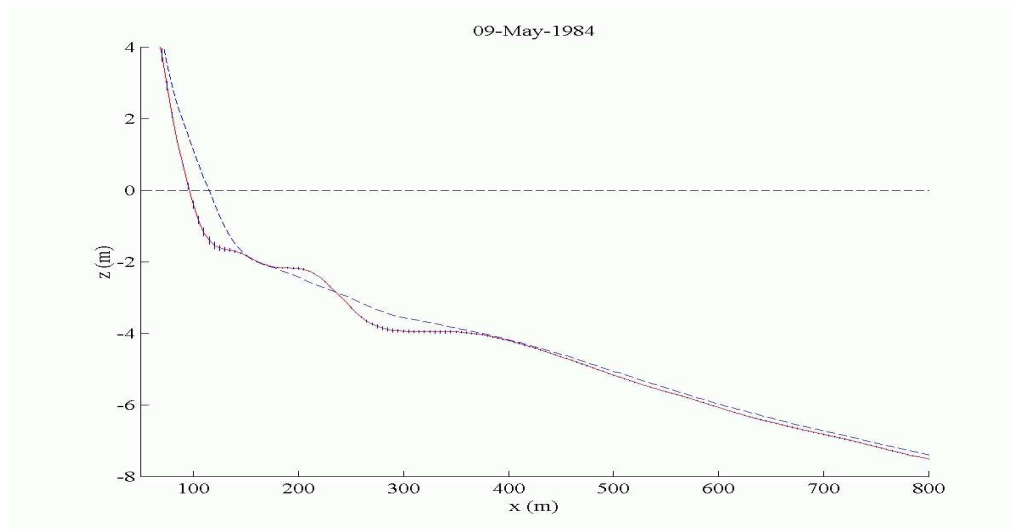
Figure 1.2.4: Cross-shore profile of the Duck beach, in the Atlantic coast of U.S.A., on $8^{th}$ May 1984. The solid line is the alongshore averaged profile (the small vertical solid lines are proportional to the alongshore variability at each point). The dashed line is the 16-year mean profile. The profile is graphed with a large vertical exaggeration in order to emphasize its subtle variations. The topography is nearly alongshore uniform and it does not display any shore-parallel bar. The most remarkable topographic features are two terraces, the edges of which are located at $x \sim 200m$ and $x \sim 400m$.

Figures 1.2.4-1.2.6 contain examples of profiles of the Duck beach, in the U.S.A. Atlantic coast, during periods when the topography was nearly alongshore uniform. These three profiles are graphed with large vertical exaggerations in order to emphasize their subtle variations. In the first example (Fig. 1.2.4), the profile did not display any shore-parallel bar, but just two terraces. 'Terraced beaches' can also be observed in many other beaches (for instance, see the 'fully dissipative beaches' reported in Wright & Short (1984)). Figure 1.2.5 shows a profile of the same beach with a typical shore-parallel bar. Finally, Fig. 1.2.6 shows again the Duck beach in a different day, when it displayed two shore-parallel bars.

These alongshore uniform or shore-parallel bars can be either considered to be part of the equilibrium profile or they can be approached as topographic features superimposed to a 'terraced' (or 'planar') equilibrium configuration, as it is always done in the case of alongshore non-uniform nearshore bars (see section 1.1.2). The two different approaches are defensible in function of the time scale studied and the specific modelling interest and approach. As these shore-parallel bars are one of the topics of this thesis, more examples are given in the next section.
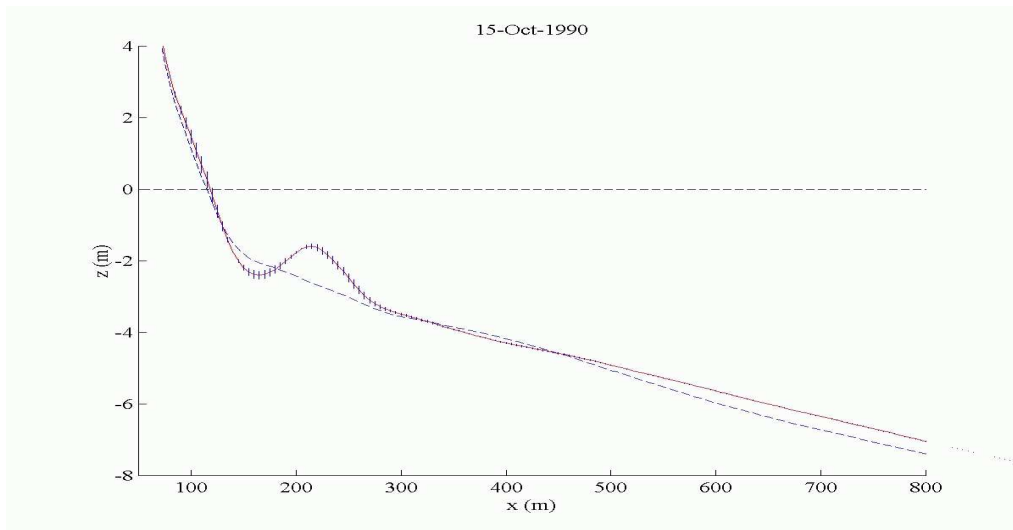
Figure 1.2.5: Cross-shore profile of the Duck beach, in the Atlantic coast of U.S.A, on $15^{th}$ October 1990. See the caption in Fig. 1.2.4 for the graph description. A nearly shore-parallel bar is located at $x \sim 200m$.
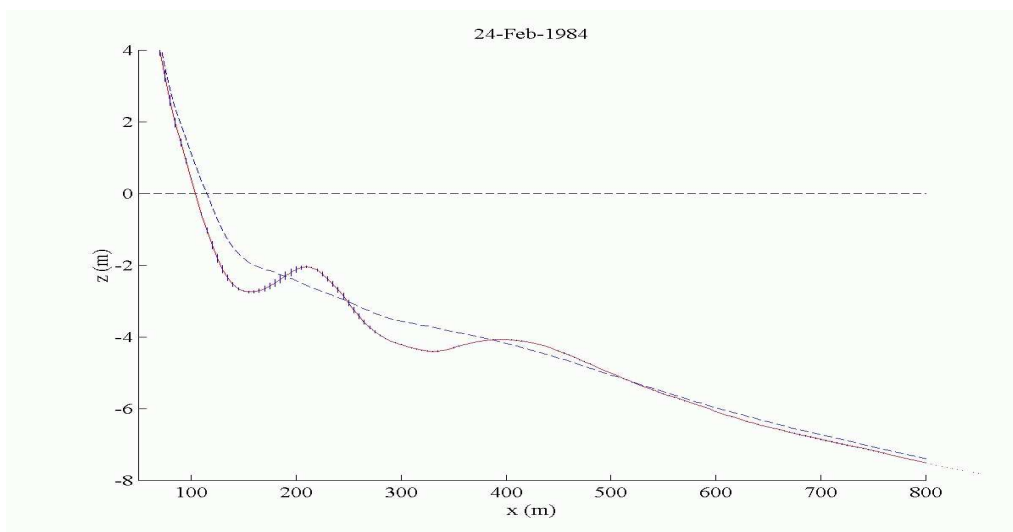


Figure 1.2.6: Cross-shore profile of the Duck beach, in the Atlantic coast of U.S.A, on $24^{th}$ February 1984. See the caption in Fig. 1.2.4 for the graph description. Two nearly shore-parallel bars are located at $x \sim 200m$. and $x \sim 400m$.

Figure 1.2.7: Planview of a time exposure image of a shore-parallel sand bar in the surf zone of the Duck beach, in the U.S.A. Atlantic coast, on $29^{th}$ August 1998. Wave breaking over the submerged shore-parallel sand bar produces white foam that appears as a white band in this 10-minute averaged image.

### 1.2.3   Examples of alongshore uniform shore-parallel sand bars

The nearshore sand bars, which have been defined in section 1.1.2, can be first classified between alongshore uniform (or 2D) systems and alongshore non-uniform (or 3D) systems. The name 'alongshore uniform or shore-parallel sand bars' stands for elongated shoals that are parallel to the coastline. In the nearshore zone of natural beaches one or two of them can be very often found and the existence of systems up to some few tens of shore-parallel bars has been reported in the literature (King & Williams, 1949; Dyhr-Nielsen & Sorensen, 1970; Winant *et al.*, 1975; Bowen, 1980; Mei, 1985; Lippmann & Holman, 1990; Bauer & Greenwood, 1990; Aagaard, 1991; Ruessink & Kroon, 1994; Wijnberg & Terwindt, 1995;

Thornton & Humiston, 1996; Gallagher *et al.*, 1998; Aagaard *et al.*, 1998; Plant *et al.*, 1999; Wijnberg & Kroon, 2002).

Figure 1.2.2 has already displayed the very persistent system of two alongshore uniform sand bars in the Noordwijk beach (The Netherlands). This topographic patterns occur all along the Dutch coast, systems of up to four bars having been reported. They show a very characteristic long term dynamics, the bars migrating persistently offshore in a yearly-averaged view (Kroon, 1994; Ruessink & Kroon, 1994; Wijnberg & Terwindt, 1995; Wijnberg & Kroon, 2002). Detailed observations of these shore-parallel bars in the Dutch coast show that sometimes they turn out to be non-uniform in the alongshore direction, as described by van Enckevort (2001). In that thesis, the non-uniform systems have been classified in four classes: irregular, undulating, crescentic and rips.

Figure 1.2.7 shows a rectified image of the nearshore zone of the Duck beach, in U.S.A. One or two very dynamical shore-parallel bars are very often found in that coast. Their behaviour is mainly governed by the interannual weather variations (Holman & Sallenger, 1993; Thornton & Humiston, 1996; Plant *et al.*, 1999; Birkemeier & Holland, 2001; Hoefel & Elgar, 2003). More examples of a single and a double bar system at the Duck beach have been shown in Figs. 1.2.5 and 1.2.6, respectively.

Finally, shore-parallel bar systems of up to tens of bars can also arise in highly protected coasts, with spacings of tens of meters. Fig. 1.2.8 shows an example of a multiple bar system in the Gulf of Mexico coast of Mississippi, in U.S.A. These types of multiple bar systems have also been observed in open beaches displaying larger spacings of hundreds of meters (Aagaard *et al.*, 1998).

### 1.2.4 Examples of alongshore rhythmic systems of sand bars

Alongshore uniformity is often broken in the nearshore leading to the growth of bumps, bars and troughs at different alongshore locations. It is also common to find several of these bars and bumps spaced quite regularly along the coast. These types of rhythmic systems of sand bars can be divided into 'transverse/oblique bars' and 'crescentic longshore bars'. The former are elongated shoals and troughs with orientations transverse or oblique to the coast and they are usually attached to the coastline by the so-called megacusps (Evans, 1938; Guilcher *et al.*, 1952; Sonu, 1968; Niederoda & Tanner, 1970; Barcilon & Lau, 1973; Hunter *et al.*, 1979; Wright & Short, 1984; Lippmann & Holman, 1990; Konicki & Holman, 2000; Yoyoki *et al.*, 2002). There is some confusion on the terminology. The term *transverse or shore-normal bars* sometimes refers to bars perpendicular to the coast or sometimes in a broader sense to bars which are not shore parallel. Since the present thesis do not include bars exactly perpendicular to the coast, we therein refer always to *oblique bars*, keeping in mind that the angle with the shore normal can range from large to very small values.

Figure 1.1.4 has already shown an example of a rhythmic system of oblique sand bars in the North coast of Germany, with spacings of hundreds of meters. The bars are visible during low tide in this natural environment (Yoyoki *et al.*, 2002). Another example of oblique bar system is often visible along the French Atlantic coast (see Fig. 1.2.9). The mean spacing between bars is about 400 meters (Guilcher *et al.*, 1952; Camenen & Larroude, 1999; Lafon

Figure 1.2.8: Photography of a multiple shore-parallel bar system in the Gulf of Mexico coast of Mississippi, in U.S.A., on $6^{th}$ March of 2001. The first six shore-parallel bars of a system of some ten bars were visible in a period of extremely low tide. The spacing between bars was some tens of meters.

*et al.*, 2002). This pattern usually arises in post-storm conditions under persistent oblique wave incidence and it migrates down-flow with respect to the Southern-directed longshore current with a daily average mean celerity of $2.5m/day$.

'Crescentic longshore bars' are also found quite often in natural beaches, being the most common example of non-uniform longshore bars (with respect to the other classes of non-uniform longshore bars described in van Enckevort (2001)). They can be described either as systems of bumps and holes located periodically along the breaker region or as previous shore-parallel bars that have become undulating. Their wave lengths are usually of the order of some hundreds of meters (Bowen & Inman, 1971; Goldsmith *et al.*, 1982; Wright & Short, 1984; Lippmann & Holman, 1990; Ruessink *et al.*, 2000; van Enckevort, 2001; Wijnberg & Kroon, 2002). In Fig. 1.2.10, one may see the aspect of the sand bar in the Duck beach ten days after the image presented in Fig. 1.2.7. The originally alongshore uniform bar was transformed into a crescentic bar with a wave length of some few hundreds of meters.

All the topographic features described above compete often in certain beaches leading to very complex morphological patterns. Figure 1.2.11 shows again a zoom of the Duck beach, which now displays an example of crescentic pattern with systems of shore-parallel and oblique bars growing in the trough and offshore part of the crescentic bar. The spacing of these latter features is much smaller than the wave length of the crescentic bar (this bar system was studied by Konicki & Holman (2000)).

Figure 1.2.9: Photography of the Southern part of the French Atlantic coast (Les Landes). A system of rhythmic oblique sand bars with a wave length of some 400 meters is often observed in this environment. The bars usually migrate southward with a daily average celerity of about 2.5$m/day$ (see Lafon *et al.* (2002))
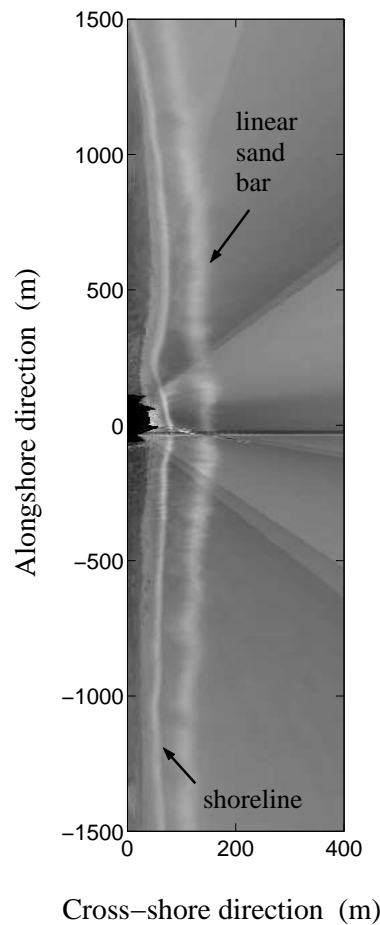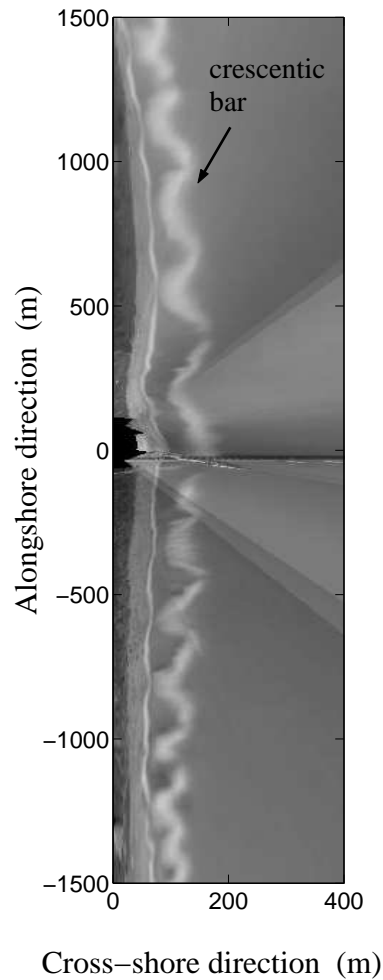
Figure 1.2.10: Planview of a time exposure image of a crescentic sand bar in the surf zone of the Duck beach, in the U.S.A. Atlantic coast, on $9^{th}$ September 1998. Wave breaking over the submerged crescentic sand bar produces white foam that appears as a white band in this 10-minute averaged image.

## 1.2.5   Separation of time scales

While shore-parallel bars are related to the dynamics of the cross-shore beach profile and thus are a 2D phenomenon, rhythmic bars are an essentially 3D morphological feature. Thus, irrespective of the fact that some transverse and oblique bars could have evolved from a previous shore-parallel bar, it is obvious that their formation is necessarily related to the morpho- and hydrodynamics of the surf zone in planview. In this respect, the processes responsible for their occurrence are expected to be distinct from those controlling the equilibrium beach profiles and the formation of shore-parallel bars.
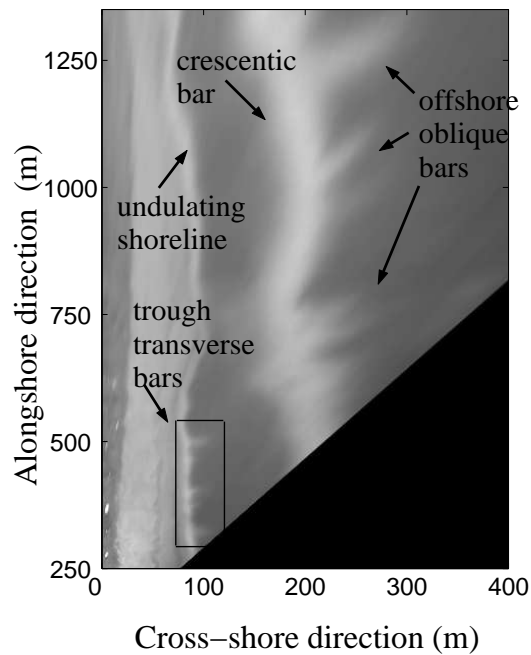
Figure 1.2.11: Planview of a time exposure image of a complex topography in the surf zone of the Duck beach, in the U.S.A. Atlantic coast, on $10^{th}$ January 1994. Wave breaking over some submerged sand bars produces white foam that appears as white bands in this 10-minute averaged image.

Another reason for distinguishing between the 2D and the 3D case is that the time scales involved are quite different. Cross-shore profile evolution and generation of shore-parallel bars are typically related to wave-induced cross-shore sediment transport processes. The time scales of formation and migration of shore-parallel bars, for instance, usually range from days to months (Kajima *et al.*, 1982; Larson, 1988; Ruessink & Kroon, 1994; Thornton & Humiston, 1996). On the other hand, alongshore rhythmic systems have been related to the circulation pattern in planview of the depth-averaged 'mean' currents, so that the induced sediment transport may be one order of magnitude greater than the transport induced only by waves (Short, 1999). Consequently, their characteristic growth times are shorter, ranging typically from hours to days, depending on their wave length (Lippmann & Holman, 1990; Falqués *et al.*, 2000; Caballeria *et al.*, 2002). Therefore, it seems + that the evolution of these two types of bar systems (alongshore uniform or 2D versus alongshore rhythmic or 3D) can be approached as different dynamical problems. This is just a first approximation because, among other reasons, the characteristic growth times are still very controversial and object of many studies (such as the one presented in this thesis).

### 1.2.6 Scientific and engineering challenge

Remarkably, after decades of research, there are not widely accepted physical theories that explain the origin and dynamics of these large-scale beach patterns. It is a problem certainly intriguing and interesting from a scientific point of view. But even more important is that these regular patterns are a visible indication that the complex dynamics of the surf zone as a whole can be understood in terms of simple physical mechanisms at least in some circumstances. Moreover, an important test for any model that intends to describe the morphodynamics of the nearshore is to reproduce the dynamical behaviour of such topographic patterns, in order to be sure that the model successfully describes these simple physical processes.

Understanding nearshore morphodynamics is not only challenging from a scientific point of view but also very interesting for coastal management purposes. Coastal engineers need to forecast beach dynamics under different weather conditions, trying to predict beach erosion or accretion. So-called quantitative integrated models for beach evolution have been developed by the coastal engineering community in the last decade. They contain fully non-linear equations that describe all the known physical processes competing in the beach. Nevertheless, due to the complex mixture of length and time scales in both the hydro- and the morphodynamics of the nearshore, no reliable long-term (months-years) forecast models are available (Gallagher *et al.*, 1998; van Enckevort, 2001; Stive & Reniers, 2003). Nature may be too complex to be described by such complete models without the guidance of a strong knowledge of the short-term (days-weeks) physical mechanisms governing this environment. Another shortcoming of these integrated models is that they request a large amount of computation time (even of the order of the real time scales of natural changes). This makes them be prohibitive for investigating the effect of the different physical processes included and the sensitivity to the parameterisations used. This is the reason why they are often said to be like a *'black-box'*.

The limitations of direct modelling motivate the use of highly idealised models. Rather than making better predictions of nearshore profile and sand bar evolution, the goal of these idealised models is improving our understanding of the mechanisms responsible for bar formation and migration. The study of a particular geophysical phenomenon is done by isolating the physical processes that are expected to be most relevant and disregarding the others. A deep understanding of the results of such simpler and faster-solvable models can give insight into the whole morphodynamical behaviour of the system. Their most important limitation is that the connection of these simple models with nature is not always obvious. But the physical knowledge they learn us is crucial to guide both data acquisition and the construction of more accurate (and complicated) integrated models.

## 1.3 Previous highly idealised models

In spite of the scarcity of systematic experimental data sets of beach profiles and nearshore sand bars, some idealised theoretical explanations for their dynamical characteristics in terms of simple physical processes have been given in the past. The concept of equilibrium profile

is still very controversial among the nearshore researchers and both its definition and its shape depend strongly on the temporal and spatial scales chosen and on the approach used for modelling. However, this concept is very useful and the existing highly idealised models for the shape of equilibrium profiles are widely used by the nearshore scientific community.

The equilibrium profiles of 'non-barred beaches' used in most of the existing morphodynamical models are based on the empirical Bruun/Dean formulas. They were built to fit observations of many profiles in the U.S.A. Atlantic coast and in the Gulf of Mexico (Dean, 1977), reproducing the typical concave-up shape observed in these systems. However, these observations extended far from the coastline (up to some few kilometers). Thus, the majority of the experimental domain was well below the shoaling zone and the surf zone profile was not described in detail. Some derivations of beach profile shapes using process-based transport formulas were performed by Bowen (1980) and Bailard & Inman (1981), being able to describe the main qualitative physical properties of the observed natural equilibrium profiles. But they were again focused on modelling the wave transport in the shoaling zone, without including any of the particular processes induced by wave breaking. In the present, there is not any widely accepted idealised process-based model that describes in a simple way the main characteristics of the equilibrium profiles in the surf zone (explaining for instance the existence of the commonly observed terraces).

In order to explain the existence and properties of nearshore sand bars, two types of physical mechanisms have been presented in the past (remember that we are focusing on highly idealised models). A first type is based on the possibility that a template in the flow field with the same spatial shape as the final topography is imprinted on the seabed through the drift transport. From now on these kind of mechanisms are called *'forced response mechanisms'* because the topography is considered to be an inactive part of the process, just responding to the flow forcing. An alternative explanation for the generation of nearshore sand bars, which has been mostly disregarded in the past, lies on the concept of morphodynamical *'self-organization mechanism'*. It is based on the observed strong interactions between the changes in the bathymetry and in the flow field. This can give rise to a positive feedback between potential bars and the coupled flow modifications so that they both grow in time. Notwithstanding the potential role of the 'forced response mechanisms' and infragravity motions in the nearshore, the 'self-organization processes' are active whenever sand, waves and currents interact and should not be disregarded. Moreover, it is very plausible that both type of mechanisms interact in natural beaches under certain conditions (Holman & Sallenger, 1993; Vittori *et al.*, 1999; Short, 1999; Wijnberg & Kroon, 2002; Reniers *et al.*, 2003).

### 1.3.1   Forced response mechanisms

The 'forced response mechanisms' for the generation of nearshore sand bars rely on the hypothesis that the initial formation of these features is a passive response of the beach bottom to some non-uniform hydrodynamical forcing that displays the same length scales of the final topographic patterns. In this sense, the growth of alongshore uniform bars has been often related to the sediment transport induced by cross-shore standing waves of either high-frequency or low-frequency (Short, 1975; Bowen, 1980; Mei, 1985; Aagaard, 1991; Komar, 1998; Short, 1999; Yu & Mei, 2000). High-frequency gravity waves that are partially

reflected by the shoreline can give rise to cross-shore standing patterns that can explain the existence of multiple shore-parallel bars with spacings of tens of meters. Two examples of alongshore uniform low-frequency infragravity waves are called 'bound long waves' and 'leaky waves' (see section 1.1.2). Both are free waves that can travel through the nearshore in the perpendicular direction with respect to the shoreline. The former exists are due to the amplitude modulation of natural high-frequency waves, which very often arrive to the beach in wave groups. When the high-frequency waves break, the 'bound long wave' is released and it progresses shoreward as a free wave. It can eventually reflect at the coastline and a standing infragravity wave pattern arises in the surf zone. Out of the surf zone, the outgoing wave travels seaward freely as a 'leaky wave' (Short, 1999). These cross-shore infragravity standing waves are an example of the type of hydrodynamic template that could lead to the generation of systems of multiple shore-parallel sand bars with spacings of hundreds of meters.

On the other hand, the so-called alongshore rhythmic 'edge waves' travel in the alongshore direction and stand in the cross-shore direction. In the nearshore, the occurrence of low-frequency infragravity edge waves can be explained by several mechanisms. For instance, some reflected bound long waves that have approached the nearshore with moderate angles of incidence can be trapped by the sloping bottom due to topographic refraction (Schaffer, 1994). In some particular situations, these waves may also be partially standing in the alongshore direction, such as in case of interaction of two edge waves progressing in opposite directions because of reflection processes (in the presence of groynes, headlands or jetties). Edge waves can display alongshore wave lengths of some hundreds of meters so that the induced sediment transport could give rise to the formation of nearshore rhythmic sand bars, both oblique and crescentic (Bowen & Inman, 1971; Holman & Bowen, 1982; Aagaard, 1991).

The major shortcoming of the standing infragravity wave hypothesis is the lack of well-established selection criterion for the mode, frequency and phase of the infragravity wave/s responsible for the growth of the features (Holman & Sallenger, 1993; Falqués *et al.*, 1996; Short, 1999; Wijnberg & Kroon, 2002). Some mechanisms have been suggested in the past that may sometimes explain the selection of a certain wave mode, frequency and phase (Aagaard, 1991; Short, 1999), but no quantitative computations that validate such hypothesis have been performed. Another important particularity is that none of these highly idealised models take into account is the possible feedback of morphological changes into the hydrodynamics. Moreover, these models do not consider the influence of the breaking phenomenon so they could likely explain the systems of bars that typically grow in deeper water (such as the shoaling zone, where breaking processes are not essential), rather than describing bars in the breaker and surf zones (Mei, 1985; Komar, 1998).

Some experimental evidences of the influence of infragravity waves in the nearshore morphology have been reported in the literature (Bauer & Greenwood, 1990; Aagaard, 1991; Short, 1999). However, many other field and laboratory observations have found evidences in support of the 'self-organization hypothesis' (Holman & Sallenger, 1993; Aagaard *et al.*, 1998; Short, 1999; van Enckevort, 2001). Finally, some few recent theoretical studies combining the two types of mechanisms have been described (Vittori *et al.*, 1999; Reniers *et al.*, 2003). This latter piece of work presents numerical results in favour of a 'self-organization mechanism' for the generation of a crescentic bar in a embayed beach under wave group forcing (so allowing
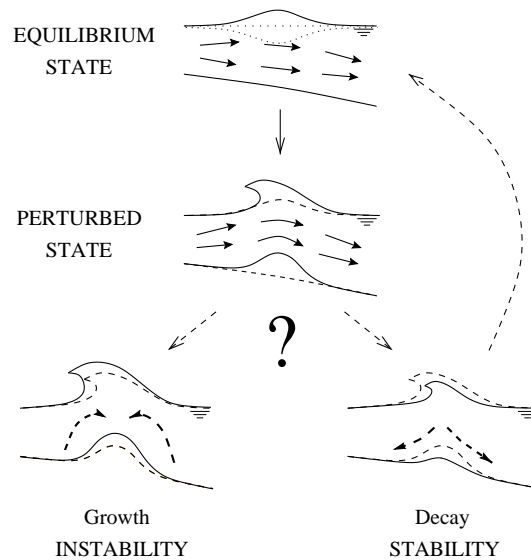
Figure 1.3.1: Self-organization mechanism in the nearshore. The solid arrows stands for the currents and the dashed arrows for the sediment transport. A steady equilibrium configuration of the underwater beach without the patterns is assumed. Then, an arbitrary small topographic perturbation is added to the equilibrium and its effect on the hydrodynamics and on the sediment transport is investigated. In this example, an arbitrary shoal superimposed to the equilibrium beach configuration induces changes in the wave breaking and the current distribution. This modifies in turn the sediment transport pattern, which may either damp or reinforce the shoal. In the latter case a positive feedback occurs between the flow and the morphology so that both perturbations will grow exponentially in time.

for the occurrence of edge waves). Their main result is the formation of a crescentic bar both with and without the presence of edge waves (with very similar wave lengths), so that the edge waves forcing is not essential. In fact, the emergence of edge waves with the wave length of the underlying crescentic pattern is found. The results even indicate that the main contribution of these infragravity waves in the sediment transport is that the underlying bathymetry is smoothed.

## 1.3.2   Self-organization mechanisms

The second type of bar generating mechanisms is based on the strong non-linear feedback that has been found in the surf zone between the hydrodynamics (mainly high-frequency waves and 'mean' currents) and the bottom evolution (Short, 1999; Plant *et al.*, 2001*a*). Figure 1.3.1 shows a small diagram illustrating a simple version of a 'self-organization process'. A steady equilibrium and uniform configuration of the beach without the pattern is assumed. Then, an arbitrary small topographic perturbation is added to the equilibrium and

its effect on the hydrodynamics and on the sediment transport is investigated. For instance, a shoal superimposed to the equilibrium beach configuration induces certain changes in the wave breaking and the current distribution. In turn, this modifies the sediment transport pattern, which may either damp or reinforce the shoal. In the former case, the equilibrium configuration is recovered so that it turn out to be stable. In the latter case a positive feedback occurs between the flow and the morphology so that both perturbations grow exponentially in time. This results in what is called a *'free instability'* of the system (a type of 'self-organization process') and may provide an explanation for the growth of nearshore sand bars, without any need for the existence of a previous spatial template in the hydrodynamic forcing.

There are several ways of testing possible 'self-organization processes' in a morphodynamical system. For instance, some *cellular automata models* have been able to describe beach cusp formation (Werner & Fink, 1993; Coco *et al.*, 2000) and shoreline sand waves (Ashton *et al.*, 2001). These highly idealised models describe the coupling between the bed evolution and the motion of water particles using very simple rules physically based (without the partial differential equation approach typically used in the description of continuum mechanics). *Stability analysis* is another classical mathematical tool that allows to search for 'free instabilities' of a morphodynamical system (Hulscher *et al.*, 1993; Calvete, 1999; Dodd *et al.*, 2002).

The first step in any stability analysis is finding a *basic state*, which physically means a simple but relevant equilibrium solution of the equations without any pattern. Then, this basic state is perturbed with arbitrary small topographic and hydrodynamic irregularities. The corresponding linear variables are introduced in the equations and then the latter are linearised. This means that only the terms proportional to the linear variables are kept (and the terms proportional to a power two or more of the linear variables are neglected). The concept behind such *linear stability analysis* is that of *'normal or linear mode'*. It comes from the fact that the dependence of the linear variables on the time and on the spatial variables of the problem can be studied separately. The 'normal modes' of a certain linearised dynamical system are the spatial configurations verifying that all the points evolve at the same time, so that these modes maintain their shape during the time evolution of the system. Therefore, they can be characterized just by their shape at a certain moment, the growth rate and the migration celerity. Many linearised dynamical systems allow for the definition of a set of 'normal modes' that form a complete basis of functions. In these cases, any solution of the corresponding set of equations can be conceptually expanded in such 'normal modes'. The origin of the name 'normal mode' comes from the classical theory of oscillators.

For all the morphodynamical problems known that have a flat-bed and an unbounded basic state, an expansion can be done in Fourier sinusoidal modes in the two horizontal directions, which can be distinguished by the different wave numbers, $(\kappa_x, \kappa_y)$ (for instance see Huthnance (1982)). In the nearshore, this simple expansion can only be done in the alongshore direction (if it is unbounded and uniform), so that the spatial structure of the normal modes is sinusoidal in the y-direction and can be characterized by an alongshore wave number, $\kappa_y$. In the bounded and non-uniform cross-shore direction, the modes have a more complicated structure that has to be approached numerically. The results of a linear stability analysis are the spatial cross-shore structure, the growth rate and the migration celerity of

each normal mode. When the basic state is stable, all the modes have negative growth rates and so they tend to disappear. But when the basic state is unstable, the analysis lead to positive growth rates of certain modes for a range of alongshore wave numbers. This results in a topography and a hydrodynamical field initially dominated by the pattern corresponding to the *'fastest growing mode'*. The wave lengths of the observed rhythmic nearshore bars in nature can then be compared with this result. A linear stability analysis also indicates whether the basic state is unstable or not and whether the equations contain the physical processes capable to produce a certain pattern by self-organization.

The information given by such linear stability analysis is only valid for the initial formation of the bars. In order to obtain information about the long-term behaviour of the system, a *non-linear stability analysis* must be performed. This means dealing with the full equations without linearising and gives essential information about the new equilibrium situation reached, such as the final amplitude, shape and migration of the patterns. Sometimes, the linear 'fastest growing mode' already contains the essential behaviour of the final equilibrium situation. But nature displays often complex situations such as the one shown in Fig. 1.2.11. The behaviour of such complex beach out of equilibrium may be described as a non-linear competition between the different normal modes of the linear stability analysis (Calvete & de Swart, 2003). In any case, a good knowledge of the 'normal or linear modes' provides a better understanding, not only of the nearshore bar generation, but also of the surf zone morphodynamics in general.

### 1.3.3   Previous stability analysis of the nearshore system

The stability analysis approach has been applied to test the possibility of a 'self-organization' origin of several types of topographic sandy bedforms in nature. The generation of river sand dunes, antidunes and alternate bars as a 'self-organization process' is well documented since the eighties (Blondeaux & Seminara, 1985; Colombini *et al.*, 1987; Schielen *et al.*, 1993; Seminara, 1995). This hypothesis has also been applied to the inner shelf to explain the growth of sand waves, shoreface-connected sand ridges and tidal sand banks (Huthnance, 1982; Pattiaratchi & Collins, 1987; Hulscher *et al.*, 1993; Trowbridge, 1995; Hulscher, 1996; Calvete *et al.*, 2001; Calvete & de Swart, 2003). Returning again to the nearshore environment, stability analysis has proved to to be suitable to study for instance the formation of sea ripples (Blondeaux, 1990; Vittori & Blondeaux, 1990).

Even if shore-parallel bars are spatially simpler features, the stability analysis approach related to nearshore bars was first suggested to explain rhythmic features (Sonu, 1968). Early applications of linear stability analysis to describe the generation of shore-parallel/oblique bar systems and crescentic bars can be found in Barcilon & Lau (1973) and Hino (1974). During the eighties, the 'edge wave forcing hypothesis' gained supporters (Holman & Bowen, 1982) and stability analysis was abandoned. In the nineties, an increasing interest in this latter approach raised, and the early investigations were revisited and extended in a systematic way by Falqués (1991), Christensen *et al.* (1994), Falqués *et al.* (1996), Deigaard *et al.* (1999), Falqués *et al.* (2000) and Caballeria *et al.* (2002).

Due to the large amount of processes competing in the nearshore, the different physical mechanisms that can account for the generation of nearshore rhythmic patterns through

self-organization were first established and studied in isolation in these works. A first set of papers described the generation of rhythmic topography due to the coupling between the growing pattern and the perturbations produced in an otherwise alongshore uniform current, that could be induced by the wind, by river discharges or by breaking waves arriving obliquely (Barcilon & Lau, 1973; Falqués, 1991; Falqués *et al.*, 1996). However, the growing shoals in the surf zone also modify the incident wave field itself. This effect can occur in isolation in case of normal wave incidence and it can be the mechanism responsible for the generation of crescentic bars and shore-normal bars in the nearshore (Falqués *et al.*, 2000; Caballeria *et al.*, 2002).

The preliminary piece of work of Hino (1974) was the first quantitative description of the interaction of the growing topography with an obliquely incident wave field and the induced longshore current at the same time. The same physical approach was later revisited and improved by Christensen *et al.* (1994). The rhythmic bar systems obtained in these models remind of nearshore oblique bars observed in nature, but many problems remain open and must be tackled. First, the orientation of the oblique bars with respect to the longshore current direction is still misunderstood. For instance, these two latter works gave contradictory results, the bars by Christensen *et al.* (1994) being at odds with the most often observed down-current orientation. Second, understanding and describing the physical mechanisms was often left aside in all these works, a fact that is linked with an obscure parameterisation of the sediment transport. Another limitation of the approach presented by Christensen *et al.* (1994) is that only the dominant mode was there obtained, instead of the whole manifold of unstable modes.

As a result of all the works presented above, the hypothesis that nearshore rhythmic sand bars stem from 'free instabilities' of the alongshore uniform equilibrium seems sensible (although many unknowns remain unsolved, specially for the case of transverse/oblique bars). It is therefore conceivable that alongshore uniform bars could also stem from a previously 'non-barred equilibrium profile' as free instabilities with zero alongshore wave number, $\kappa_y = 0$. This was not the case in the models described in the previous paragraphs of this section because the stability analysis performed were based on current-driven sediment transport (whose divergence is zero in the alongshore uniform situation) whereas cross-shore transport was assumed to be in balance.

The first step to describe the growth of shore-parallel bars is to use a sediment transport formulation accounting for physical processes that could be responsible for their generation. A physical mechanism that has been pointed out to be responsible for the growth of shore-parallel sand bars by breaking waves is the *'breakpoint-bar interaction'*. The main processes involved in this mechanism are the offshore sediment transport due to undertow (mainly inside the surf zone) and the onshore transport due to non-linearities of the incident wave field. Many authors mention this mechanism as being responsible for most of the shore-parallel bars generated in the surf zone, both in nature and in the laboratory (King & Williams, 1949; Dyhr-Nielsen & Sorensen, 1970; Dally, 1987; Larson, 1988). However, no process-based quantitative models have been built so far, and consequently this statement has never been well-substantiated. Given a set of equations that accounts for these cross-shore transport processes, it seems plausible that shore-parallel bars emerge either as an equilibrium configuration of the morphodynamic system or as free instabilities of previously 'non-barred equilibrium profiles'.

## 1.4   Aim, approach and outline of the thesis

The main goal of this thesis is to investigate theoretically the physical processes that can be responsible for the shape of equilibrium profiles and the origin and dynamics of nearshore sand bars (both alongshore uniform and alongshore rhythmic). This may fill some of the existing gaps in our current knowledge about these topographic features.

The specific objectives can be formulated as seven detailed research questions that are addressed throughout the thesis:

1. What are the main physical processes responsible for the shapes of alongshore uniform equilibrium beach profiles?

2. In which situations these equilibrium configurations are stable?

3. Can nearshore sand bars stem from instabilities of the equilibrium configurations of the morphodynamical system?

4. What physical mechanisms are able to describe the generation of these sand bar systems through self-organization and what are their crucial parameters?

5. What are the main characteristics of the shape and the dynamics of nearshore sand bars?

6. In what equilibrium beach states and under what weather conditions these sand bar systems emerge?

7. What are the essential properties of the sediment transport formulas that explain the morphodynamical behaviour of the beaches?

In order to understand deeply the basic physics governing beach morphodynamics, highly idealised morphodynamical models are used. They consist on a set of dynamical equations that are simultaneously solved in a schematised geometry. The simplest formulation that still encapsulates the physical processes that are supposed to be involved in the different studied mechanisms is chosen, so that these processes can be studied in isolation. In this sense, several approximations are systematically used throughout this thesis. A time-averaged version of the depth-averaged shallow water equations is used, with the implicit assumption that describing explicitly the vertical structure of the quantities is not essential. The effect of the filtered fast processes (for instance wave oscillatory motions and turbulence) and the possible vertical stratification are parameterised when necessary. The possible self-organization origin of nearshore bars is investigated by means of performing a stability analysis of the nearshore morphodynamical system. To focus on the results of this self-organization working hypothesis in isolation, the possible effect of the low-frequency hydrodynamical oscillations is left aside. The alongshore uniform and the alongshore non-uniform situations (2D and 3D cases) are studied separately, with the implicit assumption that their time scales are distinct enough. An exhaustive exploration of the physical parameter space is always performed.

The rest of the thesis is divided into five main chapters with the following contents:

**Chapter 2** describes in detail the general **theoretical framework** used to study the nearshore region: frame of reference, wave transformation, hydrodynamical equations and sediment transport formulations, together with a detailed description of the general assumptions used (such as the time and depth averages). The particular equations used in the other chapters follow from this general formulation.

**Chapter 3** presents a highly idealised model for describing sensible **equilibrium beach profiles**, which are the starting point of the stability analysis performed in the other chapters. At the same time, the research questions 1 and 7 posed above are addressed, with the assumptions of alongshore uniformity and equilibrium conditions. To this aim, a semi-empirical formulation for the cross-shore sediment transport coupled with a wave energy conservation equation for normally incident random waves are used. The transport formula contains in a simplified way the processes that have been recognised to be involved in the 'breakpoint-bar mechanism'. Therefore, shore-parallel bars might be sand features found in the equilibrium configuration of this system (in this case, the questions 2 to 6 would also be addressed).

**Chapter 4** addresses the research questions 2 to 7 assuming alongshore uniformity and using the working hypothesis that the formation of **shore-parallel sand bars** can result from a 'self-organization process'. To this aim, it presents a complete stability analysis in the cross-shore direction of the equilibrium profiles found in chapter 3 (studying both the linear and the non-linear regimes). The equations used describe the same physics as the equations of chapter 3, but now the possibility that shore-parallel bars emerge from free instabilities of previously 'non-barred equilibrium profiles' is investigated. The non-linear temporal evolution of the dynamical system moderately far from equilibrium is also studied and some attention is paid on describing the migration of shore-parallel bars.

**Chapter 5** addresses the research questions 2 to 7 allowing for alongshore inhomo-geneities and using the hypothesis that the formation of rhythmic systems of **oblique sand bars** can result from a 'self-organization process'. To this aim, it revisits the problem of generation of oblique sand bars (and in a lower degree 'crescentic longshore bars') from an initially alongshore uniform 'plane beach' under oblique wave incidence. The interactions of the growing features with both the oblique wave field and the generated longshore current are described. A classical process-based formulation for the sediment transport by 'mean' currents is here coupled with the hydrodynamical equations describing fluid mass and momentum conservation. In this case, the mathematical tool used is a linear stability analysis of the system of equations.

**Chapter 6** contains the **overall conclusions** of this thesis. Firstly, the aim, the approach and the main results are summarized. The seven research questions posed above are subsequently answered. Finally, some suggestions for further research about the studied topics are given.

The main publications related with the research topics presented in this thesis are specified herein. Based on **chapters 3 and 4:**

Ribas, F., Falqués, A., Hulscher, S. J. M. H. & Plant, N. G. 2003$a$ Dynamics and stability of cross-shore beach profiles. *J. Geophys. Res.* In preparation.

Ribas, F., Falqués, A., Plant, N. G. & Hulscher, S. J. M. H. 2001$b$ Self-organization in surf zone morphodynamics: alongshore uniform instabilities. In *Coastal Dynamics 2001* (ed. H. Hanson & M. Larson), pp. 1068–1077. Reston, Va.: Am. Soc. of Civ. Eng.

Hulscher, S. J. M. H., Falqués, A., Ribas, F. & Plant, N. G. 2001 Asymptotic behaviour of a coupled waveheigth-depth model near the coastline. In *Proc. $2^{nd}$ IAHR Symposium on River, Coastal and Estuarine Morphodynamics* (ed. S. Ikeda), pp. 345–354. Obihiro, Japan.

And based on **chapter 5:**

Ribas, F., Falqués, A. & Montoto, A. 2003$b$ Nearshore oblique sand bars. *J. Geophys. Res.* **108** (C4), 3119, doi:10.1029/2001JC000985.

Ribas, F., Falqués, A. & Montoto, A. 2000$a$ Normal mode analysis of the surf zone morphodynamics. In *Coastal Eng. 2000* (ed. B. L. Edge), pp. 3229–3242. Reston, Va.: Am. Soc. of Civ. Eng.

Ribas, F., Montoto, A. & Falqués, A. 2000$b$ Sensitivity of rhythmic oblique bar generation to wave-driven turbulence in the surf zone. In *Proc. $8^{th}$ European Turbulence Conf.: Advances in turbulence*, pp. 375–378.

Falqués, A., Ribas, F., Montoto, A. & Larroude, P. 1999 Nearshore oblique bars. Modelling versus observations at the Truc Vert Beach. In *Proc. $1^{st}$ IAHR symposium on River, Coastal and Estuarine Morphodynamics,* vol. 1, pp. 207–216.

# Chapter 2

# General formulation

## 2.1 Waves, currents and bed evolution

Many hydrodynamical processes at different length and time scales coexist and interact in the nearshore zone: tides, low-frequency waves, coastal currents, high-frequency waves and turbulent motions (see Fig. 1.1.2). The sandy bottom of the beach is easily eroded due to the friction forces induced by these different flows. The sediment particles are then moved by the currents and deposited further, leading to strong sediment transport processes. This latter phenomenon changes the topography, which in turn can modify the hydrodynamics. This chapter is aimed at presenting the general governing equations used in the rest of the thesis for describing these different dynamical processes, including a detailed description and justification of the main assumptions.

Bed evolution, which is slower than hydrodynamical changes, sets the time scales we seek to describe. In the framework of our approach of isolating the basic physical processes, it makes sense to perform a time average of both the equations and the variables in order to filter the faster motions. This allows to focus in the *'mean'* hydrodynamical processes that are important for the physical mechanisms we want to understand (from 1 hour to months). The effect of the faster processes (mainly high-frequency waves and turbulence) must then be parameterised. Wave orbital motions are the main forcing of our system and wave breaking, turbulent motions and bottom friction are the most important hydrodynamical dissipative mechanisms. The possible effect of low-frequency hydrodynamical oscillations in the nearshore is not taken into account in this thesis as we seek to isolate and investigate the 'self-organization processes' that can result from the interaction of sand, waves and currents. On the other hand, the long time scale tidal waves could also have a certain influence in our own time and length scales, but investigating their effect is far beyond the scope of this thesis. The time-averaged fluid velocities and sediment concentration can exhibit a certain vertical structure. For the sake of isolating the basic processes, this vertical structures are not explicitly described as we use the depth-averaged shallow water theory. The influence of this possible vertical stratifications comes into the sediment transport formula through

parameterisation if necessary. The resultant hydrodynamic formulation used is based on the previous studies by Phillips (1977) and Battjes *et al.* (1990).

This first section presents the frame of reference, the variables used and the time and depth averages. The main forcing of our system is are 'wind or swell waves' arriving to the nearshore from deep water. For clarity of presentation, section 2.2 first presents separately some kinematic and dynamic laws for small-amplitude surface gravity waves advancing over a given slowly-varying water depth in the presence of steady 'mean' currents. But this is not by means a complete description of nearshore morphodynamics because both the currents, $\vec{v}$, and the water depth, $D$, are also unknowns of our dynamical problem. Section 2.3 presents the equations that describe the dynamics of both currents and waves at the same time, taking into account their interaction. The parameterisations of the fast processes that are filtered by the time average and of the vertical stratifications that are filtered by the depth average of the equations are also presented.

Section 2.4 finally introduces the mass conservation equation that can describe the evolution in time of the movable bottom. The influence of currents and waves comes into this equation through the parameterisation of the sediment transport. Modelling this latter quantity is poorly achieved and many different formulations can be found in the literature. Section 2.5 presents the two different formulations that best fit into our approach (idealised models that describe the physical processes). In this respect, a semi-empirical model for cross-shore wave transport, including the main processes of the 'breakpoint-bar mechanism', is used in chapters 3 and 4. On the other hand, the study presented in chapter 5 uses a process-based model for transport driven by relatively depth-uniform 'mean' currents.

## 2.1.1   Frame of reference and independent variables

The first simplification that must be done in any description of a complex system (by means of an idealised physical model) is choosing only a few coordinates and variables. An infinite and rectilinear beach originally uniform in the alongshore direction can be representative of most of the open beaches in the world. Figure 2.1.1 shows a 3D view of such an schematic beach, where the frame of reference and the variables selected to describe the growth of nearshore sand bars are displayed.

We adopt a Cartesian coordinate system located in the horizontal plane of the 'mean' sea water level in case of still water, with horizontal axes $x$ and $y$, or $x_1$ and $x_2$. The first case corresponds to the vector notation, $\vec{x}$, whereas the second case makes use of the tensor notation, $x_i$, where the index $i = 1, 2$ indicate 2D vectors. The $x_2$ axis is chosen to coincide with the rectilinear shoreline and is called alongshore direction. The cross-shore direction is described by the $x_1$ axis and increases offshore. Its origin is the 'mean' shoreline, i.e. the point where the total water depth vanishes in the reference equilibrium state (the temporal average that defines the meaning of 'mean' will be given later on). This location is not pre-determined and has to be computed for each dynamical problem. For instance, in the example shown in Fig. 2.1.1, a certain elevation of the free surface is produced in the inner surf zone due to wave forcing, so that the shoreline is shifted onshore with respect to its position in case of still water. The $z$ axis is the vertical direction and increases upwards. Its origin corresponds with the position of the 'mean' sea water level (in case of still water).
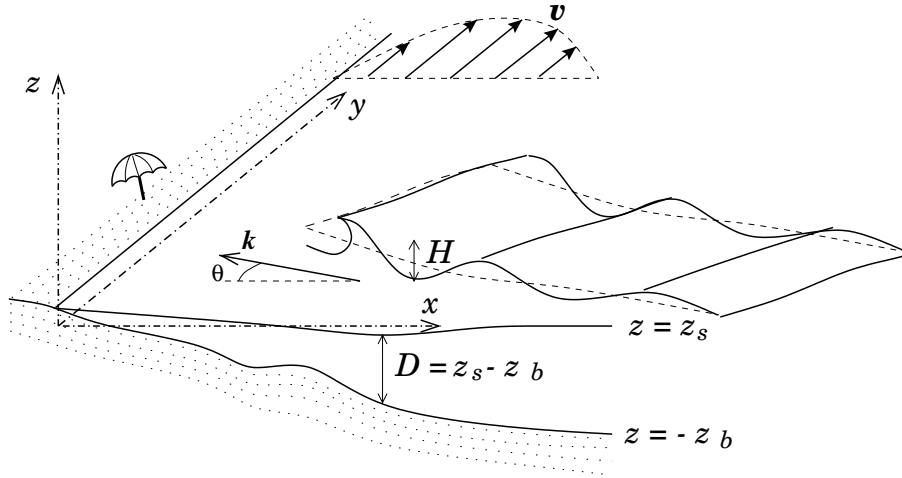
Figure 2.1.1: Frame of reference chosen to describe the growth of nearshore sand bars. The dependent variables are the wave height, $H$, the wave incidence angle, $\theta$, the wave number, $k_w$, the depth- and time-averaged fluid velocity, $v_i$, the mean free surface elevation, $z_s$ and the bottom surface, $z_b$, with the total water depth being $D = z_s - z_b$. These variables are allowed to depend on the horizontal coordinates, $(x, y)$, and on a slowly-varying time, $t$.

## 2.1.2 Dependent variables

Waves arriving to the nearshore generate a complicated 3D field of fluid velocities indicated by $\tilde{u}_\alpha(x_1, x_2, z, t^*)$ (the index $\alpha = 1, 2, 3$ is used for the tensor notation of 3D vectors). The instantaneous time, $t^*$, which can describe the rapid oscillations induced by wave orbital motion, stands for the fourth independent variable. Apart from the organized wave oscillatory motion, the other important high-frequency hydrodynamical process is the fluctuating turbulence induced mainly by wave breaking (see Fig. 1.1.2). It is useful to separate conceptually the fluid velocities of the nearshore into time-averaged ('mean') currents plus fluctuations from this average value (the corresponding integration in time will be described later on),

$$\tilde{u}_\alpha(x_1, x_2, z, t^*) = \bar{u}_\alpha(x_1, x_2, z, t) + u'_\alpha(x_1, x_2, z, t^*) + u''_\alpha(x_1, x_2, z, t^*) \ , \qquad (2.1.1)$$

where $\bar{u}_\alpha$ stands for the 'mean' currents and the fluctuations have been in turn separated into wave orbital motion, $u'_\alpha(x_1, x_2, z, t^*)$, and turbulent velocities, $u''_\alpha(x_1, x_2, z, t^*)$. A slowly-varying time, indicated by $t$, allows for describing the variations of some variables with a time scale much slower than the fast wave orbital and turbulent motions. The distinction between slowly-varying currents ('mean') and rapidly-varying motions ('fluctuations') is possible because they have widely separated time scales. This formulation is described in detail in Phillips (1977), Mei (1989) and Battjes $et\ al.$ (1990).

The the free surface elevation, $\widetilde{z_s}(x_1, x_2, t^*)$, is the other important hydrodynamical variable. It can be defined as the boundary between air and water and it can also be
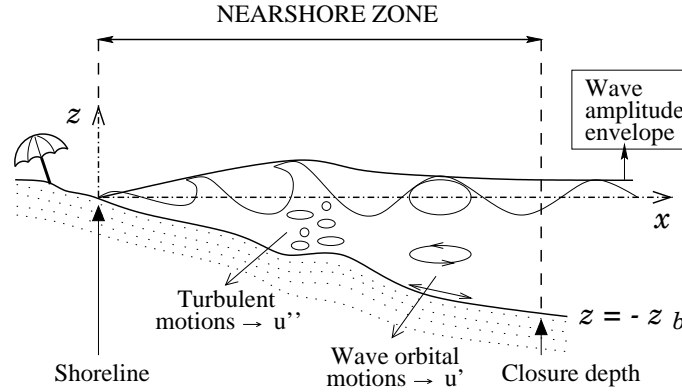
Figure 2.1.2: Cross-shore profile of a beach with the main hydrodynamical processes. The disordered turbulent eddies and the ordered wave orbital velocities are displayed, together with the envelope of the wave amplitude. This cross-shore section can be obtained from Fig. 2.1.1 taking $x_2$ equal to the parasol location, for instance.

conceptually divided into its 'mean' and 'fluctuating' contributions,

$$\widetilde{z}_s(x_1, x_2, t^*) = \bar{z}_s(x_1, x_2, t) + z'_s(x_1, x_2, t^*) + z''_s(x_1, x_2, t^*) \quad , \tag{2.1.2}$$

where $z'_s(x_1, x_2, t^*)$ stands for the rapid oscillation of the free surface elevation produced by a train of surface gravity waves entering in the nearshore region.

A sinusoidal monochromatic wave train can be described as

$$z'_s(x_1, x_2, t^*) = \frac{H}{2} e^{i\Phi} \quad and \quad u'_\alpha(x_1, x_2, z, t^*) = u'_{\alpha o} e^{i\Phi} \quad , \tag{2.1.3}$$

where $\Phi(x_1, x_2, t^*)$ is the phase, $H(x_1, x_2, t)$ is the wave height (defined as twice the wave amplitude) and $u'_{\alpha o}(x_1, x_2, z, t)$ gives the amplitudes and directions of the three components of the wave orbital velocity ($\alpha = 1, 2, 3$). It is obvious that the two latter quantities directly depends on the slow-varying time $t$, whereas the phase follows the rapid oscillations described by $t^*$. Figure 2.1.2 shows a possible cross-shore section of Fig. 2.1.1 (taking $x_2$ equal to the parasol location, for instance), where one may see represented the wave amplitude ($H/2$) and the two 'fluctuating' velocities, $u'_\alpha$ and $u''_\alpha$.

The wave number $\vec{k}_w(x_1, x_2, t)$ and the frequency $\omega(x_1, x_2, t)$ of the incident wave train also turns out to depend on the slow time $t$, although they are obtained from the wave phase,

$$\vec{k}_w = \nabla\Phi \quad , \tag{2.1.4}$$

$$\omega = -\frac{\partial\,\Phi}{\partial t^*} \quad , \tag{2.1.5}$$

where $\nabla$ is the horizontal gradient operator

$$\nabla = (\nabla_1, \nabla_2) = \left(\frac{\partial}{\partial x_1}, \frac{\partial}{\partial x_2}\right) \quad . \tag{2.1.6}$$

In our formulation, waves arrive at the nearshore with a certain angle with respect to the shore-normal direction, $\theta(x_1, x_2, t)$, that can be defined from the wave number and hence from the wave phase. The incidence angle is defined with respect to the onshore direction and it is taken positive clockwise (see Fig. 2.1.1), so that the following identities are verified,

$$\theta = \text{arctg}\left(-\frac{k_2}{k_1}\right) = \text{arctg}\left(-\frac{\nabla_2 \Phi}{\nabla_1 \Phi}\right) \quad , \tag{2.1.7}$$

$$k_{w1} = -k_w \cos\theta \quad , \qquad k_{w2} = k_w \sin\theta \quad . \tag{2.1.8}$$

The wave length, $\lambda_w(x_1, x_2, t)$, and the wave steepness, $\xi_w(x_1, x_2, t)$ are also defined from the wave phase,

$$\lambda_w = \frac{2\pi}{k_w} = \frac{2\pi}{|\nabla\Phi|} \quad , \tag{2.1.9}$$

$$\xi_w = \frac{H}{\lambda_w} = \frac{H\,|\nabla\Phi|}{2\pi} \quad . \tag{2.1.10}$$

The description of the bed evolution and the sediment transport requires the use of more variables related with the sand and the bottom topography. The concentration of sediment in suspension, which in principle is an oscillatory field depending on the fast fluid motions, is indicated by $\tilde{c}(x_1, x_2, z, t^*)$. Bottom surface, $z = z_b(x_1, x_2, t)$, evolves with a much slower time. Another variable, which is often used to describe bed evolution instead of the bottom surface, is the total water depth,

$$\widetilde{D}(x_1, x_2, t^*) = \widetilde{z_s}(x_1, x_2, t^*) - z_b(x_1, x_2, t) \quad . \tag{2.1.11}$$

## 2.1.3   Time average

As it has already been underlined in section 1.1.2, only the processes at time scales ranging from some few hours to months are explicitly described in this thesis. The fastest phenomena are filtered out from the equations through a time integration over a period of the order of $T \sim 10 - 100$ minutes, which is long compared with the characteristic hydrodynamical time scales, yet short compared with our morphodynamical time scales. Some of the variables defined in the last section are independent of the rapid oscillation of waves by definition ($H$, $\vec{k}$, $\omega$ and $z_b$). The variables that do depend on $t^*$ are separated into 'mean' and 'fluctuating' motions (see for instance Eqns. (2.1.1) and (2.1.2)). The corresponding 'mean' quantities are computed through the integral on time

$$\bar{f}(t) = \left\langle \tilde{f}(t^*) \right\rangle = \frac{1}{T} \int_{t-T/2}^{t+T/2} \tilde{f}(t^*)\, dt^* \quad . \tag{2.1.12}$$

where $t^*$ is again the instantaneous time, whereas $t$ is the final slower time we are explicitly describing. The period used for this integration can be interpreted as an arbitrary large multiple of the incident wave period, $T_p$. The use of such a multiple (instead of the wave period itself), diminishes the errors produced by the small remainders of the integral average caused by the random dispersion of the wave period around $T_p$, which is present in real wave fields.

The temporal average filters both wave and turbulent rapid motions. Even though these two fast and small scale processes are not being explicitly described in our formulation, they can strongly influence the dynamics at our slow time and large length scales. The divergence of the horizontal momentum flux related with wave orbital motions stands for the external forcing of the system and turbulent motions are an important mechanism of hydrodynamic energy dissipation. On the other hand, hydrodynamical processes at slower time scales such as low-frequency waves and tidal waves (see again Fig. 1.1.2) could also influence our time and length scales. As we are interested in describing the 'self-organization processes' related with the interaction of the bottom with high-frequency waves and 'mean' currents, we neglect the possible effect of the low-frequency hydrodynamical oscillations (see a discussion about this in section 1.3). In fact, the integration time, $T$, could also be seen as a multiple of these long periods of oscillation, so that low-frequency motions would also be filtered by the integral given in Eq. (2.1.12). The slow tidal waves are in principle considered to be an external and known forcing of the system. However, in order to focus on the simplest formulation that still allows us to describe the physical processes we are interested in, tidal motions are not taken into account either. Finally, the temporal integration also filters the fast shoreline oscillations, so that the swash zone disappears and we just deal with a 'mean' (time-averaged) shoreline. This approach follows from the books by Phillips (1977) and Battjes *et al.* (1990).

Using this temporal integration the 'mean' variables can be defined as

$$\bar{u}_\alpha(x_1, x_2, z, t) = <\tilde{u}_\alpha(x_1, x_2, z, t^*)> \text{ , for the fluid velocity,}$$

$$\bar{z}_s(x_1, x_2, t) = <\tilde{z}_s(x_1, x_2, t^*)> \text{ , for the free surface elevation,}$$

$$\bar{D}(x_1, x_2, t) = <\tilde{z}_s - z_b> \text{ , for the total water depth,}$$

$$\bar{c}(x_1, x_2, z, t) = <\tilde{c}(x_1, x_2, z, t^*)> \text{ , for the suspended sediment concentration,}$$

where $\alpha = 1, 2, 3$ and $\left\langle \tilde{f}(t^*) \right\rangle$ indicates the time average of a variable $f$ given by Eq. (2.1.12). From now on, the overbar symbol is skipped for the sake of brevity. When we need to refer to a variable that still depends on the fast time scale, we will indicate it by its symbol with the tilde $\tilde{f}$.

## 2.1.4   Depth average

The time-averaged fluid velocities and sediment concentration exhibit a certain vertical structure. In order to simplify the description of our physical system, we use the *shallow water theory* (Phillips, 1977; Pedlosky, 1987; Mei, 1989). The main hypothesis of this theory is that the horizontal scales are much larger than the vertical scales, which leads to horizontal velocities that are also much larger than the vertical velocities (due to water mass conservation). This allows us to define a characteristic value of the horizontal velocities and sediment concentration that can be representative of the whole water column. Both the variables and the governing equations are vertically averaged, so that their dependence on the vertical coordinate is not described explicitly. However, it is important to underline that some of the quantities involved in the description of the nearshore system can have a very strong vertical stratification (specially the fluid velocities, $\bar{u}_\alpha$, and the sediment concentration, $\bar{c}$).

As we use the shallow water theory, the possible influence on the described dynamics of such vertical stratification must be parameterised when it is necessary. The second important assumption done in the shallow water theory is that the hydrostatic pressure is the only contribution to the pressure field that is accounted for (Phillips, 1977).

In the framework of the shallow water theory, the fluid motions are described using a depth- and time-averaged horizontal velocity,

$$
v_i(x_1, x_2, t) = \frac{1}{D} \left\langle \int_{\tilde{z}_b}^{\tilde{z}_s} \tilde{u}_i(x_1, x_2, z, t^*) \, dz \right\rangle \quad , \qquad i = 1, 2 \quad , \tag{2.1.13}
$$

which indicates a representative value of the velocity of the water column. The variable $v_i$ is also sometimes called water mass flux velocity because it defines the total water mass flux, $\vec{\mathcal{M}}$, across a vertical plane of unit width,

$$
\vec{\mathcal{M}} = \rho \, \vec{v} \, D \quad . \tag{2.1.14}
$$

This time- and depth-averaged water mass flux (and hence the time- and depth-averaged velocity, $\vec{v}$) can be conceptually divided into three contributions,

$$
\mathcal{M}_i = \overline{\mathcal{M}}_i + \mathcal{M}'_i + \mathcal{M}''_i \quad , \qquad i = 1, 2 \quad . \tag{2.1.15}
$$

The first one is produced by the 'mean' currents (maybe depth-varying), the second one by the wave oscillatory motions and the third one by the turbulent motions,

$$
\overline{\mathcal{M}}_i = \int_{\tilde{z}_b}^{\tilde{z}_s} \rho \, \bar{u}_i(x_1, x_2, z, t) \, dz \quad , \qquad i = 1, 2 \quad ,
$$

$$
\mathcal{M}'_i = \left\langle \int_{\tilde{z}_b}^{\tilde{z}_s} \rho \, u'_i(x_1, x_2, z, t^*) \, dz \right\rangle \quad , \qquad i = 1, 2 \quad , \tag{2.1.16}
$$

$$
\mathcal{M}''_i = \left\langle \int_{\tilde{z}_b}^{\tilde{z}_s} \rho \, u''_i(x_1, x_2, z, t^*) \, dz \right\rangle \quad , \qquad i = 1, 2 \quad .
$$

The contribution to water mass transport due to turbulence, $\mathcal{M}''_i$, is normally negligible. The contribution of waves, $\mathcal{M}'_i$, arises from the correlation between the free surface elevation and the horizontal water particle velocities (it is also called *'Stokes drift contribution'*). It can be interpreted as a transport of water mass between the trough and crest levels. This mass transport due to the wave orbital motion will be computed in the next section, after choosing a certain expression for the wave induced velocities, $u'_i$. Finally, $\overline{\mathcal{M}}_i$ contains the contribution to water mass transport due to the possible existence of 'mean' currents below the trough level. The vector $\mathcal{U}_i$ stands for the depth average of these 'mean' currents that can exist from the bottom to the trough level, and it can be hence written in terms of the 'mean' mass transport, $\overline{\mathcal{M}}_i$,

$$
\mathcal{U}_i(x_1, x_2, t) = \frac{1}{D} \int_{\tilde{z}_b}^{\tilde{z}_s} \bar{u}_i(x_1, x_2, z, t) \, dz = \frac{\overline{\mathcal{M}}_i}{\rho \, D} \quad , \qquad i = 1, 2 \quad , \tag{2.1.17}
$$

Isolating $\overline{\mathcal{M}}_i$ from Eq. (2.1.15), using Eq. (2.1.14) for $\mathcal{M}_i$ and neglecting $\mathcal{M}_i''$, we can write the quantity $\mathcal{U}_i$ in terms of $\mathcal{M}'_i$ and the depth- and time-averaged current, $v_i$,

$$\mathcal{U}_i = v_i - \frac{\mathcal{M}'_i}{\rho\,D} \quad , \qquad i = 1, 2 \quad . \tag{2.1.18}$$

The existence of such 'mean' currents below the trough level can be easily understood analysing the case of normal wave incidence. Due to water mass conservation, the depth- and time-averaged velocities are zero in this case, $\vec{v} = 0$. Then, the quantity $\mathcal{U}_i$ provides an approximation for the so-called *'undertow or return currents'* (Short, 1999).

Summing up, the total depth- and time-averaged flow, $v_i$, can be conceived as representing a two layer flow. A first contribution located above the trough level is due to the water mass transport induced by the wave orbital velocities ($\mathcal{M}'_i/(\rho D)$, also called 'Stokes drift'). Hence, it follows the wave propagation direction. A second contribution located below the trough level is due to the existence of 'mean' currents ($\mathcal{U}_i$). In case of $\vec{v} \to 0$ , $\mathcal{U}_i$ is mainly offshore directed and it is called 'undertow or return current'. When $v_i$ is large compared with the 'Stokes drift', $\mathcal{U}_i \simeq v_i$ (see Eq. 2.1.18).

On the other hand, a depth average of Eq. (2.1.1) leads to an expression for the fast-varying depth-averaged velocity,

$$\widetilde{v}_i(x_1, x_2, t^*) = \mathcal{U}_i(x_1, x_2, t) + v'_i(x_1, x_2, t^*) + v''_i(x_1, x_2, t^*) \quad , \qquad i = 1, 2 \quad , \tag{2.1.19}$$

where the fluctuating $v'_i$ and $v''_i$ stand for a depth-averaged version of the wave orbital and the turbulent motions, respectively. The contribution due to the wave orbital motions can be again written in terms of an amplitude $v'_o$ and a phase $\Phi$,

$$v'_i(x_1, x_2, t^*) = \frac{k_i}{k}\, v'_o\, e^{i\Phi} \quad , \qquad i = 1, 2 \quad . \tag{2.1.20}$$

The concentration of sediment in suspension is the other quantity with a clear dependence on the vertical coordinate. The depth-integrated and time-averaged concentration is defined as follows,

$$C(x_1, x_2, t) = \left\langle \int_{\widetilde{z}_b}^{\widetilde{z}_s} \widetilde{c}(x_1, x_2, z, t^*)\, dz \right\rangle \quad . \tag{2.1.21}$$

In contrast to the definition of the depth- and time averaged fluid velocity, $v_i$, the sediment concentration has not been depth-averaged, but only depth-integrated (without dividing by the water depth). Thus, it describes the time-averaged total mass of sediment in suspension in the water column per unit area.

## 2.2 Linear surface waves over water of slowly-varying depth in the presence of currents

### 2.2.1 Motion of linear waves over still water of slowly-varying depth

The main forcing of our system are wind or swell waves arriving to the nearshore from deep water. The linear Airy-wave theory leads to the laws of motion of small-amplitude surface gravity waves advancing over still water of constant depth. Such linearisation applies to waves of small steepness, $\xi_w = H/\lambda_w << 1$. When a wave train reaches shallow areas and starts to feel the slowly-varying bottom (defined by $\nabla D << D/\lambda_w$), a new formulation must be derived. Some wave properties, such as their height $H$ and number $\vec{k}$, which were supposed to be steady in the Airy-wave theory for waves over constant depth, are now allowed to vary slowly in time and in the spatial coordinates.

The dynamical equations for small-amplitude surface gravity waves propagating over still water of slowly-varying depth are obtained by the so-called WKB method, a type of multiple-scales method (Mei, 1989). The first surprising result when solving the corresponding equations is that the obtained dispersion relation turns out to be exactly the same expression as if $D$ was constant (so using the Airy-wave theory),

$$\omega^2 = g\,k\,\tanh(kD)\,, \tag{2.2.1}$$

where $\omega(x_1, x_2, t)$ is the frequency of the wave train, $k(x_1, x_2, t)$ is the wave number and $D(x_1, x_2, t)$ is the 'mean' water depth. These three quantities define the wave kinematics and they now depend on the spatial coordinates and the slowly-varying time. The letter $g$ stands for the gravity acceleration throughout all the thesis.

From the dispersion relation, one can easily compute the phase and group velocities

$$c_i = \frac{k_i}{k}\frac{\omega}{k} = \frac{k_i}{k}\sqrt{\frac{g}{k}\tanh(kD)} \quad, \qquad i = 1, 2 \quad, \tag{2.2.2}$$

$$c_{gi} = \frac{k_i}{k}\frac{\partial\omega}{\partial k} = \frac{c_i}{2}\left(1 + \frac{2\,k\,D}{\sinh(2kD)}\right) \quad, \qquad i = 1, 2 \quad. \tag{2.2.3}$$

When studying nearshore morphodynamics, an important quantity related with wave kinematics is the amplitude of the horizontal component of the water particle orbital velocity, $u'_{1_o}(x1, x2, z, t)$, which has been presented in Eq. (2.1.3). It can also be computed within the linear wave theory,

$$u'_{1_o} \equiv u'_o = \frac{H\,\omega\cosh(k(z+D))}{2\sinh(kD)} = \frac{H\,g\cosh(k(z+D))}{2\cosh(kD)\,c} \quad, \tag{2.2.4}$$

where $z\epsilon(z_b, z_s)$. Sometimes, an approximation for the depth-averaged value of this quantity is needed because it can be representative of all the water column. This depth-averaged amplitude, $v'_o(x1, x2, t)$, which has already been presented in Eq. (2.1.20), reads

$$v'_o = \frac{1}{D}\int_{z_b}^{z_s} u'_o(x_1, x_2, z, t)\,dz = \frac{H\,c}{2\,D} \quad. \tag{2.2.5}$$

Other times, the value of $u'_o$ at the bottom, $u'_{ob}(x1, x2, t)$, is also necessary,

$$u'_{ob} = u'_o(z = z_b) = \frac{H\,\omega}{2\sinh(kD)} = \frac{H\,g}{2\cosh(kD)\,c} \quad . \tag{2.2.6}$$

Most of the properties of wave motion, such as the quantities defined above, depend on the variables in a complex non-linear way. In order to get simpler relationships, which can be very useful in some circumstances, we often use the *'very shallow water assumption'*. It means that the waves are propagating over water depths much smaller than their wave lengths, $kD << 1$. The obtained formulas are

$$\omega^2 = g\,k^2\,D \quad , \tag{2.2.7}$$

$$c_i = c_{gi} = \frac{k_i}{k}\sqrt{gD} \quad , \qquad i = 1, 2 \quad , \tag{2.2.8}$$

$$u'_o = v'_o = u'_{ob} = \frac{H}{2}\sqrt{\frac{g}{D}} \quad , \tag{2.2.9}$$

Both group and phase celerities are equal in this approximation, which results from the fact that waves in very shallow water are non-dispersive. Another result of this approximation is that the amplitude of the horizontal component of the orbital velocity, $u'_o$, is independent of water depth, so that it is equal to its depth-average, $v'_o$, and to its value at the bottom, $u'_{ob}$.

Some relevant second-order quantities can be found simply from the first-order solutions. In any conservative dynamical system undergoing small oscillations, the 'mean' potential and kinetic energies are equal. The total energy density per unit area related with the oscillatory motion of a surface gravity wave train, $E(x_1, x_2, t)$, is then found as two times the kinetic energy, $T(x_1, x_2, t)$,

$$E = 2\,T = \left\langle \int_{\widetilde{z}_b}^{\widetilde{z}_s} \rho\,\tilde{u}_i^2(x_1, x_2, z, t^*)\,dz \right\rangle = \frac{1}{8}\,\rho\,g\,H^2 \quad , \tag{2.2.10}$$

where repeated indices are implicitly summed over (Einstein summation) for $i = 1, 2$. The symbol $\rho$ stands for the water density and $H(x_1, x_2, t)$ is the wave height defined in section 2.1.2. As in many other fluid dynamical problems, the energy is propagated with the group velocity, so that the wave energy flux, $\vec{\mathcal{F}}_w(x_1, x_2, t)$, turns out to be

$$\vec{\mathcal{F}}_w = \left\langle \int_{\widetilde{z}_b}^{\widetilde{z}_s} \left( P + \frac{\rho}{2}\,\tilde{u}_i^2(x_1, x_2, z, t^*) + \rho\,g\,z \right) \vec{v}\,dz \right\rangle = E\,\vec{c}_g \quad . \tag{2.2.11}$$

In order to obtain this result for the energy flux, the pressure term $P$ has been evaluated from the Bernoulli equation (Mei, 1989).

The horizontal momentum density per unit area due to wave oscillatory motion, $\mathcal{M}'$, is equal to

$$\mathcal{M}'_i = \left\langle \int_{\widetilde{z}_b}^{\widetilde{z}_s} \rho\,\tilde{u}_i(x_1, x_2, z, t^*)\,dz \right\rangle = \frac{k_i}{k}\frac{E}{c} \quad , \qquad i = 1, 2 \quad . \tag{2.2.12}$$

This quantity can also be seen as the water mass flux per unit area above the trough level (known as 'Stokes drift'), and has been presented in Eq. (2.1.16). And last but not least, from linear wave theory we can also compute the radiation stress tensor, which describes the excess of horizontal flux of wave momentum (after subtracting the contribution of the hydrostatic pressure),

$$\mathcal{S}'_{ij} = E \left( \frac{c_g}{c} \frac{k_i k_j}{k^2} + \left( \frac{c_g}{c} - \frac{1}{2} \right) \delta_{ij} \right) \quad , \qquad i,j = 1,2 \quad , \tag{2.2.13}$$

where $\delta_{ij}$ is the Kronecker $\delta$. Since a rate of transfer of momentum is equivalent to a force, the divergence of this radiation stress is equivalent to a 'mean' horizontal force exerted by the waves over the water column through which they propagate.

An important process that has not been cited so far is the refraction of the high-frequency waves by the topography due to the fact that their phase velocity depends on the water depth (see Eq. 2.2.2). An easy parallelism can be done with the phenomenon of light refraction due to the fact that light celerity depends on the density of the fluid. A simple formulation that can describe the refraction of waves by a slowly-varying water depth is given by the Fermat principle applied to our physical system. The following development is done in the so-called *ray theory for sinusoidal waves* (Mei, 1989). Rays are defined as being orthogonal to the local crests or phase lines, $\Phi(x_1, x_2, t) = const.$. Since $k_i = \nabla_i \Phi$, the following version of the Fermat principle is verified,

$$\nabla \times \vec{k} = \hat{z} \left( \frac{\partial k_2}{\partial x} - \frac{\partial k_1}{\partial y} \right) = 0 \quad , \tag{2.2.14}$$

in any Cartesian coordinate system, which means that the wave number is irrotational. We apply this general principle to a coordinate system $(x^*, y^*)$ where $x^*$ is an axis perpendicular to the local depth contour and $y^*$ is tangential to this depth contour. Taking into account that wave properties only depend on the new $x^*$ coordinate (because $D = D(x^*)$) so that $\partial/\partial y^* = 0$, and using $k_2 = k \sin\theta^*$, leads to the following local version of the Snell's law for surface gravity waves,

$$\frac{d}{dx^*} (k \sin\theta^*) = 0 \quad , \tag{2.2.15}$$

where $\theta^*$ is the local wave incidence angle with respect to the $x^*$ axis. In case of depth contours parallel to the shoreline (alongshore uniformity), the coordinate system $(x^*, y^*)$ is unique and coincide with our $(x_1, x_2)$ coordinate system. Equation (2.2.15) can then be integrated along the ray to give the well-known global version of the Snell's law,

$$k \sin\theta = const. \quad or \quad \frac{\sin\theta}{c} = const. \quad , \tag{2.2.16}$$

where $\theta$ is now the angle of incidence with respect to the cross-shore direction, $x_1$, which has been defined in Eq. (2.1.7).

An easy application of the Snell's law (Eq. 2.2.16) is the refraction of obliquely incident waves propagating over an alongshore uniform beach. The 'very shallow water assumption' leads to a phase velocity decreasing with the water depth (see Eq. 2.2.8). The global version of the Snell's law then reads

$$\sin\theta = \frac{\sqrt{gD_b}}{\sqrt{gD}} \sin\theta_b \quad , \tag{2.2.17}$$

where $D_b$ and $\theta_b$ are the water depth and the incidence angle at the break-point, which is often used as a reference point where the value of the variables is known (by measurements). The phase lines tend to be aligned with the shoreline, so that the wave rays show smaller angles of incidence, $\theta$, as they approach the shoreline. This phenomenon often allows to do the *'small wave incidence angle assumption'*, valid for a wide range of situations in the nearshore,

$$\cos^2\theta \sim 1 \quad ,$$
$$\sin^2\theta \sim 0 \quad . \tag{2.2.18}$$

Taking both the 'very shallow water' and the 'small wave incidence angle assumptions', the following simpler relationships for the energy flux, the water mass flux and the radiation stress tensor are obtained,

$$\vec{\mathcal{F}}_w = \frac{\vec{k}}{k} E \sqrt{gD} \quad , \tag{2.2.19}$$

$$\vec{\mathcal{M}}' = \frac{\vec{k}}{k} \frac{E}{\sqrt{gD}} \quad , \tag{2.2.20}$$

$$\mathcal{S}'_{11} = \frac{3}{2} E \quad , \qquad \mathcal{S}'_{22} = \frac{1}{2} E \quad , \qquad \mathcal{S}'_{12} = \mathcal{S}'_{21} = -E \sqrt{\frac{D}{D_b}} \, \sin\theta_b \quad , \tag{2.2.21}$$

where the relation between the wave number, $\vec{k}$, and the wave incidence angle, $\theta$, comes again from Eq. (2.1.8).

## 2.2.2   Motion of linear waves in the presence of mean currents

The nearshore region is often characterized by the existence of relatively depth-uniform 'mean' currents (such as rip currents and longshore currents). Their presence influences the wave kinematics and dynamics. The corresponding governing equations, applicable to the case of slow-varying current and water depth (Mei, 1989), lead to the following dispersion relation,

$$\omega = \omega' + v_i \, k_i \quad , \tag{2.2.22}$$

where repeated indices are implicitly summed over for $i = 1, 2$. The symbol $\omega'$ stands for the intrinsic frequency of the wave train over still water (given by Eq. (2.2.1)), while $\omega$ is the absolute frequency (measurable by an observer at rest), which also takes into account the Doppler shift suffered by waves due to the current, $\vec{v}$. Another important change in wave description is that wave energy, $E$, is now not only propagated by the group velocity but also advected by the current so that the final energy flux results in

$$\vec{\mathcal{F}}'_w = E \left( \vec{c}_g + \vec{v} \right) \quad . \tag{2.2.23}$$

So far, the present section 2.2 has only described the basic kinematic properties of the wave field. Next step is finding an equation that describes the dynamical slow variations of wave height and phase as they propagate into the nearshore region. The simplest and most general expression of the dynamics of a wave train propagating over water of slowly-varying

depth in the presence of slowly-varying 'mean' currents appears to be the action conservation principle (Phillips, 1977; Mei, 1989),

$$\frac{\partial}{\partial t}\left(\frac{E}{\omega}\right) + \frac{\partial}{\partial x_i}\left((c_{gi}+v_i)\frac{E}{\omega}\right) = -\frac{\mathcal{D}}{\omega} \quad . \tag{2.2.24}$$

where repeated indices are implicitly summed over for $i = 1, 2$. The ratio $E/\omega$ can be defined as the wave action, in analogy with many mechanical problems with similar ratios of energy to frequencies that also remain invariant under slow variations of some properties of the system. This expression can account for most of the wave transformation processes in the nearshore such as shoaling, breaking and refraction by varying currents and depth, but it is not able to describe wave diffraction.

As $c_{gi}$ and $\omega$ depend on the wave number, the dispersion relation (Eq. 2.2.22) must also be used. Replacing the intrinsic frequency, $\omega'$, by its expression given by Eq. (2.2.1) and using the definitions of $k$ and $\omega$ in terms of $\Phi$ (Eqns. 2.1.4 and 2.1.5) in Eq. (2.2.22), leads to the so-called *Eikonal equation*,

$$\left(\frac{\partial\Phi}{\partial t}+v_i\frac{\partial\Phi}{\partial x_i}\right)^2 = g\sqrt{\frac{\partial\Phi}{\partial x_i}\frac{\partial\Phi}{\partial x_i}} \tanh\left(D\sqrt{\frac{\partial\Phi}{\partial x_i}\frac{\partial\Phi}{\partial x_i}}\right) \quad , \tag{2.2.25}$$

where repeated indices are assumed to be summed for $i = 1, 2$. This latter equation is simply the dispersion relation written in terms of the wave phase. Given a certain water depth, $D$, and fluid velocity field, $\vec{v}$, the results for $E$ and $\Phi$ given by Eqns. (2.2.24) and (2.2.25) allows to calculate the evolution of the wave field, $z'_s$ (described by Eq. (2.1.3)). More sophisticated formulations, like the mild-slope equation, include all the physics described by Eqns. (2.2.24) and (2.2.25) in a single complex equation, which can even account for diffraction effects (Mei, 1989).

### 2.2.3   Statistical description of random waves

The waves described by the preceding formulation have been assumed to be regular, which means that their height, period and orientation have been characterized by a single value. But natural wind-generated waves arriving in the nearshore usually show stochastically varying heights, periods and orientations. A detailed discussion about the statistical distribution of wave properties in the open sea was presented in the paper by Longuet-Higgins (1952). The two main hypothesis of that work were: a) that the wave spectrum contains a single narrow band of frequencies and orientations and b) that the waves can be considered as the sum of a large number of contributions, all of about the same frequency and orientation, but of random phase and height. He then showed that such a wave field, which could have been generated by different random events such as storms, can be characterized by a certain probability distribution of wave heights. As it happens in other oscillatory processes, the Rayleigh probability distribution turns out to be in rough agreement with reality.

The cumulative distribution function characterizing the Rayleigh distribution is

$$F(H') = Pr(H \leq H') = 1 - \exp\left(-\frac{H'^2}{H_{rms}^2}\right) \quad . \tag{2.2.26}$$

This expression describes the probability of the event $H \leq H'$, where $H$ stands for the random variable and $H'$ is a specific value of this variable. The derivative of $F(H')$ gives the corresponding probability density function (pdf), $P(H')$,

$$P(H') = \frac{2\,H'}{H_{rms}^2} \exp\left(-\frac{H'^2}{H_{rms}^2}\right) \quad , \tag{2.2.27}$$

so that $P(H')dH'$ is the probability of the event $H' < H < H'+dH'$. The root mean square (rms) average of the wave height, $H_{rms}$, is the only parameter of this distribution and is defined in the standard way,

$$H_{rms}^2 = \int_0^\infty H'^2 P(H')\,dH' \quad . \tag{2.2.28}$$

The importance of this quantity is that it characterizes the wave energy density associated with the randomly distributed wave train,

$$E = \frac{1}{8}\,\rho\,g\,H_{rms}^2 \quad . \tag{2.2.29}$$

Two important quantities related to the Rayleigh distribution that can be easily computed (and written as a function of the rms wave height) are the mean value, $\widehat{H}$, and the variance, $\sigma_H^2$,

$$\widehat{H} = \int_0^\infty H'\,P(H')\,dH' = \frac{\sqrt{\pi}}{2}H_{rms} \quad , \tag{2.2.30}$$

$$\sigma_H^2 = \int_0^\infty (H' - \widehat{H})^2\,P(H')\,dH' = H_{rms}^2 - \widehat{H}^2 = \left(1 - \frac{\pi}{4}\right)H_{rms}^2 \quad , \tag{2.2.31}$$

Given a wave field with random heights following the Rayleigh distribution, the induced fluctuations of the sea surface elevations ($z'_s$ defined in Eq. (2.1.3)) and the depth-averaged wave orbital velocity ($v'_i$ defined in Eq. (2.1.20)) are Gaussian distributed due to their oscillatory behaviour (Horikawa, 1988). The next pdf characterizes any random variable $f$ that follows a Gaussian distribution around a zero mean value, $\hat{f} = 0$, with a certain standard deviation, $\sigma_f$,

$$P(f') = \frac{1}{\sigma_f\,\sqrt{2\pi}} \exp\left(-\frac{f'^2}{2\,\sigma_f^2}\right) \quad , \tag{2.2.32}$$

As the amplitude of oscillation of both fluctuations ($H/2$ and $v'_o$) can be written as a function of $H$ (see Eq. 2.2.5 for an expression of $v'_o$), the variance of both random variables can be written in terms of $H_{rms}$. The expression for the variance of the sea surface elevation is

$$\sigma_{z_s}^2 = \frac{H_{rms}^2}{8} \quad , \tag{2.2.33}$$

and the variance of the depth-averaged wave orbital velocity is

$$\sigma_v^2 = \frac{H_{rms}^2}{8}\left(\frac{c}{D}\right)^2 \quad . \tag{2.2.34}$$

In this thesis, both *regular waves* characterized by a single wave height and *random waves* characterized by a Rayleigh distributed wave height are used. In the second case, integrals over all the possible wave heights (or wave orbital velocities) must be taken, using the corresponding probability distribution presented in Eq. (2.2.27) (or in Eq. (2.2.32)). If $F(H')$ is any quantity that depends on wave properties through an instantaneous value of the wave height, $H'$, the expected value of such quantity, $\widehat{F}$, is obtained from integrating over all the possible wave heights

$$\widehat{F}(H_{rms}) = \int_0^\infty F(H')\, P(H')\, dH' \quad . \tag{2.2.35}$$

For instance, in random wave fields, the amplitude of the wave orbital velocity at the bed is modified when taking into account that wave heights are Rayleigh distributed. Equation (2.2.6) gives the dependence of this quantity on the wave height. Averaging over all the possible wave heights leads to

$$\widehat{u'}_{ob}(H_{rms}) = \frac{\omega}{2\sinh(kD)} \int_0^\infty H'\, P(H')\, dH' = \frac{\sqrt{\pi}\, H_{rms}\, \omega}{4\sinh(kD)} \quad . \tag{2.2.36}$$

The paper by Longuet-Higgins (1952) also contains a discussion of the applicability of his approach to real wind-generated sea. The validity of his two main hypothesis was verified by means of comparing the predictions of his theory with field observations. Therefore, the period and orientation of waves arriving to the nearshore can be characterized by very narrow Gaussian distributions, so that the respective peaks can be used as representative values. This means that wave field is assumed to be monochromatic and to come from a single direction. Sometimes, two clearly distinct wave incidence directions and/or frequencies are observed in the nearshore (as in the case of swell waves coming from one direction and sea waves from another one). These types of two-directional wave fields can not be described with our formulation.

## 2.3 Hydrodynamical governing equations

### 2.3.1 Shallow water equations

The formulation presented in section 2.2 describes wave transformation over a given slowly-varying depth, $D$, and current, $\vec{v}$. But these two quantities are also unknowns of our physical problem. In fact, waves and currents must be computed simultaneously because strong interactions between them can take place. In the present section, we follow the formulation presented in the book by Phillips (1977). It uses the depth- and time-averaged hydrodynamical variables defined in section 2.1 and derives equations for the conservation of fluid mass, fluid momentum and wave energy in a horizontal plane. In the book by Mei (1989), the same set of equations are obtained but with a slightly different approach. These equations are called shallow water equations due to the fact that the influence of the vertical coordinate has been filtered. They are derived from the general 3D fluid conservation

equations by averaging over water depth and over time (as we have done to define the mass flux velocity, $\vec{v}$, in Eq. (2.1.13)).

The water mass conservation equation in a horizontal plane (in case of incompressible fluid) turns out to be

$$\frac{\partial D}{\partial t} + \nabla \cdot (D\vec{v}) = 0 \quad . \tag{2.3.1}$$

Multiplying this equation by the water density, $\rho$, one may see again that the quantity $\mathcal{M} = \rho D\vec{v}$ is the water mass flux, as it has already been said in section 2.1.2.

A depth and time average of the Navier-Stokes equations in acceleration form leads to

$$\frac{\partial v_i}{\partial t} + v_j \frac{\partial v_i}{\partial x_j} = -g\frac{\partial z_s}{\partial x_i} - \frac{1}{\rho D}\frac{\partial (\mathcal{S}'_{ij} - \mathcal{S}''_{ij})}{\partial x_j} - \frac{\tau_{bi}}{\rho D} \quad , \qquad i = 1, 2 \quad , \tag{2.3.2}$$

where repeated indices are implicitly summed over for $j = 1, 2$. This equation describes the conservation of the 'mean' total water momentum in a horizontal plane. The left hand side contains the local and advective accelerations of the fluid, whereas the right hand side stands for the different forces per unit mass that are applied to a small column of water. The first term accounts for the horizontal forces induced by the pressure gradients of the time-averaged water level. Forcing due to wave oscillatory motion comes to our formulation through the divergence of the wave radiation stress tensor, $\mathcal{S}'_{ij}$ (defined in Eq. (2.2.13)). As we have already suggested in section 2.2, this tensor accounts for the excess of horizontal momentum fluxes related with wave motion, $u'_\alpha$, so that its divergence turns out to be the horizontal force exerted by the waves over the fluid through which they propagate. The effect of the other fluctuating motion (the turbulent eddies described by $u''_\alpha$) enters into the model through the divergence of the depth-averaged turbulence Reynolds stress tensor, $\mathcal{S}''_{ij}$. This term accounts for the horizontal transfer of momentum from our length and time scales to the faster and disordered motion of small eddies. The bed shear stress, describing the dissipative force due to the bottom friction, is represented by $\vec{\tau}_b$.

Finally, conservation of wave energy density, $E(x_1, x_2, t)$ (defined in Eq. (2.2.10)), can be described as

$$\frac{\partial E}{\partial t} + \frac{\partial ((v_i + c_{gi})E)}{\partial x_i} + \mathcal{S}'_{ij}\frac{\partial v_j}{\partial x_i} = -\mathcal{D} \quad , \tag{2.3.3}$$

where repeated indices are assumed to be summed for $i = 1, 2$. The symbol $\mathcal{D}$ accounts for the rate of wave energy per unit of horizontal area that is dissipated through different sources: transference of ordered wave energy into turbulence due to the breaking process and dissipation of energy due to bottom friction and molecular viscosity. Wave energy propagates at the group velocity and can also be advected by 'mean' currents. The last term in the left hand side accounts for the exchange of energy between waves and 'mean' currents. This equation can also be derived from the wave action equation (2.2.24) in case of dealing with a constant absolute frequency, $\omega$, condition that is always verified in our case because of dealing with a steady wave field.

In order to close the hydrodynamical system, several parameterisations for the small-scale processes that are not explicitly described in our formulation must be done. The properties of wave motion leading to the computation of the radiation stress and group velocity are supposed to be well described by the linear wave theory (presented in section 2.2). We use

systematically the 'very shallow water' and the 'small wave incidence angle assumptions' so that the expressions finally used are given by Eqns. (2.2.19), (2.2.20) and (2.2.21). The parameterisations for the turbulence Reynolds stress tensor, $\mathcal{S}''_{ij}$, the rate of wave energy dissipation, $\mathcal{D}$, and the bed shear stress, $\vec{\tau}_b$, are computed in the following sections.

### 2.3.2 Turbulence Reynolds stress tensor

The inevitable Reynolds stress closure problem is generally solved in the nearshore models by means of using the depth-averaged eddy viscosity approach. The depth-averaged turbulence Reynolds stress tensor used in Eq. (2.3.2) then reads

$$\mathcal{S}''_{ij} = \left\langle \int_{\tilde{z}_b}^{\tilde{z}_s} \rho\, u''_i u''_j\, dz \right\rangle = \rho\, \nu_t\, D\left( \frac{\partial v_i}{\partial x_j} + \frac{\partial v_j}{\partial x_i} \right) \quad , \qquad i = 1, 2 \quad . \tag{2.3.4}$$

where $\nu_t$ is the turbulent eddy viscosity, also called lateral momentum mixing or diffusivity. The physics behind the turbulence phenomenon is that some water momentum (and wave energy) is firstly partially transferred to momentum (and kinetic energy) of the largest turbulent eddies. Then, the classical cascade of turbulent energy starts, leading to smaller and smaller eddies, until the energy is finally dissipated by molecular viscosity into heat. Thus, the divergence of the Reynolds stress tensor behaves as a hydrodynamical diffusive term, because momentum is transferred out from our length and time scales of motion. Notice that the depth-averaged eddy viscosity approach describes the horizontal transfer of momentum rather than the vertical one.

The turbulent eddy viscosity, $\nu_t$, intends to describe the dynamical behaviour of the small turbulent eddies and has to be parameterised. A good parameterisation for this quantity in the nearshore was given by Battjes (1975). The hypothesis done in this paper is that all the energy dissipated by breaking waves through $\mathcal{D}$ (rate of energy dissipation per unit area) is converted, in the first step, into turbulent kinetic energy per unit mass at a rate $\epsilon = \mathcal{D}/\rho L$. Taking an adequate velocity scale $V \sim (\epsilon L)^{1/3}$ and length scale $L \sim D$ for the generated turbulent eddies, where $D$ is the water depth (which behaves as a limiting length for the largest eddies), the following turbulent diffusivity is found

$$\nu_t = VL = M\left( \frac{\mathcal{D}}{\rho} \right)^{\frac{1}{3}} D \quad , \tag{2.3.5}$$

where $M$ is a parameter of O(1) that characterizes the turbulence.

Another expression for the turbulent diffusivity that can be used was derived by Longuet-Higgins (1970) using also scaling arguments,

$$\nu_t(x) = N\, x\, \sqrt{gD} \quad , \tag{2.3.6}$$

where $x$ is the cross-shore distance to the coastline and $N$ is a new non-dimensional parameter characterizing the magnitude of the turbulent diffusivity. This latter expression can be obtained from Eq. (2.3.5) for a plane sloping beach, $D = \beta x$, making the hypothesis that the rate of energy arriving with the group velocity is all dissipated into turbulence at a rate

$\mathcal{D}$. Several approximations were done by Longuet-Higgins (1970) for simplifying the wave description: very small incidence angle, $\cos\theta \sim 1$, regular waves and saturated surf zone, $H = \gamma_b D$, where $\gamma_b$ is the saturation coefficient, and the 'very shallow water assumption', $c_g = \sqrt{gD}$. This computation is described in the book by Mei (1989). The relationship between the two turbulence parameters is then

$$N = M \left( \frac{5\gamma_b^2}{16} \right)^{\frac{1}{3}} \beta^{\frac{4}{3}} \quad . \tag{2.3.7}$$

In order to find an order of magnitude for the parameter $N$, we can use approximative values for the parameters involved: $\gamma_b \sim 0.8$ (for regular waves), $M \sim 1$ and $\beta \sim 0.05$. Then $N$ turns out to be of order $O(10^{-2})$. This is also the order of magnitude recommended by Longuet-Higgins (1970).

### 2.3.3 Wave energy dissipation

Wave energy dissipation in the nearshore is mainly due to a transfer of energy from the ordered wave motion to the turbulent eddies (Battjes *et al.*, 1990). In the present thesis, we only need a computation of this quantity in case of random waves, which have been described in section 2.2. In deep water, wave heights that are randomly distributed around their root mean square, $H_{rms}$, can be well described by the Rayleigh distribution. When such a wave field arrives in shallow water, individual waves start feeling the bottom, shoaling and breaking in different places, so that the statistical properties of their wave height could change dramatically.

But this is not the case. The paper by Thornton & Guza (1983) showed experimentally that wave heights of non-broken waves in shallow water can also be quite well described by the Rayleigh probability density function, $P(H')$. Such waves break in relation to their height and the water depth, but also with a random factor. The paper by Thornton & Guza (1983) presented some experimental results verifying that the heights of broken waves can also be described by a probability density function, named $P_b(H')$, which can be expressed as a weighting of the Rayleigh pdf, $P_b(H') = P(H')W(H')$. The probability of breaking or weighting function, $W(H')$, can be given by two different formulas, the second one being more accurate because it takes into account that the largest waves are more likely to break,

$$W_A(H') = \left( \frac{H_{rms}}{\gamma_c D} \right)^4 \quad , \tag{2.3.8}$$

$$W_B(H') = \left( \frac{H_{rms}}{\gamma_c D} \right)^2 \left( 1 - \exp\left( -\left( \frac{H'}{\gamma_c D} \right)^2 \right) \right) \quad , \tag{2.3.9}$$

where $\gamma_c \sim 0.4$ is a parameter giving the expected saturation value of $H_{rms}/D$ in case of random waves and a fixed plane slopping beach profile (Thornton & Guza, 1983).

Given this statistical description of wave heights for broken and non-broken waves, the energy dissipation due to the breaking process, $\mathcal{D}$, can be estimated. We follow again the computation presented by Thornton & Guza (1983), which in turn used an idea from Battjes

& Janssen (1978). The energy dissipation due to the breaking of one wave of height $H'$ can be approximated using the analogy with a hydraulic jump,

$$\mathcal{D}(H') = \frac{\rho\, g\, f_p\, (BH')^3}{4\, D} \quad . \tag{2.3.10}$$

The symbol $B$ indicates a parameter describing the type of breaking and $f_p = \omega/(2\pi)$ is the frequency peak of our wave field. As the quantity $H$ is randomly distributed, an integral of $\mathcal{D}(H')$ over all the possible wave heights of broken waves must be taken (non-broken waves do not contribute to energy dissipation). The computation is similar to Eq. (2.2.35), but using the pdf for broken waves, $P_b(H')$,

$$\widehat{\mathcal{D}} = \frac{\rho\, g\, f_p\, B^3}{4\, D} \int_0^\infty H'^3\, P_b(H')\, dH' \quad . \tag{2.3.11}$$

As $P_b(H') = W(H')\, P(H')$, using the expression for the pdf of wave height given by Eq. (2.2.27) and one of the two formulas for the weighting function shown in Eqns. (2.3.8) and (2.3.9), one can obtain the following two alternative expressions for the energy dissipation,

$$\widehat{\mathcal{D}}_A = \frac{3\sqrt{\pi}}{16}\rho\, g\, B^3\, f_p\, \frac{H_{rms}^7}{\gamma_c^4\, D^5} \quad , \tag{2.3.12}$$

$$\widehat{\mathcal{D}}_B = \frac{3\sqrt{\pi}}{16}\rho\, g\, B^3\, f_p\, \frac{H_{rms}^5}{\gamma_c^2\, D^3} \left( 1 - \left( 1 + \left( \frac{H_{rms}}{\gamma_c\, D} \right)^2 \right)^{-5/2} \right) \quad . \tag{2.3.13}$$

The paper by Thornton & Guza (1983) showed that wave energy dissipation due to bottom friction is negligible in the surf zone, so that it is also neglected in the present thesis. Wave energy directly dissipated into heat by molecular viscosity is also negligible because the majority of the energy is first transformed into turbulent motion.

### 2.3.4 Bottom shear stress

Modelling the bed shear stress remains an unsolved problem in the nearshore environment because of the complexity of the flow pattern, which is a result of wave orbital motion and 'mean' currents, together with a mobile sandy bed. The final wave-current boundary layer structure and the corresponding Reynolds stress closure is difficult to be described.

A typical approximation used for the instantaneous bottom shear stress in the depth- and time-averaged approach is

$$\vec{\vec{\tau}}_b(t^*) = \rho\, c_d\, |\vec{\vec{v}}_b(t^*)|\, \vec{\vec{v}}_b(t^*) \quad , \tag{2.3.14}$$

where $c_d$ is the drag friction coefficient and $\vec{\vec{v}}_b$ is an instantaneous horizontal velocity representative for the boundary layer. This formula follows from the analogy with sediment transport driven by a steady and unidirectional flow (Chezy model).

Following the approach presented in section 2.1.2, the fluctuating velocity at the bottom, $\vec{\tilde{v}}_b(t^*)$, can be divided into a time-averaged contribution, $\vec{v}_b(t)$, plus the rapid-oscillating contribution due to waves predicted at the bed, $\vec{u}'_b(t^*)$ (see Eqns. 2.1.1 and 2.1.5). This latter quantity is given by

$$\vec{u}'_b(t^*) = \frac{\vec{k}}{k} u'_{ob} \cos(\omega t^*) \quad , \tag{2.3.15}$$

whose amplitude, $u'_{ob}$, has been already presented in Eq. (2.2.6). The contribution due to turbulent motion is not taken into account. The 'mean' current value at the bed, $\vec{v}_b$ is usually smaller than the depth-averaged quantity, $\vec{v}$, that is described by our depth- and time-averaged equations. In the worse case, these two vectors could even have opposite directions, which would mean that the fluid velocity displays a strong vertical stratification (as it happens for normal wave incidence, for instance). However, under certain circumstances such as the presence of large relatively depth-uniform 'mean' currents, a common approximation used is considering that $\vec{v}_b \equiv \vec{v}$ (see a discussion about this in Battjes *et al.* (1990) and Fredsoe & Deigaard (1992)). The velocity at the bed in these situations is

$$\vec{\tilde{v}}_b(t^*) = \vec{v} + \vec{u}'_b(t^*) = (v_1 - u'_{ob} \cos(\omega t^*) \cos\theta, v_2 + u'_{ob} \cos(\omega t^*) \sin\theta) \quad , \tag{2.3.16}$$

where we have used the expression for the wave number, $\vec{k}$, as a function of the wave incidence angle given by Eq. (2.1.8).

The friction coefficient, $c_d$, must represent all the influences not directly represented by $\vec{v}_b$. Changes in the definition of the velocity at the bed can be represented through changes in $c_d$. In our case, realistic values for this quantity are $c_d \approx O(10^{-2} - 10^{-3})$ (Soulsby, 1997).

Since we are interested in the wave-averaged dynamics, we need to average the bottom shear stress over the instantaneous time, $t^*$, in order to filter the rapid oscillations. We thus have to integrate the expression given in Eq. (2.3.14),

$$\vec{\tau}_b(t) = \rho\, c_d\, \frac{1}{T} \int_{t-T/2}^{t+T/2} |\vec{v} + \vec{u}'_b(t^*)|(\vec{v} + \vec{u}'_b(t^*))\, dt^* \quad . \tag{2.3.17}$$

In case of dealing with random waves, with a probability distribution for the wave heights, $P(H)$, Eq. (2.3.17) would also have to be averaged over all the wave amplitudes. In the present section we only perform the computations in case of regular waves.

The integral in time in Eq. (2.3.17) can not be analytically computed for an arbitrary $\vec{\tilde{v}}_b$, so for the sake of simplicity we just present its result in two limiting situations. The *'strong current limit'* stands for the case where the 'mean' currents are supposed to be much stronger than the wave orbital motions, $v >> u'_{ob}$. In this case, we recover the result for the bed shear stress under a steady flow (used in river morphodynamics),

$$\vec{\tau}_b = \rho\, c_d\, |\vec{v}|\vec{v} \quad . \tag{2.3.18}$$

The terms *'weak current limit'* describes the other limiting situation, where the orbital motions are supposed to be much stronger than 'mean' currents, $u'_{ob} >> v$. This case is commonly found in the nearshore region and leads to

$$\vec{\tau}_b = 2\, \rho\, c_d\, \frac{u'_{ob}}{\pi}\, \mathcal{A}_\tau\, \vec{v} \quad . \tag{2.3.19}$$

where $\mathcal{A}_\tau$ is the matrix

$$\mathcal{A}_\tau = \begin{pmatrix} 1 + \cos^2\theta & -\frac{\sin(2\theta)}{2} \\ -\frac{\sin(2\theta)}{2} & 1 + \sin^2\theta \end{pmatrix} \quad . \tag{2.3.20}$$

It is interesting to calculate the expression for $\mathcal{A}_\tau$ in case of using the 'small wave incidence angle assumption' (see Eq. 2.2.18),

$$\mathcal{A}_\tau \simeq \begin{pmatrix} 2 & -\frac{\sin(2\theta)}{2} \\ -\frac{\sin(2\theta)}{2} & 1 \end{pmatrix} \quad . \tag{2.3.21}$$

In case of waves arriving perpendicular to the shoreline, $\theta = 0$, the final expression for $\mathcal{A}_\tau$ is

$$\mathcal{A}_\tau \simeq \begin{pmatrix} 2 & 0 \\ 0 & 1 \end{pmatrix} \quad . \tag{2.3.22}$$

This latter expression can also be used in case of very small wave incidence angles ($\theta < 18^o$, see Mei (1989)). The final expression for $\vec{\tau}_b$ using this latter result for the matrix $\mathcal{A}_\tau$ (Eq. 2.3.22) is

$$\tau_{b,1} = 4\,\rho\,c_d\,\frac{u'_{ob}}{\pi}\,v_1 \quad , \qquad \tau_{b,2} = 2\,\rho\,c_d\,\frac{u'_{ob}}{\pi}\,v_2 \quad . \tag{2.3.23}$$

## 2.4 Bed evolution governing equation

### 2.4.1 A sandy bottom

The bottom of the beach consists of sand particles made of quartz (for the most part) with a density $\rho_s \approx 2500 Kg.m.^{-3}$. Their shape is usually approximated by a sphere and characterized by its diameter, $d$. In real beaches, grain diameters usually range from a small diameter, $d = 0.05mm.$ (very fine sand), to much larger sizes, $d = 2mm.$ (very coarse sand). In this thesis only non-cohesive and uniform sediment (i.e. without sorting) are described, although natural sediment always consists of a complex mixture of cohesive and non-cohesive grains of different sizes. The diameter chosen to characterize our uniform sediment represents the mean value of real grain size distributions, $d = d_{50}$.

The packing structure of the sediment particles sets the porosity of the sand layer, $p$ (the ratio of 'empty' space over the total space) and the angle of repose, $\phi$. If the slope becomes larger than the slope of repose, $\tan\phi$, spontaneous avalanches of grains could occur. For the most typical packing structures in natural sand, the porosity is about $p \approx 0.5$ and the slope of repose, $\tan\phi \approx 0.5$. Another important characteristics of the sediment is their settling or fall velocity, $w_s$, which can be defined as the downward directed saturation velocity reached by the sediment in still water. This equilibrium velocity results from a balance between the gravity force, the buoyancy force and the fluid friction. The settling velocity of the sand mainly depends on its grain size and it ranges from 0.002 to $0.3m/s$ (Bagnold, 1963; Soulsby, 1997).

## 2.4.2   Conservation of sediment mass

An important consequence of the existence of currents and wave motions in the nearshore region is that some of their energy is transferred to entraining and transporting sediment particles. The sand can then be deposited far from its original location. These strong sand transport processes make the bottom evolve. The final aim of nearshore morphodynamics is to describe these changes in the topography, so that the bottom level, $z_b$, and hence the water depth, $D$, must be allowed to vary in the formulation. The last physical law used to close our morphodynamical system is the conservation of sediment mass.

According to Caballeria (2000), the depth- and time-averaged sediment mass conservation equation, which proceeds again from the corresponding 3D equation, reads

$$(1-p)\,\frac{\partial z_b}{\partial t} \,+\, \frac{\partial C}{\partial t} \,+\, \nabla \cdot \vec{q} \,=\, 0 \quad , \qquad\qquad (2.4.1)$$

where the sediment porosity is represented by $p$ and $\vec{q}(x_1, x_2, t)$ is the total horizontal sediment flux or sediment transport, i.e. volume of sediment that crosses a vertical section of horizontal length unit per time unit $(m^2/s)$. Given a control volume, the divergence of this quantity stands for the sediment arriving through the lateral boundaries. The dependence of the sediment transport on the hydrodynamical variables allows for the possibility of a feedback between changes in the hydrodynamics and subsequent changes in the bottom. The variable named $C(x_1, x_2, t)$ stands for the depth-integrated suspended load concentration, that is, the volume of sediment in suspension per horizontal area unit (defined in Eq. (2.1.21)). The variation in time of this quantity in the equation is called storage term. Equation (2.4.1) states that any increase in the bottom level is due to either a convergence of horizontal sediment flux or a decrease in the concentration of suspended sediment per unit area.

The storage term is often neglected because changes in time of the sediment concentration are very slow compared with the rest of the terms in the equation. Indeed, this can be safely done in the nearshore in the absence of low-frequency infragravity waves (Caballeria *et al.*, 2002). As we are omitting these low-frequency motions, the final equation for the conservation of sediment mass reads

$$(1-p)\,\frac{\partial z_b}{\partial t} \,+\, \nabla \cdot \vec{q} \,=\, 0 \quad . \qquad\qquad (2.4.2)$$

In spite of neglecting the storage term, a deep understanding of the behaviour of the concentration of suspended sediment in the nearshore, $C(x_1, x_2, t)$, is necessary in order to compute the sediment transport, $\vec{q}(x_1, x_2, t)$. Next section gives some parameterisations for the quantity $C$. Modelling sediment transport is still an open problem that will be faced in section (2.5).

## 2.4.3   Sediment concentration in the nearshore

If the vertical structure of the depth-dependent concentration of suspended sediment is known, $\bar{c}(x_1, x_2, z, t)$, the depth-integrated concentration, $C(x_1, x_2, t)$, can be computed from

an integral similar than Eq. (2.1.21). Knowing this vertical distribution is specially important when we deal with large amounts of sediment in suspension. This situation is found in case of having large fluid velocities, which lead to large bottom shear stresses that put the sand into suspension. A sensible parameterisation for the vertical distribution of the 'mean' depth-dependent concentration $\bar{c}(x_1, x_2, z, t)$ in these situation is given by

$$\bar{c}(x_1, x_2, z, t) = c_b \, e^{-\left(\frac{z+D}{l}\right)} \quad , \tag{2.4.3}$$

where $c_b$ is the sediment concentration at the sea bed and $l$ is the decay length scale (Soulsby, 1997). When this latter quantity is much smaller than water depth, $l << D$, we deal with a thin layer of suspended sediment. In the opposite situation, $l >> D$, the suspended particles extend through all the water column. This often happens in the surf zone because the breaking processes generate strong turbulent eddies that maintain the sediment in suspension.

Various expressions can be found in the literature for $c_b$ and $l$. The sediment concentration at the bed, $c_b$, is usually proportional to the bed shear stress, $\tau_b$ (Soulsby, 1997). The length scale, $l$, always depends on the turbulence model used. The most simple approximation to find an expression for $l$ is the concept of equilibrium concentration, i.e. the concentration in the absence of 'mean' currents and waves. The underlying idea is that, even when the system is not in equilibrium, the vertical distribution is similar to the equilibrium situation. In the absence of 'mean' currents and waves, the settling of the grains to-wards the bed is counterbalanced by the diffusion of sand upwards due to turbulent water motions (Soulsby, 1997; Short, 1999). The corresponding sediment concentration profile is the one given in Eq. (2.4.3) with $l = k_v/w_s$, where $w_s$ is the settling velocity of the sediment and $k_v$ is the vertical turbulent eddy diffusivity. Eq. (2.4.3) is obtained assuming that $k_v$ is constant through the entire water column, which is the simplest assumption one can do.

Integration over depth of the expression for $\bar{c}$ given by Eq. (2.4.3) yields the following approximate formula for $C$,

$$C(x_1, x_2, t) = c_b \, l \left(1 - e^{(-D/l)}\right) \quad . \tag{2.4.4}$$

In case of dealing with a thin layer of suspended sediment ($l << D$), the concentration can be evaluated with

$$C(x_1, x_2, t) = c_b \, l = c_b \, \frac{k_v}{w_s} \quad . \tag{2.4.5}$$

In case of $l >> D$, and using the Taylor expansion $e^{-x} \approx 1 - x$, one may obtain

$$C(x_1, x_2, t) = c_b \, D \quad . \tag{2.4.6}$$

This latter formula describes the case of constant sediment concentration through all the water column (and equal to the concentration at the bed, $c_b$).

In some situations, it is necessary to know qualitatively the cross-shore distribution of the sediment concentration, $C(x1)$. The dependence of $k_v$ on $x_1$ can be found with simple scaling arguments similar to the ones presented in section 2.3.2 for the horizontal eddy diffusivity, $\nu_t$. As a first approximation, the vertical turbulence diffusion, $k_v$, is proportional to the fluid velocity. The settling velocity is a constant. The bed concentration, $c_b$, depends

quadratically on the fluid velocity (through the shear stress, $\tau_b$, see Soulsby (1997)). Hence in any case, the depth-averaged sediment concentration, $C$, is proportional to a power two or three of the fluid velocity at the bed. In general, both the wave induced orbital velocities and the 'mean' longshore currents increase with the water depth until the breaker region and then decrease again. In case of significant low-frequency wave motions, the velocity of the fluid can be larger in the inner surf zone, where the amplitude of oscillation of edge waves is maximum.

## 2.5   Sediment transport in the nearshore

### 2.5.1   An inexact science

The most uncertain quantity when modelling the bed evolution -hence when approaching nearshore morphodynamics in general- is the depth-averaged 'mean' horizontal sediment transport, $\vec{q}(x_1, x_2, t)$. In spite of the large engineering interest in quantifying nearshore sediment transport in order to predict beach evolution, the problem is still far from being solved (Horikawa, 1988; Fredsoe & Deigaard, 1992; Soulsby, 1997; Short, 1999).

The small scale processes leading to the entrainment and transport by currents, oscillatory wave velocity and turbulent motions at the same time are still poorly understood. The velocity of the fluid flowing over the sandy bottom constantly changes its direction and magnitude. The non-linear response of the sand particles to such complex velocity field is then very difficult to parameterise and include in our slow and large-scale processes. Another reason that causes large errors when predicting sediment transport are the uncertainties in estimating the input variables and parameters. For instance, field measurements of sediment grain diameters easily present an inherent error of 20%, which can make the predicted sediment transport change one order of magnitude (Soulsby, 1997). However, as we are interested in building idealised models, computing the quantitative behaviour of the sediment transport may not be essential but knowing its tendencies and dependences can be enough. In some situations, nearshore morphodynamical problems may depend strongly on the sediment transport formulation used and then we must remember its underlying uncertainties. But in other cases, results may be robust and insensitive to the parameterisation used.

Sand transport processes only occur if the drag and lift forces exerted by the flow over the sediment grains exceed some critical value in order to overcome the stabilizing gravitational forces. The ratio between mobilising and stabilising forces can be quantified by the *Shields parameter*, which was originally made for steady flows. However, van Rijn (1993) presented field and laboratory observations about the initiation of sand motion under waves and currents that verified the applicability of the original Shields curve in the nearshore. The threshold of motion is not exceeded often in case of low wave energy (for instance in reflective beaches and in highly protected coasts). But in 'intermediate and dissipative beach states' (see Wright & Short (1984)), the flow and wave velocities always satisfy this critical condition (Short, 1999).

Once the sand particles have been entrained, sediment transport can occur in different modes. When the particles are only moved in a very thin layer close to the bed, where grain to grain interactions are very important, we deal with *bedload transport*. It is the dominant mode of transport for slow flows and/or large grains. When the flow is fast enough and the sand is fine enough, the particles are put into suspension and then advected by the 'mean' currents or by the turbulent eddies, without interaction between grains. Moreover, due to wave breaking in the surf zone, large amounts of sediment can be stirred into suspension in the water column. This mode of transport is known as *suspended load transport* and it is often much greater than the bedload transport (Soulsby, 1997).

It is usually accepted that the total sediment transport can be divided into two components on the basis of its direction (Horikawa, 1988; Komar, 1998). In these books, *longshore transport* is assumed to be due to the longshore current generated by obliquely incident waves, whereas *cross-shore transport* is supposed to be mainly produced by wave non-linearities, by wave induced depth-dependent currents (undertow) and by the downslope component of the gravity force. However, this classification is not precise because depth-uniform 'mean' currents are often found in the nearshore with cross-shore contributions (i.e. rip currents), the waves often approach obliquely and the maximum slopes are not necessarily cross-shore oriented. So another terminology is used in this thesis to describe the different components of the total sediment transport.

The first source of transport is due to the presence of relatively depth-uniform 'mean' currents, $\vec{q}_v$, which conceptually corresponds to the longshore transport described in the previous paragraph. In this case, bedload transport is due to the friction exerted by the currents, while suspended particles are simply advected by the same currents. In our formulation this term is described in isolation, without including neither the transport by gravity, nor the transport only by waves (in the absence of 'mean' currents). An explicit term for the downslope transport due to the gravity force is used, $\vec{q}_g$. It can also account for both suspended and bedload transport and its direction is related with the maximum gradient of the bottom level. Finally, some non-linear properties of wave motion (such as wave skewness and asymmetry) and some wave induced depth-dependent 'mean' currents (such as undertow) can give rise to transport processes in the direction of wave propagation, $\vec{q}_w$ (in the absence of relatively depth-uniform 'mean' currents). Although these three kind of processes are in fact linked and interrelated, they are considered to be independent in the present study for the sake of simplicity, so that the final sediment transport results from their addition,

$$\vec{q} = \vec{q}_v + \vec{q}_g + \vec{q}_w \quad . \tag{2.5.1}$$

There are two approaches for developing a mathematical description of a physical process. The *deductive or process-based model* and the *inductive or empirically-based model*. The process-based models proceed from fundamental physical laws expected to represent our particular phenomena. The empirical models are based on field observations, from which phenomenological laws are induced. The advantages and drawbacks of deductive and inductive models for describing the sediment transport are complementary. In such an uncertain field of research, where the basic processes are not well-understood, theory must be guided by empiricism. In particular, sediment transport in the presence of steady depth-uniform currents is quite well established so that existent process-based models seem to be able to capture its essential aspects. Field measurements help to set the value of the parameters

used. On the other hand, the physics behind the sediment transport purely driven by waves is still poorly understood. So process-based wave-induced transport models rarely show significant predictive skill over either short (e.g., days) or long (e.g., years) time periods. In this case, semi-empirical models (strongly based on field measurements but with some physics incorporated) are necessary.

In this thesis, a purely process-based model called Bailard's model is used to describe sediment transport due to 'mean' currents, $\vec{q}_v$, and gravity, $\vec{q}_g$. These two contributions are dominant when focusing in the growth of rhythmic features in the nearshore (chapter 5) because the main hydrodynamical processes are related with the depth-uniform current circulation pattern generated in plan-view. The transport model proceeds from an *energetics approach* to the problem of sediment transport. This approach was first used by Bagnold (1963) for an unidirectional flow situation with fluctuations. His work is presented in section 2.5.3. This model was later revisited by Bowen (1980) and Bailard & Inman (1981), who applied it to the nearshore, where wave processes influence strongly the sediment transport. Section 2.5.4 presents their results for bedload transport by relatively depth-uniform 'mean' currents, $\vec{q}_{vb}$ while section 2.5.5 gives their results for suspended transport due to 'mean' currents, $\vec{q}_{vs}$. Then, section 2.5.7 describes the bedload and suspended load transport due to the gravity force, $\vec{q}_g$. This Bailard's formulation is considered to describe quite well sand motions due to relatively depth-uniform 'mean' currents and gravity (in the presence of waves) for depth- and time-integrated models (see Deigaard (1997) and Bayram *et al.* (2001)). Finally, section 2.5.6 gives an alternative formulation for suspended sediment transport in the presence of depth-uniform 'mean' currents. A large variety of sediment transport formulas can be found in Soulsby (1997), Komar (1998), Short (1999) and Bayram *et al.* (2001).

The alongshore uniform evolution of equilibrium profiles and the growth of shore-parallel bars in case of normal wave incidence (chapters 3 and 4) can not be related to the transport by depth-averaged 'mean' currents (because they vanish in such situation). In this case, the cross-shore transport is totally dominated by the downslope gravity transport, $\vec{q}_g$, and by the contribution due to the non-linearities in the wave orbital velocities and the undertow current, $\vec{q}_w$ (Ruessink & Terwindt, 2000). A semi-empirical model that was developed by Plant *et al.* (2001*b*) is used in this case. The approach is quite different from the *energetics approach* although it also uses some ideas from Bagnold (1963). It is developed in section 2.5.8. Before going into all these specific formulations for the sand transport, next section presents a general definition of the transport of suspended sediment that will be necessary later on.

## 2.5.2   General definition of suspended transport

The general definition of the depth- and time-averaged transport of sediment in suspension, in terms of the 3D concentration suspended sediment and the fluid velocity, is

$$\vec{q}(x_1, x_2, t) = \frac{1}{D} \left\langle \int_{\tilde{z}_b}^{\tilde{z}_s} \vec{\tilde{u}}(x_1, x_2, z, t^*)\, \tilde{c}(x_1, x_2, z, t^*)\, dz \right\rangle \quad , \qquad (2.5.2)$$

where the fluctuating 3D velocity $\vec{\tilde{u}}(x_1, x_2, z, t^*)$ and concentration $\tilde{c}(x_1, x_2, z, t^*)$ have been presented in section 2.1.2. The dominating physical process behind Eq. (2.5.2) is that the

suspended sand is mainly advected by the 'mean' currents and waves. For the sake of simplicity, the inertia of the sand grains has been neglected because it is much smaller than the other processes. The horizontal diffusion of sediment through turbulent vortices is also neglected in this formulation, even though the vertical diffusion due to turbulence is the maximum responsible for the fact that the sand remains in suspension (section 2.4.3).

Replacing the fluctuating quantities $\vec{\tilde{u}}$ and $\tilde{c}$ by the addition of their 'mean' and wave orbital contributions, the following integral expression is obtained,

$$\vec{q}(x_1, x_2, t) = \frac{1}{D} \int_{\bar{z}_b}^{\bar{z}_s} \vec{\bar{u}}(x_1, x_2, z, t) \, \bar{c}(x_1, x_2, z, t) \, dz \; +$$
$$+ \frac{1}{D} \left\langle \int_{\bar{z}_b}^{\bar{z}_s} \vec{u'}(x_1, x_2, z, t^*) c'(x_1, x_2, z, t^*) \, dz \right\rangle \quad . \tag{2.5.3}$$

The first term describes the transport of the time-averaged concentration of suspended sand by the time-averaged flow (as have been defined in section 2.1.2). It takes into account that both the sediment concentration and the 'mean' flow have a certain vertical distribution. The second term accounts for corrections due to the two oscillatory contributions, accounting also for the case of dealing with non-linear contributions. This second term arises from the possible correlation between surface elevation, sediment concentration and orbital velocity.

The suspended sediment transport can also be written in terms of the depth-averaged 'mean' current, $\vec{v}$, and sediment concentration, $C$,

$$\vec{q}(x_1, x_2, t) = C \, \vec{v} + \vec{q}_{osc} + \vec{q}_{ver} \quad . \tag{2.5.4}$$

where $\vec{q}_{osc}$ is the second term in Eq. (2.5.3) and $\vec{q}_{ver}$ are some correction terms accounting for the vertical structure of both the time-averaged current and sediment concentration,

$$\vec{q}_{ver} = \frac{1}{D} \int_{\bar{z}_b}^{\bar{z}_s} \vec{\bar{u}}(x_1, x_2, z, t) \, \bar{c}(x_1, x_2, z, t) \, dz - C \, \vec{v} \quad . \tag{2.5.5}$$

In the presence of strong enough relatively depth-uniform 'mean' currents, the first term in Eq. (2.5.4) dominates the transport. Then the suspended sediment concentration, $C$, must be parameterised in terms of the variables and parameters of the problem. On the other hand, when the depth average of the 'mean' currents is small and the vertical stratification of the flow and the concentration becomes important, the suspended transport comes from a balance between the second and the third term in Eq. (2.5.4).

### 2.5.3 Bagnold's formulation for bedload transport in the presence of depth-uniform mean currents

Some important properties of sediment bedload transport can be obtained from simple reasonings related to the entrainment and bed transport of sand by currents, applying the *energetics approach*. The formulation described in the present section was first presented in the paper by Bagnold (1963).

The stress exerted by the fluid moving over the grains is supposed to be counteracted by the resultant of the tangential components of the gravity force and the grain shear stress. The main hypothesis is that this tangential grain shear stress is equal to the normal component of gravity force times the slope of repose. Doing this simple dynamical analysis, one may obtain the concentration of sediment in motion in a thin sediment layer above the static sandy bed in a horizontal plane, $C_{bed}^{Bagn}$, that can be moved by a certain horizontal fluid stress, $\tau_b$,

$$C_{bed}^{Bagn} = \frac{|\tau_b|\,\rho_s}{g\,(\rho_s - \rho)\tan\phi}\left(1 + \frac{|\tau_b|\tan\beta}{\tau_b\tan\phi}\right) \quad , \tag{2.5.6}$$

where $\rho_s$ is the density of the sediment, $\rho$ is the density of the fluid and $\tan\phi$ is the slope of repose. This latter quantity is supposed to be much larger than the local slope, $\tan\beta$ (condition of no auto-avalanching). This assumption modifies slightly the result given in Bagnold (1963). The main assumption behind Eq. (2.5.6) is that sediment is not transported by any other mechanism, but only as bedload. Remember that in the previous sections we used the symbol $C$ for referring to the concentration of sediment in suspension in the whole water column, quantity that is considered to be negligible in the present section.

The corresponding sediment transport per unit area is equal to this sediment bedload, $C_{bed}^{Bagn}$, times the velocity of the sediment of this thin layer, $U_{sed}$. But this latter quantity is an unknown of the problem, so that the sediment flux can not be computed from the dynamics of the process. Bagnold (1963) approached the computation of the sediment transport by looking into the energy balance of the system. His main assumption was that the work done by the fluid per unit time and area for transporting the sediment load over the bed is a fixed portion of the total energy per unit time and area dissipated from the hydrodynamic system by bottom friction, $E_f = \vec{\tau}_b \vec{U} = \rho c_d |U|^3$, where $\vec{U}$ is the local current responsible for sediment transport. Analysing the forces acting over the layer of sediment in order to compute the work done by the fluid one can obtain the following expression for the transport of sediment volume per unit time and length,

$$q_{bed}^{Bagn} = \frac{E_f\,\epsilon_b\,\rho_s}{\rho_s\,g\,(\rho_s - \rho)\,(\tan\phi - \tan\beta)} = \frac{\rho\,c_d\,U^3}{g\,(\rho_s - \rho)}\,\frac{\epsilon_b}{(\tan\phi - \tan\beta)} \quad , \tag{2.5.7}$$

where $q_{bed}$ is the bedload transport rate of volume of sediment per unit length and $\epsilon_b \simeq 0.13$ is the fraction of the energy dissipation rate that is spent in transporting bedload sediment. This coefficient is also called bedload efficiency and it is always smaller than one. The original formula of Bagnold (1963) has been divided by $\rho_s\,g\,(\rho_s - \rho)/\rho_s$ in order to express $q_{bed}$ as volume (instead of weight) per time and length units. This formula describes both the transport by currents and by gravity for only steady 'mean' currents (without wave motion).

## 2.5.4  Bailard's formulation for bedload transport in the presence of depth-uniform mean currents

The paper by Bailard & Inman (1981) revisited the study of Bagnold in order to adapt it to the nearshore conditions, where wave motions are important. Firstly, they obtained a

revised formula for the instantaneous bedload sediment transport,

$$\vec{q}_{bed}^{Bail}(t^*) = \frac{\epsilon_b \, \rho \, c_d \, |\vec{v_b}|^3}{g \,(\rho_s - \rho) \tan\phi} \left( \frac{\vec{v_b}}{|\vec{v_b}|} + \hat{\imath} \, \frac{\tan\beta}{\tan\phi} \right) \quad , \tag{2.5.8}$$

where $\vec{v_b}(t^*)$ is the total flow velocity at the bed (described in Eq. (2.3.16) as a result of both currents and waves) and $\hat{\imath}$ is an unitary vector standing for the downslope direction. Again, the main approximation done to derive this equation from Eq. (2.5.7) is that the bed slope, $\tan\beta$, is much smaller than the slope of repose of the sediment, $\tan\phi$ (so that we are far from auto-avalanching conditions). The original formulas of Bailard & Inman (1981) have also been divided by $\rho_s g(\rho_s - \rho)/\rho_s$ in order to express $\vec{q}_{bed}$ as volume per time and length units. The term in front of the bracket describes the magnitude of the sediment transport. The first term inside the bracket stands for the direction of the transport by the current, while the second term gives the contribution of the downslope transport. In our formulation, the bedload transport is split into the contribution by currents and the transport due to gravity. The rest of the present section is focused on the bedload transport driven by currents, while the transport by gravity will be described later on.

As we are again dealing with currents varying fast compared with morphological changes, $\vec{v_b}(t^*)$, an integral in time of Eq. (2.5.8) must be taken in order to get the time-averaged sediment transport,

$$\vec{q}_{v,bed}(t) = \frac{\epsilon_b \, \rho \, c_d}{g \,(\rho_s - \rho)\tan\phi} \frac{1}{T} \int_{t-T/2}^{t+T/2} \vec{v_b}(t^*) |\vec{v_b}(t^*)|^2 \, dt^* \quad . \tag{2.5.9}$$

This integral can be computed exactly and we obtain

$$\vec{q}_{v,bed} = \frac{\epsilon_b \, \rho \, c_d}{g \,(\rho_s - \rho)\tan\phi} \left( |\vec{v}|^2\vec{v} + \frac{u_{ob}'^2}{2} \mathcal{A}_{qvb}\vec{v} \right) \quad , \tag{2.5.10}$$

where the expression for the rapid-oscillating bed velocities due to waves given by Eq. (2.3.15) has been used and $u_{ob}'$ is the amplitude of the wave orbital velocity at the bottom. The first term inside the bracket is dominant in case of strong 'mean' currents with respect to wave orbital motion ('strong current limit', $v >> u_{ob}'$). In this case, transport turns out to be proportional to the cube of the 'mean' flow. The second term inside the bracket is dominant in the 'weak current limit' and transport becomes proportional to the 'mean' flow. An interpretation of this latter term is that sand is first stirred by waves and then advected by the flow.

The matrix $\mathcal{A}_{qvb}$ is equivalent to $\mathcal{A}_\tau$ in Eq. (2.3.19), accounting for the fact that in case of important wave orbital motion, bedload transport can also occur in directions different from the direction of the 'mean' flow. Its form is

$$\mathcal{A}_{qvb} = \begin{pmatrix} 1 + 2\cos^2\theta & -\sin(2\theta) \\ -\sin(2\theta) & 1 + 2\sin^2\theta \end{pmatrix} \quad . \tag{2.5.11}$$

This anisotropy of the Bailard's formulation occurs because of the non-linear dependence of the sediment transport on the velocity. However, it is not reproduced by other classical sediment transport formulations such as the one by Soulsby-van Rijn (more examples of

sediment transport formulas can be found in Soulsby (1997), Komar (1998), Short (1999) and Bayram *et al.* (2001). It is again interesting to compute the expression for this matrix in the 'small wave incidence angle assumption' (see Eq. 2.2.18),

$$\mathcal{A}_{qvb} \simeq \begin{pmatrix} 3 & -\sin(2\theta) \\ -\sin(2\theta) & 1 \end{pmatrix} \quad . \tag{2.5.12}$$

When $\theta < 18^o$, we can ever use the very small incidence angle solution,

$$\mathcal{A}_{qvb} \simeq \begin{pmatrix} 3 & 0 \\ 0 & 1 \end{pmatrix} \quad . \tag{2.5.13}$$

This latter approximation for $\mathcal{A}_{qvb}$ leads to the following expression for $\vec{q}_{v,bed}$,

$$\vec{q}_{v,bed} = \frac{\epsilon_b\,\rho\,c_d}{g\,(\rho_s - \rho)\tan\phi} \left( |\vec{v}|^2\vec{v} + \frac{u'^2_{ob}}{2}(3\,v_1, v_2) \right) \quad . \tag{2.5.14}$$

The integral in Eq. (2.5.9) has only been solved in case of symmetric wave orbital motion (as represented by the velocity at the bed, $\vec{\vec{\tau}}_b$ described by Eq. (2.3.16)). We will see later on how the effect of wave asymmetries could be included in the sediment transport. Moreover, in case of random waves, transport formulas depending on wave properties (such as wave orbital velocity, for instance) should also be integrated over all the possible wave amplitudes.

## 2.5.5   Bailard's formulation for suspended load transport in the presence of depth-uniform mean currents

The paper by Bagnold (1963) also presented an estimate of the suspended load transport by 'mean' currents, using again the *energetics approach*. The physics behind it is that grains are maintained in suspension by forces arising from the diffusion of upward eddy momentum, which counteract the natural downward sediment celerity. Another assumption used is that the layer of suspended sediment is thin compared with the water depth (Bagnold, 1963).

His result was again revisited by Bailard (1981), giving an expression for the time-averaged suspended sediment transport,

$$\vec{q}_{v,sus} = \frac{\epsilon_s\,\rho\,c_d}{g\,(\rho_s - \rho)\,w_s} \frac{1}{T} \int_{t-T/2}^{t+T/2} |\vec{v}_b(t^*)|^3\,\vec{v}_b(t^*)\,dt^* \quad , \tag{2.5.15}$$

where $\epsilon_s$ is the efficiency for suspended load and $w_s$ is the fall celerity of the sediment. The paper by Bailard (1981) suggested the value $\epsilon_s \simeq 0.01$, while by comparison with sediment transport predictions using more sophisticated models, Deigaard (1997) indicated the optimum value of $\epsilon_s \simeq 0.02$. The rest of the symbols have the same meaning as in section 2.5.4.

This integral can not be computed analytically, so that numerical integration is necessary. We just give the analytical results in two limiting situations, as we have done in the other sections. In the 'strong current limit' it reads

$$\vec{q}_{v,sus}^{scl} = \frac{\epsilon_s\,\rho\,c_d}{g\,(\rho_s - \rho)\,w_s}\,|\vec{v}|^3\vec{v} \quad , \tag{2.5.16}$$

so the transport is proportional to a forth power of the 'mean' current. On the other side, using the 'weak current limit' the transport is proportional to the 'mean' flow,

$$\vec{q}\,_{v,sus}^{\,wcl} = \frac{\epsilon_s\,\rho\,c_d}{g\,(\rho_s - \rho)\,w_s}\,\frac{4\,u_{ob}'^{3}}{3\,\pi}\,\mathcal{A}_{qvs}\vec{v}\ \ , \tag{2.5.17}$$

where $\mathcal{A}_{qvs}$ is again a matrix accounting for the anisotropy of the transport under wave motion,

$$\mathcal{A}_{qvs} = \begin{pmatrix} 1 + 3\cos^2\theta & -3\sin\theta\cos\theta \\ -3\sin\theta\cos\theta & 1 + 3\sin^2\theta \end{pmatrix}\ \ . \tag{2.5.18}$$

## 2.5.6 An alternative formulation for suspended load transport in the presence of depth-uniform mean currents

In case of strong stirring by wave orgital motions (which can occur in the 'weak current limit') most of the sand is in suspension, so that the bedload transport in Bailard & Inman (1981) is much smaller than the suspended transport. In this situation, Bagnold's approach to suspended transport is not suitable either because his assumption of a thin layer of suspended sediment is not verified. An alternative formulation can be derived from the general definition of sediment transport given in section 2.5.2.

In the presence of relatively depth-uniform 'mean' currents, Eq. (2.5.4) can be simplified and gives

$$\vec{q}_v(x_1, x_2, t) = C\,\vec{v}\ \ , \tag{2.5.19}$$

where $C(x_1, x_2, t)$ is the depth-integrated and time-averaged concentration of sediment in suspension, which depends on the slow-varying variables of the problem. Section 2.4.3 presented a possible simple parameterisation for this quantity in case of constant suspended sediment through all the water column (Eq. (2.4.6)). Replacing this expression for $C$ leads to

$$\vec{q}_v(x_1, x_2, t) = c_b\,D\,\vec{v}\ \ , \tag{2.5.20}$$

where the constant of proportionality between $\vec{q}_v$ and $\vec{v}$ turns out to be proportional to the concentration at the bed, $c_b$. This quantity is proportional to the bed shear stress, $\tau_b$, which in case of strong orbital motion, is proportional to the square of the wave orbital motion (Soulsby, 1997).

For completeness, we can apply the other limiting situation to Eq. (2.5.19). In case of a thin layer of sediment of thickness $l \approx k_v/w_s$, the depth-integrated sediment concentration, $C$, is better described by Eq. (2.4.5), which leads to

$$\vec{q}_v(x_1, x_2, t) = \frac{c_b\,k_v}{w_s}\vec{v}\ \ , \tag{2.5.21}$$

In this case, the linear dependence of the vertical turbulent diffusivity, $k_v$, on the wave orbital velocity and the quadratic dependence of the bed sediment concentration, $c_b$, lead to a suspended transport by depth-averaged 'mean' currents, $\vec{q}_v$, which depends qualitatively on $\vec{v}$, $u'_{ob}$ and $w_s$ in the same way as Eq. (2.5.17).

## 2.5.7   Downslope gravitational transport

The gravitational transport due to both suspended and bedload sediment transport is parameterised using the expressions by Bailard & Inman (1981) as revisited by Fredsoe & Deigaard (1992), that reads

$$\vec{q}_g = -S_g \, \nabla z_b \ \ . \tag{2.5.22}$$

The main improvement introduced by Fredsoe & Deigaard (1992) was allowing for variable local slope of the bed, so that the term $\hat{\imath} \tan\beta$ in Bailard's formulation (Eq. 2.5.7) was changed to minus the gradient of the bottom $-\nabla z_b$. The quantity $S_g$ in Eq. (2.5.22) contains the time average of the combination of variables and parameters in front of the term $\hat{\imath} \tan\beta$ in Bailard's formulation (Bailard & Inman, 1981),

$$S_g = \frac{\rho \, c_d}{g \, (\rho_s - \rho)} \frac{1}{T} \int_{t-T/2}^{t+T/2} |\vec{\tilde{u}}_b|^3 \left( \frac{\epsilon_b}{\tan^2\phi} \, + \, \left( \frac{\epsilon_s}{w_s} \right)^2 |\vec{\tilde{u}}_b|^2 \right) dt \ \ , \tag{2.5.23}$$

and stands for the stirring of the sediment (either by current or by waves), that then is moved by the force of gravity partly through bedload and partly through suspended load.

Again, the integral for $S_g$ can not be analytically computed. The 'strong current limit' gives

$$S_g^{\,scl} = \frac{\rho \, c_d}{g \, (\rho_s - \rho)} |\vec{v}|^3 \left( \frac{\epsilon_b}{\tan^2\phi} \, + \, \left( \frac{\epsilon_s}{w_s} \right)^2 |\vec{v}|^2 \right) \ \ , \tag{2.5.24}$$

and the 'weak current limit' leads to

$$S_g^{\,wcl} = \frac{\rho \, c_d}{g \, (\rho_s - \rho)} \frac{4 \, u_{ob}'^3}{\pi} \left( \frac{\epsilon_b}{3 \tan^2\phi} \, + \, \left( \frac{2 \, \epsilon_s}{5 \, w_s} \right)^2 u_{ob}'^2 \right) \ \ . \tag{2.5.25}$$

## 2.5.8   Suspended load transport due to waves in the absence of depth-uniform mean currents

Most of the transport processes that are going to be described in the present section have been ignored in the latter sections because transport by relatively depth-uniform 'mean' currents was supposed to be dominant ($\vec{q}_v$ in Eq. (2.5.1)). We are now interested in the physics found in case of relatively normal wave incidence and alongshore uniformity, when the depth average of the 'mean' current must be nearly zero in order to conserve the water mass ($\vec{v} \simeq \vec{0}$, see Eq. (2.1.13)). In these circumstances, $\vec{q}_v$ is negligible and the transport due to wave dynamics, $\vec{q}_w$, becomes dominant. A first contribution to $\vec{q}_w$ comes precisely because of the existence of time-averaged flow fields displaying a strongly stratified vertical structure (due to waves arriving to the beach). Even if $\vec{v}$ vanishes, there is often a strong non-zero 'mean' current near the bed (called 'undertow') that can easily transport sand. Another contribution to this wave induced transport arises from the fact that the wave orbital velocity, its acceleration and the sediment concentration are not sinusoidal functions but they are strongly non-linear, specially in the nearshore (where shoaling and breaking processes are dominant).

Another strategy for computing the sand transport in these type of situations is necessary, instead of the *energetics approach* used in the previous sections. The approach and the formulation presented in Plant *et al.* (2001$b$) are here followed. The starting point is the general definition of the depth- and time-averaged suspended sediment transport presented in section 2.5.2. We are now trying to compute directly the two integrals in Eq. (2.5.3), taking into account the vertical distribution and the time dependence of the 3D fluid velocity, $\vec{\tilde{u}}(x_1, x_2, z, t^*)$, and the suspended sediment concentration, $\tilde{c}(x_1, x_2, z, t^*)$.

The first term of Eq. (2.5.3) is able to include the transport due to a non-uniform vertical distribution of the time-averaged velocity and sediment concentration. As it has already been introduced in section 2.1.4, the hydrodynamic conditions found in case of alongshore uniformity and normal wave incidence can be described in a simplified way with a two-layer flow dynamics. In this circumstances, the 'Stokes drift' (i.e. the onshore transport of water mass that takes place between the wave trough and crest levels, $\mathcal{M}'_i$ in Eq. (2.1.16)) becomes important and it must be counteracted by an offshore water mass transport below the trough level, $\overline{\mathcal{M}}_i$. The corresponding current is called undertow and it has been defined in Eq. (2.1.18). This undertow velocity is often found to be quite depth-uniform below the trough level (Plant *et al.*, 2001$b$). Therefore, the value obtained doing a depth average from the bottom to the trough level (Eq. 2.1.18) can be a good approximation to this quantity. Assuming that the concentration of sediment in suspension, $C$, is located mainly below the trough level, a condition often verified in the surf zone, the first term of Eq. (2.5.3) then reads

$$\frac{1}{D} \int_{\bar{z}_b}^{\bar{z}_s} \vec{\bar{u}}(x_1, x_2, z, t)\, \bar{c}(x_1, x_2, z, t)\, dz = C\,\mathcal{U} \quad . \tag{2.5.26}$$

The undertow current, $\mathcal{U}$, can be approximated using the mass transport due to wave oscillatory motion computed with the linear wave theory (Eq. 2.2.12). Introducing this latter expression into the definition of $\mathcal{U}$ in case of nearly normal wave incidence (Eq. 2.1.18) leads to

$$\mathcal{U} = \frac{E}{c\,\rho\,D} = \frac{g\,H_{rms}^2}{8\,c\,D} \quad . \tag{2.5.27}$$

where we have made use of the definition of the wave energy, $E$ (see Eq. 2.2.10). The variable $c$ stands for the module of the phase velocity of the incident waves, defined in Eq. (2.2.2). In this case, the direction of $\mathcal{U}$ is the opposite of wave propagation, so it is nearly shore-normal and offshore directed.

The second term of Eq. (2.5.3) is the temporal cross-covariance between the depth-integrated sediment load ($C$, computed in section 2.4.3) and the depth-averaged orbital velocity ($\vec{v}'$, presented in Eqns. (2.1.20) and (2.2.5)). Both quantities are herein supposed to be randomly distributed so that the computations must be done using the statistical description for random wave properties presented in section 2.2.3. This second term describes any kind of transport related to the linear and non-linear fluctuating components of these two quantities and it can be written in terms of the cross-correlation, $R_{cv}$, and the two standard deviations, $\sigma_v$ and $\sigma_c$,

$$\frac{1}{D} \left\langle \int_{\tilde{z}_b}^{\tilde{z}_s} \vec{u}'(x_1, x_2, z, t^*)c'(x_1, x_2, z, t^*)\, dz \right\rangle = R_{cv}\sigma_v\sigma_c \quad . \tag{2.5.28}$$

Given a certain probability distribution for the depth-averaged wave oscillatory velocity and the sediment concentration, the two standard deviations, $\sigma_v$ and $\sigma_s$, can be written in terms

of their means. If the depth-averaged wave oscillatory velocity is Gaussian distributed, Eq. (2.2.34) gives the result for $\sigma_v$. The standard deviation of the suspended sediment concentration, $\sigma_c$, can be computed assuming that the concentration follows a distribution similar to the Rayleigh distribution (because this quantity is always positive, as the wave height). Then, following the relationship between the standard deviation of the wave height and its mean (see Eq. 2.2.30), $\sigma_c$ is supposed to be proportional to its mean, $C$,

$$\sigma_c = c_1 C \quad , \tag{2.5.29}$$

where $c_1$ is a constant of proportionality of O(1), which depends on the sediment characteristics.

Replacing Eqns. (2.5.26) and (2.5.28) into Eq. (2.5.3) and using the expressions given by Eqns. (2.5.27), (2.5.29) and (2.2.34) one may obtain the following expression for the module of the wave-induced suspended sediment transport,

$$q_w = C \frac{c\,H_{rms}}{2\sqrt{2}\,D} \left( \frac{g\,H_{rms}}{2\,c^2\sqrt{2}} + c_1\,R_{cv} \right) \quad . \tag{2.5.30}$$

The direction is given by wave propagation, assumed to be nearly shore-normal. The term outside the bracket scales the transport and can be thought as a stirring term. The non-dimensional terms inside the bracket control whether the direction of the transport is onshore or offshore. Closure of the present model requires a description of the two unknowns of this expression, the sediment concentration $C$, and the cross-correlation, $R_{cv}$, in terms of computable variables.

At this point, we only require to know the correct order of magnitude of these two unknowns, $C$ and $R_{cv}$. An indication of their order of magnitude can be computed from the expression for the sediment concentration given by the bedload Bagnold's formulation ($C_{bed}^{Bagn}$ in Eq. (2.5.6)). The next step is to make use of the definition of the instantaneous shear stress (Eq. 2.3.14) as a function of the instantaneous velocity at the bed ($\vec{v}_b$, given by Eq. (2.3.16)). Replacing these expressions into Eq. (2.5.6) and after time-averaging and integrating over the Gaussian velocity pdf, a approximate expression for the 'mean' sediment concentration, $C$, can be obtained,

$$C \approx \frac{\epsilon_b\,\rho\,c_d}{8\,g\,(\rho_s - \rho)\tan\phi} \frac{c^2 H_{rms}^2}{D^2} \quad . \tag{2.5.31}$$

It is important to underline that Eq. (2.5.31) has been obtained after further simplifications for the case of values of the ratio $H_{rms}/D$ much smaller than 1.

Higher-order statistic quantities, such as the cross-correlation between the random variables $C$ and $\vec{v}'$, can also be computed using Eqns. (2.3.14) and (2.5.6), together with the Gaussian velocity distribution,

$$R_{cv}^{gauss} \approx \frac{2}{\sqrt{\pi}\tan\phi} \frac{\partial D}{\partial x} + \frac{H_{rms}}{D} \quad , \tag{2.5.32}$$

The latter result is obtained using a random distribution for the orbital velocity $\vec{u}_b'$ in Eq. (2.3.16) that is purely Gaussian, as indicated by the 'gauss' superscript. This leads to a first term of downslope transport and a second contribution to the transport by undertow.

However, there must be other wave and sediment transport processes due to wave non-linearities (not included in Eq. (2.3.16)), which are said to be responsible for the onshore transport processes on the nearshore (Gallagher *et al.*, 1998; Hoefel & Elgar, 2003). In our formulation, these non-linear interactions are accounted for in another cross-correlation term, named $R_{cv}^{oth}$. Replacing Eqns. (2.5.31) and (2.5.32) into Eq. (2.5.30) and introducing this new $R_{cv}^{oth}$ leads to a highly-idealised expression for the depth- and time-averaged cross-shore sediment transport as a function of the wave height and water depth,

$$
q_w \approx \frac{\epsilon_b \, \rho \, c_d}{16 \, \sqrt{2} \, g \, (\rho_s - \rho) \tan\phi} \frac{c^3 \, H_{rms}^3}{D^3} \left( \frac{g \, H_{rms}}{2 \, c^2 \, \sqrt{2}} + \right.
$$
$$
\left. + \, c_1 \left( \frac{2}{\sqrt{\pi} \tan\phi} \frac{\partial D}{\partial x} + \frac{H_{rms}}{D} - R_{cv}^{oth} \right) \right) \quad . \tag{2.5.33}
$$

For the details of all this derivation, see Plant *et al.* (2001*b*).

# Chapter 3

# Alongshore uniform equilibrium beach profiles

## 3.1 Preliminaries

### 3.1.1 Field observations

A hasty glance at the beach topography can easily lead to the wrong impression that the profile just deepens monotonously with the cross-shore coordinate. When watching in more detail, one may notice that the local slopes can be very different along the profile. Beach topography is relatively 'planar' in some circumstances, but the apparent monotony of its deepening is very often broken by the presence of terraces, shore-parallel bars and troughs. Moreover, beach profile shapes vary widely along the different Earth coasts. A few examples showing the variability in the cross-shore profiles of some natural beaches have been presented in section 1.2.2. More detailed descriptions of beach profile shapes worldwide can be found in Horikawa (1988), Komar (1998) and Short (1999).

It is important to recall here the definitions of the different alongshore uniform beach profiles used in this thesis (a scheme of the four types of profiles has been shown in Fig. 1.2.3). A *'terraced beach profile'* consists in a constant and gently sloping terrace in the surf zone and a concave-up shape in the shoaling part of the domain. The name *'barred beach profile'* refers to alongshore uniform profiles containing a clear trough followed by a shore-parallel bar. In the former case the derivative of the water depth in the offshore direction is always positive, while in the latter case it becomes negative in some regions. There has been a large confusion between these two first profile types in the literature, the presence of terraces having been largely disregarded. Even in very recent studies, terraces are interpreted as being shore-parallel bars (Tapia, 2003). Moreover, some *'ARGUS images'* of 'terraced beaches' may also be confusing because waves can start breaking when feeling the terrace edge, they can

regenerate along the terrace and finally break again at the shoreline. The aspect of the breaking foam in a video image in this case would be the same as if there was a shore-parallel bar at the terrace edge. A *'planar beach profile'* shows similar slopes along the surf and breaker zones (so without any terrace, bar or trough). The slope can diminish along the shoaling zone showing the typical concave-up shape. Finally, the term *'plane beach profile'* indicates an exactly constant sloping beach (so that the slope is identical along all the profile).

Apart from the spatial variability discussed above, nearshore profiles are also characterized by a strong temporal variability, the beach responding slowly but continuously to the ever-changing tides, waves and nearshore currents. The time scale of cross-shore evolution ranges from days to months, whereas the hydrodynamical forcing typically changes several times a day. This raises doubts about the widely-used concept of equilibrium profile. The beach probably attempts to achieve the equilibrium imposed by certain hydrodynamical conditions but seldom does because these external conditions vary too rapidly. However, the concept of equilibrium profile is very useful (and used) for both engineering purposes and basic knowledge about the beach dynamics (for instance, most stability analysis start from an equilibrium state). The underlying idea is that the beach would reach the equilibrium configuration if the forcing remained steady during a long enough time period.

There are some well-established general properties of beach profiles observed in nature (Komar, 1998; Short, 1999). Stormy weather conditions (large wave height and frequency) seem to be related to 'terraced or barred profiles' with gentle overall slopes whereas fair weather conditions (characterized by swell of small wave height and frequency) tend to build up 'steeper and more planar beach profiles' (with no terraces or bars). Grain size is also an important quantity when trying to describe beach characteristics, finer sand being related to more gentle beaches and coarser sand leading to steeper profiles.

Several authors have tried to combine in a single parameter the three most important quantities that settle the main characteristics of beach profiles (grain size, wave height and wave frequency). The most used one is the *dimensionless fall velocity*,

$$\Omega_0 = \frac{H_{off} f_p}{\omega_s} \quad , \tag{3.1.1}$$

where $H_{off}$ is the wave height far offshore, $f_p$ is the peak of the wave frequency and $\omega_s$ is the settling velocity of the sediment, which directly depends on the grain size. This parameter was first introduced by M. L. Goulray in 1968 for characterizing laboratory beaches and it was later on adapted to natural Australian environments by Wright & Short (1984) . The results of the latter paper were that $\Omega_0 > 6$ (corresponding to storm weather conditions and fine sediment) characterizes the so-called *'dissipative beach states'*. In this situation, waves lose all their energy in several spilling breakers along wide and flat terraces. These saturated surf zones extend as far as several hundred meters. Further offshore, in the shoaling zone, the profile is much more steep and typically concave-up. Some shore-parallel bars are often present on these wide terraces. The other limit, $\Omega_0 < 1$ (corresponding to mild weather conditions and larger grain size), gives rise to *'reflective beach states'*. These type of beaches always display steeper profiles so that a considerable percentage of the wave energy is reflected. Their topography consists of a relatively narrow surf zone with no terrace and a prominent step between the swash and the surf zones. The beaches between these two limiting cases, corresponding to $1 < \Omega_0 < 6$, are called *'intermediate beach states'*. They are

characterized by the occurrence of 2D and 3D morphological features such as shore-parallel, crescentic and transverse/oblique bars.

## 3.1.2  Previous modelling and motivation

The first models for 2D beach profile shapes tried to describe the overall deepening, without any terrace, bar or trough. From a large number of observations of beach profiles on the East and Gulf coasts of U.S.A., Dean (1977) came out with a simple empirically-based expression,

$$D(x) = K x^{2/3} \quad , \tag{3.1.2}$$

where the quantity $K$ depended on the grain size. This analytical formula fitted reasonably well the overall deepening of the profiles out to hundreds of meters from the shore (so it describes mainly the shoaling zone of the profile). It is called Bruun/Dean like expression because it was first presented by P. Bruun in 1954, through a fitting to profiles from the U.S.A. West coast and the North Sea coast of Denmark. These two authors also presented very simplified derivations of the formula from physical processes, using quite different underlying assumptions. As described in Komar (1998) and Short (1999), field data analysis performed in other locations (displaying different sand and weather conditions) gave rise to similar formulas but with other powers and expressions for the constant $K$. More recent studies are trying to overcome the two most important shortcomings of the Bruun/Dean like profiles: the infinite slope that is predicted by Eq. (3.1.2) at the shoreline and the fact that inside the surf zone different processes such as wave breaking become dominant and a different profile shape should be expected. The last problem is often solved using two segments of Bruun/Dean like profiles that are matched at the break-point (Komar, 1998; Short, 1999).

These empirically-based expressions helped a lot in classifying natural profiles, but they gave very little insight into the physical processes responsible for the observed shapes. The oldest derivations of a beach profile shape using process-based sediment transport formulas were performed by Bowen (1980) and Bailard & Inman (1981). Adapting to the nearshore conditions the transport formulation of Bagnold (1963), and using very simple parameterisations for the hydrodynamics, they both deduced cross-shore sediment transport formulas for bedload and suspended load (see section 2.5) . The water velocities leading to the motion of sand particles were supposed to be the wave orbital velocities (first and second order) and an onshore 'mean' current that was assumed to be due to the 'Stokes drift' (see section 2.1.4). After imposing zero cross-shore transport (as they were looking for equilibrium conditions), they obtained expressions for the equilibrium slopes, as a function of the water depth and the dimensionless fall velocity, $\Omega_0$. The main behaviour was a nearly monotonous decrease of the slope with the water depth. The dependence on $\Omega_0$ was in agreement with the behaviour described in Wright & Short (1984), the slope increasing with the grain size and the wave period. However, they focused on describing the wave transport in the shoaling zone, without including any of the particular processes that become important when waves start to break. Thus, the applicability of their results inside the surf zone is doubtful.

More recent studies tried to predict cross-shore profile evolution driving the Bailard sediment transport formulation with measured near-bed velocities, so eliminating the errors

concerning the computation of the hydrodynamics (Thornton & Humiston, 1996; Gallagher *et al.*, 1998).  Some important conclusions were that inside the surf zone the undertow current become crucial (this was not included in the two simplified studies presented in the previous paragraphs) and that the wave onshore transport was never well predicted by the Bailard formulation. Other contemporary observational and theoretical results showed that the non-linear shapes inherent of natural wind waves could be responsible for the onshore transport (mainly the wave asymmetries and skewness in the velocity and in the acceleration field, for more details see Stive (1986); Gallagher *et al.* (1998); Hoefel & Elgar (2003)).

A cross-shore semi-empirical transport formula that tried to overcome the shortcomings of the old studies by Bowen (1980) and Bailard & Inman (1981), including in a simplified way all this new knowledge, was recently presented by Plant *et al.* (2001*b*). This paper took two coupled sediment transport and hydrodynamical highly-idealised models as a starting point for investigating the cross-shore profile evolution. The model was derived from the Bagnold formulation for the sediment transport and the random wave transformation of Thornton & Guza (1983) for the wave transformation in case of normal incidence. The final sediment transport formula contained a simplified description of the processes that have been recognised to be important to drive nearshore cross-shore transport: the undertow offshore transport and the onshore transport due to wave non-linearities. This sediment transport formula was calibrated with measurements in a Dutch beach. Apart from presenting this new cross-shore sediment transport formulation, Plant *et al.* (2001*b*) also used it to obtain preliminary results for the corresponding equilibrium profiles. These results were promising because the often observed surf zone terraces were easily predicted.  However, no other kind of profile could be reproduced (such as 'planar or barred beaches') and a systematic exploration of the effect of the different parameters was lacking.

### 3.1.3   Aim, approach and outline of the chapter

The main objective of this chapter is to set up a simple mathematical model for describing sensible equilibrium beach profiles with two aims. Firstly, the main characteristics of natural profiles are intended to be reproduced, understanding the physical processes behind them. Secondly, these equilibrium beach states are the starting point of the stability analysis presented in the two subsequent chapters.

To attain these goals, the sediment transport law coupled with a nearshore wave transformation equation that were presented in Plant *et al.* (2001*b*) have been selected as governing equations. This highly idealised model seems able to reproduce many properties of natural profiles in spite of its simplicity.  The hydrodynamics used is as simple as possible, just including a time and depth-averaged equation for the transformation of normally incident random waves arriving to the nearshore.  The group velocity is computed with the very shallow water assumption and the water momentum conservation equations are not used, so that neither the setup/setdown is taken into account nor the 'mean' currents are explicitly described. The effects of the filtered and neglected hydrodynamical processes and the possible vertical stratification are parameterised into the sediment transport formula. The system is supposed to be uniform in the alongshore direction, focusing on the dynamics of the cross-shore direction. The underlying assumption is that alongshore inhomogeneities can develop and decay in smaller time scales (this is supposed in almost all the cross-shore
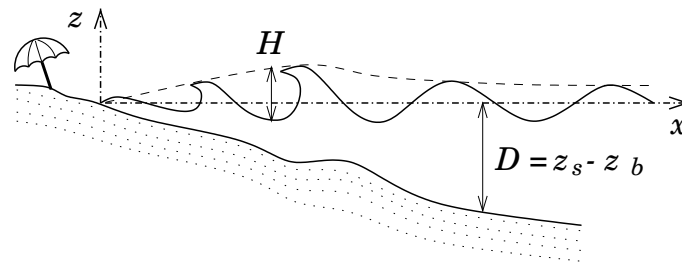
Figure 3.2.1: Coordinate system and definition of the variables for the cross-shore profile model. The dynamical system is the surf zone forced by normally incident waves. The two variables needed are the wave height, $H$, and the water depth, $D$.

profile evolution models, such as Dean (1977),Bowen (1980) and Roelvink & Broker (1993)). The final sediment transport formula used contains in a simplified way the processes that have been recognised to be involved in the 'breakpoint-bar mechanism' (see the previous chapter for the details about this mechanism). Therefore, alongshore uniform sand bars might be part of the obtained equilibrium profiles.

First, the coupled model for wave transformation and topography changes are introduced, together with the solution procedure used . The first steps of the derivation of the cross-shore transport formula and the wave energy equation have already been introduced in section 2.5.8 of the previous chapter. The formulation used in the present chapter, which is described in section 3.2, follows from that general formulation given in the previous chapter. The results for the equilibrium profiles are described in section 3.3. Some discussion about these results is given in section 3.4 and the final conclusions of the chapter are underlined in section 3.5.

## 3.2  Formulation of the general model

In this chapter, we suppose alongshore uniformity, so that the variables only depend on time and the cross-shore position. The coordinate system is defined in such a way that the origin is located at the shore (the place where the water depth is zero) and the cross-shore position, $x$, increases in the offshore direction, as shown in Fig. 3.2.1.

### 3.2.1  Wave transformation equation

The essential processes that induce cross-shore sediment transport (in the absence of relatively depth-uniform 'mean' currents) are related to the wave-driven undertow current and to the non-linearities of wave motions (Gallagher *et al.*, 1998). As a first step, they are parameterised here in the simplest conceivable way, using the root mean square (rms) wave

height, $H_{rms}$, as the only hydrodynamical variable (defined in Eq. (2.2.28)).

Since the time scale for morphological response is expected to be much longer than the inherent wave time scale, we assume that the wave processes in case of randomly distributed wave heights are adequately described by their wave-averaged statistics. For an arbitrary water depth, $D(x)$, the rms wave height profile, $H_{rms}(x)$, can be computed using the wave transformation model for random waves presented in Eq. (2.3.3). As we are interested now in the alongshore uniform situation, the variables are not allowed to depend on the alongshore coordinate ($\partial/\partial x_2 = 0$). This, together with the assumption of normal wave incidence leads to the fact that no depth- and time-averaged currents are present ($\vec{v} = 0$, because of mass conservation). The parameterization used for the wave energy dissipation, $\mathcal{D}$, is given by Eq. (2.3.13) (Thornton & Guza, 1983). The final wave transformation equation derived from Eq. (2.3.3) reads

$$\frac{\partial H_{rms}^2}{\partial t} - \frac{\partial \left( H_{rms}^2 \, c_g \right)}{\partial x} = -A_1 \, \frac{H_{rms}^5}{D^3} \left[ 1 - \left( 1 + \left( \frac{H_{rms}}{\gamma_c \, D} \right)^2 \right)^{-5/2} \right] \quad, \tag{3.2.1}$$

where the definition of the wave energy has been used (Eq. 2.2.29) and the group velocity has been computed using the 'very shallow water assumption', $c_g = \sqrt{gD}$, where $g$ is the gravity acceleration (see Eq. 2.2.8). The final constant quantifying the dissipation of wave energy reads

$$A_1 = \frac{3 \, B^3 \, \sqrt{\pi} \, f_p}{2 \, \gamma_c^2} \quad. \tag{3.2.2}$$

The parameter $\gamma_c$ is related to the saturation value of the rms wave height over the water depth in case of fixed 'plane beach profile'. The frequency peak of the incident wave field (assumed to be narrow banded) is given by $f_p$ and $B$ is an adjustable parameter of O(1) describing how waves break.

Notice that the set-up/set-down of the 'mean' free surface level has been neglected as in Plant *et al.* (2001*b*), since it is not essential for the processes being investigated. As a result, the cross-shore momentum balance (Eq. 2.3.2) is not considered and the bottom level is equal to minus the water depth, $z_b = -D$. We also consider normal wave incidence, so the effect of longshore currents is not taken into account.

### 3.2.2   Cross-shore sediment transport and bed evolution

As we suppose alongshore uniformity and normal wave incidence only the cross-shore sediment transport due to wave motions and the gravity transport play an important role. The transport due to depth-averaged 'mean' currents, $\vec{q}_v$, is neglected in Eq. (2.5.1). Two wave-induced transport processes are clearly relevant to the large-scale cross-shore transport (Gallagher *et al.*, 1998): the offshore contribution due to the existence of a near-bed offshore directed current ('undertow') and the onshore contribution due to non-linear properties of the orbital wave velocity. As we already explained in section 2.5.8, the 'undertow' current is considered to balance the onshore directed input of water mass flux driven by waves above the trough level ('Stokes drift'). We assume that this return current is relatively depth-uniform below the trough level. Given an underlying bathymetry and the rms

wave height, an approximation to the undertow magnitude can be computed analytically with Eq. (2.5.27) (Masselink & Black, 1995). The onshore transport can be associated with several non-linearities of the coupling between the orbital wave velocity and the sediment concentration. They can be produced for instance by the wave velocity skewness and asymmetry (Stive, 1986). Recent studies also underline the importance of the accelerations in wave motions for driving onshore transport (Hoefel & Elgar, 2003).

Here we use the time-averaged cross-shore sediment transport, $Q(x,t)$, derived by Plant *et al.* (2001*b*), which describes in a simple way these two wave-induced transport processes. His approach has been introduced in section 2.5.8. Nevertheless, the final sediment transport formulation used furthermore in that paper was only partially based on the Eq. (2.5.33) obtained in that section. In account of the poor knowledge of wave non-linearities and sediment processes in general, a suitable semi-empirical formulation was used. It was inferred from field measurements in the Dutch coast, with the guidance of the theoretical development presented in section 2.5.8. The final formulation, which has also been used by others (for instance see Horikawa (1988)), was

$$Q(x,t) = S(x,t)\,R(x,t) \quad . \tag{3.2.3}$$

The function $S(x,t)$ on the right-hand side of Eq. (3.2.3) describes the potential magnitude of the sediment transport stirred by waves (this is also known as wave stirring, see Roelvink & Stive (1989)). The function $R(x,t)$ gives the relative magnitude and direction of the different transport processes. Plant *et al.* (2001*b*) assumed that the wave stirring was dominated by the wave-driven velocity variance and gave an expression based on Bagnold bedload formulation applied to oscillatory currents. Following Eq. (2.5.33) and using the 'very shallow water assumption' for the wave phase celerity, $c = \sqrt{gD}$, the following expression for wave stirring can be found,

$$S(x,t) = \frac{\epsilon_b\,\rho\,c_d\,\sqrt{g}}{16\ sqrt2\,(\rho_s - \rho)\,\tan\phi}\,\frac{H_{rms}^3}{D^{3/2}} \quad , \tag{3.2.4}$$

where $\rho$ is the water density, $\rho_s$ is the sediment density, $\phi$ is the angle of repose, $c_d$ is the friction coefficient, $O(10^{-3} - 10^{-2})$, and $\epsilon_b$ is the Bagnold efficiency for bedload transport, $O(10^{-1})$.

What is important to beach profile evolution is the relative strength and cross-shore structure of the processes driving onshore and offshore transport. The function $R(x,t)$ on the right hand side of Eq. (3.2.3) describes the relative importance of the three different mechanisms that could transport sediment and has the form

$$R(x,t) = r_0\,\frac{\partial D}{\partial x} - r_1\left(\frac{H_{rms}}{D\,y_c}\right)^p\left(1 - \frac{H_{rms}}{D\,y_c}\right) \quad . \tag{3.2.5}$$

The first term describes the importance of downslope transport due to gravity. The ratio between the two parameters $r_0/r_1$ would then control the strength of downslope transport with respect to the wave-induced processes. The second term describes the competition between the two transport processes induced by wave motions: onshore transport (i.e. negative) due to non-linearities of the wave velocity and offshore transport (i.e. positive) due to undertow. Both from an experimental point of view (Ruessink *et al.*, 1999; Peters *et al.*, 2001) and from the theoretical formulation described in section 2.5.8, it follows that the

relative wave height, defined as the ratio between the wave height and the water depth, $Y = H_{rms}/D$, controls completely the transport balance. So we have chosen to represent this coupled system in terms of $Y$ and $D$ rather than $H_{rms}$ and $D$. The parameter $y_c$ in Eq. (3.2.5), called the critical relative wave height, sets the value of $Y$ at which undertow induced transport exactly balances wave non-linearities transport (in that case, there would still be some transport if the slope was non-zero). Thus it determines in which part of the domain the wave-induced transport is dominated by undertow and where by wave non-linearities. The main assumption made in Eq. (3.2.5) is that this wave-induced transport is a non-linear function of the relative wave height (where $p$ controls the degree of non-linearity). Plant *et al.* (2001*b*) showed that this parameterization was consistent with field observations of sediment transport on the Dutch coast (using $p = 1$). On the other hand, setting $p = 0$ yields the Eq. (2.5.33) presented in section 2.5.8 if the following specific values for the parameters are used,

$$r_0 = \frac{2\,c_1}{\sqrt{\pi}\tan\phi} \quad , \qquad r_1 = c_1\,R_{cu}^{oth} \quad , \qquad y_c = \frac{2\,\sqrt{2}\,c_1\,R_{cu}^{oth}}{1 + 2\,\sqrt{2}\,c_1} \quad . \tag{3.2.6}$$

Thus, the critical relative wave height, $y_c$, can be computed analytically in this limiting situation ($p = 0$) and it turns out to be proportional to $R_{cu}^{oth}$, the non-linear cross-correlation between the sediment load and the wave orbital velocity.

Finally, the sediment balance couples the local water depth with the divergence of the sediment flux, $Q$. Form Eq. (2.4.2) and using the new parameter $\mu = 1/(1 - p)$, where $p$ is the porosity of the sediment, the following equation is found

$$\frac{\partial D}{\partial t} = \mu\,\frac{\partial Q}{\partial x} \quad , \tag{3.2.7}$$

in which we have also used $z_b = -D$ and $\partial/\partial x_2 = 0$.

### 3.2.3   Scaling and parameter setting

In order to find the main balancing terms in this problem, we use appropriate scales to arrive at a set of dimensionless equations. Non-dimensional quantities (indicated by an asterisk *) are defined as

$$H_{rms} = H_s\,H_{rms}^* \quad , \qquad Y = y_s\,Y^* \quad , \qquad D = L_v\,D^* \quad , \tag{3.2.8}$$
$$x = L_h\,x^* \quad , \qquad Q = Q_o\,Q^* \quad , \qquad t = T_m\,t^* \quad .$$

The appropriate scales are explicitly defined in table 3.2.1, together with the default values chosen. Wave height far offshore is the main scaling factor. It directly scales the wave height ($H_s = H_{off}$) and it appears in all the other length scales. The parameter $y_c$ seems crucial in the sediment transport formula, so that it is chosen as the scaling of the relative wave height, $y_s = y_c$. The vertical length scale is chosen to be the water depth at the break-point. It can be approximated by the wave height far offshore divided by the critical relative wave height, $L_v = H_{off}/y_c$. The cross-shore length scale is set so that non-dimensional slopes of $O(1)$ are much smaller than the slope of repose, $tan\phi$, in order to

Table 3.2.1: Definition of the scaling constants chosen for analyzing this problem. Their default values are obtained with the following values of the parameters: $c_d = 0.005$, for the drag coefficient, $\epsilon_b = 0.15$, for the efficiency in bedload transport mode, $r_1 = 1$, for the dimensional downslope transport parameter, $\rho = 1000 Kg/m^3$, for the water density, $\rho_s = 2500 Kg/m^3$, for the sediment density, $\tan\phi = 0.5$, for the slope of repose and $\mu = 2$ for the porosity coefficient. See the text for the derivation of these expressions.

| Scale | Definition | Default value |
|:-----:|:----------:|:-------------:|
| $H_s$ | $H_{off}$ | $1\,m.$ |
| $y_s$ | $y_c$ | $0.5$ |
| $L_v$ | $\dfrac{H_{off}}{y_c}$ | $2\,m.$ |
| $L_x$ | $10\dfrac{L_v}{\tan\phi}$ | $40\,m.$ |
| $Q_o$ | $\dfrac{r_1\,\epsilon_b\,\rho\,c_d\,\sqrt{g}\,(H_{off}y_c)^{3/2}}{16\,\sqrt{2}\,(\rho_s-\rho)\,\tan\phi}$ | $4\,m^2/\,\mathrm{day}$ |
| $T_m$ | $\dfrac{L_v\,L_h}{\mu\,Q_o}$ | $10\,\mathrm{days}$ |

remain far from auto-avalanching conditions. The sediment transport is scaled in such a way that the maximum value of the wave-induced transport becomes one (from Eq. 3.2.3). The order of magnitude of this cross-shore transport scale, $Q_o$, is in good agreement with recent measurements made in wave flume experiments (Peters *et al.*, 2001). Finally, the sediment balance equation (Eq. 3.2.7) sets the morphodynamical time scale, $T_m$, which yields non-dimensional bed change rates and divergence of the sediment transport that are of equal magnitude.

The non-dimensional quantities given by Eq. (3.2.8) are introduced in Eqns. (3.2.1) and (3.2.7). After dropping the asterisks *, we arrive at the following dimensionless non-linear equations, written in terms of the relative wave height and the water depth,

$$\epsilon\left(\frac{\partial Y}{\partial t} + \frac{Y}{D}\frac{\partial D}{\partial t}\right) = \frac{\partial Y}{\partial x}\sqrt{D} + \frac{5}{4}\frac{Y}{\sqrt{D}}\frac{\partial D}{\partial x} - AY^4\left(1 - \Gamma(Yy_c)^{-5/2}\right) \quad, \qquad (3.2.9)$$

$$\frac{\partial D}{\partial t} = \frac{\partial}{\partial x}\left[Y^3D^{3/2}\left(s_0\frac{\partial D}{\partial x} - Y^p(1-Y)\right)\right] \quad, \qquad (3.2.10)$$

where $\Gamma(Yy_c) = 1 + (Yy_c/\gamma_c)^2$.

The independent and non-dimensional parameters of the model, which are defined in table 3.2.2, are $y_c^* = y_c/\gamma_c$, $s_0$, $p$, $A$ and $\epsilon$. This table also shows the range of values that has been used for these five parameters. From Eq. (3.2.6) one may infer that the critical relative wave height, $y_c$, is related with the strength of wave non-linearities, in particular it is proportional to the cross-correlation between wave orbital motions and suspended load.

Table 3.2.2: Explicit definitions of the independent parameters governing the non-dimensional equations ($y_c^*$, $s_0$, $p$, $A$ and $\epsilon$) with the corresponding range of variation. The default values for the parameters that have been kept fixed in the non-dimensional equations are: $\gamma_c = 0.5$, $\tan\phi = 0.5$, $r_0 = 2.25$, $r_1 = 1$, $H_{off} = 1m.$, $f_p = 0.14s^{-1}$ and $B = 1$. See the text for explanation.

| Name | Symbol | Definition | Values |
|:---:|:---:|:---:|:---:|
| Critical relative wave height | $y_c^*$ | $y_c/\gamma_c$ | $0.6 - 2$ |
| Morphodynamical diffusivity | $s_0$ | $\frac{\tan\phi\, r_0}{10\, r_1}$ | $0.05 - 0.5$ |
| Transport exponent | $p$ | $p$ | $1, 2, 3$ |
| Wave breaking coefficient | $A$ | $\frac{15\, B^3 \sqrt{\pi\, H_{off}}\, f_p\, y_c^{5/2}}{2\, \gamma_c^2\, \sqrt{g}\, \tan\phi}$ | $4.8\, y_c^{5/2}$ |
| Ratio of times | $\epsilon$ | $\frac{1}{T_m} \sqrt{\frac{H_{off}}{g\, y_c} \frac{10}{\tan\phi}}$ | $O(10^{-5}) \sim 0$ |

From Eq. (3.2.5), it can also be seen that $y_c$ sets in which domain of $Y$ the transport is dominated by wave non-linearities and where by undertow. As it is explicitly written in table 3.2.2, the downslope diffusivity, $s_0$, depends on the ratio $r_0/r_1$, so it sets the relative strength of the downslope transport with respect to the wave-induced transport (see also Eq. (3.2.5)). The value of these two parameters in nature is unknown, but their order of magnitude was inferred from field data by Plant *et al.* (2001*b*). So in accordance with that paper, we allows $y_c$ to range from 0.3 to 1.0 and $s_0$ from 0.05 to 0.5. The final non-dimensional parameter related with the relative wave height that appears in the equations is $y_c^*$, the ratio between $y_c$ and the wave height saturation coefficient, $\gamma_c$. We mainly keep this latter parameter constant, so that the changes in $y_c^*$ are induced through varying $y_c$. The default value for $\gamma_c$ is chosen to be consistent with Thornton & Guza (1983), $\gamma_c = 0.5$. A sensitivity analysis of the influence of $\gamma_c$ is done anyway, in order to check its influence on the parameter $A$. The default value for the exponent $p$ in the transport formula is $p = 1$, which is also in accordance with the results of the experiments described in that paper. However, the sensitivity to increasing the value of $p$ up to 3 is checked.

The coefficient $A$ in Eq. (3.2.9) comes from the ratio between a coefficient giving the strength of dissipation due to breaking and a coefficient associated with wave shoaling. Notice that $A$ depends on the wave height and frequency through the offshore wave steepness (indicated as $\xi_{off}$ from now on). As can be inferred from Eq. (2.1.10), this latter quantity is given by the ratio between the offshore wave height and length, $\xi_{off} = H_{off}/\lambda_{off}$, and it is a measure of wave non-linearities (Komar, 1998). From Eq. (2.2.1), the wave length far offshore can be approximated as $\lambda_{off} = g/(2\pi f_p^2)$ ('deep water approximation'). Thus, the offshore wave steepness reads $\xi_{off} = 2\pi f_p^2 H_{off}/g$. Replacing this expression in the wave breaking coefficient (defined in table 3.2.2) leads to the simpler expression,

$$A = \frac{15\, B^3 \sqrt{\xi_{off}}\, y_c^{5/2}}{2\, \sqrt{2}\, \gamma_c^2\, \tan\phi} \quad . \tag{3.2.11}$$

It is widely recognised that an upper limit for the wave steepness in the open sea is given by $\xi_{off} \lesssim 1/7$, which is found in case of very severe storm conditions. More typical sea conditions gives $\xi_{off} \sim 1/15$, while swell conditions lead to much smaller values about $\xi_{off} \sim 1/100$. Like the steepness, the critical relative wave height, $y_c$, also depends crucially on the wave conditions (sea or swell). In the present equilibrium model, we have chosen to explore the influence of the wave conditions through changing $y_c$ and keeping a constant default value for $\xi_{off} \sim 1/80$ (found with $H_{off} = 1m$. and $f_p = 0.14s^{-1}$). The rest of parameters included in $A$ are mainly related with the dissipation of energy due to breaking waves. The default value used for the wave height saturation coefficient is $B = 1$, as suggested by Thornton & Guza (1983). All these choices lead to a value $A_3 = 4.8\, y_c^{5/2}$. The sensitivity of the results on the offshore wave steepness $\xi_{off}$ checked anyway.

Finally, the parameter $\epsilon$ mainly comes from the ratio between the hydrodynamical time scale (given by the inverse of wave frequency, $T_h = f_p^{-1}$) and the morphological time scale, $T_m$. In fact, as the hydrodynamical equation have been divided by the shoaling coefficient, the final expression for $\epsilon$ is more complicated, but of the same order than the ratio of time scales. Using the default value for $T_m$ given in table 3.2.1, we obtain $\epsilon \sim O(10^{-5})$. The corresponding term in the wave evolution equation can then be neglected (if desired). This assumption is usually called *quasi-steady hypothesis* because it means that waves adapt instantaneously to the bottom changes.

One of the most important consequences of the scaling presented in this section is that the wave height far offshore, $H_{off}$, only appears in the non-dimensional equations through the wave steepness $\xi_{off}$. Therefore, $H_{off}$ itself turns out to be only a scaling parameter, with no influence on the non-dimensional equations.

### 3.2.4 Numerical method and solution procedure

In order to seek for a steady equilibrium solution, which does not depend explicitly on time, we impose $\partial/\partial t = 0$ in the governing equations (Eqns. 3.2.9 and 3.2.10). Then, the obtained bed evolution equation states that the divergence of the sediment transport vanishes, i.e. the transport is constant across all the domain. However, a non-zero sediment transport at the offshore boundary is nonsense (given the fact that we are describing sediment transport within the nearshore zone). Thus, a steady solution requires a zero cross-shore transport everywhere. The equilibrium wave height and water depth are then a result of setting $Q(x) = 0$, $\forall x$ and imposing the steady version of Eq. (3.2.9). The final set of equilibrium equations reads

$$\frac{\partial Y}{\partial x} = -\frac{5}{4s_0}\frac{Y^{p+1}}{D}(1-Y) + A\frac{Y^4}{\sqrt{D}}\left(1 - \Gamma(Yy_c)^{-5/2}\right) \quad , \qquad (3.2.12)$$

$$\frac{\partial D}{\partial x} = \frac{1}{s_0}Y^p(1-Y) \quad , \qquad (3.2.13)$$

where $\Gamma(Yy_c) = 1 + (Yy_c/\gamma_c)^2$. There are four independent parameters: $y_c/\gamma_c$, $s_0$, $p$ and $A$.

These two governing equations are of first order in the derivatives but they have a strongly non-linear dependence on the variables. The chosen numerical method to solve them has

been a Runge-Kutta integration from an initial condition set at the offshore boundary for the two non-dimensional variables (water depth and relative wave height). Then, integration has been performed in the onshore direction up to the coastline (defined as $D_{eq} = 0$) for different values of the initial condition (i.e. the non-dimensional water depth where we start the computations, called $D_{off}$). This is the first numerical parameter. The initial non-dimensional relative wave height far offshore is equal to $y_{off} = 1/D_{off}$ as the non-dimensional wave height far offshore is equal to one ($H_{off} = 1$, because the corresponding dimensional value is the scale of the wave height).

A difficulty found during the solution procedure is that the coastline can not be reached exactly because Eqns. (3.2.12) and (3.2.13) are singular there. The actual shoreline has been defined by a small water depth, called tolerance ($D_{eq} = tol$), which has been introduced as the second numerical parameter. In fact, due to this singularity at the coastline, it has been necessary to introduce a variable mesh that becomes finer as one gets closer to the shore. Moreover, the stability analysis performed in the following chapter requires sometimes of a very long domain, in which case the equilibrium profile must be computed till very far offshore. For those circumstances, we have also performed an integration in the seaward direction from $D_{off}$ to far offshore. A variable mesh has also been used in this case, the step becoming larger as one moves onto the offshore part of the domain. Finally, large gradients in the cross-shore distribution of the equation coefficients occur at a small region close to the break-point where we need therefore a very fine discretization. The final consequence is that we need a fine mesh in all the domain that implies having a large amount of integration steps.

## 3.3   Solution of the equilibrium equations

### 3.3.1   General description

For all the range of parameter values studied, the obtained equilibrium profiles are 'non-barred'. They can be defined as strongly 'terraced beach profiles in a limiting case (see an example in Fig. 3.3.1) and nearly 'planar profiles' in the other limit (see Fig. 3.3.2). Section 1.2.2 has given a definition of these two types of profiles. The intermediate profiles comprise a sloping terrace, which extends from the shoreline to the break-point, and a classical concave-up profile, which extends seaward from the break-point.

The physical interpretation of this shape follows from a close examination of the balance between the three transport processes. In the offshore region, where the relative wave height is well below its saturation value, equilibrium primarily results from a local balance between the offshore directed downslope transport and a small onshore transport driven by wave non-linearities. This latter source of transport prevails over undertow transport along all the shoaling zone because waves are not breaking there. As waves approach shallower areas, they become more and more non-linear with the corresponding increase in magnitude of the onshore transport. This is balanced by an increase of the local slope along all the shoaling region, which reaches a maximum where the equilibrium dimensional relative wave height equals $Y_{eq} = y_c \, p/(p + 1)$ (point $X_{b1}$ in the graphs, see Eq. (3.2.13)). Further onshore, the
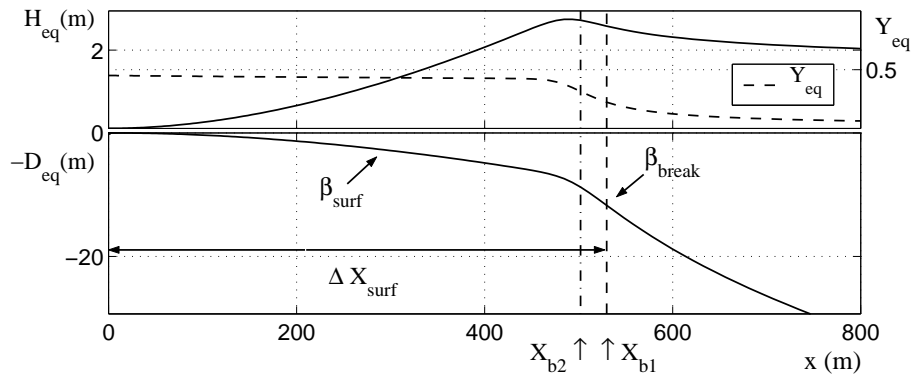
Figure 3.3.1: Example of equilibrium profile with the shape of a relatively 'terraced beach profile'. The values used for the input parameters are $y_c/\gamma_c = 0.9$, $s_0 = 0.11$, $p = 1$ and $A = 0.65$. The horizontal axis corresponds to the cross-shore position, $x$. All quantities shown are dimensional, computed with $H_{off} = 1m$. Top: The solid line is the equilibrium wave height, $H_{eq}$ and the dashed line is the relative wave height, $Y_{eq}$. Bottom: The solid line corresponds to the equilibrium topography (equal to minus water depth, $-D_{eq}$.)
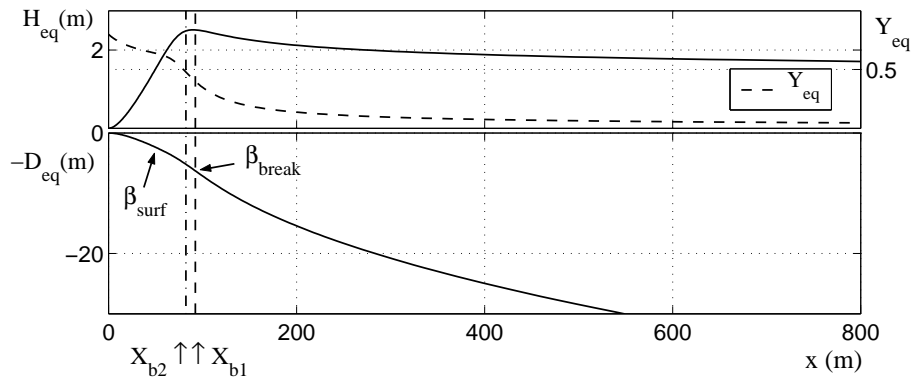


Figure 3.3.2: Example of equilibrium profile with the shape of a relatively 'planar beach profile' (see text for explanation). The values used for the input parameters are $y_c/\gamma_c = 1.6$, $s_0 = 0.11$, $p = 1$ and $A = 2.75$. See caption of Fig. 3.3.1 and text for more explanations. Top: The solid line is the equilibrium wave height, $H_{eq}$ and the dashed line is the relative wave height, $Y_{eq}$. Bottom: The solid line corresponds to the equilibrium topography (equal to minus water depth, $-D_{eq}$.)

Table 3.3.1: Definition of the four characteristic slopes used to describe the equilibrium bottom topographies. See the text for explanation.

| Name | Symbol | Definition |
|---|---|---|
| Surf zone slope | $\beta_{surf}$ | $\frac{dD}{dx}\|_{x=0.5\Delta X}$ |
| Break-point slope | $\beta_{break}$ | $\frac{dD}{dx}\|_{x=\Delta X}$ |
| Relative slope | $\beta_{rel}$ | $\frac{\beta_{surf}}{\beta_{break}}$ |
| Mean slope | $\beta_{mean}$ | $\frac{\beta_{surf}+\beta_{break}}{2}$ |

transport induced by the undertow starts to become significant because waves are breaking notably. Hence, the local beach slope must become flatter in order to reduce the downslope transport and maintain a sediment transport balance. The flattening of the slope dissipates wave energy. The relative wave height is only allowed to reach its critical value, $y_c$, at the shoreline, where the slope becomes exactly zero. This can be easily derived from Eq. (3.2.13).

As we are dealing with a random distribution of wave height, there is not a single break-point in the solutions. Two points of the domain related with the place where waves start breaking are included in all the graphs. Firstly, the vertical dashed line shows the point $X_{b1}$, which has already been defined in the previous paragraph (place where $Y_{eq} = y_c \, p/(p+1)$). Physically, it defines the place where the relative strength of the onshore transport has a maximum (so that the local slope of the profile also reaches a maximum). In that point, the waves arriving with the largest heights start to break, but most of the waves are still shoaling. The second point, $X_{b2}$, has been marked with a vertical dash-dot line in the graphs. There, the equilibrium relative wave height changes its concavity, so it is the point with the maximum derivative of $Y_{eq}$. Physically, it defines the place where most of the waves are already breaking and it is close to the point with the maximum wave height. So in this system, we deal with a breaker zone (which could be defined as the region between $X_{b1}$ and $X_{b2}$) rather than a single break-point. We have chosen $X_{b1}$ to be the *'effective break-point'* in order to compute the surf zone width of the equilibrium solutions, called $\Delta X_{surf}$ or simply $\Delta X$.

Another important property of the obtained equilibrium profiles is that, in spite of being 'non-barred', their slope can vary quite a lot with the cross-shore position (see Fig. 3.3.1, for instance). Table 3.3.1 shows the definition of four characteristic slopes of the equilibrium bottom topography. The inclination of the bottom at the centre of the surf zone (defined as $x = 0.5\,\Delta X$), is used as a characteristic value of the slope of the terraces (*'surf zone slope'*, $\beta_{surf}$). The *'break-point slope'* ($\beta_{break}$) is used to quantify the inclination of the bottom at the 'effective break-point' ($x = \Delta X$). The *'relative slope'*, $\beta_{rel}$, defined as the ratio between the two latter defined slopes, tells us whether the equilibrium profile is strongly 'terraced' or if it is more 'planar'. Finally, we can define a sort of *'mean slope'*, $\beta_{mean}$, which tells us how steep is the global profile.

### 3.3.2   Sensitivity to the model parameters

The dynamics of this problem is mainly governed by the three parameters of the dimensional sediment transport equation: the critical relative wave height, $y_c$, the downslope 'morpho-dynamical diffusivity', $s_0$ (the reason for choosing this name will be explained later on) and the exponent $p$. The influence of changing their value on the results for the equilibrium profiles is described in the next paragraphs. Model results are much less sensitive to changes in the wave steepness $\xi_{off}$ and $\gamma_c$ inside the coefficient $A$ (see Eq. 3.2.11). The important changes in this latter coefficient are mainly due to varying $y_c$. One of the most important consequences of the scaling used is that the wave height far offshore, $H_{off}$, only appears in the non-dimensional equations through the wave steepness $\xi_{off}$ (see section 3.2.3). Obtained results confirm that $H_{off}$ itself turns out to be only a scaling parameter, with no influence on the non-dimensional equations. This means that doubling its magnitude just leads to doubling all the lengths involved in the solutions, for instance.

The effect of changing the critical relative wave height, $y_c$, is very strong. A large value of this parameter implies that the undertow transport does not become significant until the system reaches a large value of the relative wave height. Therefore, the shoaling region of the domain is located near the shoreline and we obtain profiles with nearly no terrace, called 'planar beach profiles' (see an example in Fig. 3.3.2 obtained with $y_c = 0.8$). In these 'planar profiles', the water depth is already quite small when the profile can become less steep, so that the terrace is very small in cross-shore length, reaching the coastline quickly (small surf zone width, $\Delta X$). These 'planar profiles' are also characterized by large 'relative slopes' ($\beta_{rel} \to 1$) because the slope at the centre of the terrace is similar to the slope at the break-point. A hydrodynamical property of these 'planar profiles' is that the relative wave height in the terrace part is larger than $\gamma_c$ because it is equal to $y_c > \gamma_c$ (waves are over-saturated).

Figure 3.3.1 shows an example of the equilibrium profile associated with a smaller value of the critical relative wave height ($y_c = 0.45$). In this case we obtain more 'terraced beach profiles' because the undertow contribution starts to dominate the offshore transport before the relative wave height reaches the saturation value of $\gamma_c$. Consequently waves never reach this saturation (they are under-saturated) and the beach remains nearly flat over a long area. So these 'terraced beaches' are characterized by large values of the surf zone width and small 'relative slopes'.

A wide range of values for the critical relative wave height and the downslope diffusivity has been analysed (see table 3.2.2). The resultant range of equilibrium solutions contains profiles with very different characteristics and lengths scales. Figure 3.3.3 shows the relative slope, $\beta_{rel}$, and the dimensional surf zone width, $\Delta X$, of these results as a function of the two parameters of the sediment transport formula. Firstly, one may see the influence of $y_c$ in the equilibrium solutions, which has already been explained physically in the previous two paragraphs. The 'relative slope' increases with $y_c$ while the surf downslopezone width decreases. These graphs also show that increasing the downslope diffusivity, $s_0$, leads to profiles that are more 'planar' (larger relative slope). The surf zone width clearly grows with $s_0$ because the overall profile becomes less steep ($\beta_{mean}$ diminishes). The physical reason for these latter behaviour is that, as the coefficient in front of the downslope transport increases, the corresponding gradients in water depth do not need to be as large as before
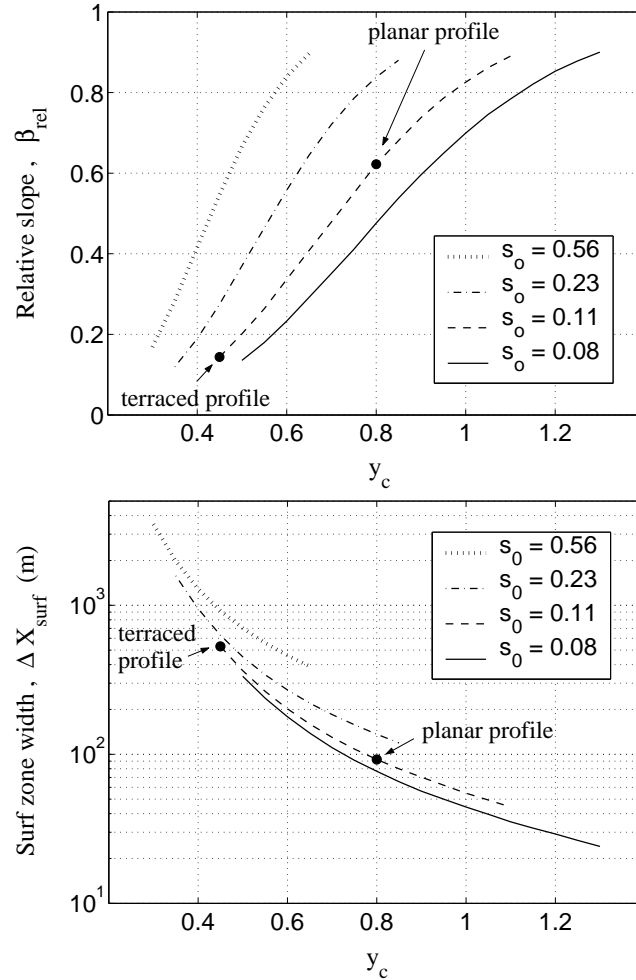
Figure 3.3.3: Sensitivity of the shape of the obtained equilibrium beach profiles to the two most important parameters of the model: the critical relative wave height, $y_c$, and the downslope 'morphodynamical diffusivity', $s_0$. The value of the exponent in the sediment transport is $p = 1$. All the quantities shown are dimensional, computed with a wave height far offshore $H_{off} = 1m$. Doubling this value would lead to surf zone widths two times larger. Top: Dependence of the 'relative slope' $\beta_{rel} = \beta_{surf}/\beta_{break}$ on $y_c$ and $s_0$. Bottom: Dependence of the dimensional surf zone width, $\Delta X_{surf}$ on $y_c$ and $s_0$. In both graphs, the beach profiles that have been shown as examples in Fig. 3.3.1 and 3.3.2 are marked with a cross.

Table 3.3.2: Dependence on the exponent $p$ in Eq. (3.2.13) of four quantities that characterizes the equilibrium profiles: the relative slope, $\beta_{rel}$, the 'mean slope', $\beta_{mean}$, the surf zone width, $\Delta X$ and the depth at the break-point, $D_b$. See the text for explanation together with section 3.3.1 for the definition of these four quantities. The values used for the other parameters are: $y_c/\gamma_c = 1$, $s_0 = 0.056$ and $A = 0.60$. The quantities shown in this table are non-dimensional.

| $p$ | $\beta_{rel}$ | $\beta_{mean}$ | $\Delta X$ | $D_b$ |
|-----|-----|-----|-----|-----|
| 1 | 0.072 | 2.4 | 11 | 5.3 |
| 2 | 0.11 | 1.5 | 9.6 | 3.6 |
| 3 | 0.14 | 1.1 | 8.5 | 2.5 |

to counteract the onshore transport by waves. So the main influence of increasing $s_0$ is a general smoothing of the gradients (leading to less steep and more 'planar beaches'). This is the typical effect of a 'morphodynamical diffusivity' parameter and this is the reason why we have chosen this name for $s_0$. In the two latter graphs, the beach profiles that have been shown as examples in Fig. 3.3.2 and 3.3.1 are marked with a cross.

The sensitivity of the solutions to variations in the exponent $p$ in the sediment transport equation (Eq. 3.2.13) has also been checked (see table 3.3.2). Increasing this exponent modifies strongly the slopes of the profiles, the 'relative slope' $\beta_{real}$ becoming larger ('less terraced beaches') and the 'mean slope' $\beta_{mean}$ decreasing significantly (milder profiles). Table 3.3.2 also shows that the surf zone width, $\Delta X$, and the water depth at the break-point, $D_b$, are smaller when a larger $p$ is used, as a result of the change in the slopes. Physically, these effects can be understood when considering that enlarging $p$ decreases the total wave transport (as the variable $Y$ is always smaller than 1 in Eq. (3.2.13)). Thus, the downslope transport can remain smaller when counteracting this total onshore transport and the 'mean slope' diminish. The strong changes induced in the 'relative slope' by increasing $p$ can be interpreted by the fact that it makes the undertow transport become negligible for a larger range of relative wave heights. Then, when it starts to counteract the wave onshore transport (for $Y_{eq} > y_c p/(p+1)$), the water depth is already quite small and the system reaches the coastline quickly. In fact, increasing the exponent $p$ in the transport formula has the same effect than increasing the downslope diffusivity, $s_0$. It smooths the profile, leading to flatter and more 'planar beaches'.

The sediment transport in the nearshore is still poorly understood. Besides, previous studies concerning sediment transport and beach profile evolution already underlined that the results can depend strongly on the sediment transport formulation used (see Short (1999), together with the results of chapter 5 of the present thesis). So it seems important to test the sensitivity of any morphological model to the transport formula itself. As a first step, we have used the more general transport formula

$$Q = \frac{1}{s_0}(Y^p - NY^q) \quad , \tag{3.3.1}$$

which includes two new parameters, $N$ and $q$. The formulation used in the rest of this chapter, given by Eq. (3.2.13), is recovered if we use $N = 1$ and $q = p + 1$. Results varying these two new parameters are not qualitatively different. Profiles are always 'non-barred' and they display a terrace with a varying relative slope. One exception is the case of $N = 0$ which means no undertow transport and gives a concave-up profile with no terrace, in accordance with the results by Bowen (1980) and Bailard & Inman (1981). The strength of the undertow transport increases with this parameter, leading to longer terraces. The second expected exception is the unrealistic case of $q < p$, which means that the wave transport is always offshore directed (the undertow being always larger than the wave asymmetry transport). The water depth always increases in the onshore direction, as it is the only way by which the downslope transport can balance the wave transport, and the coastline is never reached. When $q = p$, the two types of wave transport counteract each other and the slope becomes zero. For $q > p$, the coastline is always reached, displaying again 'terraced shapes'. Their 'relative slope' increases with the difference between the two exponents $q - p$.

## 3.4  Discussion

A method for quantitative comparison of these results with field data is not at all obvious considering the restrictions imposed by the equilibrium concept. Most natural systems are probably not in equilibrium (Plant *et al.*, 1999), at least partly owing to the fact that wave conditions are not held constant, as was assumed here. Moreover, the present model incorporates a wide range of simplifying assumptions as we aimed at building the simplest model that still encapsulated the most important physical processes. However, the equations have some physical basis so it is hoped that a qualitative comparison with natural beach profiles is still possible.

The most relevant finding presented in the previous section is the overall shape of the obtained equilibrium profiles, which comprise a gently sloping terrace along the surf zone and a concave-up profile in the shoaling zone. This separation of the surf/shoaling domain is much more realistic than the artificial profiles that are often build up by matching two Bruun/Dean formulas (Komar, 1998; Short, 1999). Also the simple Bailard-based models presented by Bowen (1980) and Bailard & Inman (1981) could only describe the shoaling part of the profiles. An important finding with respect to the results presented by Plant *et al.* (2001$b$) is the influence of changing the model parameters on the properties of the equilibrium profiles. The paper by Plant *et al.* (2001$b$) only showed strongly 'terraced beach profile', while the present results contain more diverse shapes ranging from 'terraced' to nearly 'planar profiles' (see section 1.2.2 for a definition of the different types of alongshore uniform beach profiles).

The two types of limiting profiles ('terraced versus planar') compare well with the two energy ends of the beach spectrum described by Wright & Short (1984) ('dissipative and reflective beach states', respectively, see section 3.1). From the theory (see Eq. 3.2.6 in section 3.2.2), we know that large values of $y_c$ are obtained mainly in case of large cross-correlation between sediment load and fluid velocities. There are two characteristics that can lead to this effect, large wave non-linearities (obtained in case of long period waves arriving in shallow water) and large grain size in sediment. Fine grains and small period

waves lead to less correlation because the sand remains in suspension for periods longer than wave period. Thus, the obtained equilibrium beach profiles tend to be 'planar' (large relative slope) and steep (large 'mean slope') in case of large grain size and long period waves (large $y_c$), whereas more 'terraced' (small relative slope) and less steep beaches are found in case of fine sand and short period waves (smaller $y_c$, more dissipative conditions). This behaviour is in agreement with the dependence of natural beach profiles on the non-dimensional fall velocity, $\Omega_0$, described in section 3.1.1 (Wright & Short, 1984; Komar, 1998; Short, 1999).

A hydrodynamical property of the equilibrium results is that 'planar profiles' display a relative wave height over the terrace that is larger than $\gamma_c$ (because $Y_{eq}$ is equal to $y_c$, which in turn is smaller than $\gamma_c$). Physically, this means that waves are over-saturated and would likely be significantly reflected in a natural beach. This result is in agreement with Raubenheimer *et al.* (1996), who measured and computed the relative wave height saturation value in several beaches. They concluded that this quantity is larger in less dissipative profiles.

The most important restriction of the present work is that the shoaling effect is overestimated in our model due to the approximate expression we have used for the group velocity of waves ('very shallow water assumption', $c_g = \sqrt{gD}$). However, this does not alter the qualitative results because the approximation is relatively accurate in the region of interest (the nearshore zone). The assumption is more valid for describing swell conditions than in case of storms. In order to check the influence of this approximation, some preliminary tests have been done using a more complete set of equations that include the complete expression for the group velocity, comparing the results with the ones found with our simpler model. An offshore rms wave height, $H_{off}$, has been imposed in both models at a certain water depth, $D_{off}$, which can be considered as the boundary between the nearshore and the offshore regions. Then the equations have been integrated in the shoreward direction up to the coastline. Our approximation overestimates the rms wave heights at the break-point. The error made ranges from 5% in case of swell conditions up to 25% under severe storm conditions (waves of $3m$. height and $7s$. period). However, the obtained equilibrium bottom profiles are always qualitatively and quantitatively very similar (even in the latter case). On the other hand, this approximation has a stronger effect on the calculation of the offshore part of the equilibrium profiles, which is needed for the stability analysis of the following chapter in some circumstances. The wave height integrated from a fixed offshore position, $x_{off}$, to the seaward direction becomes more and more mistaken (it goes on decreasing while it should be constant). This results from the fact that the 'very shallow water assumption' becomes less and less valid as we move toward larger water depths. Again, although the wave height is not physically sensible far offshore, the error done in the computation of the water depth is still not critical, the slope of the bottom being moderately overestimated in our model.

Some other important physical processes in real beaches that have not been included are the presence of longshore currents (due to oblique wave incidence), the wave reflection, the presence of tides, the set-up/set-down of the free surface elevation and the description of the roller dynamics during the breaking process (Reniers *et al.*, 2003)). Describing the influence of all these physical phenomena on the equilibrium beach profiles could be interesting and it might lead to qualitatively different profile shapes. However, a more complete set of equations that contain some of these processes (longshore currents and set-up/set-down)

have been used in a preliminary way for oblique wave incidence and the results are again 'terraced-like profiles'.

The present equilibrium model has not been able to reproduce profiles containing shore-parallel bars and troughs (in agreement with Plant *et al.* (2001*b*)), even though the essential processes of the 'breakpoint-bar mechanism' are included in the transport formula used (at least in an idealised way). So it seems that including undertow and wave non-linearities transport is not a sufficient condition for describing the growth of bars by this mechanism. The three included transport processes can be in balance and give 'planar or terraced profiles', without any presence of shore-parallel bars and troughs. In the present transport formula, for instance, the two wave induced transports increase in magnitude as waves propagate toward the coast in such a way that the residual wave transport is always negative (onshore directed) and decreases monotonously with decreasing $x$. This residual transport is locally balanced by the downslope transport that is produced by a 'terraced (non-barred) shape'. This is in line with the paper by Ruessink & Terwindt (2000), who presented field measurements in the Dutch coast (in a region displaying three shore-parallel bars). They showed that the undertow offshore transport and the wave onshore transport where of approximately equal magnitude. The net suspended load transport was then predicted to be a delicate balance between the onshore and the offshore components.

As it was also suggested in that paper, in such situations near equilibrium any small perturbations superimposed to this equilibrium could dominate the large-scale dynamics of the system and lead to new solutions. Thinking in mathematical terms, this means that the generation of shore-parallel bars could result from an instability of the equilibrium situation described in the present chapter without including more physics in the equations (this hypothesis will be tested in the next chapter). Of course it is also conceivable that including more physical processes that have been neglected in the present equilibrium model could also lead to 'barred equilibrium beach profiles'. In order to set the physical relevance of the obtained equilibrium profiles, it is also crucial to check their stability with respect to perturbations.

## 3.5   Conclusions

In this chapter the sediment transport model of Plant *et al.* (2001*b*) has been used to investigate the physics behind the shape of the equilibrium profiles. The set of non-linear equations leading to the equilibrium state has been solved. The resultant equilibrium beach profiles are always 'non-barred'. They comprise a gently sloping terrace, which extends from the coastline to the break-point, and a concave-up profile in the shoaling zone. The balance between the three following contributions to the cross-shore transport gives rise to the described 'non-barred profiles': an offshore transport due to undertow current, an onshore transport due to wave non-linearities and a downslope contribution. The two wave-induced transports increase in magnitude as waves propagate toward the coast in such a way that the residual wave transport is always negative (onshore directed) and decreases monotonously in the shoreward direction. This residual onshore transport is locally balanced by the downslope transport that is produced due to the local slopes of a 'terraced (non-barred) shape'.

For very dissipative conditions, obtained in case of small critical relative wave height, $y_c$, (associated to fine grain size and short period waves), long and flat terraces are obtained with a steeper profile seaward of the break-point. The other limiting profile, obtained in case of less dissipative conditions, is a 'planar beach' (similar slopes in the terrace and the shoaling zones) with a small surf zone width. The downslope diffusivity, $s_0$, plays a typical diffusive role, smoothing the gradients of the solutions and leading to flat and 'planar profiles'. Increasing the exponent $p$ in the transport formula also leads to less steep and more 'planar profiles'. The hydrodynamical parameters have a minor influence on the results. The obtained profile shapes and their dependence on the model parameters reproduce the main characteristics of the beach profiles observed in nature. Preliminary results of the sensitivity of the model to the sediment transport formula itself have also been presented. The behaviour of the obtained profiles seems to be qualitatively independent of the transport formulation used (if the latter is physically sensible).

The idealised and semi-empirical sediment transport model coupled with a wave transformation equation used has been able to describe satisfactorily some important physical properties of equilibrium profiles, in spite of its simplicity. However, the obtained equilibrium profiles are always 'non-barred' so that one of the most important properties of beach profiles (the presence of shore-parallel bars) has not been described by our physical model and/or by the equilibrium approach.

# Chapter 4

# On the growth of shore-parallel sand bars

## 4.1 Preliminaries

### 4.1.1 Field observations

Alongshore uniform 'shore-parallel sand bars' are found on almost all sandy coasts. As they display a large mobility in the cross-shore direction, explaining most of the variability of beach profiles, their study is one of the main objectives of coastal sciences (Short, 1999). Remember again that the concept of 'barred beach profile' used in this thesis refers to alongshore uniform profiles that displays a clear trough followed by a shore-parallel bar as one moves seaward. These profiles are qualitatively different from 'terraced beach profiles' (such as the ones described in the previous chapter). There has been a large confusion between these two profile types in the literature, the edge of terraces being often interpreted as shore-parallel bars (Tapia, 2003).

Several examples of shore-parallel bars have been shown in chapter 1. Figures 1.2.5 and 1.2.7 have shown a single bar in the Duck beach, in the Atlantic coast of U.S.A. The behaviour of this nearly ubiquitous bar is mainly governed by the interannual weather variations. The bar position is extremely variable on the time scale of days under average conditions and even hours during storms (Holman & Sallenger, 1993; Thornton & Humiston, 1996; Gallagher *et al.*, 1998; Plant *et al.*, 1999; Birkemeier & Holland, 2001; Hoefel & Elgar, 2003). Figure 1.2.6 has shown an also common situation of the same beach with two shore-parallel bars, the outer one having received much less attention having been much less studied. In the Dutch coast, systems of 2 or 3 shore-parallel bars are also nearly ubiquitous. These systems display a very persistent yearly-averaged cyclic behaviour. Single bars are generated in the inner nearshore in depths of 1 to 2 meters, they migrate offshore in aver-

age and finally decay in the outer nearshore at water depths of about 5 to 7 meters. The return period of this cyclic behaviour is rather constant in a specific alongshore position, but comparing different alongshore positions aong the Dutch coast it can range from 4 to 15 years (Kroon, 1994; Ruessink & Kroon, 1994; Wijnberg & Terwindt, 1995; van Enckevort, 2001; Wijnberg & Kroon, 2002). A typical 'ARGUS image' of the Noordwijk beach, in The Netherlands, has been displayed in Fig. 1.2.2. Finally, in highly protected coasts such as lakes, back-barrier lagoons and sheltered embayments, one may find multiple parallel bars with spacings of some tens of meters (systems with up to 30 bars have been described in Bowen (1980), Mei (1985), Aagaard (1991) and Yu & Mei (2000)). An example of such type of systems has been shown in Fig. 1.2.8, which displays a nice photography of a multiple bar system in the Gulf of Mexico coast of Mississippi, in U.S.A. Multiple bar systems with larger spacings of some hundreds of meters are also found in open beaches (Short, 1975; Aagaard et al., 1998). A lengthy account of the presence of shore-parallel bars in natural beaches worldwide is given in Horikawa (1988), Komar (1998) and Short (1999).

Some bar systems are well known for their seasonal formation and subsequent disappearance (Winant et al., 1975). The seasonal pattern consists of growth during large storms and decay during less energetic conditions. Bars sometimes disappear by migration onshore and welding to the subaerial beach (Wright & Short, 1984; Aagaard et al., 1998). In contrast, other bar systems, such as the ones in Duck and in the Dutch coast, are known for being very persistent over several years to decades (Lippmann et al., 1990; Kroon, 1994; Ruessink & Kroon, 1994; Wijnberg & Terwindt, 1995; Plant et al., 1999). In these cases, inter-annual cycles of bar formation near the shoreline, net offshore migration and subsequent bar decay have been observed. Modelling this long term behaviour is still far from being achieved. The main reason is that the shorter term processes (generation, migration and decay) are still poorly understood from a physics basis, in spite of the common ocurrence of these features and the considerable existing research (Wijnberg & Kroon, 2002; Hoefel & Elgar, 2003).

Short-term migration of alongshore uniform sand bars is well described by field data. Bars typically move slowly shoreward under conditions of low wave energy (velocities being of the order of $0.1m/h$, see Wijnberg & Kroon (2002)) and migrate more rapidly offshore when waves are more energetic (up to some few $m/h$, see Holman & Sallenger (1993), Gallagher et al. (1998) and Hoefel & Elgar (2003)). However, as bar formation seems to be a faster phenomena, nearly no information can be found about this process in field observations. Thus, little is understood about the physical mechanisms and wave conditions that are required to form bars. It is reported in the literature that shore-parallel bars are often generated during storms, their growth being linked to an erosion of the shoreline. The sand moves from the dry beach to feed the bar (Komar, 1998; Short, 1999). Laboratory experiments in large wave flumes were done in the past to reproduce this type of formation of shore-parallel bars at the break-point, using both regular and randomly distributed wave heights (Larson, 1988; Kajima et al., 1982; Dean et al., 1992; Bröker et al., 1992; Reniers et al., 2003). Times of formation from a few hours up to half day were obtained. The initial profiles of such experiments can be defined as steep ($\beta \sim 0.02 - 0.05$) and 'planar beach profiles' (with small 'relative slopes', using the nomenclature of chapter 3). The use of randomly distributed wave heights leaded to more diffused bars (i.e. less sharp). There are also some few field experiments reporting the generation of bars during storms that lasted some $2 - 3$ days (Thornton & Humiston, 1996; Aagaard et al., 1998). In all the experiments decribed so far, the shoreline did not evolve significantly.
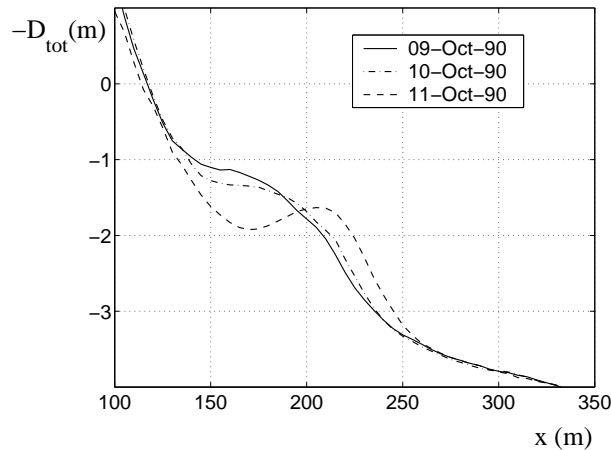
Figure 4.1.1: Bottom profiles (averaged over $400m$ alongshore) at the Duck beach, in the Atlantic coast of U.S.A., corresponding to the $9^{th}$, $10^{th}$ and $11^{th}$ October 1990 (during Delilah experiment). A bar was formed from a moderately 'terraced profile' with a growth time of 1 day. In this field experiment the measurements were performed daily. In the graph, the 'mean' water level is located at $D_{tot} = 0m$.

In order to find some insight into the physics behind this type of generation processes, some details about the bar generation episode described in Thornton & Humiston (1996) are presented in this paragraph. During October 1990, a detailed experiment (called DELILAH) was performed at the Duck beach in U.S.A., during which a bar was formed in 1 day. The used data set comprises daily surveyed beach profiles, which extend from the dunes to $8m$ water depth and span a $1Km$ wide region alongshore. In order to obtain data consistent with our assumption of alongshore-uniformity, the observations have been interpolated to a single location so that alongshore inhomogeneities at length scales less than $400m$ have been removed by filtering. Figure 4.1.1 shows the bottom profiles corresponding to the days when the bar was growing. The growth time could be resolved, being of the order of 1 day. In this case, the bar was formed from an initial profile which was moderately 'terraced', using again the nomenclature of chapter 3. The hydrodynamical conditions during this generation event were waves of $1.5m$ rms wave height (as can be seen in Fig. 4.1.2), arriving with an incidence angle of $40^o$ (at $8m$ water depth). So a strong longshore current was present. Another important remark is that the profile shown in Fig. 4.1.1 had a certain alongshore variability before the arrival of the storm. After the commencement of the storm, this alongshore variability started to smooth out so that on October, $11^{th}$, a shore-parallel bar was present (Thornton & Humiston, 1996). This initial alongshore non-uniformity probably influenced the initial dynamics of the system. The generated horizontal 'mean' currents can be very strong in case of non-uniformity in the alongshore direction. Thus, the undertow induced transport becomes less influential because the system has a different way to compensate the input of water mass above the trough level (such as rip currents, for instance). Mechanisms leading to growth in this sort of situation may be quite different from the alongshore uniform case and they may be related also with the transport induced by the horizontal circulation
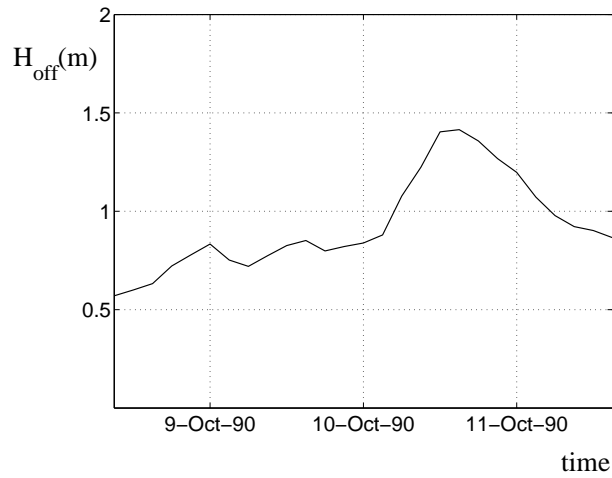
Figure 4.1.2: Root mean square wave height measured at $8m$ water depth of the Duck beach, corresponding to the $9^{th}$, $10^{th}$ and $11^{th}$ October 1990. A storm arrived on $10^{th}$ October with waves being up to $1.5m$ height during that day.

(for instance see Caballeria *et al.* (2002)). This type of situation will be described in chapter 5. Maybe, in the particular growing event shown in Fig. 4.1.1, where the rhythmicity was nor strong neither persistent, both processes were coexisting.

Another example of bar generation event in the Duck beach is described in detail in this paragraph. Now, the used measured profiles form part of the long-term beach profile survey (Birkemeier & Holland, 2001). This second data set comprises monthly surveyed beach profiles, which again extend from the dunes to $8m$ water depth and span a $1Km$ wide region alongshore. The observations have been interpolated again to a single location so that alongshore inhomogeneities have been removed. In addition, the data have been interpolated in time in order to show profile changes at 15 days intervals, trying to resolve the (inferred) initial stages of bar formation. However, it is important to remark that the generation event could not be well-captured because the measurements were not performed often enough. A shore-parallel bar was formed from a strongly 'terraced profile' between $2^{nd}$ February and $2^{nd}$ March 1999 (see Fig. 4.1.3). The growth time could not be resolved, so that we only know that it was smaller than 1 month. During the generation episode, root mean square wave heights measured offshore were between 0.5 and $1.5m$ (see Fig. 4.1.4) and their direction was mostly shore-normal. More frequent topographic measurements would be needed in order to better resolve the generation event and to know under what wave conditions it occurred.

The generation of shore-parallel bars is not only found during storms (when the profile is far from being in equilibrium with the waves), but also in milder conditions. Ruessink & Terwindt (2000) presented field measurements of cross-shore sediment transport in the Dutch coast, where shore-parallel bars are cyclically generated. The onshore and offshore transports were of nearly equal magnitude, so the system was close to equilibrium conditions.
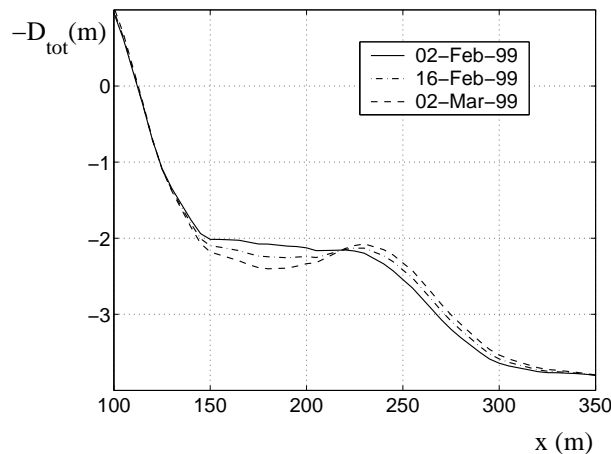
Figure 4.1.3: Bottom profiles (averaged over $400m$ alongshore) at the Duck beach during February 1999. A bar was formed from a strongly terraced profile (compared with the example shown before, see Fig. 4.1.1) with a growth time of less than 1 month. The corresponding survey consisted in measurements once a month, so that the profiles showed here have been interpolated from a monthly data set. The 'mean' water level is again located at $D_{tot} = 0m$.

## 4.1.2  Previous modelling and motivation

Ideally, beach profile evolution and bar dynamics should be predicted using process-based models that couple the nearshore hydrodynamics (which computes water motions over an arbitrary beach profile) to nearshore sediment transport (which leads to changes in the initial profile and provides feedback to the hydrodynamical system). These sort of models have been implemented in the last decades, but rarely show significant predictive skill over either short (e.g., days) or long (e.g., years) time periods (Gallagher *et al.*, 1998; Plant *et al.*, 2001*b*; van Enckevort, 2001; Stive & Reniers, 2003). One reason for failure is demonstrated by Gallagher *et al.* (1998), who showed that the underlying sediment transport formulation used by many of the models is inaccurate under some conditions. There is, therefore, a need for continued work in refining our understanding of both the short-term hydrodynamical processes and the sediment transport mechanisms that are important to driving cross-shore bathymetric changes and specifically bar evolution. Different theoretical approaches for the generation of shore-parallel bars have been presented in the past (Lippmann & Holman, 1990; Holman & Sallenger, 1993; Komar, 1998; Short, 1999; Wijnberg & Kroon, 2002). They are generally classified in two groups: the *'forced response mechanisms'* and the *'breakpoint-bar related mechanisms'*.

The 'forced response mechanisms' starts off from the concept that bars can form near equilibrium conditions because a template in the flow field is imprinted on the seabed. The first hypothesis that were tested for describing systems of multiple shore-parallel bars were related with standing high-frequency gravity waves. Reflection of the incident wave field by an abrupt coast line could lead to a standing velocity drift pattern with a certain convergence
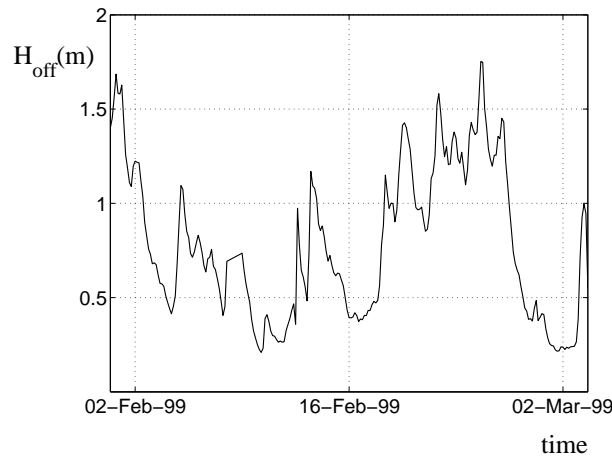
Figure 4.1.4: Root mean square wave height measured at $8m$ water depth of the Duck beach during February 1999. Wave conditions were quite variable during all the month, the wave height ranging from $0.5m$ to $1.5m$.

at the nodes or the antinodes (depending on the transport mode, see Bowen (1980)). This phenomenon has been often observed in laboratory flumes (Bowen, 1980; Mei, 1985). The small scaling that is imposed by high-frequency waves (tens of meters) only matches with the bar separation observed in highly protected coasts, as the system shown in Fig. 1.2.8. In order to obtain the spacings found in open coasts (hundreds of meters), it is more reasonable to consider the drift transport under longer waves. A first mechanism proposed to generate longer scales of cross-shore spatial modulation is based on the interaction of incident high-frequency waves and the corresponding higher harmonics that can be generated by non-linear interactions (Boczar-Karakiewicz *et al.*, 1987). However, some critical remarks to this mechanism were done by Hulscher (1996). Another classical approach, which was first suggested by Short (1975) and followed by Bowen (1980), is considering the bars generated below infragravity standing waves, such as either 'leaky waves' or 'edge waves' (see section 1.3.1).

The weakest point of the 'forced response mechanisms' described until now is the requirement of a single dominant frequency in the wave field (Holman & Sallenger, 1993; Short, 1999; Wijnberg & Kroon, 2002). For instance, in order for the edge waves to form multiple bars with a certain observed spacing, only one edge wave frequency/mode combination should be present, but no clear selection mechanism has been presented so far in the literature. Another drawback of all the previous explanations is that the influence of the growing topography on the local flow field is not considered, while it has been shown to be important due to the strong non-linearities of the system (Plant *et al.*, 1999). This is not the case in the study of Mei (1985), who presented a mechanism where the incident waves are reflected by the growing topography allowing for a ressonance process that reinforces the growth of the bars (phenomenon known as Bragg scattering in other fields of Physics). However, one concludig remark of his paper was that this mechanism could not generate bars from

an initially 'non-barred profile', but it only reinforced systems of bars that were already present (or excite the growth of a multiple bar systems in the shoaling zone if there were previous shore-parallel bars inside the surf zone). Besides, all the mechanisms presented so far do not consider the phenomenon of wave breaking, which must be relevant at least for the typical bars that emerge near the break-point. Some few field observations supporting the 'forced response mechanisms' as responsible for the generation of shore-parallel bars has been published (Bauer & Greenwood, 1990; Aagaard, 1991; Short, 1999). However, many other papers state that no clear evidences have been found either in the laboratory nor in natural open beaches that verify these mechanisms (Dally, 1987; Larson, 1988; Dean *et al.*, 1992; Holman & Sallenger, 1993; Aagaard *et al.*, 1998).

The 'breakpoint-bar related mechanisms' were first suggested because of the strong correlation observed between the position of the bar crest of many shore-parallel bars in natural beaches and the location of the break-point of the incident wave field (King & Williams, 1949; Dally, 1987; Larson, 1988; Holman & Sallenger, 1993). The first studies using this idea related bar formation with the vortices generated by plunging breakers, as this phenomenon was easily reproduced in laboratory flumes for monochromatic and regular waves. This type of process would then be again a 'forced response mechanism', the topography adapting passively to this specific wave forcing. When dealing with natural wave fields, which usually display randomly distributed wave heights, the break-point has not a unique location and a new theory for bar generation near the position where waves start to break was suggested (see Dyhr-Nielsen & Sorensen (1970) for the first qualitative description). The main processes involved in this theory are the offshore sediment transport due to the undertow current (mainly inside the surf zone) and the onshore transport due to the non-linearities of the incident wave field. This is supposed to result in a region of residual flow convergence and hence sediment accumulation close to the break-point. In order to account for the formation of 2 or more bars by the 'breakpoint-bar related mechanisms', several hypothesis have been formulated, always related with the existence of several break-points in the same beach (Short, 1999). Reformation of the waves after the first break-point is often observed, a second break-point occurring in a shallower location. Because of tidal oscillation of the 'mean' water level, two distinct break-points could also be found in the same beach. Finally, the existence of two different dominant wave conditions could also explain the presence of an outer bar generated during storms and an inner bar related with milder conditions.

Many authors recognise the 'breakpoint-bar related mechanisms' as being responsible for most of the shore-parallel bars generated in the surf zone, both in nature and in the laboratory (Dally, 1987; Larson, 1988; Roelvink & Stive, 1989; Dean *et al.*, 1992; Aagaard *et al.*, 1998; Komar, 1998; Short, 1999). However no clear quantitative description of any of this mechanisms has been presented so far in terms of simple physical processes. A consequence of this is that the complex numerical models that are used by engineers for predicting the evolution of the nearshore system are often unable to reproduce shore-parallel bar generation events. Specially when randomly distributed wave heights are used (which is the natural situation found in this environment), the formation of the trough at the shoreward side of the bar is hardly ever achieved (Larson, 1988; Bröker *et al.*, 1992; Dean *et al.*, 1992; Thornton & Humiston, 1996; Komar, 1998; Tapia, 2003; Reniers *et al.*, 2003).

Due to the few break-point bar generation events in nature reported in the literature, it is unclear if they always emerge during storms or whether this mechanism also stands

near equilibrium conditions. As it has already been told, the paper by Ruessink & Terwindt (2000) reported field measurements in the barred Dutch coast where the onshore transport due to the wave non-linearities and the undertow offshore transport turned out to be near in balance. They subsequently suggested that small perturbations superimposed to this equilibrium situation could dominate the large-scale behaviour of the system leading to the generation of bars. Among the random noise that is inherent in the stochastic nearshore system, there may be some barred-like bottom perturbations that generate changes in the wave field that in turn creates convergence of sediment over the crests, leading to a positive feedback process. After performing an experiment for the generation of break-point bars in a wave flume, Dean *et al.* (1992) stated that: *'The failure to date to adequately define this feedback mechanism appears to be one of the major impediments in our attempts to quantify the full mechanisms for bar formation and equilibration'.* Given a certain description of the nearshore system, the existence and definition of this positive feedback process could be done by perfoming a stability analysis of the equilibrium state. In spite of the clear limitations of this near-equilibrium approach (specially because shore-parallel bars are often generated under stormy weather, far from equilibrium conditions), this approach would lead to the first quantitative description of the underlying feedback process that may be behind the 'breakpoint-bar related mechanism'.

### 4.1.3   Aim, approach and outline of the chapter

The main objective of this chapter is to perform a stability analysis of the equilibrium profiles presented in chapter 3 with various aims. Firstly, checking the stability of such equilibrium states is important in order to set their physical relevance. Secondly, as the obtained equilibrium profiles have always been non-barred, we want to test the hypothesis that shore-parallel bars stem from an instability (linear or non-linear) of these equilibrium states through a 'breakpoint-bar related mechanism'. Thirdly, a quantitative description of this latter growing mechanism would allow for understanding better why, how and under what conditions shore-parallel bars grow. Finally, the non-linear temporal evolution of the dynamical system moderately far from equilibrium is studied and attention is also focused on the conditions that can lead to bar migration.

To attain these goals, the sediment transport law coupled with a nearshore wave transformation equation that were first presented in Plant *et al.* (2001*b*) have been again selected as governing equations. Then, the formulation used contain the same physical processes (and the same assumptions) as the equations of chapter 3, including the processes that have been recognised to be involved in the 'breakpoint-bar mechanism'. The difference is that now the possibility that shore-parallel bars emerge as an instability (linear or non-linear) of the previously 'non-barred equilibrium profiles' is investigated. The system is again supposed to be uniform in the alongshore direction, focusing on the dynamics of the cross-shore direction and with the underlying assumption that alongshore inhomogeneities can develop and decay in smaller time scales. To focus on the results of the 'self-organization hypothesis' due to the coupling between high-frequency waves and the topography in isolation, the possible effect of low-frequency waves is neglected. The first step in any stability analysis is finding a basic state of the dynamical system, which usually is a steady equilibrium solution. For this set of equations, the corresponding equilibrium profiles have already been presented in the previous chapter (section 3.3). The next step is describing the temporal evolution of

small perturbations superimposed to this equilibrium in the linear regime. The shape and dynamics of the 'normal modes' of the system are described by the linearised equations (see section 1.3.2 for a definition of the 'normal modes'). The results of a linear stability analysis are then the initial spatial cross-shore structure, growth rate and migration celerity of the different possible 'normal modes'. The third step of a stability analysis is relaxing the assumption of small amplitude by computing the non-linear temporal evolution of the system, which gives information about its longer-term finite-amplitude behaviour. The non-linear model used in the present chapter also allows to describe two other processes that have been recognised to be often linked to the generation of shore-parallel bars (but that are very difficult to be implemented in a linear stability analysis). Firstly, the existence of an input of sand from the beach is taken into account, linked to a possible evolution of the shoreline. Secondly, the behaviour of the system moderately far form equilibrium conditions can also be studied.

The simplified coupled model for wave transformation and topography changes used have already been introduced in section 3.2 of the previous chapter. The corresponding linearised set of equations used in the linear stability analysis are presented in section 4.2. This section also contains a detailed description of the numerical method and the solution procedure used for solving these linear equations. Section 4.3 presents the reasons why the equations may potentially be able to describe the generation of shore-parallel bars by 'self-organization' through a 'breakpoint-bar related mechanism'. Section 4.4 shows the results of the complete linear stability analysis. The equations and the solution procedure used in the non-linear model are described in section 4.5, whereas the results of this model are contained in section 4.6. Finally, some discussion is given in section 4.7 and the main conclusions of the chapter are summarized in section 4.8.

## 4.2   Formulation of the linear stability analysis

### 4.2.1   Linearised equations

In order to analyse the linear stability of the equilibrium profiles presented in the previous chapter the same non-linear dimensionless equations used there must be initially taken (Eqns. 3.2.9 and 3.2.10). The coordinate system used has been introduced in Fig. 3.2.1. We suppose again alongshore uniformity so that the variables only depend on the slowly-varying time and on the cross-shore position. The two variables used are the water depth, $D$, and the relative wave height, $Y = H_{rms}/D$. The studied domain is the nearshore zone located from the coastline, $x = x_{cl} = 0$, which is used as the origin of the coordinate system, to an offshore position, $x = x_{off}$, where the waves would not feel the bottom sufficiently to change their propagation (i.e. the position of the closure depth defined in section 1.1.1).

The first step for deriving the linearised equations is to add small perturbations to the equilibrium variables. These perturbations are supposed to have an exponential dependence on time of the form

$$(D(x,t), Y(x,t)) = (D_{eq}(x), Y_{eq}(x)) + (d(x), y(x))\, e^{\omega t} \quad , \qquad (4.2.1)$$

where $(D_{eq}, Y_{eq})$ are the equilibrium water depth and relative wave height of which the shape has been described in the previous chapter. The linear variables $(d(x), y(x))$ (which could be complex) are the cross-shore profiles of the perturbations in the water depth and in the relative wave height. The variable $d$ is defined in such a way that a positive value means a trough and a negative value refers to a crest. The complex frequency, $\omega = \omega_r + i\omega_i$, describes the feedback in this system. The perturbations will grow if $\omega_r > 0$ and decay if $\omega_r < 0$. In case of $\omega_i \neq 0$, the obtained results for the perturbations could have some kind of oscillatory motion or migration in the cross-shore direction. The assumption of exponential dependence on time is not restrictive because, as the coefficients of the resultant linear system do not depend on $t$, any solution can be expanded as a sum or an integral of this type of solutions.

Inserting Eq. (4.2.1) into Eqns. (3.2.9)) and (3.2.10) and keeping only the terms which depend linearly on the perturbations (so neglecting higher order terms) yields the following set of dimensionless linear equations

$$\epsilon\,\omega\,(D_{eq}\,y + Y_{eq}\,d) = D_{eq}^{1/2}\left(D_{eq}\,y' + \frac{5}{4}\,Y_{eq}\,d' + \frac{5}{4}\,D_{eq}'\,y\right) - \frac{5}{4}\,\frac{Y_{eq}}{D_{eq}^{1/2}}\,D_{eq}'\,d - \qquad (4.2.2)$$

$$- A\,Y_{eq}^3\,D_{eq}\left(4\left(1 - \Gamma(Y_{eq}y_c)^{-5/2}\right) - 5\frac{y_c^2}{\gamma_c^2}\,Y_{eq}^2\,\Gamma(Y_{eq}y_c)^{-7/2}\right)y +$$

$$+ A\,\frac{Y_{eq}^4}{2}\left(1 - \Gamma(Y_{eq}y_c)^{-5/2}\right)d \quad,$$

$$\omega\,d = \frac{d}{dx}\left[Y_{eq}^3 D_{eq}^{3/2}\left(s_0\,d' - Y_{eq}^{p-1}\,(p - Y_{eq}\,(p+1))\,y\right)\right] \quad, \qquad (4.2.3)$$

where $\Gamma(Y_{eq}\,y_c) = 1 + (Y_{eq}\,y_c/\gamma_c)^2$ and the comma $'$ indicates the total derivative with respect to $x$. The scaling used in the equations has already been presented in chapter 3 (see table 3.2.1). The final independent dimensionless model parameters are $y_c/\gamma_c$, $s_0$, $p$, $A$ and $\epsilon$. The explicit definition of these five parameters and the range of values used for them has been given in table 3.2.2 of the previous chapter. As has been explained in section 3.2.3, the first three parameters are the most important for describing the dynamics of this problem. For the sake of completeness, the present linear stability analysis has been done keeping the term proportional to $\epsilon$ in Eq. (4.2.2), in spite of the small value of this parameter (see table 3.2.2). Remember that the wave height far offshore, $H_{off}$, turns out to be only a scaling factor in this problem.

The final set of linear dimensionless equations consists of a second order parabolic equation for the bed evolution (Eq. 4.2.3) and a first order equation for the wave propagation (Eq. 4.2.2). Therefore, three conditions are required at the boundaries of the domain $x_{cl}$ and $x_{off}$, which are derived as follows. Far offshore, the perturbations are supposed to be zero, because we are interested in the solutions that describe the internal dynamics of the surf and shoaling zones, with no external forcing (apart from the steady high-frequency wave input). The imposed conditions are then $d(\infty) = 0$ and $y(\infty) = 0$. In principle they make the first order sediment transport and wave energy flux vanish at the offshore boundary. Since Eq. (4.2.3) is a second order differential equation we need a third boundary condition and setting it has not been straightforward. As a starting point, we are interested in perturbations of the water depth that are zero at the coastline. But Eq. (4.2.2) applied to the shoreline ($x = 0$) already tells us that $d(0) = 0$ because the equilibrium water depth is zero at the coastline and the equilibrium relative wave height is bounded. Thus, $d(0) = 0$ is

not an added boundary condition. The linearised sediment transport is also vanishing automatically at the coastline $q(0) = 0$, due to the stirring function used, $Y_{eq}^3 D_{eq}^{3/2}$. This latter quantity decays very fast near the coastline so no conditions for the perturbations can be inferred either. Another possible physical boundary condition could be related with the flux of wave energy. The wave energy, $E \propto H_{rms}^2$, should be bounded at the coast and consequently, the wave energy flux should obey the coastal boundary condition $\mathcal{F}_w = E\, c_g \propto y^2 D^{5/2} \to 0$ when $x \to 0$. Expanding this formula up to first order, we might find a suitable boundary condition for the linear variables. However, this is not the case since the expression,

$$\mathcal{F}_w \propto Y_{eq}^2 D_{eq}^{5/2} + 2 Y_{eq} D_{eq}^{5/2}\, y + \frac{5}{2} Y_{eq}^2 D_{eq}^{3/2}\, d \quad , \tag{4.2.4}$$

is found. Again, this quantity is already vanishing at the coastline without imposing any condition for the linear variables because $D_{eq}(0) = 0$. All this implies that $y(0)$ is unrestricted at first order, which is very unattractive for both analytical and numerical reasons. As the equilibrium relative wave height tends to be constant close to the shore, we suppose that its perturbation is zero there, so we use $y(0) = 0$ as the third boundary condition and we will check later on whether this condition is too restrictive. Detailed information about the behaviour of this dynamical system at the coastline can be found in Hulscher *et al.* (2001). An asymptotic expansion of the equilibrium solutions for $x \to 0$ was presented in that paper, together with a discussion about the equations and variables that should be used for decribing the dynamics of the perturbations.

Finally, a tool that is also used in this chapter is the *'Flow Over Topography problem'*, hereinafter referred to as *'FOT problem'*. It consists in solving only the hydrodynamical Eq. (4.2.2) for a given topographic perturbation $d$, which is artificially fixed. It simply means that the bed evolution Eq. (4.2.3) is switched off, so that the topography keeps constant in time.

## 4.2.2  Numerical method and solution procedure

The two linear equations obtained (Eqns. 4.2.2 and 4.2.3) constitute a boundary value problem that decribes the shape and dynamics of the perturbations $d$ and $y$. Performing a linear stability analysis of this type of problems in case of unbounded domains leads typically to sinusoidal 'normal modes' (Huthnance, 1982). In our case, the basic state is more complicated and the cross-shore domain is finite, $x \, \epsilon \, (0, x_{off})$, so that the corresponding 'normal modes' have a more complicated structure and they have to be approached numerically.

We have chosen to use a numerical spectral method that is based on expansions of the linear variables in Chebyschev polynomials. A description of numerical spectral methods can be found in Gottlieb & Orszag (1977) and Canuto *et al.* (1988). They are very useful to interpret physically the solutions of a linear stability analysis because the different modes are described separately. Moreover, they usually allow for a very good accuracy with a small number of freedom degrees (compared with the more standard finite difference methods, for instance). This type of spectral methods have been succesfully applied to several other coastal problems. More detailed explanations and some examples can be found in Falqués & Iranzo (1994), Falqués *et al.* (1996) and Calvete *et al.* (2001).

The following general steps must be taken when using a spectral method. Firstly, the linear variables of the problem are expanded in a certain basis of functions. The set of functions are chosen in order to optimize the accuracy of the numerical discretization of the problem. The derivatives of the linear variables are also written as a function of the chosen basis. The second step is introducing all these expansions in the original boundary value problem for the perturbations, so that it is transformed to an algebraic eigenproblem for the coefficients of the expansions. These coefficients become the new variables of the problem instead of the perturbations themselves. For solving the algebraic eigenproblem different methods can be applied. We have chosen to use a collocation method, which consists in imposing the equations at a set of collocation points that has previously proven to optimize the accuracy of the expansions used. The basis and the corresponding set of collocation points are usually defined in a certain domain that do not necessarily coincides with the domain of the problem. Thus, the third step of the solution procedure is to transform the set of collocation points and consequently the derivative operators to adapt them to the desired domain. The final set of equations define an algebraic discretized eigenproblem for the coefficients of the expansions that can be solved with a standard numerical method.

The present section describes step by step the application of this method to our set of equations, giving the details of the solution procedure that are needed for understanding some reasonings given in the rest of the chapter. The first step is expanding all the variables of the problem in $N-1$ polynomials of the chosen basis,

$$f(x) = \sum_{n=1}^{N-1} f_n \, g^n(x) \quad , \tag{4.2.5}$$

where $f(x)$ represents one of the linear variables ($d$ or $y$ in this problem), $g^n(x)$ are the functions of the basis chosen and $f_n$ are the corresponding coefficients of the polynomial expansion ($n = 1, ..., N-1$). In the present model, the basis used is related to the Chebyschev polynomials, which read

$$T^i(z) = cos\left(i \cos^{-1}(z)\right) \quad , \quad i = 0, 1, 2, ... \quad . \tag{4.2.6}$$

As can be seen, their natural domain is $z \,\epsilon\, (-1, 1)$. This set of polynomials has proven to provide a good accuracy when solving boundary value problems in bounded domains (Gottlieb & Orszag, 1977). In order to decrease the number of 'purely numeric solutions' inherent to any numerical method for eigenproblems, it is convenient to use a basis of functions that verify the boundary conditions of the problem (Falqués & Iranzo, 1994). In our case, both linear variables must verify two conditions, they have to vanish at the coastline, $f(0) = 0$, and at the offshore boundary, $f(x_{off}) = 0$ (see section 4.2.1). Therefore, the chosen basis consists of a linear combination of Chebyschev polynomials that vanishes at both boundaries,

$$g^n(z) = T^{n+1}(z) - \frac{(1 + (-1)^{n+1})}{2} \, T^0(z) - \tag{4.2.7}$$

$$- \frac{(1 + (-1)^{n+2})}{2} \, T^1(z) \quad , \quad n = 1, ..., N-1 \quad ,$$

instead of the Chebyschev polynomials themselves. The coordinate $z$ used in this expression is the natural coordinate where the Chebyschev polynomials are defined (see Eq. 4.2.6). For the moment the basis chosen verify the condition at the boundaries of the $z$ domain,

$g^n(-1) = g^n(1) = 0$. Later on, this formulation will have to be written as a function of the cross-shore coordinate that we are using in the present problem, $x \, \epsilon \, (0, x_{off})$. Then the basis will automatically vanish at the new boundaries. The number of boundary conditions imposed to each variable (2, 1 or 0) gives the number of polynomials that must be used in the corresponding expansion (which is equal to $N - 1$, $N$ or $N + 1$, respectively). For the details about the computation of the different basis that verify a particular set of boundary conditions, see Gottlieb & Orszag (1977).

The second step of the solution procedure is to introduce the expansions of the variables described by Eq. (4.2.5) into the linearised Eqns. (4.2.2) and (4.2.3). As follows from Eq. (4.2.5), the spatial derivatives of the linearised variables can also be written as an expansion of the derivatives of the basis, which in turn can be easily computed from Eqns. (4.2.6) and (4.2.7). The original boundary value problem for the perturbation, $f(x)$, then becomes an algebraic eigenvalue problem for the coefficients, $f_n$.

We have used a collocation method to solve the algebraic eigenvalue problem for the coefficients. It consists of imposing the equations to a set of $N-1$ Gauss-Lobatto collocation points, $z_j$ (with $j = 1, ..., N - 1$) . This set of points has proven to optimize the accuracy of the expansions in Chebyschev polynomials (for the corresponding demonstration, see Gottlieb & Orszag (1977)). The general definition of the Gauss-Lobatto collocation points is

$$z_j = \cos \left( \frac{\pi \, j}{N} \right) \quad , \qquad j = 0, ..., N \quad , \tag{4.2.8}$$

so that $z_j \, \epsilon \, (1, -1)$. However, the domain used in our problem ranges from the coastline $x = 0$ to a certain offshore position $x = x_{off}$. Therefore, a change of coordinates must be applied to the Gauss-Lobatto nodes before being introduced in the equations. The final collocation points, $x_j$, are defined through two mesh transformations,

$$z^* = \psi(z) = a \, z^3 + (1 - a) \, z \quad , \tag{4.2.9}$$

$$x = \phi(z^*) = l \, \frac{1 - z^*}{1 + b \, z^*} \quad . \tag{4.2.10}$$

The $\phi$ transformation applied to a set of points $z_j \, \epsilon \, (-1, 1)$, changes the domain to $(0, x_N)$, where $x_N = 2 \, l \, / \, (1 - b) = x_{off}$ is the new position of the last collocation point and must coincide with the desired offshore position (where the offshore boundary condition is applied). This $\phi$ transformation applied to $z_j$ concentrates a lot of final collocation nodes close to $x = 0$, the mesh density decreasing when $x$ increases up to $x_N$. Half of the nodes of the mesh are located between $(0, l)$ and the other half between $(l, x_N)$. In fact, a local increase in the density points is also found around $l$. The value of $l$ is then chosen so that the important variations in the coefficients of the linear equations occur between $(0, 2l)$. Given a particular value for $l$, the parameter $b \, \epsilon \, (0, 1)$ defines the offshore position $x_{off}$. A value of $b = 0.5$ gives $x_{off} = 4 \, l$, $b = 0.8$ gives $x_{off} = 10 \, l$ and the limiting value of $b = 1$ gives a semi-infinite domain, $x_{off} = \infty$. In order to avoid the large density of points at the coastline induced by the $\phi$ transformation, the mesh $z_j$ previously undergoes a stretching ($\psi$ transformation given in Eq. (4.2.9)). This $\psi$ transformation moves the original collocation points, $z_j$, to an intermediate mesh indicated by $z_j^*$, so that the density of nodes along the final domain $x$ is more uniform. The numerical parameter $a \, \epsilon \, (0, 1)$ controls the intensity of this stretching, being more efficient if $a$ is large.

The basis of functions and their spatial derivatives are also altered by these two mesh transformations. Firstly, the Chebyschev polynomials must be written in terms of the new mesh $x_j$ in the definition of the basis (Eq. 4.2.7). This is done through a transformation of the original collocation points, $z_j$, to the new collocations nodes, $x_j$, by using the inverse of the two transformations given in Eqns. (4.2.9) and (4.2.10),

$$z_j = \psi^{-1}\left(\phi^{-1}(x_j)\right) \quad . \tag{4.2.11}$$

Then the spatially discretized version of the derivatives of the basis can be written as

$$\frac{dg^n(x)}{dx} = \frac{dg^n(z)}{dz}\frac{1}{\psi'(z)\,\phi'(z^*)} \quad , \tag{4.2.12}$$

$$\frac{d^2g^n(x)}{dx^2} = \frac{1}{\psi'(z)\,\phi'(z^*)}\frac{d}{dz}\left(\frac{1}{\psi'(z)\,\phi'(z^*)}\frac{dg^n(z)}{dz}\right) \quad .$$

In this expression, $z^* = \psi(z)$, must be used when necessary and the derivatives of the transformations, $\phi'(z)$ and $\psi'(z^*)$, are computed as

$$\psi'(z) = \frac{d\psi(z)}{dz} \quad , \quad \phi'(z^*) = \frac{d\phi(z^*)}{dz^*} \quad . \tag{4.2.13}$$

The final expressions for the derivatives of $g^n(x)$ in Eq. (4.2.12) must be written as a function of the final collocation points, $x_j$, before being introduced in the equations. For this, the expression that gives the original collocation points, $z_j$, as a function of the final nodes (Eq. 4.2.11) must be used.

The two equations giving the algebraic eigenvalue problem for the coefficients are imposed at the final collocation points, $x_j$, defined by Eqns. (4.2.8), (4.2.9) and (4.2.10). The spatially discretized versions of the basis and its derivatives (Eq. 4.2.12) are also used. The final set of $2N - 2$ discretized equations define a generalized algebraic eigenproblem for the $2N - 2$ coefficients of the 2 expansions,

$$\sum_{m=1}^{2N-2} \mathcal{B}_k^m \, \mathcal{X}_m = \omega \sum_{m=1}^{2N-2} \mathcal{C}_k^m \, \mathcal{X}_m \quad , \qquad k = 1, ..., 2N - 2 \quad . \tag{4.2.14}$$

The scalar $\omega$ is the eigenvalue and the vector $\mathcal{X}_m = (d_n, y_n)$ is the eigenfunction, which contains the 2 sets of $N - 1$ coefficients of the expansion of the linear variables $d(x)$ and $y(x)$ in terms of the chosen basis, $g^n(x)$. The matrices $\mathcal{B}_k^m$ and $\mathcal{C}_k^m$ are formed by the values of the coefficients of the 2 linear equations at the $N - 1$ transformed collocation points. The eigenproblem given by Eq. (4.2.14) is solved numerically with a standard method.

The eigenvalue $\omega = \omega_r + i\,\omega_i$ gives the growth rate and the frequency of each eigensolution. If the basic state is unstable, the linear stability analysis show at least one solution for the perturbations having a positive growth rate, $\omega_r > 0$. The corresponding e-folding growth time is given by $\omega_r^{-1}$ (see Eq. 4.2.1). The cross-shore structure of the perturbations can be easily obtained from the coefficients of the expansion given by $\mathcal{X}_m$, through Eq. (4.2.5). The final total solution for the topography and the relative wave height corresponding to a

particular eigensolution are then given by

$$D(x,t) = D_{eq}(x) + \mathcal{A} \, \Re e \left\{ e^{\omega t} \sum_{n=1}^{N-1} d_n \, g^n(x) \right\} \quad , \tag{4.2.15}$$

$$Y(x,t) = Y_{eq}(x) + \mathcal{A} \, \Re e \left\{ e^{\omega t} \sum_{n=1}^{N-1} y_n \, g^n(x) \right\} \quad , \tag{4.2.16}$$

where $\mathcal{A}$ is an arbitrary amplitude that can not be determined by a linear staility analysis. Remember that the problem has been solved using dimensionless variables. In order to recover the dimensional values of the outputs of the model, the transformations given by Eq. (3.2.8) must be used. For instance, the dimensional e-folding growth time is found after multiplying $\omega_r^{-1}$ by the morphological time scale, $T_g = \omega_r^{-1} \, T_m$ (the different scaling constants have been shown in table 3.2.1).

The 'FOT problem' is solved with a very similar numerical method, also based on an expansion of the only variable involved, $y$, in Chebyschev polynomials and imposing the wave transformation equation at the Gauss-Lobatto collocation points. The main difference is that the final discretized problem for the $N-1$ coefficients of the expansion consists now of a set of $N-1$ algebraic linear equations,

$$\sum_{m=1}^{N-1} \mathcal{E}_k^m \, \mathcal{Y}_m = \mathcal{H}_k \quad , \qquad k = 1, ..., N-1 \quad . \tag{4.2.17}$$

The new matrices $\mathcal{E}_k^m$ and $\mathcal{H}_k^m$ contain the coefficients of the linear wave transformation equation computed for the imposed arbitrary water depth, $d$. Then, the vector $\mathcal{Y}_m = y_n$ just contains the coefficents of the Chebyschev expansion of the relative wave height. This system of algebraic linear equations can be solved with any standard numerical method.

### 4.2.3 General description of the sensitivity of the eigensolutions to the numerical parameters

The last section has described how we have approximated the original boundary value problem to a discretized algebraic eigenproblem (Eq. 4.2.14). Given a set of physical parameter values, solving numerically this eigenproblem leads to as many eigensolutions as discretization freedom degrees, $2N-2$. However, only a few of them are physical (which means that they are a good approximation to the solutions of the original boundary valueproblem) and the rest are *'purely numeric or spurious solutions'*. Selecting these *'physical solutions'* among all the eigensolutions can be a very difficult task. Basicly, two types of test must be done. Firstly, the 'physical solutions' must be independent of the numerical method used. This attribute is tested by means of analysing the dependence of the solution on the numerical parameters of the model. And second, but even more important, the 'physical solutions' must be a result of sensible physical processes. Verifying this latter property is done by means of a deep understanding of the mechanism behind the growth of each numerically convergent solution. A study of the sensitivity of the $2N-2$ obtained eigensolutions with respect to the numerical parameters is then the first step done in order to separate those that are purely numeric from those that are candidates to be physical. In the present section,

a general description of the influence of the numerical parameters on the eigensolutions is given. A detailed example of all the tests performed to two particular eigensolutions of the model in order to assess their physical validity is left for the following section.

Four parameters define the numerical method chosen for solving the linearised equations (see the previous section). These are the number of collocation points, $N$, the parameter controling the offshore boundary position, $b$, the parameter giving the location with half of the collocation points at each side, $l$, and the parameter controling the strength of the mesh stretching, $a$. In this problem the coefficients of the linearised equations mainly depend on the equilibrium profiles. Therefore, we also must check that the final physical eigensolutions are independent of the numerical parameters used for solving the equilibrium equations. These are the non-dimensional offshore water depth where we start the computation of the equilibrium solution, $D_{off}$, and the tolerance, $tol$, which is the small water depth that defines the equilibrium shoreline (remember that $D = 0$ is a singularity of the equilibrium equations, see section 3.2.4 for the details).

The most important numerical parameter in any spectral method is the number of collocation points, $N$, as the purely numeric eigensolutions are usually very sensitive to it. This parameter also sets the size of the final numerical matrices of the eigenproblem (see Eq. 4.2.14) and consequently the computational time needed for solving it. The parameters $a$ and $l$, describing the situation of the collocation points whithin the domain $(0, x_{off})$, are not as much influent. They allow for finding the spatial discretization that optimize the numerical description and lead to the smallest possible $N$. The optimal stretching in this problem is found using $a \simeq 0.5$ and the best position for $l$ in this problem is around the break-point $l \simeq X_{b1}$, where we need a fine discretization. The numerical parameters related to the computation of the equilibrium solution, $D_{off}$ and $tol$, turn out to be quite influent because they determine the specific values of the coefficients of the linear equations at the two boundaries. The values typically used for $N$, $D_{off}$ and $tol$ are given in the following section.

The parameter $b$ turns out to be surprisingly crucial in this problem. The limiting value of $b = 1$, which gives a semi-infinite domain $x \epsilon (0, \infty)$, has been the first default value used. In fact the original formula used for the $\phi$ transformation (Eq. 4.2.10) did not contain this parameter. Using a semi-infinite domain in the present linear stability analysis leads to the emergence of three growing 'normal modes', which at first sight seemed physically realistic and relatively independent of the numerical parameters. They are described in detail in appendix A. However, as it is also shown in that appendix, it was subsequently found that those modes were linked to a spurious perturbation of the wave energy flux far offshore. An expression for the non-dimensional energy flux at first order can be obtained from Eq. (4.2.4),

$$\mathcal{F}_w^{(1)} = 2Y_{eq} D_{eq}^{5/2} y + \frac{5}{2} Y_{eq}^2 D_{eq}^{3/2} d \quad . \tag{4.2.18}$$

The boundary conditions imposed to the linear variables far offshore ($d(\infty) = y(\infty) = 0$) should in principle forbid any energy input at first order. Unluckily enough, it turned out that the perturbation of the relative wave height (of these three growing solutions) did not converge to 0 fast enough in the offshore direction, so that the numerical zero reached at the last point inside the domain (very far offshore beause $b = 1$) was not small enough. This, coupled with the fact that $D_{eq}$ becomes extremely large far offshore (as explained in section 3.4), gave this numerically spurious input of wave energy at first order. The exact

boundary conditions imposed far offshore should forbid any perturbation of the wave energy flux, but they turn out to be not enough restrictive from a numerical point of view. All the details are described in appendix A. Since we are interested in the self-organized behaviour of the nearshore, any perturbation of the equilibrium variables must vanish far offshore. The reason is that in our model there is not reflection of wave energy at the shoreline, so that it makes no sense that a process occurring inside the nearshore induces an input of wave energy far offshore. Therefore, these three growing solutions do not match the physical motivation of our mathematical approach and have been rejected.

Imposing a (small enough) zero wave energy flux at the offshore boundary is therefore essential and it has been achieved in our numerical method by using a finite domain up to a certain $x_{off}$ (obtained with $b < 1$), instead of the semi-infinite one. The boundary condition applied there, $y(x_{off}) = 0$, becomes restrictive enough to avoid the spurious input of wave energy. This is proved at the end of appendix A. Besides, using a finite domain is more coherent with the fact that we are interested in describing the possible 'self-organization processes' inside the nearshore. A sensible value of $b \sim 0.8 - 0.9$ is finally used, giving $x_{off} \sim 10 - 20X_{b1}$. The final results are not sensitive to the specific value of $b$ (unless it reaches the critical value of $b = 1$). The model configuration leading to this spurious input of wave energy (so when $b = 1$) is called *'ill-posed problem'* from now on, while the *'well-posed problem'* refers to using a finite domain, $b < 1$.

### 4.2.4 Examples of convergence and physical tests performed to two particular eigensolutions

This section is focused on describing in detail the tests performed to two particular eigensolutions of the model in order to decide if they can be considered as 'physical solutions' of our problem. The same type of tests have been systematically performed to the $2N - 2$ eigensolutions of our discretized eigenproblem for each set of parameter values. A very illustrative example of the selection criteria used is given by the analysis performed to two of the unphysical growing eigensolutions found for $b = 1$ (described in appendix A). This allows to underline the main challenges that can be found when using our numerical method. Remember that in the subsequent sections $b < 1$, as stated in the last paragraph of the previous section.

The initial tests that must be performed to the $2N - 2$ eigensolutions are related with checking their independence with respect to the numerical parameters. This allows to eliminate the purely numeric eigensolutions of the discretized eigenproblem and keep those that approximate well the original boundary value problem. We have selected only two candidates between the three growing eigensolutions of appendix A, called mode 1 and mode 3. In general, the non-dimensional growth rate, $\omega_r$, is the most sensitive part of the eigensolutions (the eigenfunctions being more robust). It has been then chosen for testing its convergence with respect to the numerical parameters. The following set of graphs shows the tests of convergence that have been performed to the two growth rates ($\omega_{r1}$ for mode 1 and $\omega_{r3}$ for mode 3) with respect to the three most influent numerical parameters of this problem, $D_{off}$, $tol$ and $N$ (see the previous section). The cross-shore structure of the two chosen candidates for being physical modes can be seen in appendix A.
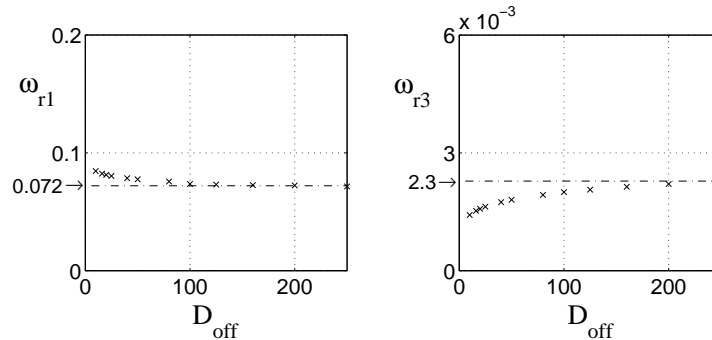
Figure 4.2.1: Test of convergence of the growth rates of two eigensolutions with respect to the value for the equilibrium water depth far offshore, $D_{off}$. The first graph shows the growth rate of mode 1, called $\omega_{r1}$, as we increase $D_{off}$. The second graph shows $\omega_{r3}$, the growth rate of mode 3. Computations have been done with the following set of physical parameter values: $y_c/\gamma_c = 1$, $s_0 = 0.23$, $p = 1$ and $A = 0.93$.

In Fig. 4.2.1 one may see the dependence of these two growth rates on $D_{off}$. The specific values for the growth rates have been obtained using a set of realistic physical parameter values (see section 3.2.3) slightly different from the ones used in appendix A. The first graph shows the growth rate of mode 1, called $\omega_{r1}$, and the second graph shows $\omega_{r3}$, the growth rate of mode 3. The point-dashed horizontal lines show the value of the growth rate that can be chosen as the convergent value. The growth rate of mode 1 converges quite well (for $D_{off} = 50$, which in dimensional terms means some $100m$, see table 3.2.1), whereas the convergence of $\omega_{r3}$ is more doubtful. This can be understood by regarding the cross-shore shape of the water depth of these solutions. Mode 1 decays much faster with increasing $x$ than mode 3 (see Figs. A.1 and A.2 of appendix A). Thus, the changes in the computation of the equilibrium state far offshore can alter more the value of $\omega_{r3}$. The final value chosen for the initial water depth to describe well both features is $D_{off} = 250$, which in dimensional terms means some $500m$. These values for $D_{off} \sim 100 - 500m$. are incredibly large taking into account that we are interested in describing the nearshore region. This behaviour responds to the fact that these solutions are critically depending on the spurious energy flux from far offshore found for $b = 1$ (see appendix A). It can also be interpreted as an initial indication that the solutions may not be physical, as their growth rate depends too much on a certain numerical parameter. The solutions presented in the rest of the chapter for $b < 1$ are much less sensitive to this numerical parameter.

Figure 4.2.2 shows the dependence of the growth rates on the tolerance, $tol$. The two graphs are equivalent to those defined in Fig. 4.2.1. Now, the growth rate of mode 3 is the least sensitive to this numerical parameter. The growth rate of mode 1 converges much more slowly and it requires very small values of the tolerance. This can be again interpreted by means of looking at the cross-shore shapes of the modes, mode 3 decaying much faster to 0 than mode 1 when they approach the coastline (see again Figs. A.1 and A.2 of appendix A). The final chosen value is $tol = 10^{-8}$, which in dimensional terms means some $10^{-5}mm$. The reason why the solutions depend so much on the computation of the equilibrium coastline
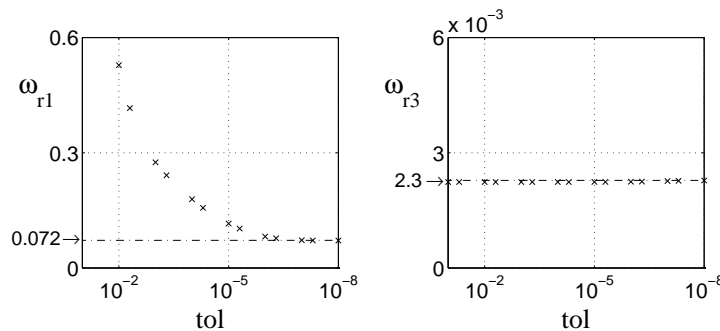
Figure 4.2.2: Test of convergence of the growth rates of two eigensolutions with respect to the tolerance, *tol*, which is the value for the equilibrium water depth where we define the coastline. The first graph shows the growth rate of mode 1, called $\omega_{r1}$, as we decrease *tol*. The second graph shows $\omega_{r3}$, the growth rate of mode 3. Notice that the horizontal axis shows exponentially decreasing values for *tol*. See the caption of Fig. 4.2.1 for more information.

is related with the fact that this dynamical problem depends strongly on the boundary condition setting.

Finally, Fig. 4.2.3 shows the dependence of the growth rates on the number of collocation points, $N$. The two graphs are equivalent to the ones defined in Fig. 4.2.1. The convergence of both growth rates is very slow and we need a large number of collocation points (compared, for instance, with the range of $N$ used in the problem tackled in chapter 5). Several reasons lead to this fact. Firstly, as it has already been proved in the previous graphs, the two studied solutions turn out to be very sensitive to computing accurately the equilibrium state until far offshore ($D_{off}$ must be very large). We then need to resolve well a domain that is very large in case of $b = 1$. Secondly, large gradients in the cross-shore distribution of the coefficients of the linear equations occur at a small region close to the break-point where we need therefore a very fine discretization. Thirdly, the shoreline is also a delicated area that must be described in detail (*tol* must be very small). The final consequence is that we need a fine mesh in all the domain that implies having a large amount of numerical freedom degrees (represented by $N$ in this numerical method) and a long computational time for solving the eigenproblem. The final value of $N$ chosen for the computations is $N = 250$. Larger values of this numerical parameter would probably do better, but we also must take into account the computational time and data space, which would increase very much. In general, the numerical relative errors accepted in the growth rates are smaller than 5%.

The convergence tests presented above seem to prove that the two candidates for being 'physical solutions' are, at least, relatively good 'mathematical solutions' of our original boundary value problem. However, an important teaching of the examples chosen to illustrate the convergence tests is that they are not a guarantee of the physical validity of a certain eigensolution. The final criterium for selecting the 'physical solutions' must be the sensibility of the physical processes behind their existence. Focusing in the case of the two examples analysed in the present section, appendix A finally proves that they turn out to
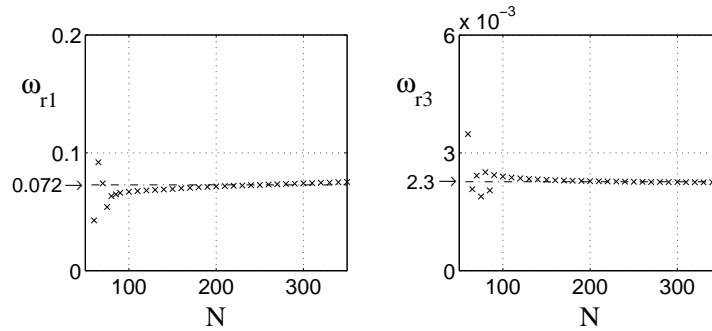
Figure 4.2.3: Test of convergence of the growth rates of two eigensolutions with respect to the number of collocation points, $N$. The first graph shows the growth rate of mode 1, called $\omega_{r1}$, as we increase the number of collocation points. The second graph shows $\omega_{r3}$, the growth rate of mode 3. See the caption of Fig. 4.2.1 for more information.

be unphysical, because their growth is linked to a spurious numerical input of wave energy from far offshore.

## 4.3   Analysis of the possible physical instability mechanism

### 4.3.1   The 'breakpoint-bar interaction' in the equations

We show in this section that the growth of break-point bars as an instability of the equilibrium profiles is plausible within the model assumptions. Moreover, as it has been underlined in the previous sections, a strong knowledge of the physics behind the growth of the solutions is necessary in order to asses their validity. This can follow from a close examination of the competition between the onshore transport due to wave non-linearities and the offshore transport due to undertow. The basic idea found in the literature for describing the 'breakpoint-bar mechanism' is that the onshore transport is dominant in the shoaling zone whereas the offshore transport is dominant in the surf zone, suggesting some sort of convergence at the break-point (Dally, 1987; Larson, 1988; Roelvink & Stive, 1989; Aagaard *et al.*, 1998; Komar, 1998; Short, 1999). However, the previous chapter of this thesis has proved that a sediment transport formula containing these two sources of transport together with a downslope contribution give equilibrium profiles that are non-barred. The two wave induced transports increase in magnitude as waves propagate towards the coast in such a way that the residual wave transport is always negative (onshore directed) and decreases monotonously with decreasing $x$. This residual transport is locally balanced by the downslope transport that is produced by a 'terraced (non-barred) shape' (with a wide range of 'relative slopes', see section 3.3). This is in agreement with the sediment transport measure-

ments in the Dutch coast made by Ruessink & Terwindt (2000). They show that the two sources of wave transport (onshore versus offshore) were of similar magnitude, so that they were locally in balance.

A possibility is that the formation of bars could be explained as an instability of such equilibrium balance due to a strong feedback between small perturbations in the topography and the corresponding induced changes in the wave height and consequently in the sediment transport. This is the hypothesis that is being developed in the present chapter. Understanding this possible feedback process requires two steps: 1) investigating what would be the effect of a small arbitrary bar (that was superimposed to the equilibrium profile) on the relative wave height and 2) understanding the accretion and/or erosion pattern produced by such small perturbations (in the relative wave height and in the water depth).

The first step should be answered by solving the 'FOT problem' above the arbitrary bar using the linear wave transformation equation (Eq. 4.2.2) and/or the corresponding non-linear expression (Eq. 3.2.9). This type of computations are not straightforward and will be presented in section 4.4.2. Here, we just seek for qualitative signs of the possibility of instabilities in the equations and this can be accomplished looking at the definition of the relative wave height, $Y = H_{rms}/D$. First, the direct effect of introducing a small bar is that the water depth is reduced, thus tending to increase the relative wave height. The effect on the wave height of a small bar depends on its position along the profile. In case the bar has the crest in the shoaling zone (in our equilibrium profiles, $x > X_{b1}$, see Fig. 3.3.1 of the previous chapter), wave shoaling would increase clearly leading to an increase in $Y$. In case of a bar situated inside the surf zone ($x < X_{b2}$ in Fig. 3.3.1), wave breaking would increase over it, so $H_{rms}$ would decrease and the final tendency of $Y$ is unpredictable beforehand. In the breaker region, ($X_{b2} < x < X_{b1}$ in Fig. 3.3.1), the final sign for the perturbation of $Y$ produced by a bar is also uncertain. However it is expected that the breaking effect is not clearly dominant over the shoaling effect in this region (because most of the waves have not broken yet), leading to a positive perturbation of $Y$.

The second step can be taken qualitatively by means of the sediment transport formula. From Eq. (3.2.10), the non-linear dimensionless sediment transport can be written as

$$Q(x,t) = S(x,t)\left(s_0\frac{\partial D(x,t)}{\partial x} - Y^p(x,t) + Y^{p+1}(x,t)\right) \quad, \qquad (4.3.1)$$

where $S(x,t)$ is the wave stirring. Undertow transport is proportional to a power $p+1$ of the relative wave height, whereas transport due to wave non-linearities has an exponent $p$. The derivative of such expression gives information of the variations that would be produced on the transport due to the changes in $Y$ induced by the arbitrary bar. This is precisely the essence of the linearised equations presented in the previous section. From the linear expression for the bed evolution equation (Eq. (4.2.3)) we can write

$$q(x) = S_{eq}(x)\left(s_0\,d'(x) - Y_{eq}(x)^{p-1}\,(p - Y_{eq}(x)\,(p+1))\,y(x)\right) \quad, \qquad (4.3.2)$$

where the subscript $'eq'$ defines again the equilibrium values, the comma $'$ can indicate the total spatial derivative and the quantities written in lower case are the perturbations. The expression multiplying the perturbation on the relative wave height, $y$, in Eq. (4.3.2) is exactly the derivative of the equilibrium wave induced transport (second and third terms of Eq. (4.3.1) at zero order). This derivative becomes zero when $Y_{eq} = p/(p+1)$ ($Y_{eq} = 0.5$ if
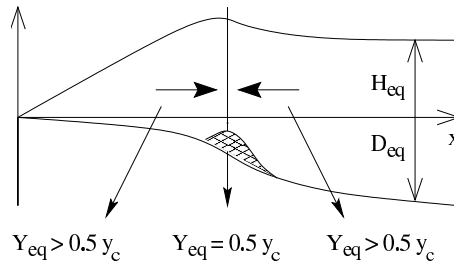
Figure 4.3.1: Scheme of the 'breakpoint-bar mechanism'. A small arbitrary bar is superimposed
to the equilibrium profile at the 'effective break-point' ($x = X_{b1}$, defined as the place where
the dimensional equilibrium relative wave height is equal to $Y_{eq} = p/(p+1)$ ($Y_{eq} = 0.5\,y_c$
in dimensional terms and using $p = 1$). If this bar induced a positive perturbation in the
relative wave height, this would in turn produce offshore transport at its most shoreward side
($Y_{eq} > 0.5\,y_c$) and onshore transport at its most seaward part ($Y_{eq} < 0.5\,y_c$). We then would
obtain convergence of sediment over bars extending at both sides of the point where $Y_{eq} = 0.5\,y_c$.

$p = 1$). Thus, this settles then the unique location where the undertow offshore transport
and the wave onshore transport react with the same strength to changes in $y$.

If we knew the sign of the perturbation of the relative wave height caused by the small
arbitrary bar, the final effect on the transport pattern could be qualitatively described
using the linearised sediment transport formula (Eq. 4.3.2). Figure 4.3.1 shows a simplified
diagram that illustrates the following explanation. Imagine first that $y > 0$, which is the
case for the solutions described in appendix A. A result of our equilibrium profiles is that the
relative wave height is larger than the critical value $Y_{eq} > p/(p+1)$ in the region shoreward
of the 'effective break-point', $x < X_{b1}$ (see Fig. 3.3.1, for instance). There, Eq. (4.3.2) states
that a positive perturbation of the relative wave height, $y > 0$, produces an increase in
undertow offshore transport larger than the increase in wave onshore transport (because
$p - Y_{eq}(x)\,(p+1) < 0$). Thus, a net offshore transport is obtained, without considering
the slope effect by the moment. The contrary applies seaward of the break-point ($x > X_{b1}$
in our equilibrium profiles, where $Y_{eq} < p/(p+1)$). There, the transport induced by wave
non-linearities reacts stronger than undertow transport to the increase in $Y$. Then, if a bar
was located at the 'effective break-point', $x = X_{b1}$ and it produced a positive $y$ along all the
domain, the perturbations would induce offshore transport at the bar most landward part
and onshore transport at its most seaward part. This would lead to a strong convergence
of sediment at its crest and the bar would grow. This is exactly the physical mechanism
behind the growth of the solutions of the 'ill-posed problem' presented in appendix A.

Three conclusions follow from the analysis presented in this section. First, the property
of our sediment transport formula that can lead to the growth of instabilities is the different
dependences in $Y$ of the two types of wave induced transport. Secondly, the location of
strongest sand convergence in our sediment transport formula is the 'effective break-point',
$X_{b1}$. Finally, a necessary condition for finding instabilities seems to be a positive perturba-
tion of the relative wave height along the bars width ($y > 0$). However as discussed at the

begining of this section, this could not happen so that the growing mechanism described above may not be applicable. For instance, solving the 'well-posed wave transformation equation' above the topographic perturbation of the first mode obtained from the 'ill-posed problem' gives a sign for $y$ that becomes negative as waves propagate to the shoreward side of the bar (this is shown in appendix A). We have focused these qualitative explanations on the transport driven by waves, because the linearised downslope gravity contribution in Eq. (4.3.2) is only playing a diffusive role, damping the growth of the instabilities (this is proved later on in this chapter).

## 4.3.2 'Energy identity' equation

The considerations given in the section above show the plausibility that the model equations could exhibit an instability leading to the generation of shore-parallel bars in a very qualitative way. In order to gain more quantitative insight into this possibility, the *'Energy identity method'* can be used. It consists of finding an analytical identity for the time derivative of the *'energy of the topographic perturbations'*. This latter expression defines a type of global magnitude of the perturbation. An application of this method to nearshore hydrodynamics along with a more detailed explanation and references can be found in Falqués *et al.* (1999). In the best cases, this method may lead to prove analytically the existence of (in)stability of the system. But in most of the problems, the 'Energy identity' just allows for setting up some necessary conditions for the occurrence of instabilities.

The first step consists in finding an expression for the linear 'FOT equation' simpler than the one given by Eq. (4.2.2). Neglecting $\epsilon$ because of their small magnitude (see section 3.2.3) and multiplying Eq. (4.2.2) by $2Y_{eq}D_{eq}$ one gets

$$\frac{\partial(W_1\,d)}{\partial x} + \frac{\partial(W_2\,y)}{\partial x} = W_3\,d + W_4\,y \quad . \tag{4.3.3}$$

The coefficents $W_1$ and $W_2$ describe wave shoaling and are equal to

$$W_1 = \frac{5}{2}\,Y_{eq}^2 D_{eq}^{3/2} \quad , \quad W_2 = 2\,Y_{eq}D_{eq}^{5/2} \quad . \tag{4.3.4}$$

The coefficents $W_3$ and $W_4$ describe wave breaking and are equal to

$$W_3 = 4\,A\,Y_{eq}^5 D_{eq}\left(1 - \Gamma(Y_{eq}y_c)^{-5/2}\right) \quad , \tag{4.3.5}$$

$$W_4 = 10\,A\,Y_{eq}^4 D_{eq}^2\left[\left(1 - \Gamma(Y_{eq}y_c)^{-5/2}\right) + Y_{eq}^2\frac{y_c^2}{\gamma_c^2}\Gamma(Y_{eq}y_c)^{-7/2}\right] \quad ,$$

where again $\Gamma(Y_{eq}\,y_c) = 1 + (Y_{eq}\,y_c/\gamma_c)^2$ and the independent parameters have been described in detail in section 3.2.3.

Further simplifications of Eq. (4.3.3) requires the use of the integrating factor technique. Given three arbitrary functions, $f$, $g$ and $h$, which are continuous and have continuous derivatives in a certain domain $(x, x_0)$, the following mathematical identity is verified,

$$f(x)\,g(x) + h(x)\,g'(x) = \tag{4.3.6}$$
$$h(x)\,exp\left[-\int_x^{x_0}\frac{f(z)}{h(z)}\,dz\right]\frac{d}{dx}\left(g(x)exp\left[\int_x^{x_0}\frac{f(z)}{h(z)}\,dz\right]\right) \quad ,$$

where the comma $'$ can identify the total derivative with respect to $x$ of a certain function in the rest of this section. By the use of this identity, the variable $y$ in the wave transformation equation (Eq. 4.3.3) can be formally integrated in the domain $(x, x_0)$ and reads

$$y(x) = -\frac{N(x)}{W_2(x)} \int_x^{x_0} \frac{M(z)}{N(z)} \frac{d}{dz} \left( \frac{d(z) W_1(z)}{M(z)} \right) dz \quad , \tag{4.3.7}$$

where the coefficents $N(x)$ and $M(x)$ indicate the integral expressions,

$$N(x) = exp \left[ \int_x^{x_0} \frac{W_3(z)}{W_1(z)} dz \right] \quad , \quad M(x) = exp \left[ \int_x^{x_0} \frac{W_4(z)}{W_2(z)} dz \right] \quad . \tag{4.3.8}$$

The equality given by Eq. (4.3.7) gives the perturbation of the relative wave height, $y(x)$, caused by a given bathimetric perturbation $d(z)$ ($x \leqslant z \leqslant x_0$). This is important from a conceptual point of view since it shows that the computation of $y(x)$ at a certain point is not local, i.e. it depends on the value of $d$ at the domain $(x, \infty)$.

The linearised bed evolution equation (Eq. 4.2.3), written in a shorter way, reads

$$\frac{\partial d}{\partial t} = \frac{\partial}{\partial x} \left( S_{eq} s_0 \frac{\partial d}{\partial x} \right) - \frac{\partial}{\partial x} \left( S_{eq} F y \right) \quad , \tag{4.3.9}$$

where the wave stirring coefficient $S_{eq}(x)$ and the wave transport coefficient $F(x)$ indicate

$$S_{eq} = Y_{eq}^3 D_{eq}^{3/2} \quad , \quad F = Y_{eq}^{p-1} \left( p - Y_{eq} (p+1) \right) \quad . \tag{4.3.10}$$

Throughout this section, the linearised variable $d(x, t)$ is supposed to include the exponential time dependence, $e^{\omega t}$, because this allows for a clearer notation to derive the 'Energy identity'.

Replacing the formal expression for $y(x)$ given by Eq. (4.3.7) into Eq. (4.3.9), leads to a single integro-differential equation for the bed evolution without the flow variables,

$$\frac{\partial d(x, t)}{\partial t} = G_1 d + G_2 \frac{\partial d(x, t)}{\partial x} + G_3 \frac{\partial^2 d(x, t)}{\partial x^2} + Q \int_x^{x_0} R(z) d(z, t) dz \quad . \tag{4.3.11}$$

Five new coefficients have been defined,

$$G_1 = \frac{S_{eq} F W_1 N}{W_2 M} \left( \frac{M}{N} \right)' - \left( \frac{S_{eq} F W_1}{W_2} \right)' \quad ,$$

$$G_2 = s_0 S_{eq}' - \frac{S_{eq} F W_1}{W_2} \quad , \quad G_3 = s_0 S_{eq} \tag{4.3.12}$$

$$Q = \left( \frac{S_{eq} F N}{W_2} \right)' \quad , \quad R = \frac{W_1}{M} \left( \frac{M}{N} \right)' \quad .$$

In order to study the (in)stability properties of this new bed evolution equation, the 'Energy identity' must be derived. This is done by means of multiplying Eq. (4.3.11) by $d$ and integrating over a certain domain $(x_L, x_0)$,

$$\frac{1}{2} \frac{d}{dt} \int_{x_L}^{x_0} d^2(x, t) dx = \int_{x_L}^{x_0} I_1(x) d^2(x, t) dx - \tag{4.3.13}$$

$$- \int_{x_L}^{x_0} I_2(x) \left( \frac{\partial d(x, t)}{\partial x} \right)^2 dx + \int_{x_L}^{x_0} \left( Q(x) d(x, t) \int_x^{x_0} R(z) d(z, t) dz \right) \quad .$$

Two new coefficients have been defined,

$$I_1 = G_1 - \frac{G_2'}{2} - \frac{G_3''}{2} \quad ,$$
$$I_2 = G_3 \quad . \tag{4.3.14}$$

Three integral identities have been used for arriving to Eq. (4.3.13). Given arbitrary functions $f(x,t)$ and $g(x,t)$, which are continuous in a certain domain $(x_L, x_0)$ and both vanishing at the two boundaries $f(x_L, t) = f(x_0, t) = g(x_L, t) = g(x_0, t) = 0$, it can be proved that

$$\int_{x_L}^{x_0} f \, \frac{\partial f}{\partial t} \, dx = \frac{1}{2} \frac{\partial}{\partial t} \int_{x_L}^{x_0} f^2 \, dx \quad ,$$
$$\int_{x_L}^{x_0} g \, f \, \frac{\partial f}{\partial x} \, dx = -\frac{1}{2} \int_{x_L}^{x_0} \frac{\partial g}{\partial x} f^2 \, dx \quad , \tag{4.3.15}$$
$$\int_{x_L}^{x_0} g \, f \, \frac{\partial^2 f}{\partial x^2} \, dx = \frac{1}{2} \int_{x_L}^{x_0} \frac{\partial^2 g}{\partial x^2} f^2 \, dx - \int_{x_L}^{x_0} g \left( \frac{\partial f}{\partial x} \right)^2 \, dx \quad .$$

The 'Energy identity' (Eq. 4.3.13) describes the dynamics of the integral of the square of the toporgaphic perturbation, $\frac{1}{2} \int_{x_0}^{x_L} d^2(x,t) \, dx = \frac{1}{2}||d||^2$, quantity that can be called 'energy of the topographic perturbation'. It is a measure of the magnitude of the perturbation because $||d||$ is large if $|d(x,t)|$ is large on average and $||d|| = 0$ means $d(x,t) = 0$ $(\forall x, t)$. Thus, the time derivative on the left hand side of Eq. (4.3.13) is positive in case of instability and negative in case of stability. The first integral on the right hand side contains the coefficient $I_1$ (defined in Eq. 4.3.14) times the square of the perturbation $d$. Thus the sign of this integral does not depend on the perturbation shape because $d^2$ is always positive. In case of dealing with a positive $I_1$ along all the domain, this term would be an instability source. The second integral is a clear damping term because both the coefficient inside $(I_2 = G_3)$, and the square of the perturbation derivative, $(\partial d/\partial x)^2$, are always positive (see Eqns. 4.3.10 and 4.3.12). Thus, as the integral has a minus sign in front, this term is always negative leading to a decay of the possible instabilities. Finally, the most complicated term is the third one because it is not written as a square of a function of the perturbation so that its sign depends on the perturbation shape.

Two different statements follows from the 'Energy identity' (Eq. 4.3.10). A *sufficient condition for stability* would be fulfilled if $I_1 < -C < 0$ along all the domain, where $C$ is an upper bound of the third term in the right hand side of Eq. (4.3.10) (in case this third term is unstabilising). On the other hand, a *necessary condition for linear instability* would be fulfilled if $I_1 > 0$ along all the domain and large enough to overcome the damping due to $I_2$ and the possible damping that could come from the third term. The final step of the analysis presented in this section is then computing the coefficients $I_1(x)$, $I_2(x)$, $Q(x)$ and $R(x)$ corresponding to our set of linear equations, in order to see if they fulfill one of the two conditions. These coefficients depend on a complicated combination of derivatives and integrals of the coefficients of the linear equations so that they must be computed numerically. The numerical computation of the integrals has been done by means of a standard Simpson's method and the derivatives have been evaluated using a standard Euler expression.

These four coefficients have been evaluated for different parameter settings corresponding to distinct equilibrium profiles. A general result is that $I_1 = 0$ in the shoaling zone, $I_1 > 0$
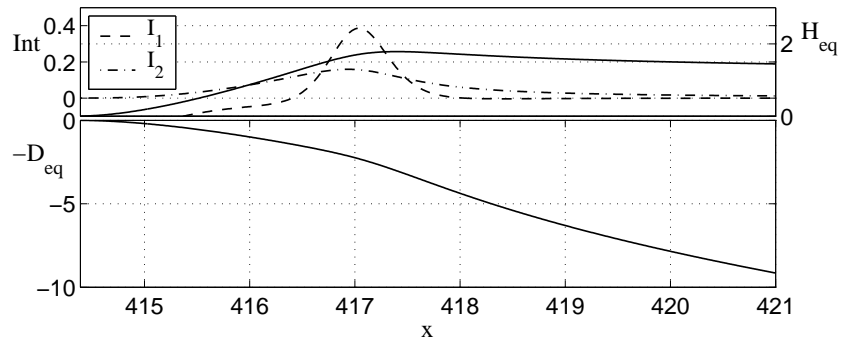
Figure 4.3.2: Example of cross-shore structure of the terms $I_1$ and $I_2$ of the 'Energy identity' (Eq. 4.3.13) in case of an equilibrium profile with the shape of a relatively 'planar beach'. The values used for the model parameters are $y_c/\gamma_c = 1.6$, $s_0 = 0.11$, $p = 1$ and $A = 1.92$. The horizontal axis corresponds to the cross-shore position, $x$. All the variables are non-dimensional (see the text for more explanations). Top: The solid line is the equilibrium wave height, $H_{eq}$, the dashed line is the instability term $I_1$ and the dot-dashed line is the damping term, $I_2$. Bottom: The solid line corresponds to the equilibrium topography (equal to minus water depth, $-D_{eq}$).
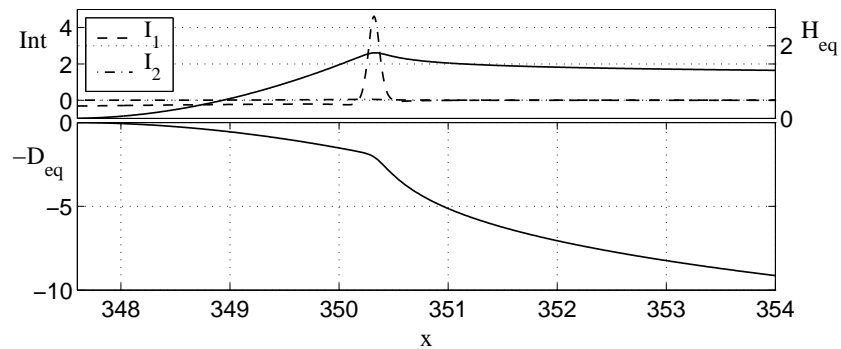


Figure 4.3.3: Example of cross-shore structure of the terms $I_1$ and $I_2$ of the 'Energy identity' (Eq. 4.3.13) in case of an equilibrium profile with the shape of a strongly 'terraced beach'. The values used for the model parameters are $y_c/\gamma_c = 1.4$, $s_0 = 0.023$, $p = 2$ and $A = 1.38$. See the caption of Fig. 4.3.2 and the text for more explanations. Top: The solid line is the equilibrium wave height, $H_{eq}$, the dashed line is the instability term, $I_1$, and the dot-dashed line is the damping term, $I_2$. Bottom: The solid line corresponds to the equilibrium topography (equal to minus water depth, $-D_{eq}$).

in the breaker region and $I_1 < 0$ along the surf zone. It is also verified that $I_2 = G_3 > 0$ along all the domain. Finally, it has been impossible in all the cases to find numerically neither an upper bound for the magnitude of the third term in the 'Energy identity', nor its sign. This is because it is the result of different integrals containing $d(x, t)$, which is unknown. Therefore, strictly speaking none of the two conditions derived can be exactly fulfilled. As an example of the cross-shore structures of the coefficients $I_1$ and $I_2$, Figs. 4.3.2 and 4.3.3 show the result for two different parameter settings (remember that the most important independent parameters of the system are $y_c/\gamma_c$, $s_0$ and $p$, see section 3.2.3). The emergence of an instability is doubtful in case of the relatively a 'planar beach' (see Fig. 4.3.2) because the instability term, $I_1$, becomes significatively negative inside the surf zone. Moreover, the damping term, $I_2$, is of nearly equal magnitude than $I_1$ as along all the domain On the other hand, the strongly 'terraced beach' shown in Fig. 4.3.3 seems more capable of exhibiting an instability as the coefficient $I_1$ turns out to be positive in nearly all the domain and it is one order of magnitude larger than the damping term, $I_2$.

The main conclusion of this section is then that the occurrence of instability seems plausible in case of 'terraced beaches'. However, even in this case some remarks must be done. Firstly, $I_1 \lesssim 0$ inside the surf zone ($x < X_{b2}$) so that the instability term would only operate for perturbations with a negligible value there. Secondly, the qualitative comparison we have done between the two first terms on the right hand side of Eq. (4.3.13) by means of comparing $I_1$ and $I_2$ must be taken with care because we do not have any information about the relationship between $d^2$ and $(\partial d/\partial x)^2$ (as their cross-shore structures are unknown). Thirdly, the third term in Eq. (4.3.13) is also unknown and it could contribute either to the instability or to the damping. Finally, remember also that in the derivation of Eq. (4.3.13), we have assumed that the water depth perturbation and the $I$ coefficients vanish at the boundaries $x_0$ and $x_L$. This condition that is not strictly verified for the $I_1$, for instance.

## 4.4 Results of the linear stability analysis

### 4.4.1 General description

A linear stability analysis has been performed for all the physically realistic range of parameter values (see section 3.2.3). All the corresponding equilibrium solutions (shown in Fig. 3.3.3) turn out to be linearly stable when using a finite domain (found with $b < 1$ in in the mesh transformation $\phi$, Eq. (4.2.10)). In contrast with the results for the 'ill-posed problem' ('unphysical solutions' presented in appendix A in case of $b = 1$), the largest growth rates of the eigensolutions of the 'well-posed problem' are always located around 0. This type of solutions are usually called *'marginally stable solutions'*. Therefore, no clear instability seems to arise from the 'well-posed problem', in spite of the expectations generated by the analysis presented in the previous sections. The convergence with respect to the numerical parameters of these growth rates around zero is again difficult to be assessed. Similar graphs than the ones shown in section 4.2.3 are obtained. Numerical methods often show this type of critical numerical convergence in case of 'marginal stability conditions'. The eigensolutions with the largest growth rates always display purely real eigenvalues and eigenfunctions, so that the corresponding patterns do not migrate at the linear regime.
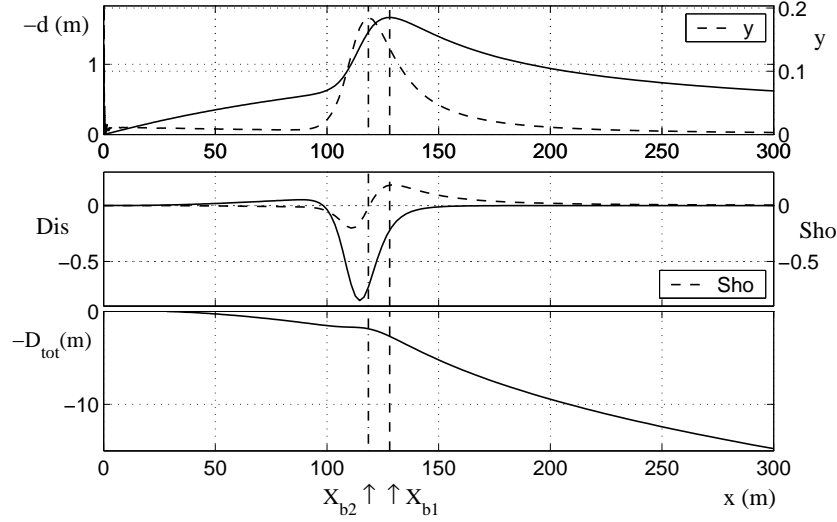
Figure 4.4.1: Example of linear mode with the largest growth rate (although $\omega_r \lesssim 0$) computed using $y_c/\gamma_c = 1.2$, $s_0 = 0.11$, $p = 1$ and $A = 0.94$. The initial equilibrium profile is a relatively 'planar beach'. The horizontal axis corresponds to the cross-shore position, $x$. All quantities shown are dimensional computed with an $H_{off} = 0.5m$. The vertical dashed line is the 'effective break-point', $X_{b1}$, and the vertical point-dashed line is another characteristic point of the equilibrium profiles, $X_{b2}$. The amplitude of the perturbations is arbitrary as it can not be determined by a linear stability analysis. See the text for more explanations. Top: The solid line is the perturbation in water depth, $-d$, and the dashed line is the perturbation in the relative wave height, $y$. Middle: The solid line shows the cross-shore structure of the linear dissipation term induced by the perturbations (corresponding to the two last terms in the right hand side of Eq. (4.2.2)). $Dis < 0$ means a decrease in wave energy with respect to the equilibrium situation, due to more breaking. The dashed line corresponds to the linear shoaling term (two first terms in the right hand side of the same equation). $Sho > 0$ means an increase in wave energy due to more shoaling. Bottom: The solid line is the resultant topography, equal to minus the total water depth, $-D_{tot} = -D_{eq} - d$.

Figure 4.4.1 shows an example of the type of cross-shore structure of the modes with $\omega_r \simeq 0$. The shape of all the 'marginally stable modes' obtained is qualitatively similar to this for all the range of physical parameters. It is characterized by a positive perturbation of the water depth along all the domain, $d(x) > 0$ , $\forall x$ (see the solid line in the top graph). A bar is located at the break-point ($x = X_{b1}$), the steepness of its sides depending on the parameter values. This $d > 0$ is coupled with a positive perturbation of the relative wave height along all the domain ($y > 0$). This specific example has been found for $y_c/\gamma_c = 1.2$, $s_0 = 0.011$, $p = 1$ and $A = 0.94$, a parameter setting similar to the one used in the example shown in appendix A. Its growth rate is negative but very close to zero, $\omega_r \simeq -10^{-9}$. All the quantities shown in this section are dimensional, computed using $H_{off} = 0.5m$. Notice that in any linear stability analysis, both the amplitude and the sign of the growing perturbations are arbitrary ($\mathcal{A}$ in Eqns. (4.2.15) and (4.2.16)). Here, we have chosen the
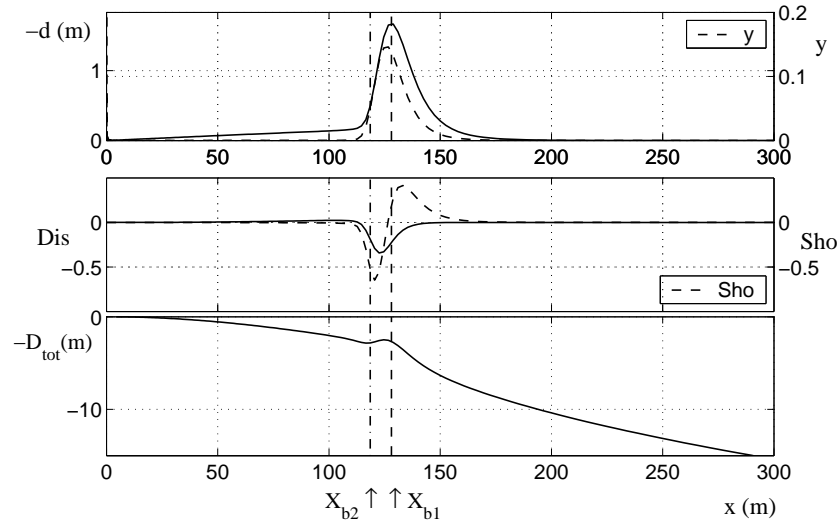
Figure 4.4.2: Example of the 'fastest growing mode' obtained with an atenuation of 0.1 in the 'morphodynamical diffusivity terms' of the linear equations (again $\omega_r \lesssim 0$). It has been found using $y_c/\gamma_c = 1.2$, $s_0 = 0.11$, $p = 1$ and $A = 0.94$. See the caption of Fig. 4.4.1 for more explanations. Top: The solid line is the perturbation in water depth, $-d$, and the dashed line is the perturbation in the relative wave height, $y$. Middle: The solid line gives the cross-shore structure of the linear dissipation term and the dashed line corresponds to the linear shoaling term. Bottom: The solid line is the resultant topography, equal to minus the total water depth, $-D_{tot} = -D_{eq} - d$.

sign so as to show that this instability mechanism is capable of generating break-point bars. The same solution can describe the formation of a trough just by switching from one sign to the other. A sensible dimensional value for the amplitude has also been introduced in order to produce a realistic aspect of the final topography that would result from the addition of the equilibrium plus the perturbation in the graphs. Predicting the final amplitude of the solutions (with its sign) needs a non-linear analysis.

The most intriguing characteristic of these solutions is their dependence on the downslope 'morphodynamical diffusivity', $s_0$. Increasing this parameter has shown a strong damping effect in the equilibrium profiles, decreasing the slopes and the gradients in the solutions (see section 3.3.2). It is expected that $s_0$ also plays a damping role in the present linear equations, as it is found in most linear stability analysis in the literature (an example can is the analysis presented in chapter 5). For checking the sensitivity of the linear stability results to the downslope 'morphodynamical diffusivity', the value of $s_0$ must be changed only in the linear bed evolution equation, maintaining the equilibrium solutions found for the default value ($s_0 = 0.11$ in our example). The reason is that we want to test the effect of this parameter in the linearised equation in isolation. Even small changes in $s_0$ induce strong variations in the equilibrium profiles and this alters a lot all the coefficients of the linear equations. Thus, the effect of changing the diffusive terms of the linear equations in
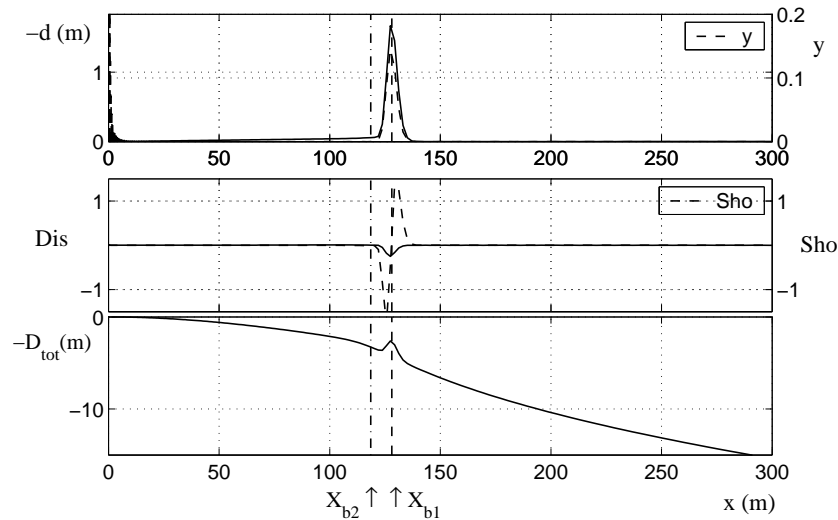
Figure 4.4.3: Example of the 'fastest growing mode' obtained with an atenuation of 0.01 in the 'morphodynamical diffusivity terms' of the linear equations (again $\omega_r \lesssim 0$). It has been found using $y_c/\gamma_c = 1.2$, $s_0 = 0.11$, $p = 1$ and $A = 0.94$. See the caption of Fig. 4.4.1 for more explanations. Top: The solid line is the perturbation in water depth, $-d$, and the dashed line is the perturbation in the relative wave height, $y$. Middle: The solid line gives the cross-shore structure of the linear dissipation term and the dashed line corresponds to the linear shoaling term. Bottom: The solid line is the resultant topography, equal to minus the total water depth, $-D_{tot} = -D_{eq} - d$.

the results would not be distinguishable. Isolating this effect is done by means of introducing an atenuation parameter, called *ate*, in front of the 'morphodynamical diffusivity terms' in the linear equations (i.e. its final expression is given by *ate* $s_0$). The surprising result is that decreasing diffusivity does not influence the magnitude of the resultant growth rates, whereas a strengthening of the potential instabilities would be expected. The obtained topographies display a more orthodox dependence on $s_0$. The results for *ate* = 0.1 and *ate* = 0.01 can be seen Figs. 4.4.2 and 4.4.3, respectively. As can be expected, decreasing $s_0$ leads to more sharp bars, which are located in a smaller region around $x = X_{b1}$ and display steeper sides.

An exhaustive exploration of the solutions has been done covering all the range of parameter values, but no clearly growing modes have been found. Analysing in detail the dependence of the magnitude of the (nearly zero) growth rates on the parameter values, it seems that the growth rates are larger when $y_c$ and $s_0$ decrease (so for initially more 'terraced beaches'). This is somehow in accordance with the prediction of the 'Energy identity' presented in the previous section. However, for $p = 1$ the growth rates are always negative. Increasing $p$ leads to some positive growth rates, although they go on being rather small and their numerical convergence is difficult to be assessed. Figure 4.4.4 shows an example with $\omega_r \gtrsim 0$ obtained for $y_c/\gamma_c = 1.4$, $s_0 = 0.023$, $p = 2$ and $A = 1.38$. This is the parameter setting used in the second example shown for the 'Energy identity analysis' in the previous
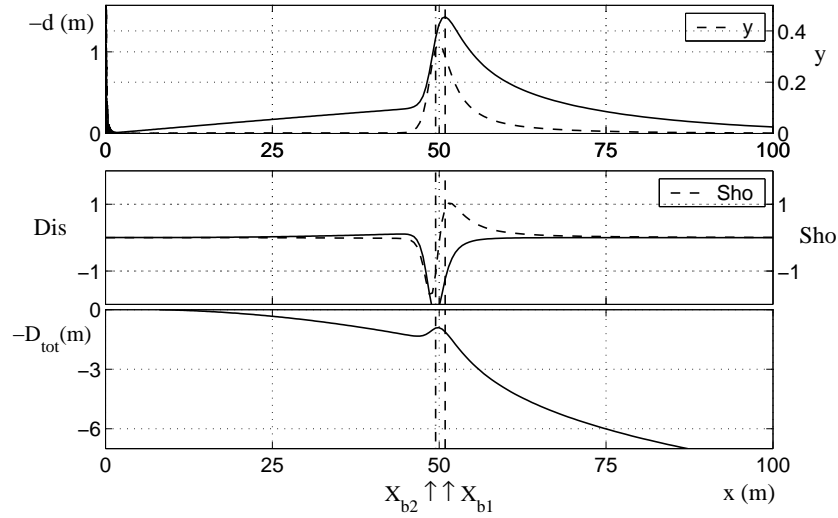
Figure 4.4.4: Example of linear mode with the largest growth rate ($\omega_r \gtrsim 0$) obtained with $y_c/\gamma_c = 1.4$, $s_0 = 0.023$, $p = 2$ and $A = 1.38$. The corresponding equilibrium profile is then a strongly 'terraced beach'. See the caption of Fig. 4.4.1 for more explanations. Top: The solid line is the perturbation in water depth, $-d$, and the dashed line is the perturbation in the relative wave height, $y$. Middle: The solid line gives the cross-shore structure of the linear dissipation term and the dashed line corresponds to the linear shoaling term. Bottom: The solid line is the resultant topography, equal to minus the total water depth, $-D_{tot} = -D_{eq} - d$.

section, for which the necessary condition for finding instability has seemed to be verified (see Fig. 4.3.3). The shape of the obtained topographic perturbation is qualitatively similar to the example shown for $p = 1$ (see Fig. 4.4.1), but the bar displays steeper slopes. Its growth rate is positive but still very small, $\omega_r \simeq 10^{-3}$, so that the corresponding dimensional growth time is very large, of the order of 10 years. The corresponding equilibrium profile can then be regarded again as physically stable in the relevant time scales of the natural cross-shore changes (from days to months).

## 4.4.2   Results of the 'Flow Over Topography problem'

In order to help to the final physical interpretation of the results presented in the previous section and in appendix A, some tests done with the linear 'FOT problem' are presented in the present chapter. A deeper observation of the behaviour of the linearised wave transformation equation (Eq. 4.2.2) for different perturbations of the water depth, $d$, allows for understanding the reasons why instabilities are not clearly arising in the 'well-posed problem'. The final physical interpretation of all the linear stability results is left for section 4.4.3. As a representative example, all the results presented in the present section are focused on the parameter setting leading to the last example of mode shown in the previous section (see Fig. 4.4.4, found with $y_c/\gamma_c = 1.4$, $s_0 = 0.023$, $p = 2$ and $A = 1.38$).
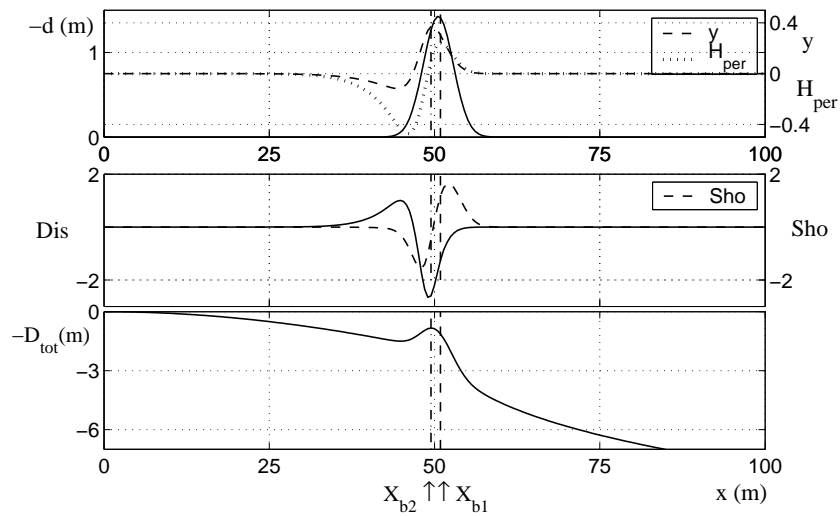
Figure 4.4.5: Example of the result of the 'FOT problem' obtained over a bar located at the 'effective break-point', $x = X_{b1}$. Computations have been done with $y_c/\gamma_c = 1.4$, $s_0 = 0.023$, $p = 2$ and $A = 1.38$. The corresponding equilibrium state is a strongly 'terraced profile', the same as in Fig. 4.4.4. The horizontal axis corresponds to the cross-shore position, $x$. All the quantities shown are dimensional computed with an $H_{off} = 0.5m$. The vertical dashed line is the 'effective break-point', $X_{b1}$, and the vertical point-dashed line is another characteristic point of the equilibrium profiles, $X_{b2}$. Remember that the amplitude of the perturbations is arbitrary as it can not be determined by a linear stability analysis. Top: The solid line is the perturbation in water depth, $-d$, the dashed line is the perturbation in the relative wave height, $y$, and the dotted line is the perturbation in the wave height, $H_{per}$. Middle: Cross-shore distribution of the dissipation and shoaling terms in the linear wave transformation equation (Eq. 4.2.2). The solid line shows the dissipation term induced by the perturbations (corresponding to the two last terms in the right hand side of Eq. (4.2.2)). $Dis < 0$ means a decrease in wave energy with respect to the equilibrium situation, due to more breaking. The dashed line corresponds to the shoaling term (two first terms in the right hand side of the same equation). $Sho > 0$ means an increase in wave energy due to more shoaling. Bottom: The solid line is the resultant topography, equal to minus the total water depth, $-D_{tot} = -D_{eq} - d$.

The first test done is to alocate an arbitrary bar at the 'effective break point', $x = X_{b1}$ and the obtained result is shown in Fig. 4.4.5. As it can be observed in the dashed line of the top graph, the perturbation of the relative wave height, $y$ is mostly positive above the bar, but it becomes negative at the end of its shoreward side. This is a result of the cross-shore shape of the corresponding perturbation of the wave height, $H_{per}$, which is shown in a dotted line in the same top graph. In turn, the behaviour of this latter quantity can be understood from the cross-shore distribution of the perturbation of the dissipation and the shoaling terms in Eq. (4.2.2), which are shown in the middle graph of the same figure. The dissipation term plotted, $Dis$, corresponds to the two last terms in the right hand side of Eq. (4.2.2) and the shoaling term, $Sho$, corresponds to the two first terms in the right hand

side of the same equation. The first effect of the bar on the propagating waves is that a positive perturbation of the shoaling is met ($Sho > 0$ for $x > X_{b1}$), leading to an increase in wave energy. This corresponds to the positive perturbation of the wave height in this region, $H_{per}(x > X_{b1}) > 0$, and subsequently, $y(x > X_{b1}) > 0$. As waves propagate inside the breaker region ($X_{b2} < x < X_{b1}$), this perturbation in the shoaling term decreases and it is nearly overtaken by the negative perturbation of the dissipative term ($Dis < 0$, meaning a decrease of wave energy due to more breaking). This makes $H_{per}(X_{b2} < x < X_{b1})$ decrease, but the perturbation of the relative wave height is still positive, $y(X_{b2} < x < X_{b1}) > 0$, because of the positive perturbation of the water depth along all the domain, $d > 0$ (remember that $Y = H/D$). Finally, as waves enter the surf zone ($x < X_{b2}$), the perturbations of the two terms of the wave transformation equation are negative ($Sho < 0$ and $Dis < 0$) so that $H_{per}(x < X_{b1})$ becomes negative enough to change the sign of $y$. This $y(x < X_{b1}) < 0$ turns out to be responsible for the inhibition of the growth of this bar, as it is explained later on.

This behaviour of $y$ and $H_{per}$ over an arbitrary bar is qualitatively equal to the results of the 'well-posed FOT problem' over the topographic perturbation of the unphysical linear solutions presented in appendix A. Figure A.3 (bottom) shows the same type of cross-shore distribution for the perturbation of the dissipation and the shoaling terms in the wave transformation equation and, subsequently, the corresponding $y$ also becomes negative inside the surf zone (see the dotted line in the top graph Fig. A.3), inhibiting the growth of the corresponding water depth perturbation.

Looking in detail at the sediment transport induced by the obtained $y$ leads to a deeper understanding of what is the effect of $y(x < X_{b1}) < 0$ (over the shoreward side of the bars) and why the feedback of this negative perturbation into the transport leads to an inhibition of the growth of the underlying topography. The following analysis consists of reproducing qualitatively the bed evolution that would follow from the $(d, y)$ corresponding to the arbitrary bar presented in Fig. 4.4.5. We focus first on the linearised wave induced transport (second term of Eq. (4.3.2), indicated by $q^{wav}$ from now on), because we want to understand why the possible source of instability that we have detected in section 4.3.1 is not strong enough. The effect of the downslope 'morphodynamical diffusivity' term is discussed later on.

This approximation to the evolution of an arbitrary bar located at the 'effective break-point' is made in several steps, which are graphed in Fig. 4.4.6. Its first graph shows the starting point, $(d_1, y_1)$, which corresponds to the solution for the perturbations presented in Fig. 4.4.5 (so again $p = 2$, $y_c = 0.7$ and $s_0 = 0.023$). The first step consists of computing the $q_1^{wav}$ induced by these perturbations, $(d_1, y_1)$ (from the second term of Eq. (4.3.2)). If this transport lasted for a certain time interval, $\Delta t$, a new water depth would be met, $d_2$. In our complete linear formulation, the evolution in time of $d$ is described by the linear bed evolution equation (Eq. 4.2.3). The new water depth $d_2$ can be qualitatively described throught a simple Euler-type dicretization of the time derivative of the variable $d$ in this latter equation, which reads

$$d_2 = d_1 + \Delta t \left( \frac{dq_1^{wav}}{dx} \right) \quad . \tag{4.4.1}$$

The amount of change from $d_1$ to $d_2$ depends on the time interval used, $\Delta t$, and on the quantitative magnitude of $q_1^{wav}$, which is directly proportional to the amplitude of $(d_1, y_1)$ (see Eq. 4.3.2). However, a linear analysis never gives information about the amplitudes of
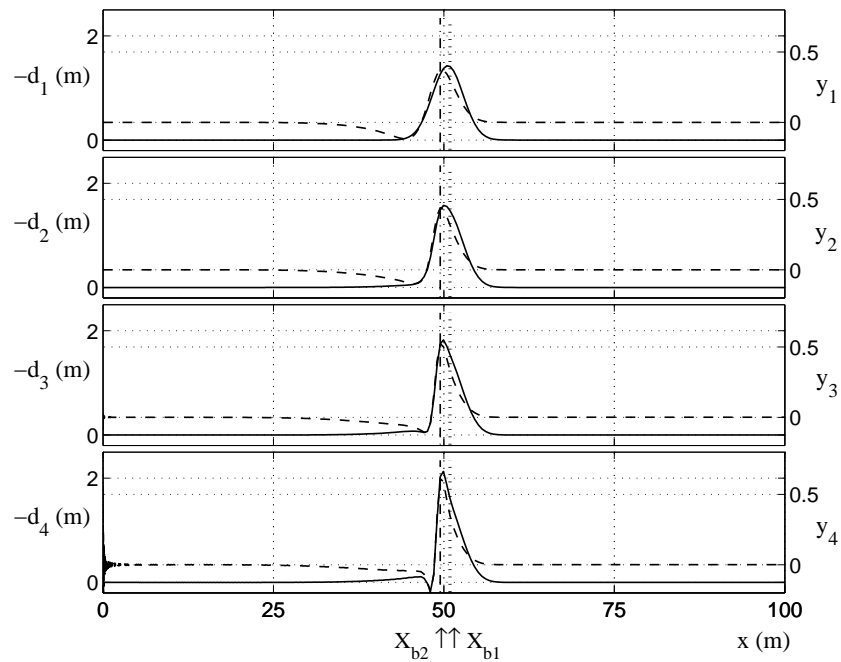
Figure 4.4.6: Approximate evolution in time of the arbitrary bar located at the 'effective break-point' shown in Fig. 4.4.5 (see the caption of that figure for a description of the coordinate system and the variables). As the present analysis just aims at reproducing qualitatively the bed evolution, the amplitude of the starting topographic perturbation and the time interval are set so that the changes in the bottom are noticeable (see the text for more explanations). First: Starting point, the solid line being the perturbation in water depth, $-d_1$, and the dashed line being the perturbation in the relative wave height, $y_1$. Second: Result of the first temporal step, the solid line being the obtained perturbation in water depth, $-d_2$, and the dashed line being the obtained perturbation in the relative wave height, $y_2$. The water depth $d_2$ is computed from $q_1^{wav}$ (the wave transport induced by $d_1$ and $y_1$) using Eq. (4.4.1). The new $y_2$ is found solving the 'FOT problem' over $d_2$. Third: Result of the second temporal step, the solid line being the obtained perturbation in water depth, $-d_3$, and the dashed line being the obtained perturbation in the relative wave height, $y_3$. Fourth: Result of the third temporal step, the solid line being the obtained perturbation in water depth, $-d_4$, and the dashed line being the obtained perturbation in the relative wave height, $y_4$.

the perturbations, so that the amplitude of $d_1$ can be freely chosen. As the present analysis just aims at reproducing qualitatively the bed evolution, the amplitude of $d_1$ and the time interval are set so that the changes in the bottom are noticeable. The second graph of Fig. 4.4.6 shows the water depth perturbation that is obtained after the first time step, $d_2$. This same graph also contains the perturbation of the relative wave height, $y_2$, that is found solving the 'FOT problem' over $d_2$.

More time steps of given by Eq. (4.4.1) can be taken, obtaining $d_3$ and $d_4$. The third and fourth graphs of Fig. 4.4.6 show $(d_3, y_3)$ and $(d_4, y_4)$, respectively. The evolving topography can be qualitatively characterized by an accretion of the crest of the bar together with a strong erosion of its shoreward side. The first process occurs in the region $x > X_{b2}$ and it can be explained by the local convergence of sediment found in case of $y > 0$ due to the 'breakpoint-bar interaction' described in section 4.3.1. As it has been shown there, an onshore directed perturbation of the transport is found at the seaward side of the bar $x > X_{b1}$ and an onshore directed transport is met at the shoreward side, $X_{b2} < x < X_{b1}$, leading to sand deposition at its crest. However, in the discrete and crude time evolution shown in Fig. 4.4.6 a simultaneous strong steepening of the shoreward side of the bar takes place at $x < X_{b2}$. This is due to a local onshore transport caused by the $y(x < X_{b2}) < 0$ that is found in this latter region.

From the considerations given above we could infer that the 'breakpoint-bar mechanism' is working well at least along the region $x > X_{b1}$. However, a linear stability analysis can only describe solutions that grow with a uniform rate along all the domain, which is not verified for this arbitrary bar. Moreover, the downslope difusivity, which has not been taken into account in the crude time evolution presented in Fig. 4.4.6, becomes very strong due to the large slopes that occur in the shoreward side of the bar. It turns out that this damping effect always overtakes the instability caused by the 'breakpoint-bar interaction'. Thus, in order that the 'breakpoint bar instability' described in our equations operates correctly, it is crucial to obtain a positive perturbation in the relative wave height along all the domain. In fact, this characteristic is fulfilled by the $y$ obtained in the results of the linear stability analysis presented in the previous section (see Fig. 4.4.1 and Fig. 4.4.4). However, these topographic perturbations do not grow either. An interpretation for such behaviour is given in the next subsection.

Finally, in order to obtain a deeper understanding of the behaviour of the wave transformation equation used, the 'FOT problem' has also been solved for two more topographies: an arbitrary bar located inside the surf zone and another located at the shoaling zone. When the bar is located inside the surf zone $x < X_{b2}$, the obtained perturbation in the wave height is always negative because the linear wave transformation equation is clearly dominated by an increase of the wave dissipation term over the bar (inducing a negative perturbation in the wave energy and hence in the $H_{per}$). The corresponding $y$ is positive over the seaward side of the bar and negative over its shoreward side. This leads to a cross-shore distribution of the induced transport that would make this bar migrate offshore and decay. The solution of the 'FOT problem' over an arbitrary bar located in the shoaling zone, $x > X_{b2}$, has also been tested. The wave transformation equation is now clearly dominated by the shoaling term, which increases at the seaward side of the bar and decreases at its shoreward side. This induces a positive perturbation of the water depth over the bar and also a clear positive perturbation of the relative wave height. The resultant sediment transport structure would lead to onshore migration and decay of the feature.

### 4.4.3   Interpretation of the linear results and preliminary discussion

Before entering into the physical interpretation of the results of the linear stability analysis presented in section 4.4.1, the physical validity of the solutions of the discretized linear equations must be assessed. In particular, the behaviour of the wave transformation equation

and the variable $y$ must be carefully analysed, as they turned out to be critical in the 'unphysical solutions' shown in appendix A. In this respect, the first point to put forward is that the relative wave height linked to all the topographic perturbations shown in the two last sections decreases fast towards zero in the offshore direction (the contrary happened for those 'unphysical solutions'). For instance, the value of $y$ at the last point inside the domain in the example shown in Fig. 4.4.1 is $y_{N-1} = O(10^{-6})$). This value is small enough to guarantee a good numerical description of the corresponding hydrodynamical boundary condition ($y_N = y(x_{off}) = 0$). Secondly, the magnitude of the perturbation of the wave height, $H_{per}$, is now always sensible. As an example, the value of $H_{per}$ at the 'effective break-point' ($x = X_{b1}$) for the mode shown in Fig. 4.4.1 can be roughly evaluated from the graphs. Imagine that we have a small perturbation of the topography that is $d = 0.5m$ height at $x = X_{b1}$ (the amplitude used in Fig. 4.4.1 is 3 times larger because we wanted to show a noticeable bar in the final topography). The corresponding perturbation on the relative wave height becomes $y(X_{b1}) \simeq 0.032$. The values for the equilibrium variables are $D_{eq}(X_{b1}) \simeq 4.4m$ and $Y_{eq}(X_{b1}) \simeq 0.3$. Provided that $H = Y D$, one can find the expression, $H_{per} = y D_{eq} + d Y_{eq}$. Therefore, the perturbation of the wave height produced by a bar of $0.5m$ is $H_{per}(X_{b1}) \simeq 0.3m$. This value is much more sensible than the one produced by the 'ill-posed wave transformation equation' (see appendix A). Thirdly, it must be underlined that the spurious input of wave energy that was found using the 'ill-posed wave transformation' ($b = 1$) is never met with the 'well-posed problem' ($b < 1$), as has already been put forward in appendix A.

Although the results of the 'well-posed wave transformation equation' are physically sensible, the results of the complete linear stability analysis described in section 4.4.1 are somehow surprising and deserve to be deeper understood. Section 4.3 has given some reasons in favour of the possibility that an instability due to the 'breakpoint-bar interaction' occurs. A necessary condition (although not sufficient) for finding instability has been qualitatively fulfilled at least for certain parameter settings (see section 4.3.2). Moreover, the cross-shore shape of the 'marginally stable solutions' obtained from the linear stability analysis (described in section 4.4.1) seems to verify the two steps that should lead to a feedback process due to the 'breakpoint-bar interaction': the perturbation in $Y$ is positive along all the domain, so that the subsequent sand transport should lead to convergence at the bar crest (see section 4.3.1).

In spite of all this, the 'fastest growing linear solutions' obtained have $\omega_r \simeq 0$. The clue for understanding this enigm is the effect of the downslope 'morphodynamical diffusivity' on these solutions. As explained in section 4.4.1, decreasing this parameter does not modify significally the growth rates, but it leads to sharper bars located in a smaller region around $x = X_{b1}$ (and hence displaying larger slopes, see Figs. 4.4.1, 4.4.2 and 4.4.3). The shape of the topography shown in the latter figure seems to indicate that the topography would tend to a Dirac $\delta$ function if $s_0 \to 0$. The same suggestion can be inferred from the crude bed evolution of the arbitrary bar located at the 'effective break-point' that has been shown in Fig. 4.4.6. Our interpretation of the result of the linear stability analysis is as follows. The topographic shape of the only growing 'normal mode' that can arise due to the 'breakpoint bar interaction' described by our equations without diffusivity ($ate = 0$) is a Dirac $\delta$ function. This has then made us to choose the name *'Dirac $\delta$ instability'*. However, when the downslope transport term is connected, it becomes very strong due to the infinite slopes that characterizes the Dirac $\delta$ function, counteracting its growth. Given a certain value for $s_0$, the 'marginally

stable solutions' from the linear stability analysis always display the necessary slopes so that the downslope transport (damping term) and the wave transport ('Dirac $\delta$ instability' term) are in balance. Therefore, the growth rates of the solutions are always around 0.

Appendix B presents a simple analytical model that captures the same type of 'Dirac $\delta$ instability'. In that appendix we present a simple transport formula (Eq. B.1) that displays a convergence/divergence cross-shore pattern similar to the one used in the present chapter. Again the instability term of that simple formula leads to a convergence of transport only at one point of the domain ($x = 0$), imitating the very localized convergence of sand at the breaker region that is found in our linearised transport formula. That simple formula also contains a downslope damping term. The bed evolution equation that follows from that transport formula is analytically solvable. The shape of the obtained solutions and their dependence on the downslope 'morphodynamical diffusivity' are very similar to those of the 'marginally stable solutions' of the present linear model (compare Figs. B.5, B.6 and B.7 with Figs. 4.4.1, 4.4.2 and 4.4.3). The dependence of the growth rates on the downslope 'morphodynamical diffusivity' in that simple model is also very intriguing, the solutions becoming more stable when de diffusivity decreases! (see Fig. B.2). The simple model is also analytically solvable in the limiting case of neglecting the downslope 'morphodynamical diffusivity' and the solution is the Dirac $\delta$ function. The results of that simple model are then in complete agreement with the interpretation given in the previous paragraph for the existence of the 'marginally stable solutions' of the present linear stability analysis.

This strong sensitivity on the downslope 'morphodynamical diffusivity' is not found in previous morphodynamical models. Commonly, morphodynamical systems display 'normal modes' with finite slopes even in case of zero diffusivity (examples can be found in Falqués *et al.* (2000),Calvete *et al.* (2001) and also in chapter 5 of the present thesis). The results of the present linear stability analysis (and the analytical simple model) show that the contrary occurs in our linear model, so that the equations including diffusivity turn out to be stable.

There are more questions that must be answered, related with the reasons presented in section 4.3 in favour of the possibility that our linearised equations are unstable. The main result of the 'Energy identity' (Eq. 4.3.13) presented in section 4.3.2 has been the qualitative fulfillment of a necessary condition for instability in the case of 'terraced beaches'. A first issue to put forward is that the condition derived there is not a sufficient condition for instability (but only a necessary condition). This means that it was not intended to be a guarantee of instability, but just an indication of the possibility of instability. Moreover, some remarks done in the last paragraph of that section must be here recalled. The first one is that the instability term related with $I_1$ in Eq. (4.3.13) would only operate for perturbations with a negligible value inside the surf zone ($x < X_{b2}$) because $I_1 < 0$ there (see Fig. 4.3.3). The contrary occurs in the 'marginally stable solutions' of the linear stability analysis, $d$ being positive and significantly different from zero along all the surf zone. This can be seen in Fig. 4.4.4, which has been found using the same parameter setting as in Fig. 4.3.3. The second remark that must be recalled is that the spatial derivatives of the topographic perturbations shown by the 'marginally stable solutions' can be very large (see again Fig. 4.4.4). Thus, the term $(\partial d/\partial x)^2$ can be significantly larger than $d^2$. Therefore, although $I_1 >> I_2$ (see Fig. 4.3.3), the damping term of the 'Energy identity' can become of the same order of the unstabilising term (comparing the first and the second term of the right hand side of Eq. (4.3.13)).

Section 4.3.1 has also shown the plausibility that the model equations could exhibit an instability leading to the generation of shore-parallel bars in a very qualitative way. One conclusion of that section is that a necessary condition for the occurrence of instability due to the 'breakpoint-bar interaction' included in our linear bed evolution equation seems to be $y(x) > 0$ , $\forall x$. The results of the 'FOT problem' presented in section 4.4.2 indicate that $d(x) > 0$ $(\forall x)$ is the only way of obtaining $y(x) > 0$ $(\forall x)$ using our 'well-posed linear wave transformation equation'. This is in agreement with the topographic shape of the 'marginally stable solutions'. However, this property $(d(x) > 0$ , $\forall x)$ that seems to be necessary for growth in the analysis of section 4.3.1 has two important consequences. Firstly, as has been explained in the last paragraph, the fact that $d(x < X_{b2}) > 0$ diminishes the unstabilising effect of the first term in the right hand side of the 'Energy identity'. Secondly, the property $(d(x) > 0$ , $\forall x)$ means that there is no formation of troughs in the profile and hence the sand needed to feed the possible bars should be supplied through the boundaries. This is not the case for the 'marginally stable solutions' because the corresponding transport is zero along all the domain (the downslope transport always balances the wave induced transport).

A preliminary conclusion of all the previous paragraphs is that our simplified linearised sediment transport formulation has not encapsulated well the 'breakpoint-bar mechanism' and we should try a more complex formulation. Firstly, the sediment transport formula used is not intended to describe neither the sand transport coming from the shelf (which in fact is very small), nor the exchange of sand between the nearshore zone and the dry beach (which can be significant in case of erosive conditions). This leads to another strong limitation of our linearised transport formula. The perturbation induced to the coastline position turns out to be of second order in our formulation. As our linearised equations are developed up to first order, we deal with a fixed shoreline. This, together with the boundary conditions chosen to describe the linear variables, make the sediment transport to be zero at the coastline. This hypothesis is inherent to performing a linear stability analysis of our set of equations, but it is in contradiction with the often observed bar generation events linked to a strong erosion of the shoreline (Komar, 1998; Short, 1999).

The wave tranformation equation used is also partially responsible for the fact that bars are not steming from 'self-organization'. To confirm this statement, it is important to recall the solutions of the 'ill-posed problem' presented in appendix A. These solutions are an example where our sediment transport formula has been able to describe the generation of break-point bars with a re-distribution of the sand within the nearshore domain. The 'ill-posed wave transformation' formulation has lead to $y(x) > 0$ $(\forall x)$ even in case of a perturbation in the water depth that displays a trough inside the surf zone. In contrast, the solutions of the 'well-posed wave transformation equation' over such type of topography display a local $y < 0$ above the trough. Adding more physics to the 'well-posed wave transformation equation' may lead to get $y(x) > 0$ $(\forall x)$ even in the presence of troughs so that the present sediment transport equation might be good enough.

Before adding more physics into any of the model equations, one may test the possibility that the 'breakpoint-bar mechanism' operates correctly just by relaxing the assumption of linearity. Firstly, there is still the option that the formation of break-point bars would be linked to non-linear instabilities of the system. Secondly, it might also be the case that the generation of shore-parallel bars would always be related to an evolution of the shoreline. It has been often stated in the literature that break-point bars are generated in strongly ero-

sive situations (Komar, 1998; Short, 1999). This suggests that an onshore migration of the shoreline might be essential for the formation of bars. In such case, the sand needed for the growth of the bar could come from the dry beach. As explained above, the 'marginally stable results' obtained in the present linear model also indicate that an input of sand through the boundaries may be essential to get growth. These two processes can only be approached with a finite amplitude model. A third limitation of a linear stability analysis is that it can only describe solutions that grow with a uniform rate along all the domain. The results of the linear 'FOT problem' suggest that the 'breakpoint-bar interaction' might never verify this assumption. A fourth possibility is that break-point bars could only emerge far from equilibrium conditions as bar generation events are often found under stormy weather (Thornton & Humiston, 1996; Aagaard *et al.*, 1998). In these situations the underlying profile can not be in equilibrium with the wave conditions before the bar starts growing, which is another implicit assumption of our linear stability analysis. Finally, another important consideration is that the response time of bar systems can be large compared with the time over which wave conditions can be considered steady. Therefore, a non-linear model that uses non-steady wave heights at the offshore boundary (following the time-evolving wave conditions) might be able to better encapsulate the physics behind the generation of shore-parallel bars.

## 4.5 Formulation of the non-linear model

This section presents a non-linear model that allows to release the assumption of linearity done in the previous sections. This lets us to investigate the possible emergence of instabilities from the equilibrium states given in chapter 3 (in the non-linear regime). A possible exchange of sand with the dry beach is now allowed, linked to a possible evolution of the shoreline. The behaviour of the system far form equilibrium conditions can also be studied. Finally, the present finite amplitude model could be used with non-steady boundary conditions. This would allow for simulating more realistic weather conditions (by using a variable $H_{rms}$).

In the framework of the present thesis, this model is first used to test the results obtained from the linear stability analysis. The possibility that non-linear instabilities arise from the equilibrium profile is also checked. A third aim is to test the influence of allowing for a certain evolution of the shoreline on the generation of break-point bars. Some numerical experiments of the non-linear temporal evolution of the system moderately far from equilibrium are subsequently performed. Finally, the migration of bars is also studied. On the other hand, investigating the behaviour of the system very far from equilibrium conditions and/or under non-steady boundary conditions is far beyond the scope of the present thesis and it is left for further research.

### 4.5.1 Non-linear equations

As we intend to analyse the non-linear stability of the equilibrium profiles presented in the previous chapter, the same coordinate system and variables are used (they can be seen in

Fig. 3.2.1). The studied finite domain lies from the coastline (indicated by $x_{cl}$ from now on), to a certain offshore position ($x_{off}$). The same set of equations (Eqns. 3.2.9 and 3.2.10) are also considered, together with steady boundary conditions.

The non-dimensional parameter $\epsilon$ in Eq. (3.2.9) (which is the ratio between the hydro-dynamical and the morphological time scales) is set to 0 in the present finite amplitude analysis as it has been shown to be very small (see section 3.2.3). Remember that this assumption (called quasi-steady hypothesis), means that the hydrodynamical field adapts instantaneously to the evolving topography. The equations that follows from Eqns. (3.2.9) and (3.2.10) are then

$$\frac{\partial Y}{\partial x} = \mathcal{F}(Y, D, D_x) = -\frac{5}{4}\frac{Y}{D}\frac{\partial D}{\partial x} + A\frac{Y^4}{\sqrt{D}}\left(1 - \Gamma(Yy_c)^{-5/2}\right) \quad , \tag{4.5.1}$$

$$\frac{\partial D}{\partial t} = \mathcal{G}(Y, Y_x, D, D_x, D_{xx}) = \frac{\partial}{\partial x}\left[Y^3 D^{3/2}\left(s_0\frac{\partial D}{\partial x} - Y^p(1 - Y)\right)\right] \quad , \tag{4.5.2}$$

where again $\Gamma(Yy_c) = 1 + (Yy_c/\gamma_c)^2$. The scaling used in the equations has already been presented in chapter 3 (see table 3.2.1). The final independent parameters of the model are again $y_c/\gamma_c$, $s_0$, $p$ and $A$. The explicit definition of these four parameters and the range of values used for them has been given in table 3.2.2 of the previous chapter. As it has been explained in section 3.2.3, the first three parameters are the most important for describing the dynamics of this problem. Remember that the wave height far offshore, $H_{off}$, turns out to be a scaling factor in this dyamical system. The functionals $\mathcal{F}$ and $\mathcal{G}$ indicate the dependence of the left hand side of the equations on the model variables and derivatives, being a useful notation for the description of the numerical method.

The final set of finite amplitude dimensionless equations consists of a second order parabolic equation for the bed evolution (Eq. 4.5.2) and a first order equation for the wave propagation (Eq. 4.5.1). So three conditions are required at the boundaries of the domain $x_{cl}$ and $x_{off}$. As explained above, investigating the behaviour of the system under non-steady boundary conditions is beyond the scope of the present thesis, so that the boundary conditions are chosen in accordance with the linear model: $Y$ is set to be constant at $x_{off}$ and $D$ is set to be constant at both boundaries ($x_{cl}$ and $x_{off}$). However, some differences exist between the formulation of the linear and the non-linear models. The most noticeable is that the present finite amplitude model can follow the possible migration of the coastline when the topography evolves, if necessary. Its motion is computed numerically in a very simplified way, as a first step towards more accurate descriptions of the coastline evolution in further models. The description of how we evaluate the shoreline evolution is done in the following section.

## 4.5.2   Numerical method and solution procedure

A standard finite difference method has been chosen for solving the set of finite amplitude equations (see Ames (1977) for a detailed description of finite difference methods). Both the spatial and the temporal coordinates have been discretized with constant steps, $\delta_x$ and $\delta_t$,

$$x_i = x_0 + \delta_x\,i \quad , \quad \text{where} \quad i = 0, 1, ..., n_x \quad , \tag{4.5.3}$$

$$t_k = \delta_t\,k \quad , \quad \text{where} \quad k = 0, 1, ..., n_t \quad , \tag{4.5.4}$$

where the position $x_0$ is located onshore of the coastline position $x_{cl}$ (so that this latter quantity can evolve with time if necessary), while $x_{n_x}$ corresponds to the steady position of the closure depth defined in the previous section, $x_{n_x} = x_{off}$. The variables of the problem are also numerically approximated. Given a function $f(x, t)$, which can represent any of our two variables, $Y(x, t)$ or $D(x, t)$, its numerical approximation in our discretized spatial and temporal domains is indicated by $f_i^k$ (where the spatial index $i$ and the temporal index $k$ are the ones defined in Eqns. (4.5.3) and (4.5.4) from now on).

Equations (4.5.1) and (4.5.2) are spatially discretized using second order approximations to the spatial derivatives. The first and the second derivatives of $f(x, t)$ with respect to $x$ at a certain point are approximated by using the value of the function at the two surrounding points of the discretized domain, $f_{i-1}^k$ and $f_{i+1}^k$. The expressions used for all the time steps, $k$, are

$$\left(\frac{\partial f}{\partial x}\right)_i^k = \frac{-f_{i-1}^k + f_{i+1}^k}{2\,\delta_x} \quad , \quad \text{for} \quad i = 1, ..., n_x - 1 \ , \tag{4.5.5}$$

$$\left(\frac{\partial^2 f}{\partial x^2}\right)_i^k = \frac{f_{i-1}^k + f_{i+1}^k - 2\,f_i^k}{\delta_x^2} \quad , \quad \text{for} \quad i = 1, ..., n_x - 1 \ . \tag{4.5.6}$$

The first order derivative computed at the offshore boundary is also needed in some steps of the solution procedure. It is computed with a second order backward-scheme, which uses the two closer points inside the domain,

$$\left(\frac{\partial f}{\partial x}\right)_{n_x}^k = \frac{3\,f_{n_x}^k - 4\,f_{n_x-1}^k + f_{n_x-2}^k}{2\,\delta_x} \quad . \tag{4.5.7}$$

The water depth $D(x, t)$ evolves in time following the parabolic bed evolution equation (Eq. 4.5.2). Its time derivative (left hand side of the equation) is computed numerically with a first order expression,

$$\left(\frac{\partial D}{\partial t}\right)_i^{k-1} = \frac{D_i^k - D_i^{k-1}}{\delta_t} \quad , \quad \text{for} \quad i = 1, ..., n_x - 1 \quad \text{and} \quad k = 1, ..., n_t \ . \tag{4.5.8}$$

Given the water depth in a certain time step, $D_i^{k-1}$, one would like to compute its value in the following time step, $D_i^k$. The question arises of which expression one may use for describing numerically the spatial terms in the bed evolution equation ($\mathcal{G}$ in the right hand side of Eq. (4.5.2)). In one-step methods the calculated value of $D_i^k$ depends only on the data at the preceeding time step, $\mathcal{G}^{k-1}$. The simplest one-step method is the classical explicit first order Euler formula,

$$D_i^1 = D_i^0 + \delta_t\,\mathcal{G}_i^0 \quad , \quad \text{for} \quad i = 1, ..., n_x - 1 \ . \tag{4.5.9}$$

However, once a value for $D$ has been obtained for a few time steps, it is natural to make use of some of this information to calculate the value at the next time step, $D^k$, rather than just use the value at the preceeding time step. Methods that use information at more than the last time step are referred to as multi-step methods. Various levels of accuracy can be achieved with them, depending on the number of preceeding data points that are used. Using a variable time step also increases the accuracy. The most precise methods for

time evolution are the implicit methods, which also make use the value of $\mathcal{G}$ at the final time step, which is unknown beforehand. The two latter improvements are quite difficult to be implemented in a numerical code. For instance, an implicit method requires for solving at the same time the discretized wave transformation equation and the bed evolution. In the present model, the temporal evolution for $k = 2, ..., n_t$ (i.e. after the first time step has been taken) is computed with an explicit method called second order Adams-Bashforth integration scheme, which uses a combination of the values of $\mathcal{G}$ at the two preceeding time steps for computing $D_k$,

$$D_i^k = D_i^{k-1} + \delta_t \left( \frac{3}{2} \mathcal{G}_i^{k-1} - \frac{1}{2} \mathcal{G}_i^{k-2} \right) \quad , \quad \text{for} \quad i = 1, ..., n_x - 1 \quad . \tag{4.5.10}$$

The most important condition needed for avoiding numerical instabilities in second order diffusive equations is the so-called Von-Neumann or Courant-Friedrichs-Levy condition. Given a certain spatial step, $\delta_x$, this condition settles the largest time step that can be used,

$$\delta_t \leq K \frac{\delta_x^2}{2\nu} \quad . \tag{4.5.11}$$

The parameter $\nu$ indicates an estimate of the diffusive coefficient in front of the term $\partial^2 D / \partial x^2$, which in our case is $\nu \simeq s_0 Y_{eq}^3 D_{eq}^{3/2}$ (see Eq. 4.5.2). The constant $K$ depends on the problem and must be set by trial and error.

The solution procedure used in the present model is as follows:

- **Initial state:** A numerical experiment starts with an initial bathymetry, $D_i^0$, that must be known at all the discretized points of the domain ($i = n_{cl}, n_{cl+1}, ..., n_x - 1$ from now on), from the coastline, $x_{n_{cl}}$, to the offshore position $x_{n_x}$. Remember that the index $n_{cl}$ must be larger than $n_0$ in order to allow for a possible evolution of the coastline position. Most of the numerical experiments performed start from a situation close to equilibrium. Given a certain physical parameter setting, this near-equilibrium situations can be built by superimposing some topographic perturbation to the equilibrium profile that results from the parameter values used. First, the computation of the equilibrium profile is done in the same way as in chapter 3. Two offshore conditions are imposed, $(D_{n_x}^{eq}, Y_{n_x}^{eq}) = (D_{off}, Y_{off})$, and then we integrate numerically the set of equilibrium Eqns. (3.2.13) and (3.2.12) in the onshore direction up to the coastline. The condition for defining the coastline is again that the water depth at $x = x_{n_{cl}}$ is smaller than a certain reference value, $D_{n_{cl}+1}^k < D_{min}$. A perturbation with the desired cross-shore shape, $D_i^{per}$, is subsequently added to the equilibrium water depth to obtain the initial state for the non-linear model, $D_i^0 = D_i^{eq} + D_i^{per}$.

  Other numerical experiments start from an initial water depth that is analytically computed. The most common analytical profile used is a 'planar beach' defined as follows. Firstly, a constant slope is imposed from the coastline, $x = x_{cl}$, to a certain position located offshore of the break-point, $x = x_{p1} >> X_{b1}$ ($D_i^0 = \beta (x_i - x_{cl})$, where $\beta$ is the slope, which can be chosen). At $x = x_{p1}$, the water depth is matched to

  $$D_i^0 = a (x_i)^2 + b x_i + c \quad , \quad \text{with}$$
  $$a = \frac{\beta}{2.0 (x_{p1} - x_{p2})} \quad , \quad b = -2 a x_q \quad , \quad c = D_{p1} - a (x_{p1})^2 - b x_{p1} \quad ,$$

where $i = (p1, ..., p2)$. This last shape is just used in a small interval $x \, \epsilon \, (x_{p1} - x_{p2})$ with the aim of imposing a zero slope at a certain point, $x_{p2}$. There, the profile is matched to a horizontal bed, $D_i^0 = D_{p2}^0$, until the last point of the described domain is reached, $i = (p2, ..., n_x)$. This parameterization for arbitrary 'planar profiles' guarantees the continuity of $D$ and its first derivative.

After the equilibrium topography has been computed with any of these two methods, the discretized version of the first order wave transformation equation (Eq. 4.5.1) is solved. A certain value for the relative wave height is again imposed at the offshore boundary, $Y_{n_x}^k = Y_{off}$ (steady conditions). Integration is performed in the onshore direction until the coastline is reached, using a standard fourth order Runge-Kutta method.

- **First time step:** The first time step is taken using the Euler method described in Eq. (4.5.9) because we just have the information at the time step before, $k = 0$. It allows to compute $D_i^1$ from $D_i^0$, $Y_i^0$ and their spatial derivatives. After the first time step has been accomplished, the wave transformation equation (Eq. 4.5.1) is again used to find the new $Y_i^1$. The boundary conditions are chosen to be steady in all the numerical experiments presented in this thesis, so that $D_{n_{cl}}^k = 0$, $D_{n_x}^k = D_{off}$ and $Y_{n_x}^k = Y_{off}$ (for all the time steps $k$).

- **Subsequent time stepping:** The regular time integration loop consists of using the Adams-Basforth integration scheme (Eq. 4.5.10) to find $D_i^k$ making use of the result of the two preceeding time steps. From time to time, after a temporal step has been accomplished, the water depth at the spatial step nearest to the coastline, $D_{n_{cl}+1}^k$, turns out to be very small. This can be interpreted as if the coastline has moved one spatial step offshore (beach accretion). A very simplified way of following such possible accretive motion is to impose that the water depth at $i = n_{cl} + 1$ must be always larger than the reference value used in the equilibrium integration, $D_{min}$. When this condition is not achieved after a certain time step is accomplished, $D_{n_{cl}+1}^k < D_{min}$, a new offshore displaced coastline index is defined, $n_{cl}^{new} = n_{cl}^{old} + 1$, so that $D_{n_{cl}^{new}}^k = 0$. The opposite physical effect can also occur and a condition that accounts for erosion of the coastline has also been implemented. When the water depth one spatial step offshore of the coastline is larger than a certain reference value, $D_{n_{cl}+1}^k > D_{max}$, a new onshore displaced coastline index is defined, $n_{cl}^{new} = n_{cl}^{old} - 1$, so that $D_{n_{cl}^{new}}^k = 0$. In this latter case, the value for the water depth at the new first point of the domain, $D_{n_{cl}^{new}+1}^k$, is unknown beforehand (as it is the water depth at the old coastline point, $D_{n_{cl}^{old}}^k$). It is computed in our model by linear extrapolation from its nearest point in the domain, $D_{n_{cl}^{new}+2}^k$. After the new topography is known, we integrate again the 'FOT equation' in order to find the new $Y_i^k$.

The present non-linear model could also be used with non-steady boundary conditions, by varying the boundary conditions $D_{n_{cl}}^k$, $D_{n_x}^k$ and $Y_{n_x}^k$ at each time step. This would allow for simulating more realistic weather conditions (following a time-dependent $H_{off}(t)$). The effect of a variable exchange of sediment transport at both boundaries could also be investigated. All these possible numerical experiments are left for further research. The result of a certain temporal evolution must be independent of the numerical discretization used. In order to verify this condition, given a physical parameter setting, initial tests

have been performed using different values for the numerical parameters $D_{off}$, $Y_{off}$, $\delta_x$, $\delta_t$, $D_{min}$ and $D_{max}$. The results of such tests have proved numerically the accuracy of the discretization scheme used.

## 4.6 Results of the temporal evolution of the non-linear equations

### 4.6.1 Temporal evolution of initially 'barred beaches'

The first set of numerical experiments performed with the finite amplitude model starts from initial topographies that results from the superposition of different artificial topographic perturbations to the equilibrium profiles, $D_i^0 = D_i^{eq} + D_i^{per}$. For different physical parameter settings, bars of various shapes have been superimposed to the corresponding equilibrium configurations at different cross-shore positions. The subsequent temporal evolution of these initially 'barred profiles' have been performed using steady boundary conditions. The specific values of the variables $D$ and $Y$ imposed at the boundaries correspond with their values in the equilibrium state. The main result is that, for all the parameter settings used, the temporal evolution of these 'barred profiles' always tends towards the corresponding 'terraced equilibrium states'. Some representative examples of this first set of of numerical experiments are shown in the following figures.

The first numerical experiment shown is the temporal evolution of an arbitrary bar added at the 'effective break-point' of the equilibrium profile, $x = X_{b1}$ (vertical dashed line in the graphs). The computations have been done with the parameter values $p = 1$, $s_0 = 0.011$, $y_c = 0.45$ and $A = 0.46$, which corresponding equilibrium profile is a relatively 'terraced profile'. The result of the temporal evolution can be seen in Fig. 4.6.1. The bar decays in time, the system clearly tending towards the 'terraced equilibrium configuration' (shown by the thickest solid line in the graphs). The time needed for reducing by half the inital amplitude of the bar is about 4 days (see the legend of Fig. 4.6.1). This quantity is called e-folding damping time from now on, $T_d$. The perturbation on the wave height induced by the bar can be see in the bottom graph of Fig. 4.6.1.

The second numerical experiment has been performed after superimposing an arbitrary bar inside the surf zone ($x < X_{b1}$) with the same parameter setting (see Fig. 4.6.2). A clear decay towards the equilibrium is also met, with an e-folding damping time of about 2 days. At the same time, the bar shows an onshore migration towards the break-point. The third temporal evolution starts from an initial state given by the equilibrium profile plus a bar located seaward of the 'effective break-point' ($x > X_{b1}$). As can be seen in Fig. 4.6.3 the decay is also very clear ($T_d \simeq 4$ days) and a certain onshore migration can be detected.

These results have been similarly reproduced for different parameter settings, corresponding to a wide range of equilibrium profiles. Together with the persistent decay of the bars, a secondary result of all the numerical experiments performed has been a clear offshore migration of the arbitrary bars initially located inside the surf zone and a slower onshore

Figure 4.6.1: Example of non-linear temporal evolution of an arbitrary bar located at the 'effective break-point' of the corresponding equilibrium profile. Computations have been done with $y_c/\gamma_c = 0.9$, $s_0 = 0.11$, $p = 1$ and $A = 0.46$, which corresponding equilibrium profile is a relatively 'terraced profile'. The horizontal axis corresponds to the cross-shore position, $x(m)$. All quantities shown are dimensional computed with an $H_{off} = 0.5m$. The vertical dashed line is the 'effective break-point', $x = X_{b1}$. Top: Temporal evolution of the water depth, $D$. The initial topography is indicated by a solid line and the topographies obtained with the subsequent time steps are indicated with different types of lines, which can be seen in the legend. The thickest solid line is the equilibrium profile corresponding to the parameter setting used. Above the main graph, there is a smaller one which contains a zoom of the region around the bar, so that its evolution can be easily followed. Bottom: Temporal evolution of the wave height, $H$.

migration of the bars initially located seaward of the break-point. These migration processes are in agreement with what has been previously suggested by the results of the linear 'FOT problem' (see section 4.4.2). Even though the coastline has been allowed to evolve in all these numerical experiments, no motion has been detected.
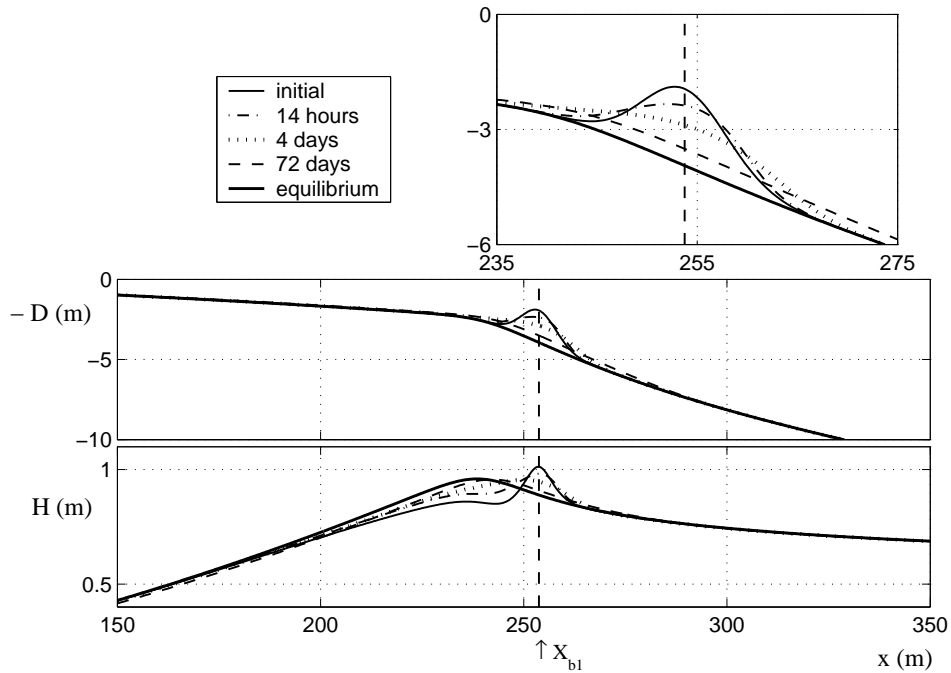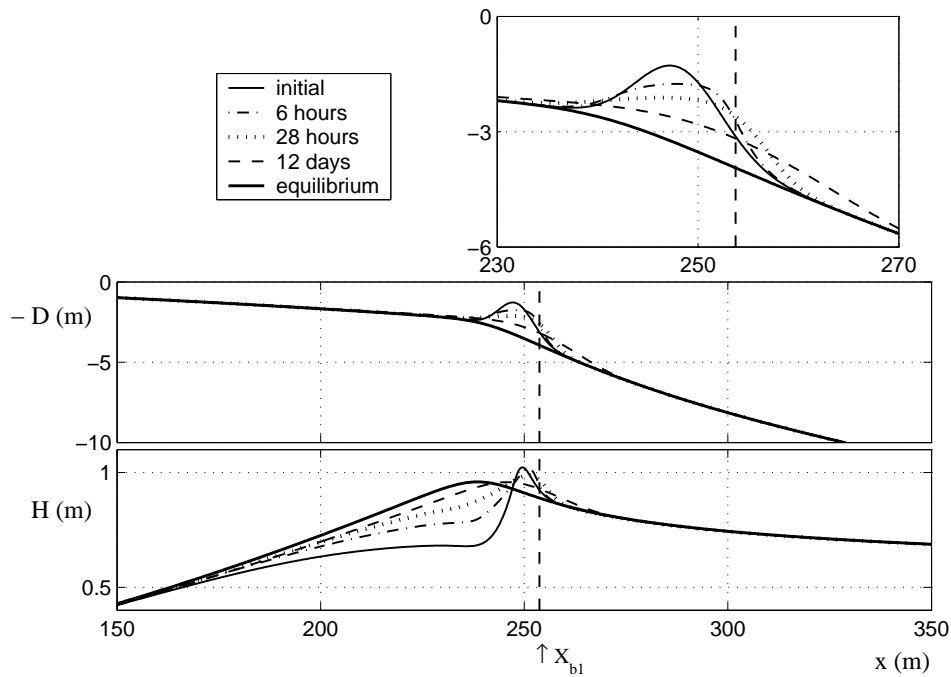
Figure 4.6.2: Example of non-linear temporal evolution of an arbitrary bar located shoreward of the 'effective break-point' of the corresponding equilibrium profile. Computations have been done with $p = 1$, $y_c = 0.45$, $s_0 = 0.11$ and $A = 0.46$. See the caption of Fig. 4.6.1 for more explanations. Top: Temporal evolution of the water depth, $D$. Bottom: Temporal evolution of the wave height, $H$.

## 4.6.2   Temporal evolution of initially 'planar beaches'

The second set of non-linear numerical experiments performed starts from initially constant sloping beaches of different arbitrary slopes, $\beta$. The specific parameterization of these 'planar profiles' has been described in section 4.5.2. For different physical parameter settings and different $\beta$, the temporal evolution of these initial states has been performed, subject to steady boundary conditions. The results are again very clear, initially 'planar beaches' evolving always to the equilibrium 'terraced profiles' correponding to the parameter settings.

As a representative example, the parameter setting used in the figures shown in the previous section is again chosen, $p = 1$, $s_0 = 0.011$, $y_c = 0.45$ and $A = 0.46$. The corresponding temporal evolution can be seen in Fig. 4.6.4. The initially 'planar beach profile' clearly tends to the equilibrium 'terraced configuration' that corresponds with the values used for the physical parameters. A clear onshore migration (i.e. erosion) of the coastline is also obtained, which indicates that the simplified formulation used for its evolution is sensible.
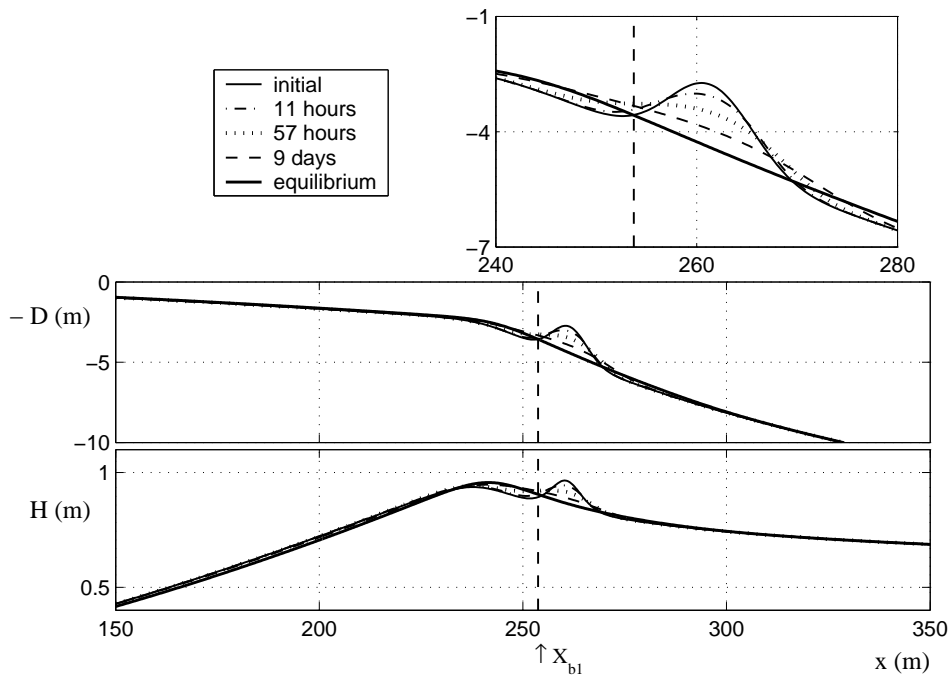
Figure 4.6.3: Example of non-linear temporal evolution of an arbitrary bar located seaward of the 'effective break-point' of the corresponding equilibrium profile. Computations have been done with $p = 1$, $y_c = 0.45$, $s_0 = 0.11$ and $A = 0.46$. See the caption of Fig. 4.6.1 for more explanations. Top: Temporal evolution of the water depth, $D$. Bottom: Temporal evolution of the wave height, $H$.

## 4.6.3   Interpretation of the non-linear results

These non-linear results validate the linear stability analysis presented in section 4.4, as the bars superimposed to the equilibrium are always eroded (see Figs. 4.6.1, 4.6.2 and 4.6.3). In addition, it rules out any possible finite amplitude instability. Therefore, the equilibrium profiles presented in chapter 3 (all of them, the 'terraced' and the 'planar') are found to be stable both in the linear and in the non-linear regimes.

It has been suggested in the literature that break-point bar generation is always linked to an erosion of the shoreline (Komar, 1998; Short, 1999) , the sand arriving to the bar from the dry beach. However, in spite of allowing for an evolution of the shoreline in the present finite amplitude model, bars are not forming either. On the other hand, erosion of the shoreline has been found to be linked to the formation of 'terraced profiles' from initially 'planar beaches'. Even when starting from initial states that are moderately far from the equilibrium configuration, no bars emerge, the corresponding 'terraced equilibrium profiles' being always reached (see Fig. 4.6.4). Bars neither do occur as temporary features in the evolution of the system to the equilibrium.
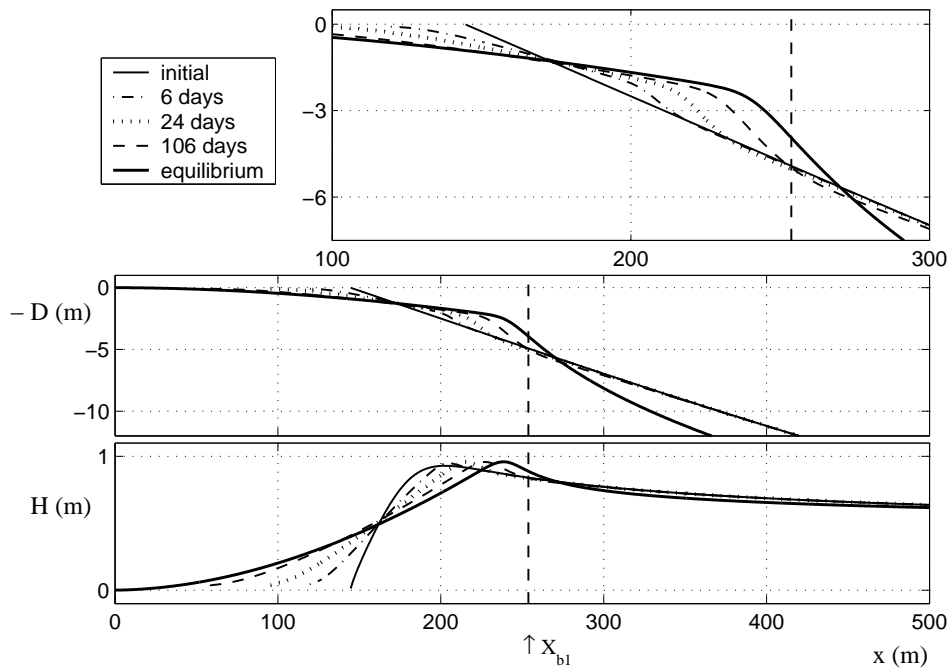
Figure 4.6.4: Example of non-linear temporal evolution of an initially 'planar beach'. Computations have been done with $p = 1$, $y_c = 0.45$, $s_0 = 0.11$ and $A = 0.46$. See the caption of Fig. 4.6.1 for more explanations. Top: Temporal evolution of the water depth, $D$. Bottom: Temporal evolution of the wave height, $H$.

On the other hand, the non-linear model has been successful in describing the onshore migration of the bars located inside the surf zone and the slow offshore migration of bars located in the shoaling zone. This is in accordance with the behaviour of shore-parallel bars in natural beaches and also with the results of other models that describe sand bar migration (Gallagher *et al.*, 1998; Plant *et al.*, 1999; Hoefel & Elgar, 2003). The model has also been able to follow the evolution of the shoreline when it has been necessary.

## 4.7   Final discussion

The main result of the present chapter is that the 'terraced profiles' described in chapter 3 turn out to be a strong attractor of the nearshore system for dissipative conditions. This fact is in accordance with preliminary results of the researchers Dr. N.G. Plant, from the Naval Research Laboratory (U.S.A.) and Dr. T.J. O'Hare, from the University of Plymouth (U.K.), who are using independently this same set of equations, but with different mathematical approaches. Their resultant profiles are always 'terraced beaches' too (personal communication by the authors). Many previous models display the same property, terraces

being obtained instead of bars, specially when realistic randomly distributed wave heights are used (Larson, 1988; Bröker *et al.*, 1992; Dean *et al.*, 1992; Thornton & Humiston, 1996; Komar, 1998; Tapia, 2003; Reniers *et al.*, 2003).

The previous considerations suggest that more attention should be paid to the existence of 'terraced profiles' in natural beaches, which are qualitatively different from 'barred profiles' (see the scheme in Fig. 1.2.3). The presence of terraces has been largely disregarded in field observations, bars being always the main protagonists. These two types of profiles has even been mistaken in the literature (Larson, 1988; Tapia, 2003; Reniers *et al.*, 2003). Besides, some 'ARGUS images' of 'terraced beaches' could be confusing because waves could break above the the terrace edge, so that the aspect of the corresponding breaking foam in a video image could be the same as if there was a shore-parallel bar. In some few cases, the formation of terraces in laboratory flumes has been reported (instead of shore-parallel bars), specially linked to randomly distributed wave height conditions (Bröker *et al.*, 1992; Dean *et al.*, 1992).

However, it is still true that 'barred beaches' with a clear trough often occur in natural beaches. One of the aims of this chapter, which has not been achieved, was to reproduce the formation of break-point bars through a 'self-organization mechanism'. This has not been possible with the simplified version of the 'breakpoint-bar interaction' included in our set of equations. Many models for cross-shore evolution suffers from the same problem, the formation of the trough at the shoreward side of the bar being hardly ever reproduced in case of randomly distributed wave height (Larson, 1988; Dean *et al.*, 1992; Thornton & Humiston, 1996; Komar, 1998; Tapia, 2003; Reniers *et al.*, 2003).

The main limitation of the linear stability analysis performed is that break-point bars are intended to be generated from equilibrium states under constant wave conditions. This idealization can hardly be fully achieved in nature because of variable wave conditions, but this approach has been the first step for trying to describing quantitatively and understanding better the 'breakpoint-bar interaction'. Another limitation of the linear model is that it is unable to allow for an evolution of the shoreline position. Using a fixed shoreline is in contradiction with the often observed bar generation events that are linked to a strong erosion of the shoreline (Komar, 1998; Short, 1999), although other reported bar generation events do not show any motion of the coastline (Larson, 1988; Bröker *et al.*, 1992; Dean *et al.*, 1992; Thornton & Humiston, 1996).

The limitations discussed so far have been partially released by building a non-linear model with the same set of equations that allows for investigating the finite amplitude temporal evolution of the system, including possible motions of the shoreline. Results have confirmed that, even in this case, bars are not reproduced by this set of equations. However, neither the dynamical evolution of states far from equilibrium conditions has been performed, nor the effect of non-steady boundary conditions has been investigated. Further research is needed into this direction, specially considering that generation events are often found under storms and that the response time of bar systems is often longer than the time over which wave conditions can be considered steady. Thus, neither the bar itself nor the underlying profile are in equilibrium with wave conditions, but the profile is probably a temporal state of the system, which permanently tries to adjust towards a moving target equilibrium (Holman & Sallenger, 1993).

On the other hand, including more physical processes in our two simplified equations could also be the way to encapsulate correctly the 'breakpoint-bar interaction'. In this respect, the first restriction of our wave transformation equation is that, due to the approximate expression we have used for the group velocity of waves (shallow water assumption), the shoaling effect is overestimated. For instance, this approximation changes the computation of the offshore part of the equilibrium profiles, systematically estimating at to high the value of the bottom slope and hence leading to water depths excessively large far offshore. An influence on the linear wave transformation equation is also expected so that the behaviour of the 'FOT problem' may be qualitatively different. An important physical process that has not been taken into account either is the time needed by the waves to react to the local changes in the bathymetry. This leads to a spatial lag between the measured and computed maximum undertow return velocities (Reniers *et al.*, 2003). The sediment transport pattern computed is different from reality if the *'wrongly computed'* local return velocities are used. However, the model by Reniers *et al.* (2003) includes this lag effect (through the introduction of a spatial weighting function in the computation of the undertow current) and the generation of the trough is not well reproduced either.

Only bedload sediment transport has been described in this work. Including suspended transport could increase the stirring magnitude, but it is not expected that it would change qualitatively the results because the final formula for the cross-shore transport would not be qualitatively different. This increase in wave stirring would enlarge the possible growth rates of the perturbations. Other important physical processes in real beaches that have not been included are the presence of longshore currents (due to oblique wave incidence), the description of wave reflection, the presence of tides, the existence of set-up/set-down in the 'mean' water level, the description of the roller dynamics during the breaking process (Reniers *et al.*, 2003)) and the interaction of the shore-parallel bars with rhythmic features, which often coexist. Some of them might have a significant effect on the generation of bars through the 'breakpoint-bar mechanism'.

Even though the present mathematical model only deals with ordinary differential equations, its discretization has not been straightforward at all. Several sources of difficulties have been found when trying to perform a suitable numerical description. Firstly, the nonlinear equations are singular at the shoreline. This causes problems both to compute the equilibrium solutions and to impose the boundary conditions for the linear stability analysis at this point. Also, large gradients in the cross-shore distribution of the equation coefficients occur in a small region close to the break-point, where we need therefore a very fine discretization. The final consequence is that we have needed a fine mesh in all the domain (which implies having a large amount of freedom degrees) in order to compute accurately both the equilibrium profiles and the linear modes (see section 4.2.2). Finding suitable boundary conditions for the offshore boundary has also been challenging in this dynamical problem. As a first step, the use of a semi-infinite domain together with a boundary condition not enough restrictive has allowed for an unphysical input of wave energy from far offshore (see appendix A). This shortcommig has been subsequently corrected by means of using a finite domain. If one aims at describing cross-shore profile processes using numerical models, a previous careful analysis of the influence of the boundary conditions and the numerical discretization used is strongly recommended.

## 4.8   Conclusions

In this chapter the sediment transport model of Plant *et al.* (2001*b*) has been used to investigate the stability of the equilibrium profiles found in chapter 3, using the same set of equations. First, a linear stability analysis of such equilibrium profiles has been done by allowing for arbitrary, small amplitude perturbations. Subsequently, the non-linear set of equations have been used to study the finite amplitude temporal evolution of different initial profiles. The main result of this chapter is that all the range of equilibrium profiles described in chapter 3 ('terraced' and 'planar') turn out to be stable both in the linear and in the non-linear regimes. Therefore, more attention should be paid to the commonly observed terraces in natural beaches as they turn out to be a strong attractor of the nearshore morphodynamical system.

The physical mechanism included in our linear and non-linear equations is a possible convergence of sediment at the 'effective break-point' of our equilibrium solutions that would be found in case a bar located at this point induced an increase in the relative wave height along all its width. Then, shoreward of the 'effective break-point' (in the surf zone), the increase in relative wave height would produce a larger effect in undertow induced transport than in onshore transport, and the contrary would apply seaward of the 'effective break-point'. Thus, bars located at this point would experience an offshore transport on their shoreward side and an onshore transport on their seaward side, so that they would grow. The plausibility that this feedback process occurs leading to the growth of an instability has been quantitatively verified with the 'Energy identity' method for the linear equations. A necessary condition (not sufficient!) for instabilities to arise in relatively 'terraced beaches' has been fulfilled.

In spite of all these considerations, the generation of break-point bars has not been found as an instability of the equilibrium profiles using this set of equations (neither linear nor non-linear). The linear model used is not able to capture the possible feedback process leading to the generation of shore-parallel bars. A 'Dirac $\delta$ instability' tries to emerge at the 'effective break-point' of the 'terraced profiles', but its growth is inhibited by the downslope transport induced by the inherent infinite slopes. The sediment transport formula by Plant *et al.* (2001*b*) only seems to show a potential source of instability if a positive perturbation of the relative wave height is found along all the width of the bar. However, this is not the case in the present wave transformation equation, so that the 'breakpoint-bar interaction' has not been well captured by the coupled model. Neither a finite amplitude model including this simplified version of the interaction has been able to reproduce the formation of shore-parallel bars. Even starting the non-linear temporal evolutions from initial states moderately far from equilibrium and allowing for a shoreline evolution, the corresponding 'terraced equilibrium profiles' are always reached. On the other hand, the finite amplitude model has been successful in describing the offshore migration of the bars located inside the surf zone and the slow onshore migration of bars located in the shoaling zone.

The idealised and semi-empirical sediment transport model coupled with a simple wave transformation equation that was presented by Plant *et al.* (2001*b*) have been carefully tested. It has shown to describe satisfactorily the main characteristics of 'planar and terraced profiles', but it has never lead to 'barred profiles'. On the other hand, the migration direction of shore-parallel bars in natural beaches is well-reproduced with this model. Althought it

has been often claimed that the 'breakpoint-bar mechanism' is responsible for the generation of shore-parallel bars, the present attempt to verify this statement quantitatively has failed. Therefore, this still remains as an important open question in the nearshore sciences.

# Chapter 5

# On the growth of oblique sand bars

## 5.1 Preliminaries

### 5.1.1 Field observations

Some natural beaches exhibit systems of several sand bars that are obliquely oriented with respect to the shore normal. The angle with the normal can range from very small values (nearly 'shore-normal bars') to very large values (nearly shore-parallel). They are often attached to the coastline by megacusps and their spacing can be quite regular. Some visual examples of oblique bar systems can be seen in Figs. 1.1.4, 1.2.9 and 1.2.11 of chapter 1. Further references on these topographic systems can be found in Sonu (1968), Komar (1998), Short (1999) and Wijnberg & Kroon (2002). Chapter 4 has been devoted to shore-parallel bars, whereas the present chapter is focused on oblique bars, the processes leading to their formation being essentially different to those related with shore-parallel bars. Most of the experimental literature on nearshore sand bars has been devoted to shore-parallel bars and so far little attention has been paid to oblique bars. Moreover, the various descriptions of oblique bars in the literature seem to deal with rather different types of bars and it is difficult to state common characteristics of these features, even from a qualitative point of view. However, table 5.1.1 presents some sites where oblique bar systems have been described, giving estimates of the hydrodynamics and the morphology.

Oblique bars can occur both in open coasts and in closed environments (for instance lakes and bays). They are hardly observed in high energy conditions since their growth seems to be related always to post-storm conditions. Some systems can be considered to occur in moderate wave energy coasts, such as the oblique bars in the Truc Vert beach, in the French Atlantic coast (site 2, see a photography of this system in Fig. 1.2.9, and further

Table 5.1.1: Field observations of oblique bar systems. Qualitative description of some beaches where these rhythmic patterns have been observed with the corresponding references. The first column describes the geographic situation of the beaches (bay, lake, gulf or open sea), which is indicative of the amount of wave energy that can reach the system. The second column deals with the relationship of the bar systems with the tidal cycle. Then, the slope and the possible existence of a previous shore-parallel bar are indicated. The observed dimensional spacings of the bar systems are called $\lambda$ and they are given in meters. The last column describes the bar orientation with respect to the longshore current. See the text for more explanations.

| Site * | Situation | Tides | Slope | Shore-parallel bar | $\lambda$ (m) | Orientation |
|--------|-----------|-------|-------|--------------------|---------------|-------------|
| 1 | Bay | Intertidal | 0.01 | Inexistent | $\sim 20$ | Oblique |
| 2 | Open | Intertidal | 0.01 | Coexistent | $\sim 400$ | Down-current |
| 3 | Open | Subtidal | 0.04 | Coexistent | $12 - 180$ | Oblique |
| 3 | Open | Subtidal | 0.02 | Coexistent | $22 - 360$ | Oblique |
| 4 | Lake | Subtidal | 0.03 | Inexistent | $30 - 120$ | Down-current |
| 5 | Open | Intertidal | 0.02 | Inexistent | $90 - 760$ | Down-current |
| 6 | Gulf | Intertidal | 0.002 | Inexistent | $65 - 220$ | Oblique |
| 7 | Gulf | Intertidal | 0.004 | Unknown | $\sim 50$ | Oblique |
| 8 | Bay | Unknown | 0.001 | Unknown | $\sim 650$ | Oblique |
| 9 | Open | Unknown | 0.004 | Inexistent | $200 - 530$ | Up-current |
| 10 | Open | Intertidal | 0.01 | Linked | $100 - 300$ | Down-current |

\* Numbers correspond with the following beaches:
1 Trabucador beach, Ebro Delta, Mediterranean coast, Spain (Falqués, 1989)
2 Atlantic coast, France (Guilcher *et al.*, 1952; Lafon *et al.*, 2002), see Fig. 1.2.9
3 Duck beach, Atlantic coast, U.S.A. (Konicki & Holman, 2000), see Fig. 1.2.11
4 Lake Michigan, U.S.A. (Evans, 1938)
5 Several Oregon beaches, Pacific coast, U.S.A. (Hunter *et al.*, 1979)
6 St. James Island, Florida, Gulf coast, U.S.A. (Niederoda & Tanner, 1970)
7 Ochlockonee Point, Florida, Gulf coast, U.S.A. (Barcilon & Lau, 1973)
8 Bethany beach, Delaware, U.S.A. (Barcilon & Lau, 1973)
9 Durras beach, New South Wales, Australia (Chappel & Eliot, 1979)
10 New South Wales, Australia (Wright & Short, 1984; Short, 1999)

details in Camenen & Larroude (1999), Michel & Howa (1999) and Lafon *et al.* (2002)). Earlier field studies describe similar oblique bar systems all along the French Atlantic coast (Guilcher *et al.*, 1952). Also the bars in the Duck beach, in the Atlantic coast of U.S.A. (site 3, see Konicki & Holman (2000), see a photography in Fig. 1.2.11) and in Oregon, in the Pacific coast of U.S.A.(site 5, see Hunter *et al.* (1979)), can be considered as growing under moderate wave energy. Examples of bars in low energy environments are those at the Trabucador beach, in the Alfacs bay of the Ebro Delta, in the Spanish Mediterranean coast (site 1, see Falqués (1989)), at Lake Michigan, in U.S.A. (site 4, see Evans (1939)) or those mentioned by Niederoda & Tanner (1970) (site 6) and Barcilon & Lau (1973) (site 7 and 8) located mostly in the Gulf coast of U.S.A. Regarding to the influence of tides, these topographic systems can be either subtidal or intertidal referring to whether the bars are permanently covered by water or if they are alternately submerged and exposed following the tidal cycle. In the latter case, they have been often called *ridge and runnel systems*

in the literature (Wijnberg & Kroon, 2002). Oblique bars are often observed in beaches with oblique wave incidence, so coexisting with longshore currents and they are sometimes reported to migrate down-flow (Komar, 1998).

Oblique bar systems emerge in quite different equilibrium beach topographies (before the growth of the features), which can be characterized by the mean slope and the presence or not of a shore-parallel sand bar. Some of them are clearly linked to a previous shore-parallel bar. This is the case of those reported by Wright & Short (1984) and Short (1999) in the 'intermediate accretionary beach states' found in several sites of the coast of Australia (site 10). Other oblique bar systems, although they coexist with shore-parallel bars, do not exhibit a special relationship with them. This is the case of those observed at Duck (see Fig. 1.2.11). There are also some complex cases such as the very persistent system observed at the Truc Vert beach, where the oblique bars are attached to the shoreline at the trough between the coast and a shore-parallel bar, which is quite further seaward and is slightly crescentic. Finally, oblique bars exist in places where there is no evidence of the presence of any shore-parallel bar. This is the case of the impressive system at Cape Cod in the Atlantic coast of U.S.A.(see a photo in Komar (1998)), the bars in the Oregon coast, the system observed in the Lake Michigan or the bars at the inner side of the Trabucador beach.

The alongshore bar spacing, $\lambda$, defined for instance as the distance between the shore attachments (i.e. between the corresponding megacusps), ranges from tens to hundreds of meters, which is also the order of magnitude of the surf zone width, $X_b$. Hino (1974) reported observed spacings scattering between 3 and 8 times $X_b$, with a mean of $4X_b$. In analysing several field data sets from the literature, Falqués *et al.* (1996) also found a relatively constant value of $\lambda \sim 1 - 6X_b$. This is remarkable accounting that the spacings ranged from 3 to $640m$. ($\lambda = 3m$. corresponding to a laboratory experiment). Often, oblique bar systems are just quasi-regular, which means that the spacing is not constant but shows quite large deviations from the mean value (see $\lambda$ in table 5.1.1). The cross-shore span of the bars is usually of the same order or smaller than the surf zone width.

The relationship between the bar orientation and the longshore current driven by the obliquely incident wave field is an open question. At some sites, the offshore end of the bar is shifted down-current with respect to the shore attachment. Evans (1939) described clearly the growth of this type of *'down-current oriented bars'*. Also the bars at the Truc Vert beach in France and at the Oregon coast are oriented down the prevailing swell from the Atlantic and the Pacific respectively. It seems, however, that the bars can orient themselves *'up-current'* too (Chappel & Eliot, 1979; Short, 1994; Konicki & Holman, 2000). In most cases, the hydrodynamics during the formation of the bars is not reported so that the bar orientation with respect to the longshore current is not known.

## 5.1.2   Previous modelling and motivation

The existing literature on nearshore morphodynamics often cite the *'forced response mechanisms'* as being the most probable responsible for the generation of nearshore rhythmic patterns (Komar, 1998; Short, 1999). This is in line with the corresponding hypothesis for shore-parallel bars that has been described in section 4.1.2. The theory for the generation of alongshore rhythmic patterns by infragravity standing waves is based on the papers by

Table 5.1.2: Previous models that predicted the generation of oblique bars and other rhythmic patterns in the nearshore using stability analysis. In the table, the first column indicates the wave incidence used in the model (normal, oblique or no waves). The second column shows the initial beach profile before the growth of the bedforms ('planar or barred beach'). Then the type of stability analysis is described (linear or non-linear). The fourth column describes what kind of rhythmic pattern was obtained . Finally, $\lambda_p$ is the predicted spacing of the modelled rhythmic pattern, where $V$ is the maximum of the longshore current, $\beta$ is the beach slope, $X_b$ is the surf zone width in case of initially 'planar beaches' and $X_c$ is the distance from the shoreline to the crest of the shore-parallel bar in case of initially 'barred beaches'.

| Ref [*] | Wave incid. | Profile | Analysis | Pattern | $\lambda_p$ |
|---------|-------------|---------|----------|---------|-------------|
| a | No waves | Plane | Linear | Shore-normal | $2\pi V^2/(g \sin\beta)$ |
| b | Oblique | Plane | Linear | Down-current | $\sim 4X_b$ |
| c | Oblique | Plane | Linear | Up-current | $\sim 6X_b$ |
| d | No waves | Plane | Linear | Shoals | $1 - 4X_b$ |
| e | Oblique | Barred | Linear | Crescentic | $8 - 15X_c$ |
| f | Normal | Plane | Linear | Crescentic | $3 - 4X_b$ |
| g | Normal | Plane | Non-linear | Crescentic | $4 - 5X_b$ |
| g | Normal | Plane | Non-linear | Shore-normal | $\sim 0.5X_b$ |
| h | Normal | Barred | Non-linear | Crescentic | $2 - 4X_c$ |

[*] Letters correspond with the following references:
a Barcilon & Lau (1973), corrected by Falqués (1991)
b Hino (1974)
c Christensen *et al.* (1994)
d Falqués *et al.* (1996)
e Deigaard *et al.* (1999)
f Falqués *et al.* (2000)
g Caballeria *et al.* (2002)
h Damgaard *et al.* (2002)

Bowen & Inman (1971) and Holman & Bowen (1982). They showed how the superposition of two or more low-frequency edge waves of the same frequency and specific mode numbers and wave lengths can generate a drift velocity pattern on the sediment capable of forming 'crescentic patterns' (in the former paper) and oblique sand bars of different shapes (in the latter paper). However, the two edge waves have to be *'phase-locked'* and the reason why this should be the case in nature is not clear (see a discussion on this in Falqués *et al.* (1996) and Short (1999)). There is also a lack of physical reasons for the selection of a certain edge wave mode and frequency in natural beaches, although some explanation can exist under certain circumstances (Short, 1999). Some attempts to verify experimentally the validity of the infragravity wave model has been presented in the past (Aagaard, 1991), but recent field observations and theoretical pieces of work discarded infragravity waves as a primary mechanism (van Enckevort, 2001; Reniers *et al.*, 2003).

Apart from the possibility that the hydrodynamical forcing by low frequency edge waves may potentially play an important role on the origin of nearshore rhythmic bars, the impor-

tance of *'self-organization mechanisms'* in the hydro- and morphodynamical coupling should not be disregarded. The hypothesis of a 'self-organization origin' of nearshore oblique bars was first proposed by Sonu (1968). Several stability analysis of the nearshore dynamical system have been performed since then. Table 5.1.2 summarizes the results of the previous models that predicted the generation of oblique bars and other rhythmic patterns using this mathematical approach.

Some different physical interactions that can account for the 'self-organization origin' of nearshore rhythmic patterns were studied and established in these works. A classification into two main groups can be done: the *'bed-flow'* and the *'bed-surf mechanisms'*. The former accounts for the interaction between the growing topographic pattern and the perturbations induced in the longshore current generated by obliquely incident breaking waves. In principle, these effects should be similar to the ones leading to the growth of alternate bars in rivers and shoreface-connected sand ridges in the continental shelf (without wave effects). However, the growing shoals in the surf zone do not only produce a deflection of the current but also a modification of the incident wave field (for instance, of the breaking intensity). This effect, hereinafter referred to as 'bed-surf interaction', is usually mixed with the 'bed-flow coupling', but it can occur in isolation in case of wave incidence perpendicular to the coast.

The paper by Barcilon & Lau (1973) presented a first theoretical model where 'shore-normal bars' stemmed from an instability of the longshore current due to the morphodynamical coupling ('bed-flow interaction'). While that work was certainly pioneering, their results are invalidated by a mathematical error (Falqués, 1991). The initial approach of Barcilon & Lau (1973) was further pursued in a systematic way for the wave-driven longshore current by Falqués *et al.* (1996). Several instability modes were found with $\lambda$ ranging between $1 - 4X_b$. They can be described more appropriate as alternating shoals and troughs, reminiscent of alternate and multiple free bars in rivers, rather than nearshore oblique bars. None of these models described the waves explicitly, but they just used an analytical formulation for the longshore current. The 'bed-surf interaction' in case of normal wave incidence was studied in detail in Falqués *et al.* (2000) and Caballeria *et al.* (2002). These papers presented the first linear and non-linear stability analysis (respectively) of the nearshore system in case of waves arriving perpendicularly to the shore. They showed that the 'bed-surf interaction' may result in the formation of 'crescentic patterns' of $\lambda \sim 4X_b$ (alternating shoals and troughs at both sides of the mean breaking line) and of 'shore-normal bars' of a much smaller spacing $\lambda \sim 0.5X_b$.

Hino (1974) was the first to perform a morphodynamical stability study accounting for both the 'bed-flow' and the 'bed-surf interactions' at the same time (using oblique wave incidence). His analysis predicted the growth of shoals and troughs similar to oblique bars ('down-current oriented') with an alongshore spacing of about $4X_b$. In spite of the success of his model, the parameterisations of the wave field and sediment transport were not very realistic and the numerical solution procedure had a low resolution. In fact, later research by Christensen *et al.* (1994) was not able to reproduce the results of Hino in the appropriate limiting case. This latter paper presented an instability analysis accounting for both the 'bed-flow and bed-surf effects' in much more realistic conditions and with a robust numerical solution procedure. 'Up-current oriented bars' with a spacing of about $6X_b$ were obtained. However, a number of aspects of the theoretical approach of Christensen *et al.* (1994) deserve

further attention.  Firstly, the orientation of the modeled bars is at odds with the most
often observed 'down-current orientation'.  Secondly, as we will show in the present thesis,
nearshore morphodynamics is very sensitive to the sediment transport formulation so a more
transparent and realistic formulation should be adopted.  Thirdly, the physical processes
behind the instability were not investigated in depth.  Finally, their results relied only on
the dominant instability mode.  Describing the whole manifold of unstable modes is very
important with regard to a future non-linear stability analysis or even if one thinks of the
externally forced problem.  It is well known that the behaviour of a forced system may be
dominated by free modes which are not the dominant ones in the free behaviour analysis
(Marqués & Lopez, 2000; Lopez & Marqués, 2000).

All the modelling studies mentioned above deal with instabilities of an equilibrium state
with a monotone beach profile, i.e without shore-parallel bars.  The first similar analysis done
in case of an initially 'barred beach profile' (with a shore-parallel bar) is that of Deigaard
*et al.* (1999).  This paper predicted a modification of the shore-parallel bar leading to a
kind of 'crescentic longshore bar', but it did not explain the growth of oblique bars (even
for waves approaching obliquely).  The second published work on stability analysis of an
initially 'barred beach' can be found in Damgaard *et al.* (2002) (using normal wave incidence
and performing a non-linear analysis).  The resultant topography was again a 'crescentic
longshore bar'.  In this latter paper, the authors mention the 'bed-surf interaction' as the
main physical mechanism behind the instability.  More recent publications about generation
of 'crescentic bars' from initially alongshore uniform 'barred profiles' are those by Calvete
*et al.* (2003), Caballeria *et al.* (2003) and Reniers *et al.* (2003).

### 5.1.3   Aim, approach and outline of the chapter

The main objective of this chapter is to gain understanding about the origin of oblique bar
systems (and in a lower degree of 'crescentic longshore bars').  To this end, the morpho-
dynamical linear stability analysis of a long rectilinear coast is revisited in case of oblique
wave incidence.  The hypothesis that the formation of rhythmic sand bars might result from
a 'self-organization process' is again assumed.  A quantitative description of the underly-
ing growing mechanisms would allow for understanding better why, how and under what
conditions oblique bars grow.  The initial beach profile is a monotone sloping beach (i.e.
without shore-parallel bars), similar to the profiles found in chapter 3.  This is linked with
a secondary aim of this chapter, which is checking the stability of these type of 'non-barred
equilibrium profiles' when allowing for variations in the alongshore direction.

To attain these goals, a theoretical formulation for the sediment transport by relatively
depth-uniform 'mean' currents is here coupled with the time and depth-averaged hydrody-
namical equations describing fluid mass and momentum conservation.  The most simple set
of equations that still encapsulates the processes responsible for the generation of oblique
bars is used.  To this end, several different parameterisations of the sediment transport by
depth-uniform currents are used, each of them being dominant under certain hydrodynam-
ical conditions.  The effect on the final equations of the filtered fast processes (for instance
wave oscillatory motions and turbulence) and the possible vertical stratification are again
parameterised when necessary.  The transformation of wave properties along the nearshore
is very crudely described.  The strongest hypothesis of the hydrodynamical equations is that

the refraction of waves due to the growing topographic patterns is not considered. Moreover, waves are assumed to be regular and monochromatic, their shoaling process seaward of the breaking line is not considered and the breaking is described with the 'saturated surf zone assumption'. Two more working hypothesis are the shallow water wave kinematics approximation for computing the group velocity and the small incidence angle assumption. The wave-current interactions are also not included and the possible effect of the low-frequency hydrodynamical oscillations is neglected. This latter assumption is set forth in order to isolate the 'self-organization interactions' between the sandy bottom and the high-frequency waves and 'mean' currents. The interactions of the potential growing features with both the oblique wave field and the corresponding generated longshore current are therefore described. The emphasis is placed in an exploration of different possible sediment transport conditions and in the physical mechanisms for growth that may dominate under these different conditions. In the study presented here both 'up-current' and 'down-current oriented bars' can potentially be obtained and an explanation for this behaviour may be given. The mathematical tool used is a linear stability analysis of the set of equations, which gives the spatial cross-shore structure, the growth rate and the migration celerity of each 'normal mode'. Another improvement with respect to previous theories is that not only the dominant growing mode but the whole manifold of 'normal modes' are investigated.

Section 5.2 presents the governing equations of the problem, which follows from the formulation presented in chapter 2. The equilibrium solution of the equations, which is used as a reference basic state, is presented in section 5.3. Then the theoretical setting of the morphodynamical linear stability analysis is described (section 5.4). The numerical results of the linear stability analysis found for the different 'sediment transport modes' are presented in section 5.5. The physical origin of the instability along with the reason for both possible bar orientations are investigated in section 5.6. A comparison with natural morphological patterns and some discussion are given in section 5.7. The main conclusions of the chapter are presented in section 5.8.

## 5.2 Formulation of the general model

In this morphodynamical linear stability analysis we account for nearshore horizontal patterns growing from a reference topography which is alongshore uniform and unbounded (see Fig. 5.2.1). The $y$ axis is chosen to coincide with the rectilinear coastline, the cross-shore and the vertical coordinates are $x$ and $z$, running seaward and upward, respectively.

### 5.2.1 Hydrodynamical equations

Fluid motion is described by means of imposing water mass and momentum conservation. The *'shallow water hypothesis'* presented in section 2.3 is again asserted, so that the depth- and time-averaged versions of the equations are used (Eqns. 2.3.1 and 2.3.2). We rewrite them here because of their importance for this chapter,

$$\frac{\partial D}{\partial t} + \nabla (D\vec{v}) = 0 \;\; , \tag{5.2.1}$$
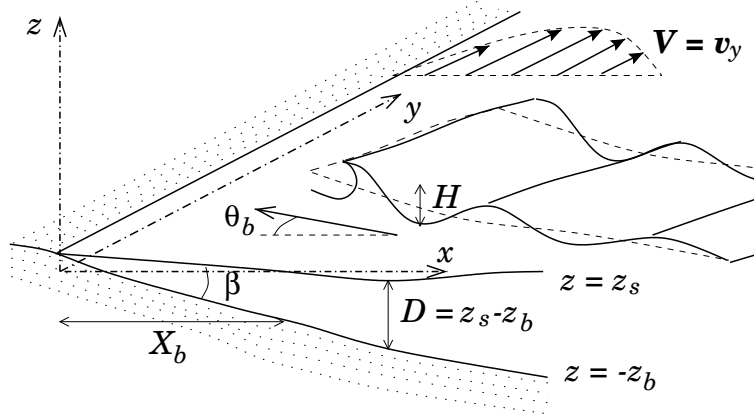
Figure 5.2.1: Coordinate system and reference basic state from which oblique bars can grow due to instability. The dynamical system is the surf zone forced by obliquely incident waves. The basic state is characterized by a uniform longshore flow, $v_y = V$, free surface, $z_s$, and bottom surface, $z_b$, where total depth is $D = z_s - z_b$.

$$\frac{\partial v_i}{\partial t} + v_j \frac{\partial v_i}{\partial x_j} = -g \frac{\partial z_s}{\partial x_i} - \frac{1}{\rho D} \frac{\partial (\mathcal{S}'_{ij} - \mathcal{S}''_{ij})}{\partial x_j} - \frac{\tau_{bi}}{\rho D} \quad , \quad i = 1, 2 \quad , \tag{5.2.2}$$

where $\vec{v} = (v_1, v_2)$ is the depth-averaged horizontal velocity, $x_1 = x$, $x_2 = y$ and repeated indexes are implicitly summed over for $j = 1, 2$. The total water depth is $D = z_s - z_b$, where the 'mean' free surface elevation is $z_s$ and the bottom level is $z_b$. The small scale processes accounting for the bottom friction, $\tau_{bi}$, the wave radiation stress tensor, $\mathcal{S}'$, and the Reynolds turbulence stress tensor, $\mathcal{S}''$, must be parameterised. As we are interested in using the simplest hydrodynamical description that can drive the sediment transport in a sensible way, a number of simplifications have been made to describe the small scale processes. For instance, we use systematically the *'very shallow water assumption'* and the *'small wave incidence angle approximation'*, which have been presented in section 2.2.1.

The wave radiation stress tensor, $\mathcal{S}'$, is computed from the linear wave theory and the final expression we use is Eq. (2.2.21), which is obtained using the Snell's law for the refraction of the waves by the alongshore uniform constant sloping beach used as reference basic state (Eq. 2.2.17). In principle, the wave energy, $E$, should be described by a certain wave evolution equation such as Eq. (2.3.3). However, as a first step we use a much simpler description. Firstly, wave height of the incidence wave field is supposed to be regular instead of randomly distributed. Secondly, we use the *'saturated surf zone assumption'* inside the surf zone, $H = \gamma_b D$ (where $\gamma_b$ is the breaking index). Replacing this latter expression for $H$ into the formula for the total energy (Eq. 2.2.10), the expression for the radiation stress tensor becomes

$$\mathcal{S}'_{11} = \frac{3}{16} \rho g (\gamma_b D)^2 \quad , \qquad \mathcal{S}'_{22} = \frac{1}{16} \rho g (\gamma_b D)^2 \quad , \tag{5.2.3}$$

$$\mathcal{S}'_{12} = \mathcal{S}'_{21} = -\frac{1}{8} \rho g (\gamma_b D)^2 \sqrt{\frac{D}{D_b}} \sin\theta_b \quad ,$$

where $D_b$ and $\theta_b$ are the water depth and the wave incidence angle at the breaking line, respectively. Finally, wave forcing is neglected out of the surf zone, $\partial \mathcal{S}'_{ij}/\partial x_j \simeq 0$, which means that the wave height is supposed to be constant there, without any shoaling. The validity of all these assumptions will be examined in the discussion of this chapter (section 5.7.3).

The bottom shear stress is parameterised using Eq. (2.3.23). This equation is met using the hypothesis of small incidence angle and strong orbital velocity with respect to the 'mean' currents. The bottom shear stress turns out to be proportional to the 'mean' flow through a coefficient that depends on the wave orbital velocity, $u_o$, and the drag coefficient, $c_d$. Using Eq. (2.2.9) for the wave orbital velocity and the saturated surf zone assumption described above, Eq. (2.3.23) reads

$$\frac{\tau_{b1}}{\rho\,D} = \frac{2\,c_d\,\gamma_b\,\sqrt{g}}{\pi\,\sqrt{D}}\,v_1 \quad , \qquad \frac{\tau_{b2}}{\rho\,D} = \frac{c_d\,\gamma_b\,\sqrt{g}}{\pi\,\sqrt{D}}\,v_2 \quad . \tag{5.2.4}$$

The turbulence Reynolds stress is computed with the depth-averaged eddy viscosity approach presented in Eq. (2.3.4). The eddy viscosity, $\nu_t$, is computed following Longuet-Higgins (1970) (Eq. 2.3.6) inside the surf zone, so that the final expression for the turbulence Reynolds stress in this region is

$$\mathcal{S}''_{ij} = \rho\,N\,x\,\sqrt{g}\,D^{3/2}\left(\frac{\partial v_i}{\partial x_j} + \frac{\partial v_j}{\partial x_i}\right) \quad , \qquad i,j = 1,2 \quad , \tag{5.2.5}$$

where $N$ is the turbulence parameter. Out of the surf zone, $\nu_t$ has an exponential decay.

## 5.2.2  Alongshore sediment transport and bed evolution

The total sediment transport in the nearshore can be written as an addition of three terms: the contribution of the relatively depth-uniform 'mean' currents, $\vec{q}_v$, the transport by waves, $\vec{q}_w$, and the downslope gravity transport, $\vec{q}_g$ (see Eq. 2.5.1). In case of alongshore uniformity and an equilibrium situation, the cross-shore component of the depth-averaged 'mean' current, $v_1$, and its contribution to the sediment transport, $q_{v1}$, vanish (due to the conservation of water mass in this direction). The balance between the other two transport contributions in the cross-shore direction ($\vec{q}_w$ and $\vec{q}_g$) leads to a certain equilibrium beach profile (found imposing $q_x = 0$, as in the analysis presented in chapter 3). Using the expression in Eq. (2.5.22) for the gravity transport, this balance between the cross-shore components of the sediment transport read

$$q_w\,\frac{k_x}{k} = S_g\,\frac{dz_b^o}{dx} \quad . \tag{5.2.6}$$

where $z_b^o$ is the bottom level of the corresponding equilibrium profile and $\vec{k}$ is the wave number, which indicates the direction of wave propagation.

Out of equilibrium, the dynamics of the cross-shore profiles ('2D dynamics') can lead to the formation and migration of terraces and shore-parallel sand bars (this has been the focus of chapter 4). The dynamical evolution of these features is typically slower than the dynamics of the '3D features' we pretend to describe in the present chapter (Ruessink et al.,

2000; Plant *et al.*, 2001*b*). This allows us to assume that when alongshore inhomogeneities develop, the possible unbalance in the transport directly related to waves can be neglected in comparison with the transport driven by the generated relatively depth-uniform 'mean' currents. This assumption essentially means that the *'2D morphodynamics is frozen'*, while we look at the dynamics in a horizontal plane ($q_w$ is assumed to be given by Eq. (5.2.6) and it is not perturbed). This makes sense as long as the two time scales are disparate. Moreover, wave-driven cross-shore currents (undertow) are usually weaker than longshore currents and rip currents. It seems that even small amplitude topographic irregularities can drive a quite strong horizontal circulation. This is so, for instance, in case of 'shore-normal bars' in low energy environments (Niederoda & Tanner, 1970). In fact, all the morphodynamical stability analysis of the nearshore presented so far (see table 5.1.2) have been implicitly based on this assumption for the sediment transport due to waves.

Using Eqns. (2.5.22) and (5.2.6) for the wave and the gravity transport, the general definition of the total sediment transport in the nearshore (Eq. 2.5.1) leads to

$$\vec{q} = \vec{q}_v - S_g \, \nabla z_b + S_g \, \nabla z_b^o \quad . \tag{5.2.7}$$

Taking into account that the total bottom level is $z_b = z_b^o(x) + h(x,y,t)$, where $h$ is the deviation of the bottom level from the equilibrium profile, we arrive at the following expression for the sediment transport,

$$\vec{q} = \vec{q}_v - S_g \, \nabla h \quad . \tag{5.2.8}$$

Therefore, the study presented in this chapter is based on the transport of sand due to the depth-averaged 'mean' currents, $\vec{q}_v$, together with a gravity contribution. This latter term comes from the unbalance between the wave-driven transport of the equilibrium situation and the downslope gravity transport.

The sediment transport related to relatively depth-uniform currents in the presence of waves can be parameterised using the Bailard formulation, which has been presented in section 2.5. This model leads to a sum of terms of the form $\alpha_m(u_o) \, |\vec{v}|^{m-1} \, \vec{v}$ with several exponents, $m = (1, 3, 4)$, each one being dominant in different hydrodynamical and sediment transport conditions. Bedload transport gives $m = 3$ in the *'strong current limit'* and $m = 1$ in the *'weak current limit'* (see Eq. 2.5.10). Suspended transport gives $m = 4$ in the 'strong current limit' (Eq. 2.5.16) and $m = 1$ in the 'weak current limit' (Eq. 2.5.17). The term $\alpha_m$ is called *'wave-stirring function'* and it changes in the different sediment transport conditions, always being a function of the wave orbital velocity and several constants. The final sediment transport formula used in the present chapter is

$$\vec{q} = \alpha_m(u_o) \, |\vec{v}|^m \left( \frac{\vec{v}}{|\vec{v}|} - \gamma \, \vec{\nabla} h \right) \quad . \tag{5.2.9}$$

Each combination of $m$ and $\alpha_m$ is representative of certain hydrodynamical and sediment characteristics and it is called *'sediment transport mode'*. We study the effect of these single terms in isolation instead of the complete Bailard formula (which is given by their addition), in order to get better insight into the physical mechanisms governing under each 'sediment transport mode'.

The coefficient $\gamma$ in the gravity term of Eq. (5.2.9) comes from the ratio $S_g(u_o, v) \, / \, \alpha_m(u_o)$ for each 'sediment transport mode' (see Eq. 5.2.8). Different expressions for $S_g$ have been

described in section 2.5.7, this coefficient being always a function of $u_o$ and $\vec{v}$. For instance, Bailard's parameterisation for bedload sediment transport in the 'strong current limit' gives $\gamma \sim (\tan\phi)^{-1}$, where $\phi$ is the angle of repose of the sediment. This expression results from the first term in Eq. (2.5.24) divided by the first term of Eq. (2.5.10). More variability can be expected in case of suspended load, including a certain cross-shore distribution related with the wave orbital velocities and $|\vec{v}|$. In the 'weak current limit' $\gamma$ would be proportional to $u_o^2 / (|\vec{v}| \, w_s)$ (obtained from the second term in Eq. (2.5.25) divided by Eq. (2.5.17)). In the 'strong current limit', $\gamma$ would depend on $|\vec{v}| / w_s$ (from the second term in Eq. (2.5.24) divided by Eq. (2.5.16)). In both cases, one may infer that the quantity $\gamma$ is zero at the shoreline and increases in the offshore direction until it reaches a maximum around the breaking point and then decreases again (both $|\vec{v}|$ and $u_o$ show this type of behaviour). From a physical point of view, the gravity term in Eq. (5.2.8) accounts for the tendency of the bottom irregularities to smooth out if they do not cause positive feedback into the flow due to downslope gravitational transport. The coefficient $\gamma$ is therefore named *'morphodynamical diffusivity'*.

The divergence of the sediment transport gives the time evolution of the bottom level. This is described by means of imposing the conservation of sediment mass, which has been derived in section 2.4 (Eq. (5.2.10)). The expression is reproduced here (with $p$ being the porosity),

$$(1-p)\frac{\partial z_b}{\partial t} + \nabla \cdot \vec{q} = 0 \ . \tag{5.2.10}$$

## 5.2.3 Scaling and parameter setting

Before solving the dynamical equations, the variables are scaled to deal with non-dimensional equations. Dimensionless quantities are indicated by an asterisk $^*$ in the next definitions

$$x = L_h \, x^* \quad , \quad D = L_v \, D^* \quad , \quad \vec{v} = U \, \vec{v}^* \quad , \quad Q = Q_o \, Q^* \quad , \quad t = T_m \, t^* \ . \tag{5.2.11}$$

Table 5.2.1 shows the definitions and the default values of the scales used in this problem. The natural horizontal length scale is the width of the surf zone, $L_h = X_b$, and the vertical length scale is an approximation of the equilibrium water depth at the breaking point, $L_v = X_b \beta$. Fluid velocities are normalized with the maximum longshore current magnitude in the equilibrium situation (which was predicted by Longuet-Higgins (1970)),

$$U = \frac{5 \, \pi \, \gamma_b}{16 \, c_d} \, \beta' \, \sqrt{g \, \beta' \, X_b} \, \sin\theta_b \quad , \tag{5.2.12}$$

where $\theta_b$ is the wave incidence angle at the breaking line, $\gamma_b$ is the breaking coefficient and $\beta' = 8\beta / (8 + 3\gamma_b^2)$ is the *'effective beach slope'* that takes into account the set-up of the 'mean' water level found in the equilibrium situation. The computation of both $U$ and $\beta'$ will be made in the following section.

An estimate of $Q_o$ can be obtained by using Bailard's parameterisation for suspended load in the 'weak current limit' (Eq. 2.5.17), together with the 'small wave incidence angle approximation',

$$Q_o = \frac{\epsilon_s \, c_d}{s \, g \, w_s} \frac{16 \, U_o^3}{3 \, \pi} \, U \quad , \tag{5.2.13}$$

Table 5.2.1: Scaling constants chosen for analysing this problem.  Their default values are obtained with the following values of the parameters:  $\beta = 0.01$, for the beach constant slope, $c_d = 0.001$, for the drag coefficient, $\theta_b = 5^o$, for the wave incidence angle at the breaking line, $\beta' = 8\beta / (8 + 3\gamma_b^2) = 0.008$, for the 'effective beach slope', $\gamma_b = 0.8$, for the breaking coefficient, $\epsilon_s = 0.01$, for the efficiency in 'suspended transport mode', $\rho = 1000\,Kg/m^3$, for the water density, $\rho_s = 2500\,Kg/m^3$, for the sediment density, $s = (\rho_s - \rho)/\rho = 1.5$, for the relative density and $\mu = 1/(1 - p) = 2$, with $p = 0.5$ being the porosity.  See the text for the derivation of these expressions.

| Scale | Definition | Default value |
|-------|------------|---------------|
| $L_h$ | $X_b$ | $100\,m.$ |
| $L_v$ | $X_b\,\beta$ | $1\,m.$ |
| $U$ | $\frac{5\,\pi\,\gamma_b}{16\,c_d}\,\beta'\sqrt{g\,\beta'\,X_b}\,\sin\theta_b$ | $1.5\,m/s.$ |
| $Q_o$ | $\frac{5\,\epsilon_s\,g}{24\,s\,w_s}\,\gamma_b^4\,(\beta'\,L_v)^{(3/2)}\,\sqrt{X_b}\,\sin\theta_b$ | $30\,m^2/\mathrm{day}$ |
| $T_m$ | $\frac{L_v\,L_h}{\mu\,Q_o}$ | $1.5\,\mathrm{days}$ |
| $T_h$ | $\frac{L_h}{U}$ | $1.5\,\mathrm{min.}$ |

where $\epsilon_s$ is the efficiency for suspended load transport, $s = (\rho_s - \rho)/\rho = 1.5$, is the relative density of the sediment, $w_s$ is the fall celerity of the sediment and $U_o$ is the scale of the wave orbital velocity.  This latter quantity can be computed following the 'very shallow water assumption' (Eq. 2.2.9),

$$U_o = \frac{\gamma_b}{2}\sqrt{g\,L_v}\ .\qquad\qquad(5.2.14)$$

Replacing the two velocity scales $U_o$ and $U$ in Eq. (5.2.13), an estimate of the sediment transport magnitude is obtained,

$$Q_o = \frac{5\,\epsilon_s\,g}{24\,s\,w_s}\,\gamma_b^4\,(\beta'\,L_v)^{(3/2)}\,\sqrt{X_b}\,\sin\theta_b\ .\qquad\qquad(5.2.15)$$

In case of using the 'strong current limit', the expression $16\,U_o^3\,/\,3\,\pi$ in Eq. (5.2.13) has to be replaced by $U^3$ (see Eq. 2.5.16).  The resultant expression is similar to Eq. (5.2.15) but with its right hand side multiplied by $3\,(\sin\theta_b\,\beta')^3\,/\,c_d^3$.  This can lead to a larger $Q_o$ by a factor 8 in case of $\theta_b = 10^o$.

Two time scales emerge in a natural way in this problem.  The hydrodynamical time scale, $T_h = X_b/U$, follows from scaling the three hydrodynamical equations.  The morpho-dynamical time scale, $T_m$, results from scaling the bed evolution equation.  This latter time scale is the one chosen to normalize the time variable and it is obtained by setting the order

of magnitude of all the terms in Eq. (5.2.10) to 1, which leads to

$$T_m = \frac{L_v \, L_h}{\mu \, Q_o} \quad , \tag{5.2.16}$$

where $\mu = 1/(1-p)$, with $p = 0.5$ being the porosity, and $Q_o$ is the characteristic magnitude of the sediment flux. As a general estimate, we replace the expression for $Q_o$ given by Eq. (5.2.15) into Eq. (5.2.16) to obtain the following morphological time scale,

$$T_m = \frac{24 \, s \, w_s}{\mu \, 5 \, \epsilon_s \, g \, \beta \, \beta' \, \gamma_b^4 \, \sin\theta_b} \quad , \tag{5.2.17}$$

having in mind that in the 'strong current limit' this would be multiplied by the expression $c_d^3 \, / \, 3 \, (\sin\theta_b \, \beta')^3$. For instance, the morphological time would be a factor 8 smaller in case of $\theta_b = 10^o$.

Introducing the dimensionless variables into Eqns. (5.2.1), (5.2.2) and (5.2.10) and also in the parameterisations used (Eqns. 5.2.3, 5.2.4, 5.2.5 and 5.2.9), we arrive at a set of dimensionless non-linear equations that are not explicitly written here. Some new parameters emerge in a natural way in these equations,

$$r = \frac{c_d}{\beta} \quad , \qquad F^2 = \frac{U^2}{g \, \beta \, X_b} \quad \text{and} \qquad \epsilon = \frac{T_h}{T_m} \quad ,$$

where $F$ is the Froude number, which controls the terms that depend on the free surface elevation, $r$ is the frictional parameter (instead of $c_d$), which controls the normalized friction terms and $\epsilon$ is the ratio of time scales. Using the definition for the scaling constants presented in table 5.2.1, the Froude number turns out to be a dependent parameter, $F = F(r, \theta_b, \gamma_b)$, and the ratio of time scales is found to be much smaller than one, $\epsilon \ll 1$. This latter result would allow for applying the 'quasi-steady hypothesis', by which the explicit time derivatives could be neglected in the hydrodynamical equations ($\epsilon \simeq 0$). However, in the present model we have kept the terms proportional to $\epsilon$ for the sake of completeness.

The next step is finding the range of physically realistic values for the independent parameters of the model: $\theta_b$, $r$, $N$, $\gamma_b$, $\gamma$, $m$ and $\alpha$. The wave incidence angle, $\theta_b$, has been varied from $1^o$ to $35^o$. Larger angles are not usually found in the surf zone due to the topographic refraction by the sloping beach (Falqués, 2003). Besides, our model would fail with these larger angles (due to the 'small wave incidence angle approximation' used). Typical values of the drag coefficient for the bottom friction and the mean beach slope can be taken from the literature, $c_d = (0.0005 - 0.02)$ and $\beta = (0.001 - 0.05)$ (for instance see Dodd *et al.* (1992)). This could give in principle a wide range for the friction parameter, $r = c_d/\beta$. Nevertheless, coarse sediment (large $c_d$) is normally related to steep beaches (large $\beta$). The result is that $r$ can be considered to range only from 0.1 to 1. According to Longuet-Higgins (1970), the turbulence parameter is set to $N = (0.001 - 0.01)$. The breaking index has been fixed to $\gamma_b = 0.8$ which is a common value for regular waves, as can be found in Horikawa (1988).

A default value $\gamma = 1$ has been used for the 'morphodynamical diffusivity'. Bailard's parameterisation for bedload sediment transport gives exactly this value ($\gamma \sim (\tan\phi)^{-1}$, see section 5.2.2). Some cross-shore variability is expected in case of suspended load but typical values are also of the order of 1. In the present work this quantity is set constant for the

sake of simplicity, as in many other morphodynamical problems. Sensitivity analysis with respect to values ranging from 0.1 to 10 has been performed. Some discussion about the influence of a 'morphodynamical diffusivity' with a certain cross-shore structure is found in Falqués *et al.* (2000).

Following Bailard's parameterisation for the sediment transport, three different powers of the current, $m = (1, 3, 4)$, have been considered in Eq. (5.2.9). In the 'limit of weak current' with respect to wave orbital velocity, the term with the exponent $m = 1$ is dominant. The name *'wave-dominated beaches'* hereinafter refers to this situation. The exponents $m = 3$ or $m = 4$ are representative of the 'strong current limit' (with respect to wave orbital motion), for bedload and suspended load respectively. This situation is referred to as *'current-dominated beaches'*. Two different parameterisations for the 'wave stirring function' $\alpha$ have been used. As was found in case of normal wave incidence (Falqués *et al.*, 2000), the most relevant characteristic of the 'wave stirring function' (from a morphodynamical point of view) is whether the gradient of the ratio, $\alpha/D$, where $D$ is the total water depth, is directed shoreward (case a) or seaward (case b) inside the surf zone. This behaviour will be also corroborated by the results described in the present chapter. The ratio $\alpha/D$ is called *'potential wave stirring'*. A shoreward directed 'potential wave stirring' (case a) is represented by a uniform 'stirring function' ( $\alpha(x) = const.$ ), whereas a stirring increasing quadratically inside the surf zone ( $\alpha(x) = D(x)^2$ ) and uniform beyond the breaking line is representative of case (b). No important differences are expected using other descriptions of $\alpha$ as long as $\alpha/D$ displays the two described behaviours.

From a physical point of view, case (b) characterizes beaches dominated by wind/swell waves and suspended transport, so that the 'wave stirring' is expected to increase seaward with the wave height up to the breaking line. For instance, Bailard's parameterisation in case of suspended load and 'weak current limit' ($m = 1$) predicts an $\alpha$ function which depends on $u_o^3 \sim D^{3/2}$ (see Eq. 2.5.17), so that $\alpha/D$ increases seaward. The computations have been actually done with $\alpha \sim D^2$ but no important difference are expected as long as $\alpha/D$ increases offshore. When there is a significant low frequency wave energy, there can be an associated 'wave stirring' in the inner surf zone, close to the coast. In this case, the $\alpha$ function would be more or less uniform in the cross-shore direction (case a). Different options, but with a seaward decreasing $\alpha/D$, are not expected to produce big changes either. Finally, a constant $\alpha$ has been mainly used in case $m = 3, 4$ since this is the case in the Bailard's parameterisation for strong current with respect to the orbital velocity (Eqns. 2.5.10 and 2.5.16).

## 5.3   Solution of the equilibrium equations

The linear stability approach to the formation of bars by 'self-organization' starts by defining a basic or reference state where bars are not present. This is an equilibrium (i.e. steady) and alongshore uniform state that results from applying equilibrium conditions to the dynamical equations of the problem.

The topography of the basic state is given by an imposed equilibrium beach profile, $z_b = z_b^o(x)$, which is supposed to come from the balance between the transport by waves

and the gravity contribution (Eq. 5.2.6). Because of the assumption of 'frozen 2D dynamics' used in this chapter (see section 5.2.2), checking $q_x(x) = 0$ to seek for the basic topography does not make sense. Thus, any $z_b^o(x)$ profile could be adopted if it is not far from the observed profiles in nature. As described in chapter 3, these tend to be upward concave, but very often with a gently sloping terrace along the surf zone. Therefore, a constant sloping beach with a suitable $\beta$ is sensible as basic topography, ($z_b^o(x) = -\beta x$ in dimensional variables, see Fig. 5.2.1). The validity of this assumption will be discussed in section 5.7.3.

Obliquely incident waves generate a longshore current, $\vec{v} = (0, V(x))$, (due to the momentum conservation in the alongshore direction) and an elevation of the 'mean' free surface, $z_s = z_s^o(x)$ (due to the momentum conservation in the cross-shore direction). As we have used the same parameterisations as Longuet-Higgins (1970) for the small scale processes, the equilibrium state is given by the analytical solution described in that paper. The computation is as follows. Using the non-dimensional variables $z^* = z/L_v$ and $x^* = x/L_h$ given by Eq. (5.2.11), the cross-shore contribution of Eq. (5.2.2) inside the surf zone ($x < X_b$) is

$$0 = -\frac{\partial z_s^{o*}}{\partial x^*} - \frac{3\,\gamma_b^2}{8}\frac{\partial D_o^*}{\partial x^*} \tag{5.3.1}$$

Integrating this simple equation we obtain an analytical expression for the dimensionless equilibrium free surface elevation for $x < X_b$,

$$z_s^{o*}(x) = -\frac{3\,\gamma_b^2}{8 + 3\,\gamma_b^2}\,x^* \quad, \tag{5.3.2}$$

which consists of the well-known set-up due to the decrease of wave radiation stress due to breaking. Since wave forcing has been neglected out of the surf zone no set-down has been obtained there. Remember that regular waves assumption leads to a single breaking line, $x = X_b$. The validity of such approximations will be analysed in the discussion of the present chapter (section 5.7.3). Using Eq. (5.3.2) and the basic topography $z_b^{o*}(x) = -x^*$, the dimensionless total equilibrium water depth becomes

$$D_o^*(x) = \frac{8}{8 + 3\,\gamma_b^2}\,x^* \;. \tag{5.3.3}$$

Out of the surf zone ($x > X_b$), there is no forcing, $\partial \mathcal{S}'_{ij}/\partial x_j \simeq 0$, because we have neglected the wave shoaling. Therefore, the cross-shore contribution of Eq. (5.2.2) in this region gives $D_o^*(x) = D_o^*(X_b)$. Recovering the dimensional quantities is done by means of multiplying by the scales in Eq. (5.2.11). For instance, from Eq. (5.3.3) the dimensional water depth is $D_o(x) = \beta\,X_b\,D_o^*(x) = \beta'\,x$. Thus, the final 'effective beach slope' taking into account the set-up, $\beta' = 8\,\beta\,/\,(8 + 3\,\gamma_b^2)$, is smaller than the topographic slope, $\beta$.

Before solving the alongshore momentum equation, one can infer from the mass conservation (Eq. 5.2.1) that the depth-averaged velocity only have a contribution in the alongshore direction in the equilibrium situation, $\vec{v}^o = (0, V)$. Taking this into account, replacing the total basic water depth obtained in the previous paragraph, $D_o = \beta'\,x$, and using non-dimensional variables, the alongshore contribution of Eq. (5.2.2) reads

$$0 = -\frac{V^*}{\sqrt{x^*}} + \sqrt{x^*} + \frac{1}{x^*}\frac{\partial}{\partial x^*}\left(\frac{N\,\beta'\,\pi}{c_d\,\gamma_b}x^{*2}\sqrt{x^*}\frac{\partial V^*}{\partial x^*}\right) \quad. \tag{5.3.4}$$
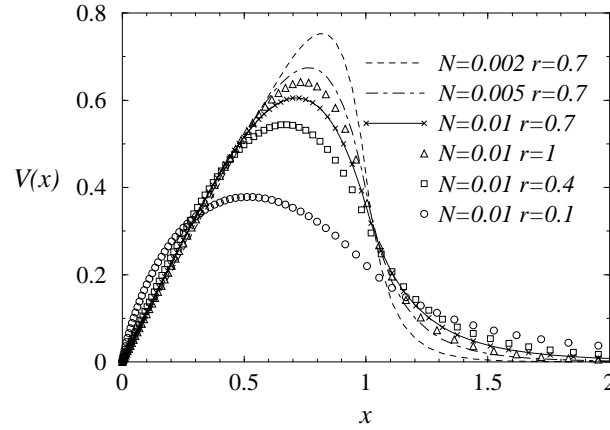
Figure 5.3.1: Effect of the bottom friction and the turbulence parameters $(r, N)$ on the cross-shore distribution of the basic longshore current. All the variables are non-dimensional, with $x = 1$ being the surf zone width and $V = 1$ being the maximum longshore current without turbulence.

The solution of this equation leads to the Longuet-Higgins' velocity profile,

$$V^* = \begin{cases} b_1 \, x^{*\,p_1} + b_3 \, x^* & , \quad 0 < x^* < 1 \\ b_2 \, x^{*\,p_2} & , \quad x^* > 1 \end{cases} \quad , \tag{5.3.5}$$

with

$$
\begin{aligned}
p_1 &= -\tfrac{3}{4} + \left(\tfrac{9}{16} + \tfrac{1}{P}\right)^{1/2} \;, & p_2 &= -\tfrac{3}{4} - \left(\tfrac{9}{16} + \tfrac{1}{P}\right)^{1/2} \;, \\
b_1 &= \left(P\,(1 - p_1)\,(p_1 - p_2)\right)^{-1} \;, & b_2 &= \left(P\,(1 - p_2)\,(p_1 - p_2)\right)^{-1} \;, \\
b_3 &= \left(1 - \tfrac{5}{2}P\right)^{-1} \;, & P &= \tfrac{N\,\beta'\,\pi}{c_d\,\gamma_b} \;.
\end{aligned}
$$

The dynamics of the basic longshore current is then governed by the parameter $P$, which depends on the friction and turbulence parameters $P = P(r, N)$. We assume $P < \frac{2}{5}$ (see the book by Horikawa (1988) for more details). Figure 5.3.1 shows the dependence of the normalized longshore current, $V^*(x^*)$, on $r$ and $N$. Remember that the dimensional longshore current is recovered by means of multiplying by the velocity scale in Eq. (5.2.11), $V = UV^*$, with $U$ given in table 5.2.1. When the dissipation due to turbulence decreases (smaller $N$), the cross-shore distribution of the longshore current becomes sharper, with a stronger gradient at the breaking line. The limiting solution when $N = 0$, is very simple,

$$V^* = \begin{cases} x^* & , \quad 0 < x^* < 1 \\ 0 & , \quad x^* > 1 \end{cases} \quad . \tag{5.3.6}$$

The effect of friction is more complicated because the parameter $c_d$ is found both in the normalized solution for $V^*$ and in the scaling factor $U$. Decreasing friction leads to a larger $U$ together with a less peaked $V^*$. The final effect is the intuitive decrease in the magnitude of the dimensional velocity, $V$.

## 5.4 Formulation of the linear stability analysis

### 5.4.1 Linearized equations

Equations (5.2.1), (5.2.2) and (5.2.10), together with the parameterisations used (Eqns. 5.2.3, 5.2.4, 5.2.5 and 5.2.9), define a dynamical system of four equations for the unknowns $\vec{v}$, $z_s$ and $z_b$. Once the equilibrium or basic state has been computed, the stability analysis can be applied in a standard way. A small perturbation assumed to be periodic in time and in the alongshore coordinate is added to this basic state,

$$(v_1, v_2, z_s, z_b) = (0, V(x), z_s^o(x), z_b^o(x)) + e^{i(\kappa y - \omega t)}\, (u(x), v(x), \eta(x), h(x)) \quad, \qquad (5.4.1)$$

where $V(x)$ is the equilibrium longshore current, $z_s^o(x)$ is the equilibrium free surface elevation and $z_b^o(x)$ is the bottom level. The solution for these three equilibrium quantities has been given in the previous section. The linear variables $(u(x), v(x), \eta(x), h(x))$ could be complex magnitudes and contain the cross-shore distribution of the perturbations of the four variables of the system. The linear variable $h$ is defined in such a way that a positive value means a crest and a negative value refers to a trough. This definition is different from the one used for the perturbation of the water depth in the previous chapter (see section 4.2.1). The complex frequency, $\omega = \omega_r + i\omega_i$, describes again the feedback in this system. It is important to remark that the dependence of the variables $(v_1, v_2, z_s, z_b)$ on the frequency is also different from the definition used in the previous chapter (see again section 4.2.1). In the present chapter, the perturbations will grow if $\omega_i > 0$ and decay if $\omega_i < 0$. The possible migration of the perturbations in the alongshore direction is described by $\omega_r$. The assumption of periodicity in the alongshore direction and of exponential dependence on time is not restrictive because, as the coefficients of the resultant linearised system do not depend on $y$ and $t$, any solution can be expanded as a sum or an integral of this type of solutions. A last remark is that the introduced wave number describes the spacing in the alongshore direction, $\kappa = \kappa_y$.

The linearised equations are obtained by means of replacing Eq. (5.4.1) into the governing Eqns. (5.2.2) (5.2.1) and (5.2.10) and keeping only the linear terms. Using the dimensionless variables defined in section 5.2.3 (Eq. 5.2.11), but skipping the asterisks $^*$ for simplicity, we arrive at the following set of dimensionless linearised equations,

$$-i\,\omega\,\epsilon\,u = -\frac{d\eta}{dx} - i\,\kappa\,V\,u - \frac{2\,r\,\gamma_b}{\pi F}\,\frac{u}{\sqrt{D_o}} - \frac{3\,\gamma_b^2}{8}\left(\frac{d\eta}{dx} - \frac{1}{F^2}\frac{dh}{dx}\right) +$$

$$+ \frac{i\,\kappa\,5\,\gamma_b^2\,\sin\theta_b}{16}\sqrt{\frac{D_o}{D_{ob}}}\left(\eta - \frac{h}{F^2}\right) + \vartheta_x \quad, \qquad (5.4.2)$$

$$-i\,\omega\,\epsilon\,v = -i\,\kappa\,\eta - i\,\kappa\,V\,v - \frac{dV}{dx}\,u + \frac{r\,\gamma_b}{\pi F}\left(\frac{V\,(F^2\,\eta - h)}{2\,D_o^{3/2}} - \frac{v}{\sqrt{D_o}}\right) -$$

$$- \frac{i\,\kappa\,\gamma_b^2}{8}\left(\eta - \frac{h}{F^2}\right) + \frac{5\,\gamma_b^2\,\sin\theta_b}{16}\sqrt{\frac{D_o}{D_{ob}}}\left(\frac{d\eta}{dx} - \frac{1}{F^2}\frac{dh}{dx}\right. +$$

$$\left. + \frac{1}{2\,D_o}\frac{dD_o}{dx}\left(\eta - \frac{h}{F^2}\right)\right) + \vartheta_y \quad, \qquad (5.4.3)$$

$$-i\,\omega\,\epsilon\,(F^2\,\eta - h) = -\frac{d(D_o\,u)}{dx} - i\,\kappa\,D_o\,\upsilon - i\,\kappa\,V\,(F^2\,\eta - h)\quad, \tag{5.4.4}$$

$$-i\,\omega\,h = \alpha'\,\gamma'\,V^m\left(\frac{d^2h}{dx^2} - \kappa^2 h + \frac{m}{V}\frac{dV}{dx}\frac{dh}{dx}\right) - \frac{d\alpha'}{dx}\,V^m\left(\frac{u}{V} - \gamma'\,\frac{dh}{dx}\right) -$$
$$- \alpha'\,V^{m-1}\left(\frac{u}{V}\frac{dV}{dx}\,(m-1) + i\,\kappa\,m\,\upsilon + \frac{du}{dx}\right)\quad, \tag{5.4.5}$$

where the momentum mixing terms read

$$\vartheta_x = \frac{2}{F}\frac{d\nu'}{dx}\frac{du}{dx} + \frac{\nu'}{F}\left(2\frac{d^2u}{dx^2} - \kappa^2\,u + i\,\kappa\,\frac{d\upsilon}{dx} + \frac{2}{D_o}\frac{dD_o}{dx}\frac{du}{dx}\right)\quad, \tag{5.4.6}$$

$$\vartheta_y = \frac{1}{F}\frac{d\nu'}{dx}\left(\frac{d\upsilon}{dx} + i\,\kappa\,u\right) + \frac{\nu'}{F}\left(\frac{d^2\upsilon}{dx^2} - 2\,\kappa^2\,\upsilon + \frac{1}{D_o}\frac{dV}{dx}\frac{d(F^2\,\eta - h)}{dx} +\right.$$
$$\left.+ i\,\kappa\,\frac{du}{dx} + \frac{1}{D_o}\frac{dD_o}{dx}\left(\frac{d\upsilon}{dx} + i\,\kappa\,u - \frac{1}{D_o}\frac{dV}{dx}\,(F^2\,\eta - h)\right)\right)\quad. \tag{5.4.7}$$

The parameters that control the dynamics of these linearised equations have already been described in section 5.2.3, except for three modified parameters. The 'morphodynamical diffusivity' has been corrected with the slope, $\gamma' = \beta\,\gamma$. A new nondimensional eddy diffusivity appears, $\nu' = N\,x\,\sqrt{D_o}$, and $\alpha'$ is the 'wave stirring', $\alpha$, normalized with the scale for the sediment transport, $Q_o$. This stirring function has not been perturbed in the equations, i.e. it has been kept equal to its value for the equilibrium solution. Moreover, the refraction of the waves by the varying topography has only been accounted for in the computation of the equilibrium state (through the Snell's law given by Eq. (2.2.17)). As a first step, the modifications of wave refraction due to bathymetric perturbations are neglected in the present work because of the inherent difficulties of using the Eikonal equation (Eq. 2.2.25). The implications of this latter assumption are explained in section 5.7.3.

The final set of linear dimensionless equations defines a boundary value problem of 3 parabolic equations of second order in the derivatives and 1 first order equation. Therefore, we need 2 boundary conditions for three of the variables and 1 condition for the other. On the other hand, these same equations applied at the coastline become of first order in the derivatives so that they can be used as 3 'well-posed' mixed boundary conditions at $x = 0$ (this is found by replacing $V(0) = \nu'(0) = 0$ in Eqns. (5.4.2)-(5.4.7)). The perturbations are imposed to be zero far offshore ($\vec{v}(\infty) = \vec{0}$ , $\eta(\infty) = 0$ and $h(\infty) = 0$) because we are again interested in the solutions that describe the internal dynamics of the surf and shoaling zones, with no external forcing (apart from the steady high-frequency wave input).

The linear equations presented in this section describe the dynamics of our system in case of dealing with a *'fixed breaking line*, defined as $x = X_b$. But even at first order of the development, the perturbations in water depth due to the growing patterns result in a displacement of the breaking line position. The reason is that waves tend to break in a more seaward position if there is a growing shoal close to the equilibrium breaking line and in a more shoreward position if there is a deepening trough around there. This effect has

been considered in the present study because earlier pieces of work found that it can have a strong potential influence (Falqués *et al.*, 2000). A description of the complete formulation used in order to account for a *'variable breaking line'* is given in appendix C. The final linearised governing equations consist not only of the differential Eqns. (5.4.2)-(5.4.5) but also of the two integro-differential Eqns. (C.6) and (C.7).

Finally, a powerful tool to interpret the results of this linear stability analysis is the *'FOT problem'*, which has already been presented in section 4.2.1. In this case, it consists in solving only the three hydrodynamical Eqns. (5.4.2)-(5.4.4), together with the two integro-differential Eqns. (C.6) and (C.7) for a given topographic perturbation $h$ (which is artificially fixed).

## 5.4.2   Numerical method and solution procedure

The boundary value problem given by Eqns. (5.4.2)- (5.4.5) are numerically solved using a spectral method similar to the one used for solving the linearised equations in the previous chapter (see section 4.2.2). As we have already explained the details of the application of this spectral method in that section, only the most important steps and the main differences are herein underlined. The linear variables have already been expanded in Fourier polynomials in the alongshore direction (see Eq. 5.4.1). This can not be done in the cross-shore direction because the coefficients of the equations depend on $x$. The linear variables are then expanded in $N$ Chebyschev polynomials in the cross-shore direction (similarly to Eq. (4.2.5)). The main difference with the expansion described in the previous chapter is that the numerical freedom degrees of the present model are $N$ because we do not impose any specific boundary condition for the variables at the coastline (see the previous section). The basis used is then a combination of Chebyschev polynomials different from the one given in Eq. (4.2.7). Like the present linear variables, the new basis must vanish only at the offshore boundary, so that it reads

$$g^n(x) = T^n(x) + (-1)^{n+1} \quad , \qquad n = 1, ..., N \quad . \tag{5.4.8}$$

The coordinate $x \, \epsilon \, (0, x_{off})$ is the cross-shore coordinate that we are using in the present problem.

After introducing into the four linear differential equations the expansions of the linear variables and their spatial derivatives in terms of the basis $g^n(x)$ (Eqns. 4.2.5 and 4.2.12), a set of algebraic equations for the coefficients of the expansions are obtained. The collocation method is again used, which means that the equations are imposed at the $N$ Gauss-Lobatto collocation points $(x_j \, , \, j \, = \, 1, ..., N)$ (which have first undergone the two transformations given by Eqns. (4.2.9), (4.2.8) and (4.2.10)). We then arrive at an eigenproblem for each alongshore wave number $\kappa$ of the form

$$\sum_{m=1}^{4N} \mathcal{J}_k^m \, \Psi_m = \omega \sum_{m=1}^{4N} \mathcal{L}_k^m \, \Psi_m \quad , \qquad k = 1, ..., 4N \quad . \tag{5.4.9}$$

This eigenproblem is solved numerically with a standard method.

The eigenvalue, $\omega = \omega_r + i \, \omega_i$, gives the complex frequency of each eigensolution, while the eigenfunction, $\Psi_m = (u_n, v_n, \eta_n, h_n)$, contains the 4 sets of $N$ coefficients of the Chebyschev

expansions. Thus, the eigenfunction gives the cross-shore structure of the corresponding pattern and the eigenvalue indicates its dynamics. The new matrices $\mathcal{J}_k^m$ and $\mathcal{L}_k^m$ contain the values of the coefficients of the 4 linear equations at the $N$ transformed collocation points. The complex frequency $\omega$ has been defined different in this chapter (see Eq. 5.4.1), so that the growth rate of the eigenfunctions is now given by $\omega_i$. In this case, $\omega_i > 0$ means growth and $\omega_i^{-1}$ gives the corresponding e-folding growth time. The migration celerity of the emerging topographic pattern is $c_m = \omega_r / \kappa$ and their alongshore spacing is $\lambda = 2\pi / \kappa$. The final total solution for the linear variables corresponding to a particular eigensolution are then obtained from

$$v_1(x, y, t) = \mathcal{A}\,\Re e \left\{ e^{i\,(\kappa\,y - \omega\,t)} \sum_{n=1}^{N} u_n\, g^n(x) \right\}\ , \tag{5.4.10}$$

$$v_2(x, y, t) = V(x) + \mathcal{A}\,\Re e \left\{ e^{i(\kappa\,y - \omega\,t)} \sum_{n=1}^{N} v_n\, g^n(x) \right\}\ , \tag{5.4.11}$$

$$z_s(x, y, t) = z_s^o(x) + \mathcal{A}\,\Re e \left\{ e^{i(\kappa\,y - \omega\,t)} \sum_{n=1}^{N} \eta_n\, g^n(x) \right\}\ , \tag{5.4.12}$$

$$z_b(x, y, t) = z_b^o(x) + \mathcal{A}\,\Re e \left\{ e^{i(\kappa\,y - \omega\,t)} \sum_{n=1}^{N} h_n\, g^n(x) \right\}\ , \tag{5.4.13}$$

where $\mathcal{A}$ is again an arbitrary amplitude that can not be determined by a linear stability analysis.

Given a set of physical parameter values and a wave number $\kappa$, as many eigensolutions as discretization freedom degrees are obtained from the eigenproblem ($4N$, see Eq. 5.4.9). However, only a few of them are physical, which means being sensible and independent of numerical parameters. The types of tests performed to verify the reliability of the final *'physical solutions'* are similar to the ones described in sections 4.2.3 and 4.2.4. The present dynamical problem turns out to be much more convergent than the linear stability analysis presented in the previous chapter (see section 4.2.3). The numerical discretization used herein shows to be well-conditioned and accurate. The only important numerical parameter is now the number of collocation points $N$. A value of $N = 120$ guarantees numerical relative errors in the growth rates of less than 1%. This time, a semi-infinite domain is always used ($b = 1$ in Eq. (4.2.10)). All the solutions presented in the following chapter always display good numerical convergence. Verifying the physical sensibility of the processes behind these numerically convergent solutions will be done in section 5.6, by means of a deep understanding of each growing mechanism.

The growth rate curves that will be shown in the following section contain the positive and convergent $\omega_i$ of the 'physical eigensolutions' for different values of the wave number, $\kappa$. The dispersion curves show the corresponding $\omega_r$ as a function of $\kappa$. Hereinafter we refer to each 'physical eigensolution' as a *'cross-shore normal mode'* (or simply as a *'normal mode'*) because it contains the cross-shore structure of the modes. Remember that the alongshore distribution of the modes are simply sinusoidal waves characterized by a certain $\kappa$. Several convergent 'cross-shore modes' can be obtained for a certain set of parameter values and they are referred to as modes $[1, 2, 3, ...]$, according to the maximum magnitude of their growth rate, from large to small. The pattern associated to the wave number with the maximum

growth rate for the mode 1 (referred to as $\kappa_M$ and $\omega_{iM}$ respectively) would initially amplify the fastest so that it would determine the initial aspect of the beach and the dominant wave length. These are the eigenfunctions we will show by default. There can also be secondary modes that have different cross-shore structures than the dominant one. In order to obtain the final dimensional value of the outputs of the model, the non-dimensional spacing, $\lambda$, has to be multiplied by $X_b$, the non-dimensional e-folding growth time, $\omega_i^{-1}$, has to be multiplied by $T_m$ and the migration celerity, $c_m$, by $X_b/T_m$ (the scaling constants have been shown in table 5.2.1).

The 'FOT problem' is again solved with a spectral method. The main difference is that we are dealing now with a system of 3 equations and 3 variables. The final set of discretized equations for the $3N$ coefficients of the basis expansions define now a set of $3N$ algebraic linear equations of the form,

$$\sum_{m=1}^{3N} \mathcal{M}_k^m \, \Phi_m = \mathcal{N}_k \quad , \qquad k = 1, ..., 3N \quad . \tag{5.4.14}$$

The new matrices $\mathcal{M}_k^m$ and $\mathcal{N}_k^m$ contain the coefficients of the three hydrodynamical equations computed for the imposed arbitrary perturbation of the topography, $h$. The vector $\Phi_m = (u_n, v_n, \eta_n)$ contains the coefficients of the Chebyschev expansions of the three hydrodynamical variables. This system of algebraic linear equations is again solved with standard numerical techniques.

## 5.5   Results of the linear stability analysis
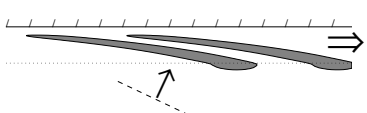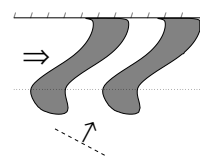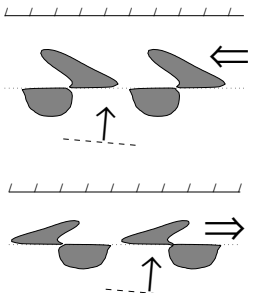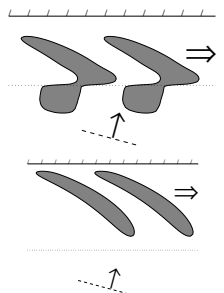
### 5.5.1   General description

Three different types of rhythmic patterns have been found: 'very oblique down-current oriented bars', 'up-current oriented bars' and 'crescentic/down-current oriented bars'. The key point that switch from one type of pattern to another is mainly the 'sediment transport mode' ($m$ and $\alpha$). The wave incidence angle, $\theta_b$, has also a noticeable effect on the results. Table 5.5.1 summarizes the various topographic patterns obtained as a function of these three parameters.

### 5.5.2   Very oblique down-current oriented bars

In case of 'current-dominated beaches' ($m = 3, 4$) and for any 'wave stirring function', a system of 'very oblique down-current oriented bars' emerges for $\theta_b > 5^o$. The spacing is several times the surf zone width and the angle of orientation of the bars with respect to the shore normal is about $80^o$.

A typical example of dispersion line and growth rate curve for this case is shown in Fig. 5.5.1. As it can be observed, there exist more than one instability mode. The whole

Table 5.5.1: Summary of the different topographic features obtained as a function of the 'sediment transport mode' and the wave incidence angle. In the pictures included in this table, the big double arrow indicates the direction of bar migration. The dashed line and the arrow perpendicular to it indicate the direction of wave incidence. The breaking line is represented with a pointed line parallel to the shoreline.

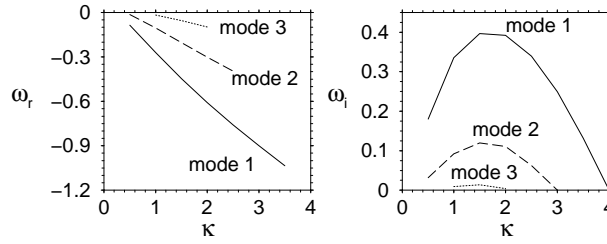| $\theta_b$ | $1 - 5^o$ | $5 - 15^o$ | $15 - 35^o$ |
|---|---|---|---|
| **m=3,4**  any $\alpha$ | STABILITY | **Very oblique down-current**  $\lambda \sim 2 - 6X_b$ | |
| **m=1**  $\alpha = $ const | STABILITY | **Up-current**  $\lambda \sim 0.5 - 1.5X_b$ | |
| **m=1**  $\alpha = $ quadr | **Crescentic**  $\lambda \sim 1.5 - 2X_b$ | **Down-current**  $\lambda \sim 1 - 1.5X_b$ | STABILITY |

Figure 5.5.1: Dispersion line and growth rate curve for $m = 3$ and uniform $\alpha(x)$. Parameter values are: $\theta_b = 20^o$, $r = 0.7$, $\gamma_b = 0.8$, $\gamma = 1$ and $N = 0.01$. All the variables are non-dimensional. The values for the maximum growth rate, $\omega_{iM} = 0.40$, and the corresponding wave number, $\kappa_M = 1.75$ and frequency, $\omega_{rM} = -0.53$, of the first mode are extracted from this graph.

pattern migrates down-stream and it is almost non dispersive ($\omega_r$ is proportional to $\kappa$). The ratio between the period and the growth time is $2\pi\omega_i / \omega_r \sim 4$ so the bars grow faster than they move. Nearly all the quantities and graphs shown in this section are non-dimensional. Remember that the corresponding dimensional values must be computed by means of multiplying by the corresponding scales (see table 5.2.1). The topography and flow perturbations corresponding to the wave number with maximum growth rate for the two first modes can be seen in Fig. 5.5.2. One may see that the sequence of modes corresponds to a structure of super-harmonics: the number of crests and troughs at any particular cross-shore section increases with the mode number. In order to see the real aspect of the beach, the equilibrium basic state should be added (a constant sloping bottom and the basic longshore current, see Eqns. (5.4.10)-(5.4.13)). As an example, Fig. 5.5.3 shows the total topography for the first mode. These 3D graphs are the only ones given in dimensional quantities throughout all the section. Remember that the amplitude $\mathcal{A}$ in Eqns. (5.4.10)-(5.4.13) is arbitrary since it can not be determined by a linear stability analysis. It is chosen in order to produce a realistic aspect of the final topography, where the bars are noticeable. The perturbations in the flow cause a meandering and an acceleration/deceleration of the basic longshore current.

The obtained bedform shape is robust under changes of $\theta_b$, $r$, $N$ and $\gamma$. Only the maximum growth rate, $\omega_{iM}$, the corresponding wave number, $\kappa_M$, and the migration celerity, $c_M$, depend on these parameters. Figure 5.5.4 shows the dependence of these three quantities on $\theta_b$ and $r$ for the first mode. As it can be seen, $\omega_{iM}$, $\kappa_M$ and $c_M$ increase with $r$ and $\theta_b$, positive growth rates being obtained only in case of $\theta_b > 5^o$. The number of secondary modes also increases with $\theta_b$ and $r$. Their shape and dynamics depend on these parameters similarly to those of the dominant mode. Figure 5.5.4 also shows that, in the studied range of parameters, $\kappa_M$ ranges from 1 to 3. This means that the alongshore spacing of the bars ranges from 2 to 6 times the surf zone width. The maximum growth rate, $\omega_{iM}$, goes from 0.1 to 1 and $c_M$ is in between 0.1 and 0.5. Remember that all the quantities given so far in this section are non-dimensional. The corresponding dimensional values will be given in section 5.5.6 using a reasonable estimate for the morphological time scale.
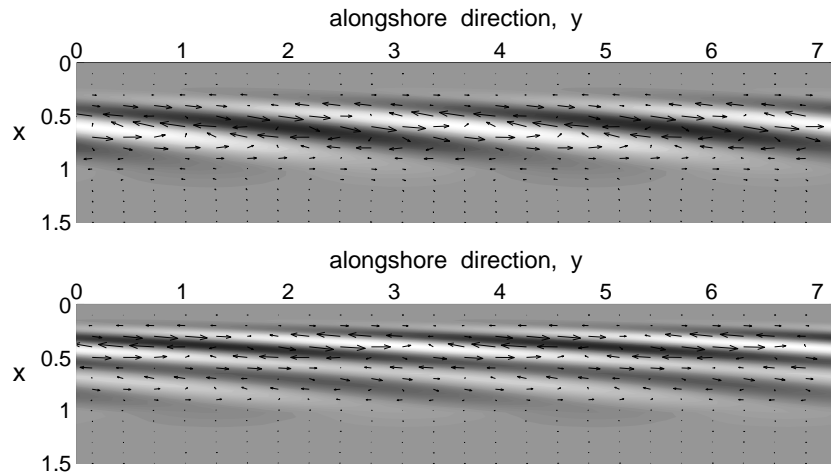
Figure 5.5.2: Example of a 'very oblique down-current oriented bar system'. Non-dimensional topography and current perturbations corresponding to the maximum wave number of mode 1 (top) and mode 2 (bottom) in case of $m = 3$ and uniform $\alpha(x)$. These eigensolutions correspond to the instability curves shown in Fig. 5.5.1. The alongshore direction, $y$, is on the horizontal axis while the vertical axis is the cross-shore direction, $x$, running seaward. All the variables are non-dimensional, $x = 0$ being the coastline and $x = 1$ the breaking line. White areas correspond to crests and dark areas to pools. To see the real aspect of the beach, the basic state should be added (a constant sloping bottom and the basic longshore current). Remember that the amplitude of the perturbations is arbitrary since it can not be determined by a linear stability analysis. Waves come from the bottom left corner so the longshore current goes from left to right. Then, the perturbations in the flow would cause a meandering and acceleration/deceleration of the longshore current.

The turbulence parameter, $N$, and the 'morphodynamical diffusivity', $\gamma$, have a clear damping role on the instability. Increasing $N$ smooths the gradients in the horizontal current field that are coupled to this pattern (see Fig. 5.5.2). However, the growth is never totally suppressed within the realistic range of values of $N$. In contrast, there is a critical value of $\gamma$ above which the alongshore uniform beach is stable, $\gamma_c \simeq 3$. Another interesting finding is that, even though small values of the diffusive parameters give rise to quite long wave lengths of the topographic patterns, for $\gamma = 0$ or $N = 0$ there is still a dominant wave length (i.e. a maximum in the instability curve). This is in contrast with many morphodynamical stability studies (Schielen *et al.*, 1993; Hulscher, 1996; Falqués *et al.*, 1996; Calvete *et al.*, 2001) and in accordance with Deigaard *et al.* (1999). It is interpreted as a result of including 'bed-surf interaction', which was not taken into account in the former papers. A typical example of the flow structure coupled to the growth of these bars is shown in Fig. 5.5.2. Strong gradients in the current field seem to be necessary, the longshore current decelerating at the crests of the bars and accelerating at the troughs. One may also observe the slight onshore deflection of the longshore current on the crests and the offshore deflection at the troughs.
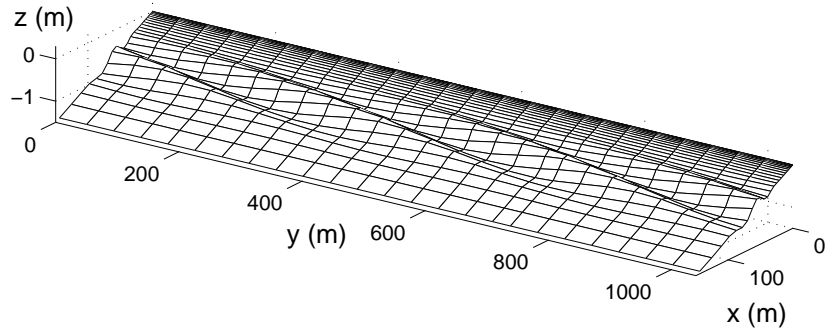
Figure 5.5.3: Final aspect of the beach in case of 'very oblique down-current oriented bars'. Dimensional total topography (obtained from Eq. (5.4.13)) corresponding to the maximum wave number of mode 1 in case of $m\!=\!3$ and uniform $\alpha(x)$. This example corresponds to the solution shown in Fig. 5.5.2. Here, the variables have been made dimensional, using $X_b = 100m$. and $\beta = 0.01$. The amplitude of the linear solutions can not be determined by a linear stability analysis. The amplitude $\mathcal{A}$ in Eq. (5.4.13) has been chosen in order to produce a realistic aspect of the final topography. The alongshore direction is $y$, the cross-shore direction is $x$, running seaward, and the vertical direction is $z$, running upwards.
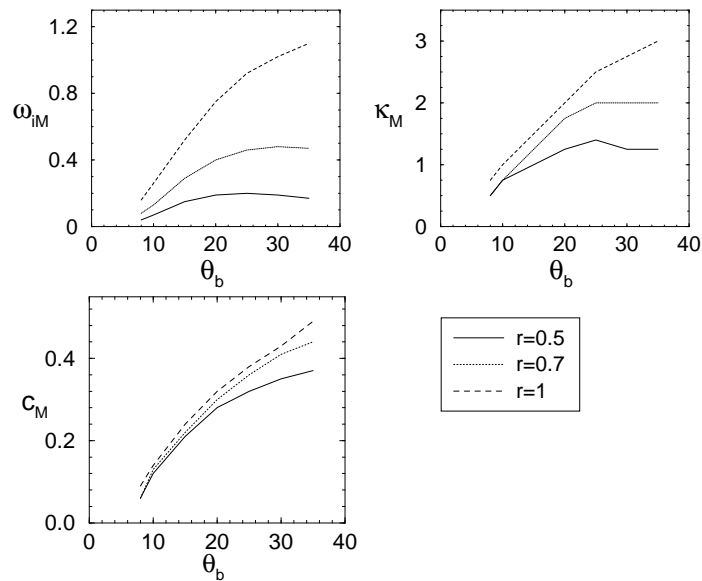


Figure 5.5.4: Effect of the wave incidence angle and the bottom friction on the maximum growth rate, wave number and migration celerity of mode 1 in case of $m\!=\!3$ and uniform $\alpha(x)$.
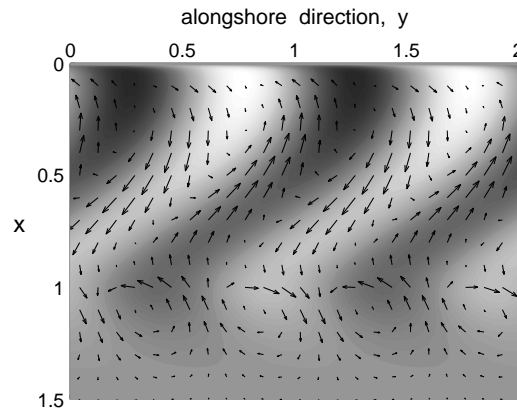
Figure 5.5.5: Example of a 'up-current oriented bar system'. Non-dimensional topography and current perturbations corresponding to the maximum wave number of the dominant mode in case of $m=1$ and uniform $\alpha(x)$. The graph description is the same as in Fig. 5.5.2.

## 5.5.3   Up-current oriented bars

In case of 'wave-dominated beaches' ($m=1$) the two different used 'wave stirring functions' lead to different solutions. A uniform stirring across the surf zone leads to the generation of 'up-current oriented bars' if $\theta_b > 5^o$. They display an angle of orientation of about $50^o$ with respect to the shore normal and their alongshore spacing is of the order of the surf zone width.

An example of the non-dimensional topography and flow perturbation patterns associated to this mode for the dominant wave number in a typical case is shown in Fig. 5.5.5. Figure 5.5.6 displays the total topography corresponding to this solution using dimensional quantities (obtained from Eq. (5.4.13)). The shape is reminiscent of the large scale 'shoreface-connected sand ridges' on the shelf, reported in Calvete *et al.* (2001). A distinctive feature is a shoal that grows at the seaward end of each crest, probably due to the 'bed-surf interaction', which is obviously not present in the case of the shelf ridges. The corresponding growth rate and dispersion curves can be seen in Fig. 5.5.7. Secondary modes are very scarce for this 'sediment transport mode'. The bars migrate down-stream and they are again nearly non dispersive (except for very large wave lengths). For the maximum amplified pattern, the ratio between the period and the growth time is $2\,\pi\,\omega_i\,/\,\omega_r \sim 1.6$.

Figure 5.5.8 shows the dependence of $\omega_{iM}$, $\kappa_M$ and $c_M$ on $\theta_b$ and $r$ for the first mode. When $\theta_b \rightarrow 0^o$, $\omega_{iM}$ drops to zero quickly, so these bars develop only for relatively oblique wave incidence, for $\theta_b$ above some $5^o$. This is consistent with the fact that in case of $\theta_b = 0^o$ instability was not found for this 'sediment transport mode' (Falqués *et al.*, 2000). On the other hand, for more oblique incidence ($\theta_b > 20^o$), $\omega_{iM} \rightarrow 1$. The alongshore spacing ranges from 0.5 to 1.5 times the surf zone width, since $\kappa_M$ goes from 4 to 12. The non-dimensional migration celerity increases in magnitude with $\theta_b$. Now, the shape of the pattern is rather
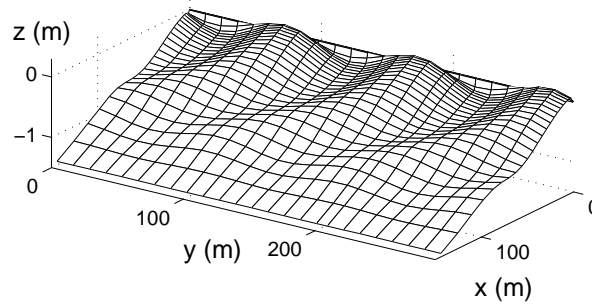
Figure 5.5.6: Final aspect of the beach in case of 'up-current oriented bars'. Dimensional total topography (obtained from Eq. (5.4.13)) corresponding to the maximum wave number of mode 1 in case of $m = 1$ and uniform $\alpha(x)$. This example corresponds to the solution shown in Fig. 5.5.5. The graph description is the same as in Fig. 5.5.3.
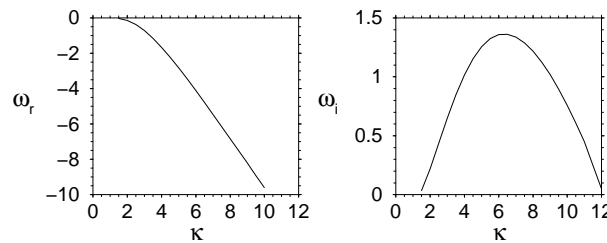


Figure 5.5.7: Dispersion line and growth rate curve for $m = 1$ and uniform $\alpha(x)$. These are the instability curves that correspond to the eigensolution shown in Fig. 5.5.5. Parameter values are: $\theta_b = 20^o$, $r = 0.7$, $\gamma_b = 0.8$, $\gamma = 1$ and $N = 0.01$. All the variables are non-dimensional. As it can be seen $\omega_{iM} = 1.36$, $\kappa_M = 6.25$ and $\omega_{rM} = -4.45$.

sensitive to $r$, specially because of the changes produced by this parameter in the longshore current profile. When $r$ is small, the longshore current is smooth (see Fig. 5.3.1) and the pattern grows close to the shore. Increasing $r$ also increases slightly $\kappa_M$ and $c_M$, whereas $\omega_{iM}$ decreases. Again, $N$ and $\gamma$ have a diffusive damping role. The flow pattern coupled to the growth of these bars is characterized by an offshore deflection of the longshore current at the crests and an onshore deflection at the troughs (see Fig. 5.5.5).

## 5.5.4   Crescentic/down-current oriented bars

Results are more rich in case of a 'stirring function' increasing quadratically with the water depth from the shoreline up to the breaking line and constant beyond, which is also realistic in case of 'wave-dominated beaches' ($m = 1$). There is instability only for incidence angles below some $10^o - 15^o$. When $\theta_b$ ranges from $3^o$ to $15^o$, the 'fastest growing mode' can be
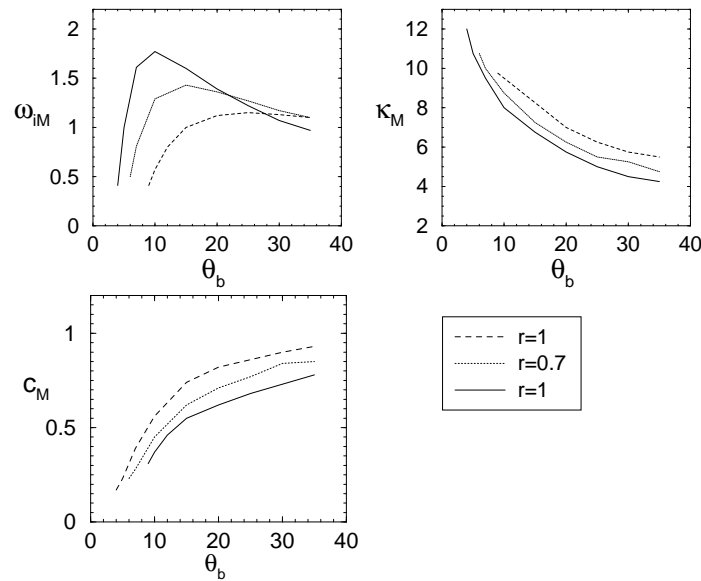
Figure 5.5.8: Effect of the wave incidence angle and the bottom friction on the maximum growth rate, wave number and migration celerity in case of $m=1$ and uniform $\alpha(x)$.

defined as a 'crescentic/down-current oriented bar system'. It consists of alternating shoals and troughs at both sides of the breaking line with the inner shoals being bar-shaped and oblique to the coast. These inner bars are 'down-current oriented', with an angle with the shore normal of some $60^o$, and their spacing is of the order of the surf zone width. From now on we refer to this solution as mode A1.

Figure 5.5.9 shows a typical dispersion line and growth rate curve for this 'sediment transport mode' in case of $\theta_b = 5^o$. A secondary mode, named A2, also occurs, with a shorter spacing. Whereas mode A1 migrates down-flow, mode A2 has a nearly zero celerity, $wi_M \approx 0$. Both topographic patterns are dispersive since $c_M$ depends on $\kappa$. Figure 5.5.10 displays the non-dimensional topography and current perturbations of modes A1 and A2. Mode A1 reminds of the 'crescentic pattern' that was obtained in case of normal wave incidence (Falqués *et al.*, 2000). Mode A2 consists of 'down-current oriented bars' (the angle with the shore normal being again some $60^o$), without any shoal out of the surf zone. Its wave number is always larger than that of the first mode. Figure 5.5.11 shows the dimensional total topography for mode A1 (obtained from Eq. (5.4.13)). The ratio between the period and the growth time for the first mode is $2\pi\omega_i / \omega_r \sim 10$ so the bars grow faster than they move.

Figure 5.5.12 shows the quantities $\omega_{iM}$, $\kappa_M$ and $c_M$ of the 'crescentic/down-current oriented feature' (mode A1) as a function of $\theta_b$ and $r$. For $\theta_b > 5^o$, the 'crescentic/down-current oriented bar system' displays a constant wave number, $\kappa_M = 5$ and migrates down-flow ($c_M \simeq 0.5$). The alongshore spacing corresponding to this mode A1 is then some 1.5
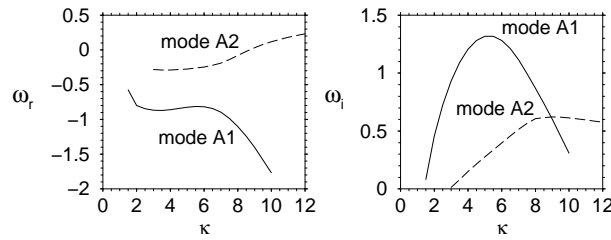
Figure 5.5.9: Dispersion line and growth rate curve for $m=1$ and quadratic $\alpha \sim D^2$. Parameter values are: $\theta_b = 5^o$, $r = 0.5$, $\gamma_b = 0.8$, $\gamma = 1$ and $N = 0.01$. All the variables are non-dimensional. As it can be seen, $\kappa_M = 5.25$, $\omega_{iM} = 1.32$ and $\omega_{rM} = -0.82$.



Figure 5.5.10: Example of a 'crescentic/down-current oriented bar system'. Non-dimensional topography and current perturbations corresponding to the maximum wave number of mode A1 (left) and mode A2 (right) for $m=1$, $\alpha \sim D^2$ and $\theta_b = 5^o$. These eigensolutions correspond to the instability curves shown in Fig. 5.5.9. The graph description is the same as in Fig. 5.5.2.

times the surf zone width. The obtained bedform shape is very robust under changes in $r$, $N$ and $\gamma$. These parameters have a clear damping role in these modes. The perturbed flow associated to these bedforms can also be seen in Fig. 5.5.10. An onshore deflection of the current can be seen over the crests of the inner bars and an offshore deflection occurs over the shoals out of the surf zone.

For very small wave incidence angles, $\theta_b < 2^o - 3^o$, results are more complex. Modes A1 and A2 remain, changing their characteristics, and new modes emerge, named B1 and B2. As can be seen in the phase celerity graph of Fig. 5.5.12, mode A1 changes from down-flow to up-flow migration in this range of angles whereas mode B1 always migrates down-flow. Both modes can be described as 'crescentic features' (alternating shoals and troughs at both
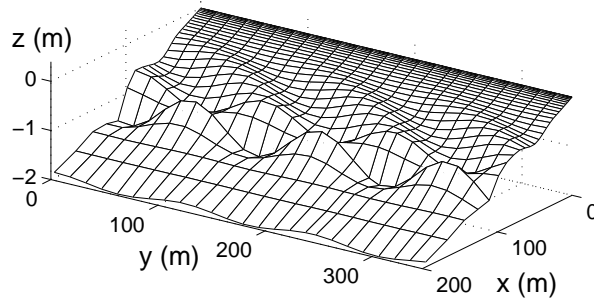
Figure 5.5.11: Final aspect of the beach in case of 'crescentic/down-current oriented bars'. Dimensional total topography (obtained from Eq. (5.4.13)) corresponding to the maximum wave number of mode 1 in case of $m = 1$, $\alpha \sim D^2$ and $\theta_b = 5^o$. This example corresponds to the solution shown in Fig. 5.5.10. The graph description is the same as in Fig. 5.5.3.
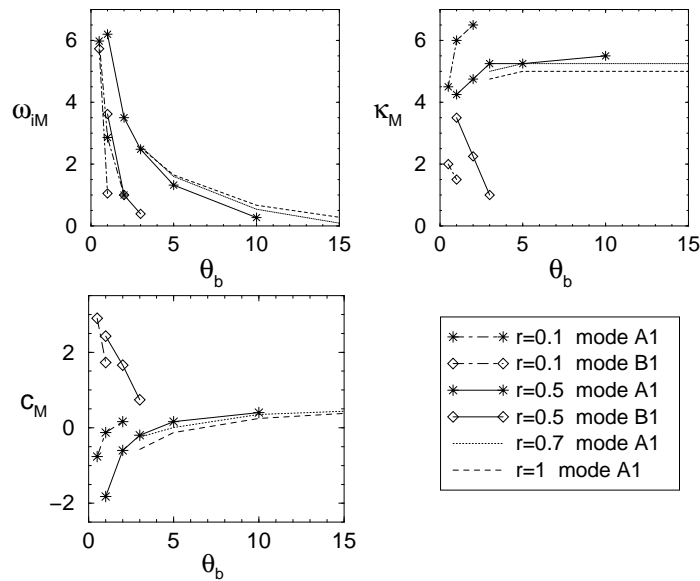


Figure 5.5.12: Effect of the wave incidence angle and the bottom friction on the maximum growth rate, wave number and migration celerity of modes A1 and B1 in case of $m = 1$ and $\alpha \sim D^2$.
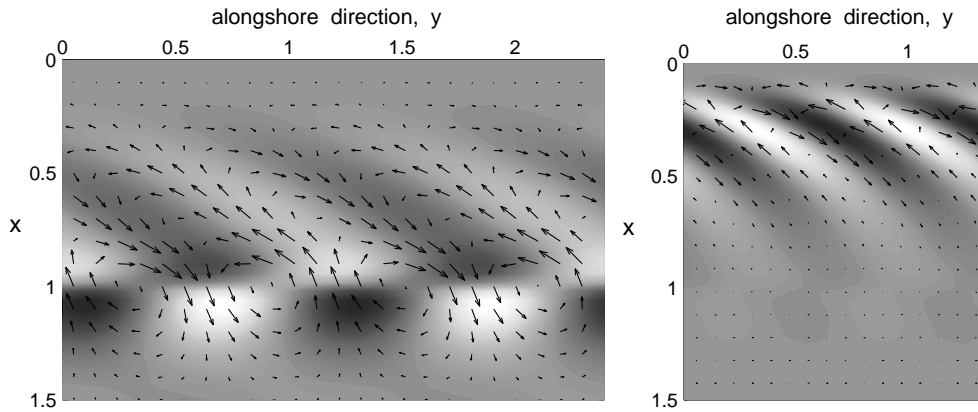
Figure 5.5.13: Example of a 'migrating crescentic bar system'. Non-dimensional topography and current perturbations corresponding to the maximum wave number of mode A1 (top) and mode B1 (bottom) in case of $m=1$, $\alpha \sim D^2$ and $\theta_b = 1^o$. The graph description is the same as in Fig. 5.5.2.

sides of the breaking line). Figure 5.5.13 shows the non-dimensional topography and flow perturbations corresponding to modes A1 and B1. The former still displays elongated inner shoals with the shape of 'down-current oriented bars', whereas the inner shoals of mode B1 are 'up-current oriented bars'. Figure 5.5.12 also demonstrates that in case of $\theta_b \to 0$ the wave number of both modes tends to $\kappa_M \simeq 4$. Mode B1 only exists for very small incidence angles up to $\theta_b \sim 2^o - 3^o$, his migration speed, growth rate and wave number decreasing to 0 very fast for larger $\theta_b$. Figure 5.5.14 shows the dispersion line and growth rate curve for $\theta_b = 1^o$. In addition to the two dominant modes (A1, B1), the existence of secondary modes with a quite shorter alongshore spacing (modes A2 and B2) can be seen in this latter picture. They consist again of alternating shoals and troughs around the breaking line and 'down- or up-current oriented bars' inside the surf zone (see Fig. 5.5.15).

In order to understand these results, it is convenient to recall the solution found in case of exactly normal wave incidence, $\theta_b = 0^o$. In this limiting situation, 'migrating crescentic bars' are also obtained, which display the same characteristics as the solutions for small wave incidence angle found in the present work. Appendix D presents in detail the results for normal wave incidence and makes a comparison with our solutions for $\theta_b = 1^o$. An interesting
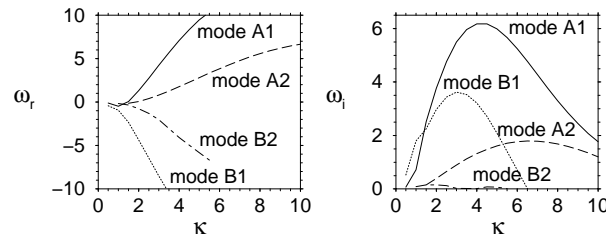
Figure 5.5.14: Dispersion line and growth rate curve for $m = 1$, $\alpha \sim D^2$ and very small wave incidence angle. These are the instability curves that correspond to the eigensolutions shown in Fig. 5.5.13. Parameter values are: $\theta_b = 1^o$, $r = 0.5$, $\gamma_b = 0.8$, $\gamma = 1$ and $N = 0.01$. As it can be seen, $\kappa_{MA1} = 4.25$, $\omega_{iMA1} = 6.2$ and $\omega_{rMA1} = 7.7$.

finding is that the 'non-migrating crescentic pattern' that was described by Falqués *et al.* (2000) for $\theta = 0^o$ has not been recovered when supposing slightly oblique waves. This is clearly seen since the phase celerity in the present results does not tend to zero for $\theta_b \to 0$ (see Fig. 5.5.12). The reason may be the symmetry-breaking produced by the obliqueness of wave incidence. This has the important implication that $\theta_b \to 0^o$ may be a singular limit in nearshore morphodynamics.

## 5.5.5   Influence of a 'variable breaking line'

The results presented above have been obtained using a 'variable breaking line', which means that not only the four linearised Eqns. (5.4.2)- 5.4.5 but also the two integro-differential Eqns. (C.6) and (C.7) presented in appendix C have been solved. In order to investigate the effect of dealing with a 'variable breaking line' in the problem, some results obtained with a 'fixed breaking line' (so without using Eqns. (C.6) and (C.7)) are described in the present section.

When the linear stability analysis is performed with a 'fixed breaking line', some of the topographic patterns presented in the sections above can vary. In case of 'current-dominated beaches' ($m = 3, 4$) a new dominant mode emerges, which consists of a system of 'shore-normal bars' attached to giant cusps (see Fig. 5.5.16, top). The corresponding perturbation on the current is seaward over the crests and shoreward over the shoals. As secondary modes, we find the 'very oblique down current oriented bars' described in section 5.5.2. Whereas these 'very oblique bars' are not altered if the displacement of the breaking line is taken into account, the growth of the 'shore-normal bars' is absolutely inhibited.

In order to investigate the reason of this inhibition, we have solved the 'Flow Over Topography problem' (including the breaking line variations) above the 'shore-normal bar system' (see Fig. 5.5.16, bottom). The 'FOT problem' procedure has been presented in section 5.4. Surprisingly enough, the variations of the breaking line totally reverse the cross-shore flow pattern, which is now characterized by a strong onshore current over the
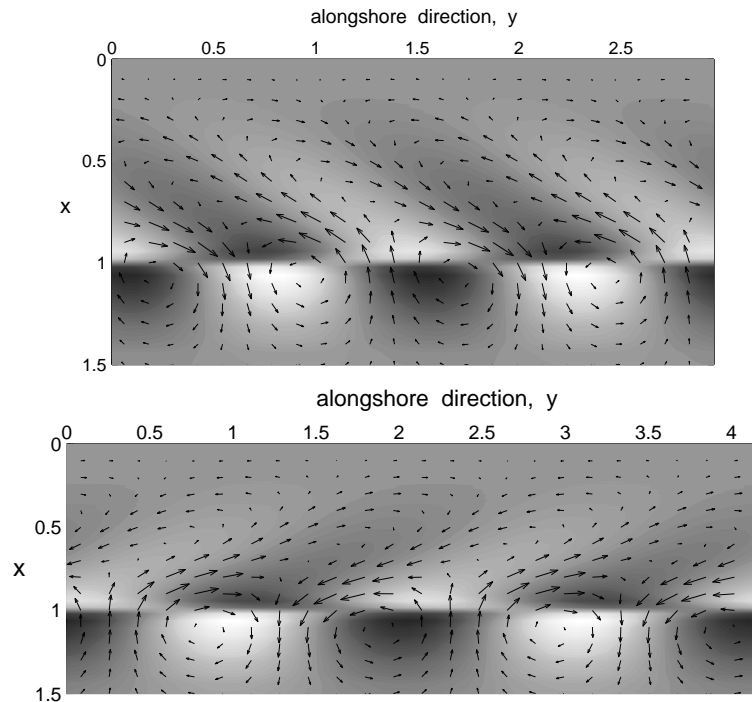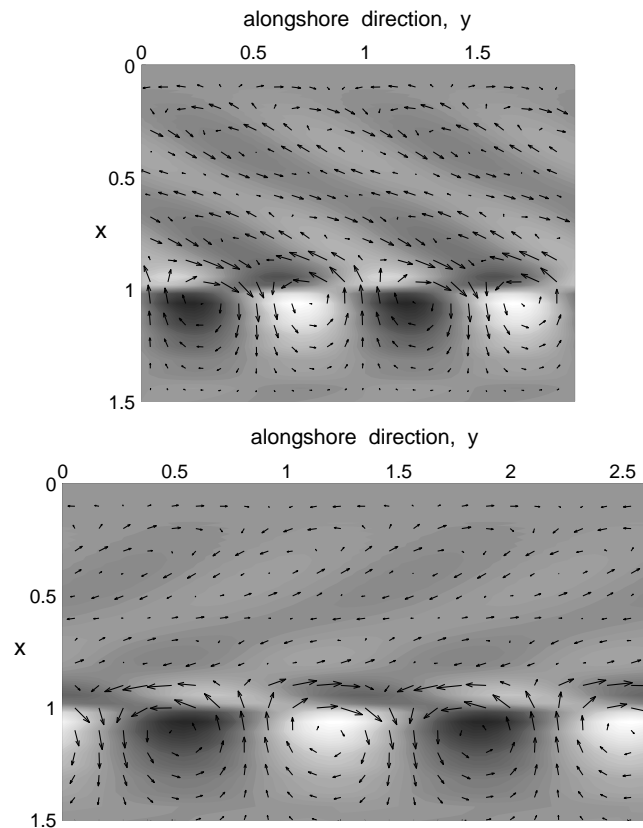
Figure 5.5.15: Secondary modes for the 'migrating crescentic bars'. Non-dimensional topography and current perturbations corresponding to the maximum wave number of mode A2 (top) and mode B2 (bottom) in case of $m = 1$, $\alpha \sim D^2$ and $\theta_b = 1^o$. These eigensolutions correspond to the instability curves displayed in Fig. 5.5.14. The graph description is the same as in Fig. 5.5.2.

crests. This is due to the fact that the 'shore-normal bars' crossing the equilibrium breaking line produce a decrease in the water depth, so that the breaking line is displaced seaward. The meaning of this displacement is that the waves are now breaking in this new seaward position, whereas they were still unbroken there in the equilibrium basic state. Thus, a possible physical interpretation for the change of sign of the cross-shore flow over such features is that the increase in the cross-shore extension of the breaking over the bars results in a stronger onshore force, capable of reversing the current. This flow pattern tends to damp the bars, as will be explained in the next section.

In case of dealing with 'wave-dominated beaches' ($m = 1$) and considering a 'stirring function', $\alpha(x)$, uniform along the surf zone, the solutions when dealing with a 'fixed breaking line' are again 'up-current oriented bars' (but they occur for a wider range of wave incidence

Figure 5.5.16: Effect of using a 'variable breaking line' in the 'shore-normal bars'. Top: Non-dimensional topography and current perturbations corresponding to the dominant mode in case of 'current-dominated beaches' ($m = 3, 4$) and uniform $\alpha$, when the displacement of the breaking line is not taken into account in the model. Parameter values are: $\theta_b = 5^o$, $r = 0.5$, $\gamma_b = 0.8$, $\gamma = 5$ and $N = 0.01$. The corresponding non-dimensional wave number is $\kappa_M = 3.75$ and the growth rate, $\omega_{iM} = 2.11$. Bottom: Result of the 'FOT problem' solved including a 'variable breaking line' above the 'shore-normal bars' shown in the top graph. The current perturbation produced by the displacement of the breaking line totally reverses the initially offshore directed flow over the bars.

angle). For $\theta_b$ small, nearly 'shore-normal bars' are obtained. For higher wave incidence angles, the patterns are more oblique and similar to the 'up-current oriented bars' presented in section 5.5.3 (see Fig. 5.5.17, top). When including a 'variable breaking line', the 'shore-normal bars' obtained for small wave incidence angle disappear for the same reason as in case of 'current-dominated beaches' (paragraph above). For larger incidence angles, the 'up-current oriented bar pattern' is nearly not modified by the variations of the breaking line. This is in accordance with the result obtained when solving the 'FOT problem' over this feature including a 'variable breaking line' (see Fig. 5.5.17, bottom). The current induced in this latter case is very similar to the current observed for the 'up-current oriented bars' presented in section 5.5.3 (see Fig. 5.5.17, top). This is probably due to the fact that the

alongshore direction, y
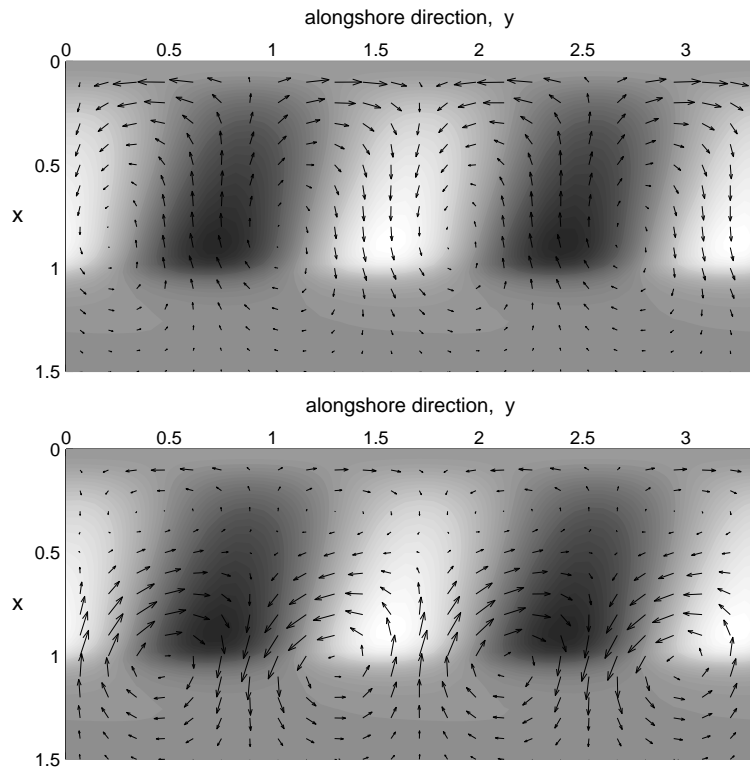


alongshore direction, y
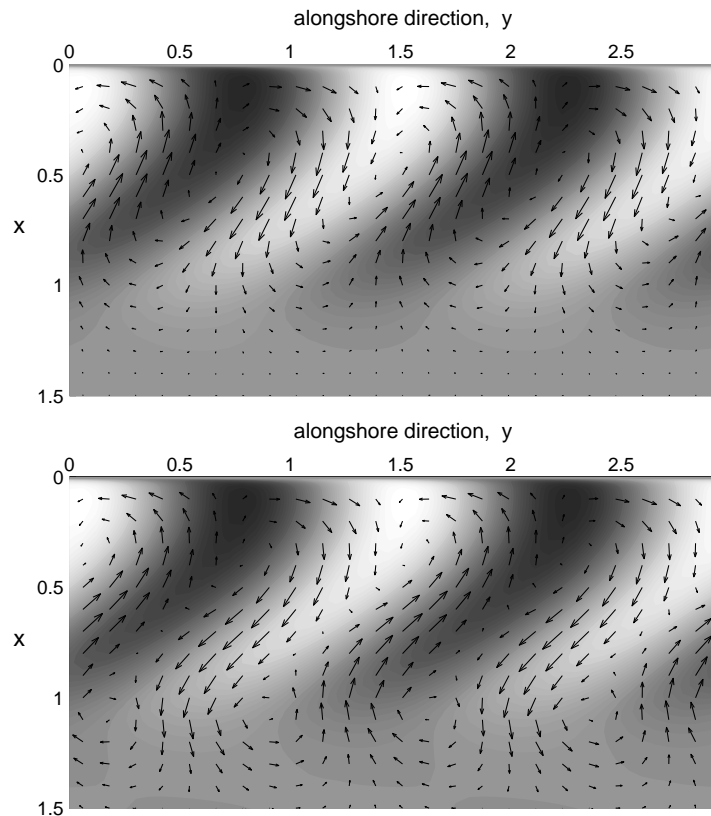


Figure 5.5.17: Effect of using a 'variable breaking line' in the 'up-current oriented bars'. Top: Non-dimensional topography and current perturbations corresponding to the dominant mode in case of 'wave-dominated beaches' ($m = 1$) and uniform $\alpha$, when the displacement of the breaking line is not taken into account in the model. Parameter values are: $\theta_b = 15^o$, $r = 0.5$, $\gamma_b = 0.8$, $\gamma = 5$ and $N = 0.01$. The corresponding non-dimensional wave number is $\kappa = 4.25$ and the growth rate, $\omega_i = 1.51$. Bottom: Result of the 'FOT problem' solved including a 'variable breaking line' above the 'up-current oriented bars' shown in the top graph. The current perturbation produced by the displacement of the breaking line is now negligible.

hydrodynamics responsible for its growth is dominated by the longshore current rather than the wave breaking. An explanation for this behaviour is given in the next section.

Finally, when using a 'stirring function', $\alpha(x)$, quadratically increasing, the solutions do not depend dramatically on the inclusion of a 'variable breaking line'. The main differences are that in case of using a 'fixed breaking line', the pattern emerges also for large incidence angles, $\theta_b > 10^o$, and it has slightly larger growth rates. Solving the 'FOT problem' with and without a 'variable breaking line', reveals that the flow is almost the same in both situations. This is due to the fact that the 'crescentic/down-current oriented bar pattern' consists of alternating shoals and troughs on both sides of the breaking line, with the perturbations

vanishing at the breaking line. Therefore, there is no displacement of the breaking line position and the flow remains unchanged.

### 5.5.6    Dimensionalisation

An estimate of the dimensional values of the growth times and migration celerities of the obtained rhythmic patterns can be found by account of the time scale, $T_m$ (see table 5.2.1). As a general estimate we use Eq. (5.2.17) to obtain

$$T_m = 10^3 \, \frac{w_s}{g \, \beta^2 \, \sin\theta_b} \; , \tag{5.5.1}$$

where the factor 1000 in front this expression comes from the combination of constants $24\,s\,(8+3\,\gamma_b^2)\,/\,(40\,\mu\,\epsilon_s\,\gamma_b^4)$. Remember that in case of 'current-dominated beaches', $T_m$ would be multiplied by $c_d^3\,/\,3\,(\sin\theta_b\,\beta')^3$. This would lead to morphological times 8 times smaller in case of a representative angle of about $\theta_b = 10^o$. Another important effect of dealing with strong current is that increasing friction ($c_d$) clearly leads to larger time scales. The system of 'very oblique down-current oriented bars' found in the 'strong current limit' (section 5.5.2) displays a non-dimensional growth rate increasing with friction (see Fig. 5.5.4). This effect could be surprising, but it is counteracted by the decrease of the time scale with $c_d$. The final dimensional growth times linked to the 'very oblique down-current oriented bars' turn out to be quite independent of friction.

Other consequences of Eq. (5.5.1) are that finer sediment ($w_s$ smaller) would give in principle shorter times, but smaller grain sizes are usually also related to gentler equilibrium slopes ($\beta$ smaller) so that the resultant trend is not clear. It is remarkable that the magnitude of the morphological time does not depend explicitly on the wave height. However, higher waves tend to cause gentler equilibrium slopes and, indirectly, larger morphological time. The most clear trend of Eq. (5.5.1) is the decrease of time scale by increasing the incidence angle. As a representative case we can look at a beach of $\beta = 0.01$ built up of sediment with $d = 0.1mm.$ for which the fall velocity would be $w_s \simeq 0.01m/s$. For waves with $\theta_b = 5^o$ the morphological time scale would be of about $32h$. For $\theta_b = 10^o$, this would become some $4h$. In case of a beach slope of $\beta = 0.05$ and $d = 0.3mm.$, morphological times 5 times shorter would be obtained. As the growth rates computed with the model are of order 1, typical dimensional values of the e-folding growth time, $T_g = \omega_i^{-1}\,T_m$, are given by $T_m$.

From the morphological time scale (Eq. 5.5.1), an estimate of the dimensional alongshore migration celerity of the patterns can be found,

$$V_{mi} = c_M \, \frac{X_b}{T_m} = 10^{-3} \, c_M \, \frac{g \, \beta \, H_b \, \sin\theta_b}{w_s} \; . \tag{5.5.2}$$

Thus, $V_{mi}$ increases with $H_b$ and $\theta_b$, which makes sense. In the first case discussed above, ($\beta = 0.01$, $d = 0.1mm.$ and $\theta_b = 5^o$) this leads to $70m/day$ for waves of $H_b = 1m.$, assuming that $c_M$ is order 1. In the same case but using very oblique wave incidence, the migration would be about 8 times faster. However, this only gives an estimate of the maximum celerity, by assuming $c_M \sim 1$. We should recall that $c_M$ can be smaller and even zero or negative (stationary topographic pattern or up-flow migrating).

## 5.6   Physical mechanisms for growth

The reasons for the growth of the bars can be understood from a close examination of the interaction between the flow and the morphology. We must seek for the topographic patterns that produce a flow structure causing accretion over the shoals and erosion at the troughs, essential condition to have growth. This requires two steps: 1) understanding the accretion/erosion pattern created by a particular flow and 2) understanding the flow caused by a given topography. Sections 5.6.1 and 5.6.2 present a first introduction to these two steps, respectively. Later on, this knowledge is applied to each particular type of bar in order to gain some insight into the generating physical mechanisms.

### 5.6.1   Bottom evolution equation

The first step is accomplished by deriving a simple bottom evolution equation (called 'BEE' from now on) only from fluid and sediment mass conservation, complemented by the sediment transport parameterisation we are considering. Inserting the transport formula (Eq. 5.2.9) into the equation for the bed evolution (Eq. 5.2.10) and replacing $\nabla \cdot \vec{v}$ from the water mass conservation equation (Eq. 5.2.1), results in

$$\frac{\partial h}{\partial t} - \frac{\partial}{\partial x}\left(\alpha\,\gamma\,|\vec{v}|^m\,\frac{\partial h}{\partial x}\right) - \frac{\partial}{\partial y}\left(\alpha\,\gamma\,|\vec{v}|^m\,\frac{\partial h}{\partial y}\right) =$$
$$= -(m-1)\,\alpha\,|\vec{v}|^{m-2}\,a_T \;-\; \alpha\,|\vec{v}|^{m-1}\,\vec{v}\cdot\nabla\ln\left(\frac{\alpha}{D}\right) \quad, \tag{5.6.1}$$

where $a_T = \vec{v}\cdot\nabla\vec{v}\cdot\vec{v}\,/\,|\vec{v}|$ is the tangential component of the advective acceleration of the fluid. The details of the derivation can be seen in Caballeria (2000). The free surface perturbation $\eta$ has been neglected here for simplicity. Its effect is negligible because the maximum value of the Froude number due to the longshore current, $F_M = \max\left(V(x)/\sqrt{g\,D_0(x)}\,\right)$, is small (this was shown in Falqués *et al.* (1996) for a linearised version of the 'BEE').

The 'BEE' can also be linearised with respect to small perturbations superimposed to the equilibrium solution (Eq. 5.4.1) and reads

$$\frac{\partial h}{\partial t} + m\,\alpha\,\frac{V^m}{D_0}\frac{\partial h}{\partial y} - \frac{\partial}{\partial x}\left(\alpha\,\gamma\,V^m\,\frac{\partial h}{\partial x}\right) - \frac{\partial}{\partial y}\left(\alpha\,\gamma\,V^m\,\frac{\partial h}{\partial y}\right) =$$
$$= (m-1)\,\alpha\,V^{m-1}\,\frac{\partial u}{\partial x} - \alpha\,V^{m-1}\,u\,\frac{d}{dx}\left(\ln\frac{\alpha\,V^{m-1}}{D_0^m}\right) \quad. \tag{5.6.2}$$

In absence of all the terms but the first two on the left hand side, a first order wave equation is obtained that describes the migration of bedforms along the coast with a local celerity $m\,\alpha\,V^m\,/\,D_0$. Notice that, taking into account that $V = O(1)$, the order of magnitude of this advection term is the same as the migration celerity found in section 5.5.6, $V_{mi} = Q_o\,/\,(\beta\,X_b)$. By adding the other two terms on the left hand side, an advection-diffusion equation is obtained, with a diffusion coefficient $\alpha\,\gamma\,V^m$. Therefore, in absence of the terms on the right hand side, the bedforms would in principle decay and migrate. Only the terms on the right can hence lead to growth of the bedforms. A growing shoal needs $\partial h/\partial t > 0$ and, therefore, a positive right hand side in Eq. (5.6.2).

In accordance with Eq. (5.6.1), the first term in the right hand side of Eq. (5.6.2) describes the effect of the acceleration of the flow. This term appears only in 'current-dominated beaches' ($m > 1$), in which case $\alpha \, V^{m-1} \, (m-1) > 0$. So accretion occurs when $\partial u / \partial x > 0$. The second term in the right hand side of Eq. (5.6.2) takes into account the gradients in the 'wave stirring', the water depth and the longshore current. This term produces accretion whenever the cross-shore component of the perturbation of the current, $u$, opposes the gradient in the function $\alpha \, V^{m-1} / D_0^m$. The physical interpretation of both terms will be better understood later on for each type of pattern.

## 5.6.2  'Flow Over Topography problem'

The second step of this theoretical analysis is completed by understanding the flow caused by each kind of pattern in order to see if it is favourable to its growth. Whereas the bed evolution equation can be analytically solved in some simplified conditions, the results of the three hydrodynamical equations are too complicated to be fully interpreted. However, some general properties of the flow perturbations generated by the different topographic patterns can be understood in terms of a competition between the 'bed-flow' and the 'bed-surf effects' presented in section 5.1.

An important interaction between the growing topographies and the longshore current ('bed-flow effect') is the following one. A ridge on an otherwise horizontal sea bed tends to deflect a current running obliquely through it in such a way that the current veers toward the normal to the crest as it goes over the ridge. This phenomenon, called *'refraction of the current'*, can be explained as a consequence of water mass conservation and is essential for the generation of large scale tidal sand banks (Pattiaratchi & Collins, 1987). In case of nearshore bars, current refraction produces an offshore deflection of the current over 'up-current oriented bars' (similarly to 'shoreface-connected sand ridges' described in Calvete *et al.* (2001)) and an onshore deflection over 'down-current oriented bars'.

However, the hydrodynamics over surf zone oblique bars is also driven by the 'bed-surf effects'. In case of normal wave incidence, the 'bed-surf interaction' tends to create an onshore flow at the surf zone shoals (due to an increase in breaking and the gradients in set-up) and an offshore flow at the troughs between them (rip currents, see Falqués *et al.* (2000) and Caballeria *et al.* (2002)). Nevertheless, the actual direction of the current if 'bed-surf effect' dominates is very sensitive to the particular shape of the shoal because there are in fact two opposing hydrodynamical forces: an onshore force at the seaward part of the shoal (where breaking is increased by the increased bottom slope) and an offshore force at the shoreward part (where breaking is reduced by the reduced bottom slope). When wave incidence is oblique, new effects that are still not understood can take place.

## 5.6.3  Very oblique down-current oriented bars

In case of 'current-dominated beaches' ($m = 3, 4$), the two terms on the right hand side of the 'linear BEE' (Eq. 5.6.2) are non-vanishing. The presence of both potentially destabilizing terms causes that the emerging type of bars cannot be predicted beforehand. Nevertheless, it is still possible to understand their formation once they are known as a model output.

Instability turns out to be dominated by the acceleration term, the one proportional to $\partial u/\partial x$ in the 'linear BEE'. Two reasons lead to this statement. Firstly, as shown in Fig. 5.5.2, the flow pattern associated to these bars has strong gradients. If $U$ is the scale for the cross-shore flow component, the term with $\partial u/\partial x$ in the 'BEE' scales as $(m-1)\,Q_o\,U^m/L_x$, where $L_x$, the typical distance associated to those gradients, is quite smaller than $X_b$. The term that is proportional to $u$ scales as $Q_o\,U^m/X_b$. Since $L_x \ll (m-1)\,X_b$, the term proportional to $\partial u/\partial x$ becomes dominant. The second reason is that the term proportional to $u$ has a stabilizing effect. The sign of the coefficient in front of $u$ depends on whether $(\alpha/D_0)\,(V/D_0)^{m-1}$ is an increasing or a decreasing function. As $\alpha$ is kept constant, $\alpha/D_0$ decreases seaward. A careful examination of the current distribution $V(x)$ for the Longuet-Higgins equilibrium solution (see Fig. 5.3.1) shows that $V/D_0$ is always a decreasing function. Therefore, $\alpha\,V^{m-1}/D_0^m$ is also decreasing and, as a result, $u$ must be positive to have growth. However, 'down-current oriented bars' are predicted instead by the model with the corresponding onshore deflection of the current, $u < 0$ (caused by the 'bed-flow effect'). Thus, this second term in Eq. (5.6.2) leads to a soft erosion of the pattern.

The flow pattern coupled to the growing features clearly favours the instability generated by the acceleration term (see Fig. 5.5.2). The cross-shore component of the perturbation of the current, $u$, goes from negative to positive values when moving offshore across the bars. Thus, $\partial u/\partial x > 0$ over the crests of the bars and, therefore, the bars grow (since the coefficient in front of this derivative in Eq. (5.6.2) is always positive). The hydrodynamical effect that leads to this behaviour of $u$ remains unknown. Neither the 'bed-flow effect' ('refraction of the current') nor the 'bed-surf effect' (in case of normal wave incidence) described in the section above can give a conclusive explanation for the strong acceleration of $u$ over the crests. However, a secondary effect of the 'current refraction' could explain part of the acceleration of $u$ over the crests. As quite oblique waves are necessary to the generation of such features, the other possible effects leading to this strong acceleration are probably related with the radiation stress terms in the momentum conservation equations that depend on the wave incidence angle.

Anyway, once the hydrodynamics is given as a result of the model, an interpretation of the physical mechanism can be made. The acceleration of $u$ in the onshore direction is linked to a deceleration of $v$ in the down-flow direction due to the water mass conservation (this can also be seen in Fig. 5.5.2). As the sediment transport is proportional to $\vec{v}$, there is an induced decrease of sediment carrying capacity in the down-flow direction, which produces the accretion of the bars. This is in agreement with the acceleration terms of the 'linear and non-linear BEE'.

In case of using a 'fixed breaking line' for 'current-dominated beaches' and uniform $\alpha$, a system of 'shore-normal bars' has emerged (see Fig. 5.5.16, top). The corresponding hydrodynamics is characterized by an onshore flow over the bars and an offshore flow on the troughs. Thus, $u > 0$ and the second term of the right hand side of Eq. (5.6.2) clearly favours growth (as $\alpha\,V^{m-1}/D_0^m$ is decreasing). When considering the variations of the breaking line over these 'shore-normal bars', the flow is completely reversed (see Fig. 5.5.16, bottom), so that $u < 0$ and the growth is inhibited. Now, the effect of the acceleration term of Eq. (5.6.2) is negligible since there is no clear acceleration of $u$ over the crests.

## 5.6.4   Up-current oriented bars

When dealing with 'wave-dominated beaches' ($m = 1$) the situation is more simple (and hence more predictable). The first term on the right hand side of the 'linear BEE' vanishes and only the second one remains (see Eq. 5.6.2), leading to

$$\frac{\partial h}{\partial t} + \frac{\alpha\,V}{D_0}\frac{\partial h}{\partial y} - \frac{\partial}{\partial x_j}\left(\alpha\,\gamma V \frac{\partial h}{\partial x_j}\right) = -\alpha\,\frac{d}{dx}\left(\ln\frac{\alpha}{D_0}\right)u\;. \qquad (5.6.3)$$

When a uniform 'wave stirring' $\alpha$ is chosen, the $\alpha/D_0$ function is decreasing offshore with the result that the coefficient in front of $u$ is positive everywhere. Consequently, the growth of a shoal needs a seaward deflection of the current over it, $u > 0$ (and a shoreward deflection over the troughs). This type of flow is originated by the 'current refraction' over 'up-current oriented bars' and this is the shape of the patterns that stem from our model. This physical mechanism is similar to the one leading to the generation of 'shoreface-connected sand ridges' in the continental shelf (Calvete *et al.*, 2001).

The 'bed-surf interaction' could also play a role in this system. For small wave incidence angle, it would tend to create onshore flow over the bars hence counteracting the 'current refraction'. But it is also true that at the shoreward part of the bars the 'bed-surf force' pushes the water seaward. Neither the net result of these opposing effects nor the influence of wave obliqueness is clear a priori. In order to understand the role of the 'bed-surf interaction', the corresponding 'FOT problem' has been solved. For arbitrary 'up-current oriented oblique bars' one may see that an onshore flow perturbation is generated by the 'bed-surf effect' in case of small incidence angle (and this inhibits its growth, as for the 'shore-normal pattern' described in section 5.5.5 in case of using a 'fixed breaking line). When waves approach the coast with larger angles ($\theta_b > 10^o$), the 'current refraction' dominates generating the offshore flow over the crests that makes the bars grow. This causes that the features only emerge above a critical angle of incidence. The formation of this type of bars is then certainly due to the 'bed-flow interaction'.

A physical interpretation of this instability can be made by decomposing the term given in Eq. (5.6.3) into two terms proportional to $-\vec{v}\cdot\nabla\alpha$ and to $\vec{v}\cdot\nabla D$ respectively. Since the sediment carrying capacity of the flow is proportional to $\alpha$, a current running in the opposite direction of $\nabla\alpha$ (i.e. $-\vec{v}\cdot\nabla\alpha > 0$) produces a down-stream decrease of sediment flux and, therefore, accretion occurs. A current running into deeper water (i.e. $\vec{v}\cdot\nabla D > 0$) slows down due to mass conservation (in fact, $\nabla\cdot\vec{v} < 0$). This causes a convergence of the sediment flux since it is proportional to a the flow velocity and, thereby, accretion takes place.

## 5.6.5   Crescentic/down-current oriented bars

The last type of pattern is obtained in 'wave-dominated beaches' with a non-uniform 'wave stirring', so an $\alpha/D_0$ increasing from the shoreline to the breaking line and decreasing beyond. Thus, the coefficient in front of $u$ in the right hand of Eq. (5.6.3) is negative inside the surf zone and positive out of the surf zone. Consequently, the growth of a shoal in the

surf zone needs an onshore deflection of the current over it (and an offshore deflection over the troughs). The contrary occurs for shoals and troughs out of the surf zone.

As it was found in Falqués *et al.* (2000), this is the sort of circulation produced by the 'bed-surf effect' over a 'crescentic pattern' in case of normal wave incidence. For slightly oblique incidence with a small angle until $\theta_b < 2 - 3^o$, the longshore current is very weak so that the 'bed-surf effect' still dominates. The obtained bedforms (modes A1 and B1 in section 5.5.4) are similar to the two 'migrating crescentic patterns' found for normal wave incidence (modes A and B in appendix D). However, the existence of this small current is enough for breaking the symmetry of the problem and suppressing the growth of the 'non-migrating crescentic pattern' that was obtained in Falqués *et al.* (2000).

The influence of the current increases with $\theta_b$. As shown in Fig. 5.5.13, the inner shoals of mode A1 are elongated with the shape of 'down-current oriented bars', while the contrary occurs for mode B1. Since the 'current refraction' produces an onshore deflection over 'down-current oriented bars', this effect favours mode A1 whereas mode B1 disappears for $\theta_b > 2^o - 3^o$. At the troughs between the bars an offshore deflection of the current takes place. If a surf zone bar extends close to the breaking line (and this is so for the dominant mode A1), this seaward flow crosses the breaking line and therefore, a shoal forms in front of the nearest surf zone trough (a kind of delta). Thus, a structure of surf zone 'down-current oriented bars' with outer shoals in front of their troughs occurs. For $\theta_b$ up to $10^o - 15^o$, the growth of these outer shoals is still favoured by the 'bed-surf effect', but in case of larger angles, this effect is not dominant anymore and the structure disappears. The physical mechanism explaining these features is very similar to the one described in the section above because they rely on the same term of the 'linear BEE' (Eq. 5.6.3).

## 5.7   Discussion

### 5.7.1   Comparison with field observations

A quantitative comparison of the model results with field observations is not at all obvious considering the restrictions imposed by both the linearised analysis and the existing field data. The outputs of our linear stability analysis are the shape of the 'fastest growing mode', including its spacing, the growth time and the migration celerity. These results are only applicable at the beginning of the formation of the features. The main inputs of the model are the 'sediment transport mode' and the wave incidence angle as non-dimensional parameters and the surf zone width as the main scaling factor. They must be known during the initial stages of growth, but all this information (inputs to be introduced in the model and outputs to compare with) is largely lacking at most of the literature on field data (see table 5.1.1). This happens mainly because of the inherent difficulties to know beforehand the precise moment when bars will start growing. The shape, spacing and celerity described in these sites correspond to the finite-amplitude features and the hydrodynamics responsible for the growth is hardly ever given. In the sites where certain wave conditions are persistent, the available 'mean' values for the surf zone width and the wave incidence angle can be used for comparison.

Table 5.7.1: Field observations of oblique bar systems. Representative values of the incidence angle far offshore, $\theta_\infty$, the wave height, $H_b$, the corresponding surf zone width, $X_b$, and a mean value of the experimental spacing of bar systems, $\lambda_e$, are given. The range of the spacings predicted by the model, $\lambda_t$, together with the 'sediment transport mode' used, $m$, are also shown. All the lengths are measured in meters.

| Site * | Orientation | $\theta_\infty$ | $H_b$ | $X_b$ | $\lambda_e$ | $\lambda_t$ | $m$ |
|---|---|---|---|---|---|---|---|
| 2 | Down-current | $27^o$ | 1.5 | 180 | 380 | 360-1000 | 3,4 |
| 4 | Down-current | $30^o$ | 0.5 | 20 | 90 | 40-120 | 3,4 |
| 5 | Down-current | $20^o$ | 1.5 | 90 | 300 | 180-540 | 3,4 |
| 1 | Unknown | - | 0.25 | 30 | 20 | 15-45 | 1 |
| 3 | Unknown | - | 2 | 150 | 170 | 75-230 | 1 |
| 3 | Unknown | - | 1.5 | 50 | 80 | 25-80 | 1 |

* Numbers correspond with the sites shown in table 5.1.1.

Five different sites where some hydrodynamical information is given have been used for a reasonable qualitative comparison with our theoretical predictions (see table 5.7.1). The wave incidence angle far offshore, $\theta_\infty$, and the wave height at the breaking line, $H_b$, are shown in this table. Data is obtained either from the papers or from personal communication by the authors. As we have already remarked, these two parameters describing wave field have in general a large uncertainty. The incidence angle at the breaking line, $\theta_b$, which is the one described in our model, is smaller than the angle reported in this table because of refraction when waves approach the breaking line. For instance, a typical wave of $8s$ period arriving at a water depth of $8m$ with an angle of $\theta = 30^o$, is refracted to $\theta = 15^o$ at $2m$ water depth (before breaking). The surf zone width has been estimated as $X_b = H_b/\beta\gamma_b$, where $\beta$ in the five sites can be found in table 5.1.1. The mean value of the observed spacing between bars, $\lambda_e$, is also shown along with the predicted spacing range from the model, $\lambda_t$. This latter quantity has been computed as the surf zone width times the non-dimensional $\lambda_t$ obtained from the model for the corresponding 'sediment transport mode', $m$.

The Truc Vert beach (site 2) and the Oregon coast (site 4) are exposed to persistent Atlantic and Pacific obliquely incident swell. For instance, Guilcher *et al.* (1952) explained that relatively oblique wave incidence angles are essential for the growth of the bar systems in the French Atlantic coast. These systems do not grow in the Southern part of this French coast, where the North Spanish coast is met, because the shoreline has another orientation so that the angle of incidence becomes much smaller (nearly normal wave incidence). Figure 1.2.9 has shown a photography of the French Atlantic coast with this noticeable bar system and a detailed description of the hydrodynamics can be found in Camenen & Larroude (1999) and Lafon *et al.* (2002). The wave obliqueness is also remarked for the bars on the Lake Michigan (site 5). Therefore, the approximation of longshore current larger than wave orbital motion seems applicable ('current-dominated beaches', characterized by $m = 3, 4$ in our model). These three sites usually show persistent systems of 'very oblique down-current oriented bars' with a spacing several times the corresponding surf zone width (as shown in Fig. 1.2.9). The rhythmic patterns obtained with our model for this 'sediment

transport mode' also display the same shape. As can be seen in table 5.5.1, predicted and observed spacings correlate well (although the experimental spacings are quite different).

One of the best descriptions of oblique bar systems for much more variable wave conditions can be found in Konicki & Holman (2000) (site 3). These bars are secondary features to a preexisting shore-parallel bar and grow both outside of the bar or attached to the coast (fourth and fifth row in table 5.7.1, respectively). The former ones are called 'offshore bars' and they are exposed to large waves while the latter are the called 'trough bars' because they are located in the trough of the previous shore-parallel bar, where the wave energy has been reduced by breaking above this shore-parallel bar. Figure 1.2.11 has shown an example of such system where both 'offshore and trough bars' are visible. They have an orientation of about $30 - 40^o$ with respect to the shore normal. From the measurements presented in Konicki & Holman (2000), the orientation of the bars with respect to the longshore current can not be inferred. The system of bars found in Trabucador beach (site 1, which is facing the Alfacs Bay in the Ebro Delta, Spain) is also generated under variable wave conditions. Neither of these two sites show a preferred wave incidence angle so that comparison is more qualitative than in the first three sites. However, they might be related with 'wave-dominated beaches' as wave incidence angles are usually not very large. They have then been compared with the case of $m = 1$. The corresponding bar systems have spacings of the order of $X_b$, in correlation with the predicted spacings. Finally, the 'crescentic/down-current oriented bar system' obtained in our model reminds of the bar systems linked to a 'crescentic longshore bar' described by Wright & Short (1984). However, no quantitative data (along with hydrodynamics) has been found to compare with.

Dimensional e-folding growth times obtained are also in agreement with the experimental data. Field observations give guiding values of the order of 1 day (for example see Lippmann & Holman (1990)). The order of magnitude of the obtained morphological time has been given in section 5.5.6 and it ranges from a few hours to a few days. Guiding migration celerities are also reported in the literature. Konicki & Holman (2000) reported a variety of migration celerities ranging up to $40\,m/day$. Celerities from 5 to $10\,m/day$ were observed at Oregon beaches (Hunter *et al.*, 1979) and about $1 - 2\,m/day$ at Lake Michigan (Evans, 1938). The velocities reported by Konicki & Holman (2000) refer only to the periods of time when the bars were active (significant wave energy). However, we do not know whether this is the case for the other two cases or if mean values for a large period of time were given there. According to Eq. (5.5.2) and using $H_b \sim 1.5m$. and non-dimensional celerities of $c \sim 0.2 - 0.6$, the predicted celerity for Duck bars is about $50\,m/day$, which is not in disagreement with observations. In the case of Oregon and Lake Michigan, the model results tend to overestimate the reported celerities by a factor 20. This may be due to a number of reasons. First, the large uncertainty on the observed values already mentioned above. Also, the prediction of the model applies to the migration during the initial formation while the observed bars are already finite amplitude features. Finally, some uncertainty is also inherent in the estimate of the morphological time $T_m$, which alters the computation of the dimensional celerities.

### 5.7.2   Wave conditions for bar growth

The influence of the parameters of the model on the generation of bars has also been described in this chapter. The question of which are the wave conditions leading to the growth of rhythmic topography, which is very relevant, can be answered regarding the influence on the solutions of some parameters and assumptions. None of the pioneering studies on nearshore morphodynamical stability addressed it (Barcilon & Lau, 1973; Hino, 1974; Christensen *et al.*, 1994). According to these studies, oblique or 'shore-normal bars' should be almost ubiquitous and this is obviously not the case. The discussion presented here is only qualitative since an accurate prediction of the influence of wave conditions is impossible without using more precise parameterisations of the small scale processes.

The 'morphodynamical diffusivity', $\gamma$, was able to set the transition from stability to instability in case of normal wave incidence (Caballeria *et al.*, 2002). That paper predicted stability for very high values of the 'morphodynamical diffusivity' (corresponding to large waves), growth of a 'crescentic pattern' for lower values and dominance of 'shore-normal bars' for even smaller values. The transition from stability to instability falling from very high wave energy to moderate energy can also be found in case of oblique wave incidence. As an example, let us focus on the case $m=4$, and 'strong current limit', which is representative of 'current-dominated beaches'. Remember that $\gamma$ is obtained from the ratio $S_g(u_o,v)/\alpha_m(u_o)$ (see section 5.2.2). According to Bailard (1981), the current driven transport scales as $\alpha_4 \sim \epsilon_s |\vec{v}|^4/w_s$ (see Eq. 2.5.16), while the downslope correction coefficient in front of $\nabla h$ scales as $S_g \sim \epsilon_s^2 |\vec{v}|^5/w_s^2$ (see Eq. 2.5.24). Working out from those equations leads to the following estimate for the 'morphodynamical diffusivity',

$$\gamma = \frac{\epsilon_s U}{w_s} \simeq \epsilon_s \, \frac{\beta \sin\theta_b}{c_d w_s} \, \sqrt{gH_b} \ . \tag{5.7.1}$$

The numerically obtained threshold value above which there is stability is $\gamma_c \sim 3$ (see section 5.5.2), from where a threshold value of $H_{bc} \sim 2m.$ can be obtained for the wave height, after assuming representative values of $c_d = 0.005$, $\beta = 0.01$, $\theta_b = 20^o$ and $w_s = 0.01m/s$. Thus, also in case of oblique wave incidence very high energy would correspond to absence of alongshore rhythmicity in agreement to the *'fully dissipative state'* described in Wright & Short (1984)). The transition wave height of $2-3m.$ given in that paper is not in disagreement with our critical value $H_{bc} \sim 2m$. It is also remarkable that all the oblique bar systems reported in table 5.7.1 are observed for wave heights below $2m$. Finally it can be noted that decreasing sediment size leads to more 'dissipative states' in Wright & Short (1984), in agreement with the fact that small $w_s$ and $c_d$ leads to stability, according to Eq. (5.7.1). Of course, low energy below the threshold for sediment transport would lead to stability too.

Another important aspect of the occurrence of oblique bars in our model is that they need relatively fixed wave conditions during the time of growth, which ranges from a few hours to a few days. This is difficult to meet specially during the beginning and the peak of a storm but it is more likely for the swell period after the peak. So, oblique bars would form preferably in environments or during periods with relatively steady wave conditions. Also, the growth time is comparable or larger than the tidal period so the present study applies in principle only to micro-tidal beaches. How tidal oscillation can interfere with the mechanisms described here is still unknown from a theoretical point of view. Nevertheless,

observations show that oblique bars certainly emerge on mesotidal conditions too (Camenen & Larroude, 1999), in which case the features are often intertidal bars (instead of subtidal). It seems possible that the mechanism described here is probably not inhibited by the tidal variability.

Looking at the consistency of the model hypothesis for each type of bar, 'very oblique down-current oriented' bars grow for moderate incidence angle and strong current, which makes sense. 'Crescentic/down-current bars' form under nearly normal incidence and weak current (with respect to wave orbital velocity), which is also consistent. However, 'up-current oriented bars' grow for quite oblique wave incidence but weak current, which is not very likely.

### 5.7.3   Implications of the model assumptions

In the basic equilibrium state, the waves are refracted as they approach to the coast obliquely. When small perturbations grow on the topography, small changes occur on the local incidence angle. These perturbations on wave refraction due to the growing bars (and also to the currents) have been neglected. In our opinion, this is the main limitation of the present study since recent research in case of shore normal wave incidence showed that wave refraction is essential for the growth of shore-normal bars (Caballeria *et al.*, 2002). Consistently, this type of bars are not obtained in the present model. However, that paper also showed that the 'crescentic pattern' was not altered by wave refraction because of their small cross-shore span in comparison with their alongshore length scale. The two systems just emerged for different parameter values. Similarly, we do not think that refraction has a significant influence for the initial growth of the 'very oblique down-current oriented bars' because they are very elongated with a very small cross-shore span. In contrast, some influence could be expected in case of 'up-current oriented bars' since they are not so oblique with the result that their cross-shore span is larger. Including wave refraction effects in the linear stability analysis is not technically straightforward and is left for future research.

Another important assumption refers to the parameterisation of the sediment transport used, which is related only to the depth-averaged currents, $\vec{v}$ (see section 5.2.2). As it has already been discussed, this makes sense as long as the transport induced by the relatively depth-uniform 'mean' currents are clearly larger than the transport induced by the undertow and the wave non-linearities. When this happens, we can separate the time scales for cross-shore evolution from the dynamics in a horizontal plane. The estimate for the growth times presented in section 5.7.1 provides a check on this assumption of '2D frozen dynamics' (used in the derivation of the sediment transport in the present chapter). Since the times obtained for oblique bar growth are clearly smaller than the typical scales of changes in the cross-shore beach profile (Plant *et al.*, 2001*b*), the separation of time scales performed between the alongshore uniform and the alongshore non-uniform situations makes sense.

The different 'sediment transport modes' have been investigated in isolation. They are characterized herein by $\alpha_m$ and $m$ of the term $\alpha_m |\vec{v}|^m$ of the sediment transport formula (Eq. 5.2.9). This has allowed for a better insight on the physical mechanisms that generate each topography. There are some transport formulations that display exactly this shape, for instance the formula by Soulsby-van Rijn (Soulsby, 1997). Moreover, we think that

studying the effect of the different 'sediment transport modes' separately also provides a
general overview of the behaviour for more realistic parameterisations, which can comprise
an addition of terms with different powers of $|\vec{v}|$ (such as Bailard formulation). As a first
test of this latter conjecture, a new linear stability analysis has been performed using the
complete bedload Bailard formulation. In this case, the transport related to a current in
the presence of waves results in a sum of two terms proportional to the 'mean' velocity with
two different exponents (1 and 3, see Eq. (2.5.10)). The preliminary performed numerical
experiments suggest that the results described in the present chapter for the two limiting
situations ('current-dominated beaches' represented by $m=3$ and 'wave-dominated beaches'
represented by $m=1$) are not easily recovered. The anisotropy of the Bailard formulation
in case of coexistence of wave motion and 'mean' currents (with different directions, see the
matrix in Eq. (2.5.11)) generates new physical mechanisms that can lead to the dominance
of different patterns. This anisotropy has not been included in the investigation done in
the present thesis, but the transport has been always assumed to be in the direction of the
depth-averaged 'mean' currents. This is because many other transport formulations with
the form $\alpha_m|\vec{v}|^m$ do not display any kind of anisotropy (for instance the formula by Soulsby-
van Rijn, see Soulsby (1997)). These isotropic formulations view the oscillatory motion just
as a stirring agent unable of causing a net transport, but only mobilising the sediment.
The stirred sand particles are then available for being transported by the relatively depth-
uniform 'mean' currents. On the contrary, the formulation by Bailard can display sediment
transport in a direction different from the 'mean' current direction. It is expected that
using realistic isotropic formulations, the results of the present chapter would probably
be recovered. Nevertheless, due to the strong sensitivity of this model on the sediment
transport conditions, further research should be done in this direction, performing numerical
experiments with several different transport formulations.

Some approximations in the computation of the wave radiation stress tensor have been
assumed in this research (see section 5.2.1): (a) 'very shallow water' wave kinematics, $c_g \simeq
c \simeq \sqrt{gD}$, (b) 'small wave incidence angle', (c) regular waves and (d) 'saturated surf zone',
$H = \gamma_b D$ and wave forcing neglected out of the surf zone, $\partial \mathcal{S}'_{ij}/\partial x_j \simeq 0$. The 'very shallow
water assumption' is sensible since for a typical wave of 8 s of period on 1 m water depth, for
instance, it only gives a relative error of 2%. The 'small wave incidence angle approximation'
is not crucial either. In case of $\theta_b = 15^o$, it produces relative errors of 4%, 5% and 10%
on $\mathcal{S}'_{11}$, $\mathcal{S}'_{22}$ and $\mathcal{S}'_{12}$, respectively. Even if the model has been forced to larger angles, all
the features predicted have already a significant growth rate for moderate angles of about
$5 - 15^o$. The approximation is considered acceptable in this range. The results of the model
for larger incidence angles at the breaking line $(15 - 35^o)$ have to be considered with care.
Notice that these large angles are not very common in nature because waves are strongly
refracted in the shoaling zone (see a quantitative example in section 5.7.1 and also in Falqués
(2003)).

Using regular waves (assumption (c)) is not a real limitation with respect to random
waves with a single narrow peak in frequency. In the equilibrium state, it leads to a single
breaking line. All the variables are continuous across the breaking line and only their gra-
dients can undergo discontinuities. However, this is not crucially different from the strong
gradients that are found when waves start breaking even in case of more realistic random
wave descriptions. Out of the equilibrium, waves enter the model essentially through the ra-
diation stress, which needs the energy density distribution. The only essential characteristic

of this energy distribution for the instability mechanisms described here is a strong decrease in energy inside the surf zone, as waves approach the coast, which is larger on the shoals and weaker at the troughs. This behaviour occurs with both regular and random waves.

Ignoring the gradients in the radiation stress out of the surf zone and using the saturated surf zone approximation (assumption (d)) is the simplest way to explore the effect of wave breaking as the main driving force of nearshore hydro- and morphodynamics. This assumption does not influence the longshore momentum balance because the combination of a constant cross-shore energy flux with the Snell's law for wave refraction results in $\partial \mathcal{S}'_{yx}/\partial x = 0$ in the shoaling zone. On the other hand, changes in the cross-shore momentum balance due to this assumption are noticeable. For the basic equilibrium, this approximation has only a small effect on the 'mean' water depth because it suppresses the set-down caused by wave shoaling. Taking this set-down into account would just introduce a small correction in the total water depth for the basic state, $D_0(x)$, not larger than about 4%. Out of equilibrium, making this assumption can only modify the 'crescentic features' that grow out of the surf zone, where the gradients in radiation stress, $\partial \mathcal{S}'_{xx}/\partial x$, are proportional to the bathymetric gradients, $\partial D/\partial x$. There are several reasons to suspect that even considering wave forcing in the shoaling zone would not change dramatically the 'crescentic pattern'. A simple computation shows that a given gradient in water depth, $\partial D/\partial x$, produces a gradient in the radiation stress tensor that is about 4 times larger in the surf zone than in the shoaling zone. Besides, a linear stability analysis of the nearshore in case of normal wave incidence has been carried out very recently using a wave transformation equation similar to Eq. (2.3.3), without using the approximations done in the present thesis (Calvete *et al.*, 2003). Results indicate that the 'crescentic pattern' is also obtained with similar characteristics than the result obtained with our more simple model.

The bottom friction used is proportional to the fluid velocity. This assumption is valid for weak currents with respect to the wave orbital motions so it is in principle applicable in case of 'wave-dominated beaches' ($m = 1$). The same linearised formula for the bottom friction has been used in case of $m = 3, 4$ although a quadratic friction would be in principle more consistent for 'current-dominated beaches'. The reason for this choice is that the equilibrium basic state used, which is analytical, can only be computed with a linear friction (Longuet-Higgins, 1970). However, some tests have been performed with a quadratic friction in the linearised equations and the resultant topography is the same. Just a slight modification of the growth rates is obtained.

Finally, the validity of using a constant sloping beach as basic topography, $z_b^o(x) = -\beta x$, can be examined. From a hydrodynamical point of view, the essential aspect of our analysis is that the ocean is split between a single surf zone close to the coast and an offshore zone where wave forcing is absent. In this respect, any monotonic beach profile (i.e. decreasing $z_b(x)$) is equivalent. Therefore, a 'plane beach' with a suitable $\beta$ seem sensible as a simple basic topography. In contrast, a basic 'barred profile' leading to more than one surf zone would be essentially different.

The natural continuation of this work is solving the fully non-linear equations. Then, the dynamics of the system far from equilibrium could be studied, establishing the final amplitude, shape and celerity of the bars. Notice that in any stability analysis, finding linear solutions only means that they have potential for growth but the fully non-linear

analysis is needed to decide which modes would finally dominate the shape of the profile (Calvete *et al.*, 2001). This non-linear analysis would also permit to use variable boundary conditions (both far offshore and at the shoreline).

## 5.8   Conclusions

The present theoretical study has shown that 'free instabilities' of the topography coupled to the flow in the nearshore provides a possible mechanism for the formation of sand bars and alongshore rhythmic topography. Even though this is in line with previous research by Hino (1974) and Christensen *et al.* (1994), the richness of the morphodynamical behaviour is much larger that what was foreseen in those earlier studies.

   Essentially, three different types of rhythmic patterns have been found: 'very oblique down-current oriented bars', 'up-current oriented bars' and 'crescentic/down-current oriented bars' (a summary is found in table 5.5.1). The patterns are called 'down-current or up-current oriented' according to whether the offshore end of the bar is shifted down-current or up-current with respect to the shore attachment. The 'crescentic/down-current oriented pattern' displays alternating shoals and troughs at both sides of the breaking line with the inner shoals being bar-shaped and oblique to the coast. All these rhythmic bar types emerge in the surf zone and they usually migrate down-stream. The key points that switch from one type of pattern to another are mainly the 'sediment transport mode' and the wave conditions. The name 'current-dominated beaches' refers to the conditions where the relatively depth-uniform 'mean' currents are much larger than wave orbital velocities and they are represented by $m = 3, 4$ in the formula. For these conditions, the model predicts the growth of 'very oblique down-current oriented bars', in case the wave incidence angle is above some $5^o$. The bars have an alongshore spacing of $\lambda \sim 2 - 6\, X_b$. The name 'wave-dominated beaches' indicates the opposite conditions, the 'mean' currents being smaller with respect to wave orbital velocities ($m = 1$ in the sediment transport formula). This situation displays a richer behaviour, depending on the cross-shore distribution of the 'wave stirring', $\alpha$. For a uniform $\alpha$, which represents the case of significant low frequency wave energy, 'up-current oriented bars' emerge with $\lambda \sim 0.5 - 1.5\, X_b$ (if $\theta_b > 5^o$). For non-uniform $\alpha$, which is representative in case of dominance of high frequency wave motion, there is instability for small to moderate incidence angles below some $10^o - 15^o$. For very small angles, 'migrating crescentic patterns' are obtained (consisting of shoals and troughs alternating around the breaking line), similarly to the 'crescentic patterns' obtained in case of normal wave incidence. Above $\theta_b \simeq 2^o - 3^o$, 'down-current oriented bars' emerge, often linked to alternating shoals out of the surf zone. Their spacing is $\lambda \sim 1 - 1.5\, X_b$. The dimensional e-folding growth time of the bars ranges from a few hours to a few days and it is favoured by steady wave conditions. Migration celerity can be up to tens of meters per day.

   The parameters related to the bed shear stress and the turbulence lateral mixing have a minor influence, mainly playing a diffusive role. The parameter setting the downslope gravitational sediment transport is also clearly diffusive. It is remarkable that, in contrast with earlier studies, this latter effect is not essential to select a preferred bedform spacing. It seems to be determined by the optimum size of the hydrodynamical cells induced by the 'bed-surf interaction'. The effect of the growing topography on the breaking line location

has proved to have a strong influence on the instabilities.

Some insight has been obtained into the physical mechanisms that make bars grow. These lie on a positive feedback between the evolving topography and the perturbations thereby caused on the hydrodynamics. These hydrodynamical perturbations are due to the effects of the topography on both the longshore current ('bed-flow effect') and the incident wave field ('bed-surf effect'). The growth of the bars is then associated with a very specific distribution of the current distribution for each particular case. In general terms, the oblique bars produce a meandering of the current that veers onshore over the crests of 'down-current oriented bars' and offshore over the crests of 'up-current oriented bars'. When bars are very oblique (some $80^o$ with respect to the shore normal), a deceleration of the longshore current over the crests seems to be essential to have growth. When there are shoals inside the surf zone, an onshore flow over them is obtained due to changes in the wave breaking and the setup.

In qualitative agreement with model results, the available field observations indicate that 'very oblique down-current oriented bars' emerge in case of 'current-dominated beaches', with spacings of several times the surf zone width (bar systems in Oregon coast, French Atlantic beaches and Lake Michigan). On the other hand, the two studied beaches that are not clearly 'current-dominated' display bars with spacings about the surf zone width (bars in Duck beach, U.S.A. and in the Ebro Delta, Spain). Even though there is no quantitative field description of patterns matching 'crescentic/down-current oriented bars', it is clear that these patterns reproduce the qualitative characteristics of some 'intermediate beach states' reported from the Eastern Australian coast. According to Caballeria (2000), bars almost perpendicular to the coast could also be expected in case of oblique wave incidence. They have not been found in the present study likely due to disregarding the topographic wave refraction. An accurate prediction of the range of wave conditions potentially leading to the formation of the bars is impossible without precise parameterisations of the small scale processes in the surf zone. This latter is in itself a large research field and was beyond the scope of the present work. Nevertheless, the model predictions of the wave conditions potentially leading to generation of bar systems are not in disagreement with the natural beach states described by Wright & Short (1984). The 'fully dissipative states' ($\Omega_0 > 6$ in section 3.1.1 of the present thesis) are characterized by the absence of alongshore rhythmic systems of sand bars, which would only emerge in 'intermediate beach states' ($1 < \Omega_0 < 6$).

A Bailard-type transport formulation related only to the relatively depth-uniform 'mean' currents (with a contribution of the downslope transport) has been able to reproduce the initial growth and migration of oblique bars in a sensible way. An essential characteristic of the formulation used in order to reproduce the mechanisms described in the present thesis is that it depends on the depth-uniform currents in an isotropic way. This means that the oscillatory motion is just a stirring agent unable of causing a net transport but only mobilising the sediment. The stirred sand particles are then available for being transported by the relatively depth-uniform 'mean' currents.

# Chapter 6

# Overall conclusions and further research

Tot ho torno a trobar: una per una
les barques en son lloc, i els pescadors;
la platja, al vespre, igual, plena d'olors,
i la mar rebolcant-se al clar de lluna.

D'*Altres vistes al mar*, Joan Maragall

## 6.1 Summary of the aim, the approach and the main results of the thesis

The shape of natural beaches is typically considered to be a result of the superposition of a long-term averaged alongshore uniform profile plus shorter-term variations, which include the formation and migration of nearshore sand bars. These bars are elongated shoals of sand, usually parallel to the coast. One or two shore-parallel bars are found very often in natural beaches and their time of formation ranges from a few days to about 1 month. In other circumstances, nearshore bars can also be oriented with a certain angle with respect to the shoreline. In this case, they are usually attached to the shoreline by a megacusp and it is common to find several bars spaced quite regularly along the coast. These alongshore rhythmic systems of oblique sand bars show wave lengths from tens of meters to about 1 kilometer and their growth time can vary from a few hours to a few days. Remarkably, after decades of research, there are not widely accepted models that explain the origin and migration of any of these intriguing large-scale morphological patterns. Tackling these open questions is not only challenging from a scientific point of view but also very interesting for testing sediment transport formulations with engineering purposes.

The shape of equilibrium profiles and the origin and dynamics of different types of nearshore sand bars (both shore-parallel and oblique bars) have been investigated in the present thesis, asserting the working hypothesis that bar growth may stem from 'self-organization' processes. The aim is to understand deeply the basic physical processes responsible for these patterns. Highly idealised morphodynamical models have been used, which solve simultaneously a set of hydrodynamical equations coupled with a bed evolution equation (based on different sediment transport laws). The simplest formulation that still encapsulates the essential physics has been chosen, so that the different mechanisms can be studied in isolation. In this respect, several approximations have been systematically done throughout the thesis. A time-averaged version of the depth-averaged shallow water equations has been used, assuming that an explicit description of the vertical structure of the variables is not essential. The effect of both the possible vertical stratifications and the filtered fast processes (for instance wave oscillatory motions and turbulence) has been parameterised when necessary. The possible 'self-organization origin' of nearshore bars has been investigated by means of a stability analysis of the nearshore morphodynamical system. To focus on the potential 'self-organization processes' related only to high-frequency waves and 'mean' currents, the possible effect of low-frequency waves has been left aside. Finally, the alongshore uniform and the alongshore non-uniform situations have been studied separately, with the implicit assumption that the associated time scales are distinct enough. An exhaustive exploration of the physical parameter space has always been performed.

- **Chapter 3:** The first model presented in this thesis is focused on describing the shape of alongshore uniform equilibrium beach profiles and the growth and evolution of shore-parallel sand bars (assuming alongshore uniformity). A semi-empirical cross-shore transport formula has been used, coupled with a wave transformation equation describing the shoaling and breaking processes of normally incident random waves (Plant *et al.*, 2001*b*). The transport law contains an onshore contribution due to the non-linear wave properties, an offshore contribution due to the undertow current and a term accounting for the downslope transport.

  In this chapter the cross-shore model has been used to predict **equilibrium beach profiles**. The balance between the three transport contributions has given rise to 'terraced (non-barred) profiles'. The two wave-induced transports increase in magnitude as waves propagate toward the coast in such a way that the residual wave transport is always negative (onshore directed) and decreases monotonously in the shoreward direction. This residual onshore transport is locally balanced by the downslope transport that is produced due to the local slopes of the 'non-barred shapes'. Some important properties of this type of equilibrium beach profiles have been subsequently studied. They display a gently sloping 'terraced surf zone' with a concave-up shoaling zone in case of 'fully dissipative conditions' (stormy weather and fine sand). For 'less dissipative conditions' the entire profile becomes more 'planar' with similar surf zone and shoaling zone slopes. The 'mean slope' of the beach increases as the wave-induced transports become larger. The obtained profile shapes and their dependence on the model parameters have reproduced the main characteristics of the beach profiles observed in nature, except for the common emergence of shore-parallel bars.

- **Chapter 4:** The stability of these equilibrium profiles with respect to arbitrary cross-shore (alongshore uniform) perturbations has been tested in this chapter using linear and non-linear stability analysis. The model presented in chapter 3 has been again

used, now investigating whether the simplified version of the 'breakpoint-bar interaction contained in the equations can lead to the growth of **shore-parallel sand bars** as 'free instabilities' of the previously 'non-barred equilibrium profiles'. The growth mechanism is based on a convergence of sediment at the break-point of the incident wave field due to a potential positive feedback between changes in the bottom and in the wave height.

In spite of finding positive indications of the validity of the 'self-organization working hypothesis', the final results have pointed out that the equilibrium profiles are always stable using this set of equations (both in the linear and the non-linear regimes). More attention should then be paid to the frequent occurrence of terraces in natural beaches, since they have turned out to be a strong attractor of the dynamical system. The linear results have indicated that a 'Dirac $\delta$ instability' tries to emerge at the 'effective break-point' of the 'terraced profiles', but its growth is always inhibited by the downslope transport induced by the inherent infinite slopes. The non-linear temporal evolutions subsequently performed have also given the corresponding equilibrium terraces as final states. Even starting from initial states moderately far from equilibrium and allowing for a potential shoreline migration, the simplified version of the 'breakpoint-bar interaction' has not been able to reproduce the formation of shore-parallel bars. Although it has been often claimed that this interaction is responsible for the generation of these bars in natural beaches, the present attempt to verify this statement quantitatively has failed. Therefore, this still remains as an important open question in the nearshore sciences.

The used sediment transport formula has only shown a potential source of instability if a positive perturbation of the relative wave height is found along all the width of the bar. However, this has never occurred using the present wave transformation equation, with the result that the 'breakpoint-bar interaction' has not been well captured by the coupled model. On the other hand, the transport model has been successful in describing the main properties of 'terraced (non-barred) equilibrium profiles', together with the often observed offshore migration of the bars initially located inside the surf zone and the slow onshore migration of bars located in the shoaling zone.

- **Chapter 5:** The second model presented is focused on the origin of alongshore rhythmic systems of **oblique sand bars**. The coupling of the incident wave field and the longshore current with the evolving topography has been theoretically examined in case of oblique wave incidence and non-uniformity in the alongshore direction. The process-based sediment transport law used in this chapter is mainly proportional to a power of the depth-averaged 'mean' current. The surf zone hydrodynamics is modelled with the water momentum and mass conservation equations, the transformation of the incident wave field being very crudely described.

In this case, it has been clearly shown that a positive feedback can occur and it leads to the initial growth of several types of oblique sand bars as 'free instabilities' of the system. Even though this is in line with previous research by Hino (1974) and Christensen *et al.* (1994), the richness of the morphodynamical behaviour is much larger than what was foreseen in those earlier studies. Essentially, these instabilities lead to the growth of 'down-current or up-current oriented bars' usually migrating down-stream. These bars emerge in the surf zone, the most common being the 'down-current oriented', and they are sometimes linked to shoals beyond the breaking line (similarly to the 'crescentic pattern', with alternating shoals and troughs at both sides of the break-

ing line, obtained by Falqués *et al.* (2000) for normal wave incidence). In qualitative agreement with available field observations, model results indicate that 'very oblique down-current oriented bars' emerge with spacings of several times the surf zone width in case of 'current-dominated beaches'. This latter name refers to the situation where strong and relatively depth-uniform 'mean' currents are present and dominate the transport (with respect to the wave orbital motions). In 'wave-dominated beaches' (the opposite situation), the shape of the 'fastest growing pattern' depends on the cross-shore distribution of the 'wave stirring'. Rhythmic systems of 'crescentic/down-current oriented bars' with spacings similar to the surf zone width stem if the stirring of sediment is mainly produced by high-frequency waves. When there is a notice-able influence of low-frequency waves in the stirring, 'up-current oriented bars' emerge (they are less frequent in the parameter space).

The dimensional e-folding growth time of the bars ranges from a few hours to a few days and it is favoured by steady wave conditions. Migration celerities can be up to tens of meters per day. The model predictions of the wave conditions potentially leading to generation of rhythmic systems of oblique bars are not in disagreement with Wright & Short (1984). The 'fully dissipative states' are characterized by the absence of rhythmic features, which can only emerge in intermediate beach states. The main physical mechanism responsible for bar growth is a positive feedback between the evolving topography and the perturbations thereby caused on both the longshore current ('bed-flow effect') and the incident wave field ('bed-surf effect').

The Bailard-type transport formulation related only to relatively depth-uniform 'mean' currents (with a contribution of the downslope transport) has been able to reproduce the initial growth and migration of oblique sand bars in a sensible way. An essential characteristic of the formulation used in order to reproduce the mechanisms described in this chapter is that it depends on the depth-averaged 'mean' current in an isotropic way. This means that the oscillatory motion is considered to be just a stirring agent unable of causing a net transport, but only mobilising the sediment. The stirred sand particles are then available for being transported by the relatively depth-uniform 'mean' currents.

## 6.2 Specific answers to the original research questions

The specific objectives of this thesis have been formulated as seven detailed research questions in the introduction. The obtained answers are specified herein:

1. *What are the main physical processes responsible for the shapes of alongshore uniform equilibrium beach profiles?*

   The obtained **equilibrium beach profiles** can display a gently sloping 'terraced surf zone' with a concave-up shoaling zone, in case of 'fully dissipative conditions' (characterized by stormy weather and fine sand). For 'less dissipative conditions' the entire profile gradually becomes more 'planar' with similar surf zone and shoaling zone slopes (the gradients in the profile are smoothed). The overall slope of the beach increases as the wave transport becomes larger. On the other hand, the common

emergence of shore-parallel bars could not be reproduced in the present thesis. The crucial distinction between a 'terraced profile type' and a 'barred profile type' is that the latter shows a clear trough at the shoreward side of the bar.

The balance between the three following contributions to the cross-shore transport gives rise to the described 'non-barred profiles': an offshore transport due to undertow current, an onshore transport due to wave non-linearities and a downslope contribution. The two wave-induced transports increase in magnitude as waves propagate toward the coast in such a way that the residual wave transport is always negative (onshore directed) and decreases monotonously in the shoreward direction. This residual onshore transport is locally balanced by the downslope transport that is produced due to the local slopes of a 'terraced (non-barred) shape'.

2. *In which situations these equilibrium configurations are stable?*

   When allowing for the presence of alongshore non-uniform irregularities the **equilibrium configurations** are stable in case of 'fully dissipative' conditions (stormy weather and fine sand). On the other hand, they can become unstable in case of 'intermediate beach states', although the latter still remain stable for certain ranges of the parameter values. On the other hand, assuming alongshore uniformity the equilibrium profiles turn out to be stable for all the range of conditions (both in the linear and in the non-linear regimes). More attention should then be paid to the terraces commonly found in natural beaches, since they may turn out to be a very stable feature in a long-term time scale.

3. *Can nearshore sand bars stem from instabilities of the equilibrium configurations of the morphodynamical system?*

   The present theoretical study has not been able to describe the origin of **shore-parallel sand bars** as an instability of previously alongshore uniform 'non-barred equilibrium profiles' (neither in the linear nor in the non-linear regimes). On the contrary, the **oblique sand bars** can clearly stem from 'free instabilities' of the equilibrium states (when allowing for the presence of alongshore non-uniform irregularities).

4. *What physical mechanisms are able to describe the growth of these sand bar systems through self-organization and what are their crucial parameters?*

   The coupling between the topography patterns and the nearshore circulation and wave breaking ('bed-flow' and 'bed-surf mechanisms') provides a possible mechanism for the formation of **oblique sand bars**. The growth of the bars is associated to a very specific flow pattern. A meandering of the longshore current always occurs, it veers onshore over the crests of 'down-current oriented bars' and offshore over the crests of 'up-current oriented bars'. When the bars are very oblique (some $80^o$ with respect to the shore normal), a deceleration of the longshore current over the crests seems to be essential to have growth. When there are shoals inside the surf zone, an onshore flow over them is obtained due to changes in the wave breaking and the set-up. The crucial parameters governing these mechanisms (within the present model) are the sediment transport conditions and the wave incidence angle.

   On the other hand, although it has been often claimed that the 'breakpoint-bar mechanism' is responsible for the generation of **shore-parallel sand bars** in natural beaches, the present attempt to verify this statement quantitatively has failed. A 'Dirac $\delta$ instability' tries to emerge because of a certain convergence of sand transport at the

'effective break-point' induced by the wave height perturbations. However, its growth is suppressed by the downslope transport produced by the inherent infinite slopes. Therefore, quantifying the 'breakpoint-bar mechanism' still remains as an important open question in the nearshore sciences.

5. *What are the main characteristics of the shape and the dynamics of nearshore sand bars?*

   With regard to **alongshore rhythmic systems** and according to the results of the present thesis, the oblique bars can be classified as 'down-current or up-current oriented', depending on whether the offshore end of the bar is shifted down-current or up-current with respect to the shore attachment. In the limit of strong relatively depth-uniform 'mean' currents compared to wave orbital motions, 'very oblique down-current oriented bars' are obtained with a spacing of several times the surf zone width. In the limit of weak currents and depending on the cross-shore distribution of wave stirring, systems of either 'up-current oriented bars' or 'crescentic/down-current oriented bars' can occur, with spacings of the order of the surf zone width. The latter pattern can be described as alternating shoals and troughs at both sides of the breaking line with the inner shoals being bar-shaped and oblique to the coast. The dimensional e-folding growth time of the bars ranges from a few hours to a few days, depending mainly on the wave incidence angle and the sediment transport conditions. Bars usually migrate down-stream with celerities up to tens of meters per day.

   With regard to **shore-parallel sand bars**, although their generation has not been reproduced in this thesis, the non-linear model has been successful in describing qualitatively their migration (in case of steady wave conditions). The bars located initially inside the surf zone show an offshore migration toward the breaker region, whereas the bars located in the shoaling zone migrate onshore more slowly.

6. *In what equilibrium beach states and under what weather conditions these sand bar systems emerge?*

   The existence of persistent oblique incident waves dissipating their energy inside the surf zone and generating longshore currents seems to be crucial for the generation of **oblique sand bars**. Their emergence is clearly favoured by steady wave conditions. The 'crescentic/down-current oriented pattern' tends to grow for wave incidence nearly normal to the shore while the 'very oblique down-current oriented bars' occur for moderately oblique wave incidence. The 'up-current bars' also stem under oblique wave incidence but they occur less frequently in the parameter space. The range of model parameters leading to growth corresponds to 'intermediate beach states' in between the 'fully dissipative' and the 'fully reflective situations'.

   With regard to **shore-parallel bars**, the 'Dirac $\delta$ instability' detected in the equations indicates that the major potential for growth would be under 'dissipative conditions' (so in case of strongly 'terraced equilibrium profiles').

7. *What are the essential properties of the sediment transport formulas that explain the morphodynamical behaviour of the beaches?*

   The Bailard-type transport formulation related only to relatively depth-uniform 'mean' currents (with a contribution of the downslope transport) seems to be able to reproduce the initial growth and migration of **oblique sand bars** in a sensible way. The essential

property of the formulation that allows for encapsulating the described mechanisms is that the transport depends on the 'mean' currents in an isotropic way.

The semi-empirical sediment transport formulation containing the offshore transport by undertow and the wave onshore transport (also with a contribution due to the downslope transport) can describe satisfactorily the main properties of 'planar and terraced **equilibrium beach profiles**'. However, it is not able to reproduce the growth of **shore-parallel sand bars**. Many models for cross-shore transport suffers from the same problem, the formation of a trough at the shoreward side of the bar being hardly ever reproduced in case of randomly distributed wave height. On the other hand, the migration direction of shore-parallel sand bars in natural beaches is well-reproduced with this formula.

## 6.3   Further research

Taking into account the results of the present thesis and the limitations imposed by the model assumptions, further research about the following topics is recommended:

- **Modelling equilibrium beach profiles and shore-parallel bars:** Further investigation is needed in order to describe the generation of shore-parallel bars through the 'breakpoint-bar interaction'. In the present thesis, neither the dynamical evolution of the states far from equilibrium conditions has been performed, nor the effect of non-steady boundary conditions has been studied. Further research should be done into this direction, specially considering that bar generation events often occur under storms, so that the response time of bar systems is often longer than the time over which wave conditions can be considered steady. Thus, neither the shore-parallel bar itself nor the underlying profile are probably in equilibrium with wave conditions, the beach being in a temporary state and trying permanently to adjust toward a moving target equilibrium.

  On the other hand, including more physical processes in the two simplified equations could also be the way to encapsulate correctly the 'breakpoint-bar interaction'. In this respect, the first step should be releasing the 'very shallow water assumption' in the wave transformation equation, which leads to an overestimate of the shoaling effect. Another important physical process that should be taken into account is the existing spatial lag between the maximum in the wave height and the maximum of the undertow return velocity. It is also recommendable to use a more realistic sediment transport formula for both suspended load and bedload, which should be previously carefully tested against field measurements. Moreover, checking the sensitivity of the results of any future model to changing the transport formula itself is needed. Other physical processes that are present in natural beaches but have not been included in the present model are the presence of longshore currents (due to oblique wave incidence), wave reflection processes, the roller dynamics during the breaking process, the existence of set-up/set-down in the 'mean' free water level, the presence of low-frequency infragravity waves and tidal oscillations and the interaction of the alongshore uniform profile with the possible alongshore rhythmic bar systems. Finally, if one aims at describing cross-shore profile processes using numerical models, a previous careful

analysis of the influence of the boundary conditions and the numerical discretization used is strongly recommended.

- **Modelling oblique sand bars:** Many unknowns remain still unsolved in the modelling of nearshore oblique sand bars. First, the results presented both in this thesis and in the previous studies (Hino (1974) and Christensen *et al.* (1994)) seem to depend on the sediment transport conditions (for instance the bar orientation with respect to the longshore current). Therefore, the sensitivity of these results to the formula itself should be carefully tested. Second, the effect of the refraction of the incident waves due to the growing perturbations should also be taken into account in future nearshore stability analysis under oblique wave incidence (Caballeria *et al.*, 2002). Thirdly, including more physical processes in these future models is recommended in order to test the effect of the assumptions done in the available models. In this respect, the first step should be including a more realistic description of the wave transformation along the nearshore profile (mainly including the shoaling and breaking processes of a random wave field and the interaction between the waves and the 'mean' currents). Other physical processes that could be included in future models are the description of wave reflection and the interaction with low-frequency infragravity waves.

  The generation of oblique bars is often found in natural 'barred beaches' (Konicki & Holman, 2000). The only linear stability analysis of a 'barred beach profile' that has been performed so far in case of oblique wave incidence resulted in the transformation of the initially uniform shore-parallel bar into a 'crescentic bar', but oblique bars did not emerge (Deigaard *et al.*, 1999). Thus, further research is needed into this direction. Another strong limitation of all the existing studies about oblique bars is that none of them describe the tidal oscillations neither of the free surface elevation nor of the shoreline position. Nevertheless, observations show that oblique bars often occur on mesotidal conditions, the bars being exposed and covered twice a day following the tidal cycle (for instance in the Dutch and French coasts, see Wijnberg & Kroon (2002)). How tidal oscillations can interfere with the mechanisms described in these previous studies is still unknown. Finally, investigating the non-linear evolution of the system is essential to determine the final amplitude long-term state. The response of the system to non-steady weather conditions should also be analysed together with the dynamics far from the equilibrium state.

- **Field observations:** A quantitative comparison of the results of the theoretical studies for bar generation with field observations has never been performed, although this would be the only reliable way to test the theoretical results. Performing such comparison is not at all obvious considering the restrictions imposed by both the highly idealised models and the available field data. However, the 'ARGUS project' has now opened new possibilities for describing experimentally the main properties of this type of patterns and under which conditions they emerge (Konicki & Holman, 2000; Wijnberg & Kroon, 2002). A systematic study of the shape and dynamics of nearshore sand bars worldwide should be tackled. Besides, more attention should be paid to the commonly observed terraces (which are distinct from shore-parallel bars since no troughs are present). According of the results of the present thesis, 'terraced profiles' may be a strong attractor of the morphodynamical system.

- **Sediment transport formulations:** In some circumstances, nearshore morphodynamics can be quite sensitive to the sediment transport formulation used. Describing

the sediment transport processes in the surf zone is still a matter of large discussion. When transport is mainly due to relatively depth-uniform 'mean' currents, there are many different formulas that have been investigated and tested. Much less work has been done on cross-shore transport formulations, although they are crucial for trying to forecast beach profiles and predict beach erosion or accretion. In order to improve both the highly idealised models built by the physicists and the complex non-linear models used by the coastal engineers, it is essential to understand better the simple processes governing sand transport. In this respect, more field experiments and small-scale theoretical studies about these phenomena are needed.

# Appendix A

# Linear stability results for the growth of shore-parallel bars in a semi-infinite domain

This appendix briefly describes the linear stability solutions that are found by means of solving Eqns. (4.2.2) and (4.2.3) in a semi-infinite domain ($x \, \epsilon \, (0, \infty)$, which is obtained using $b = 1$ in the mesh transformation $\phi$ given in Eq. (4.2.10)). As it has been said in section 4.2.3, when the critical value $b = 1$ is used in this transformation, there is a spurious input of wave energy at first order arribing from the offshore boundary. This fact disqualifies the corresponding solutions from being physically acceptable, as it is demonstrated at the end of this appendix. These 'unphysical solutions' are anyway described in this thesis because they are very illustrative of the criteria used for selecting the 'physical solutions' (among all the eigensolutions of our discretized equations). Moreover, they help to understand how the 'breakpoint-bar interaction' is operating in our set of equations. And finally, this also allows to underline the main challenges that can be found when using numerical spectral methods.

All the equilibrium solutions shown in Fig. 3.3.3 turn out to be unstable under the linear stability analysis performed using $b = 1$. Three different types of growing eigensolutions with a positive real part of the eigenvalue ($\omega_r > 0$) emerge for all the range of parameter values. The three modes are numbered according to their growth rate value, $\omega_r$, from large to small. The convergence tests presented in section 4.2.4 prove that these candidates for being 'physical solutions' are, at least, relatively good 'mathematical solutions' of our initial boundary value problem (because they are relatively independent of the numerical parameters). These initial convergence tests lead to eliminating the 'purely numeric solutions'. However, the most important test that allows to select the final 'physical solutions' is that they must be sensible from a physical point of view.

The first step to verify this latter property is looking to the cross-shore shape of the two variables. The topographic shapes of the three growing solutions are similar to the cross-shore shape of shore-parallel sand bars in nature, their crest being located next to the
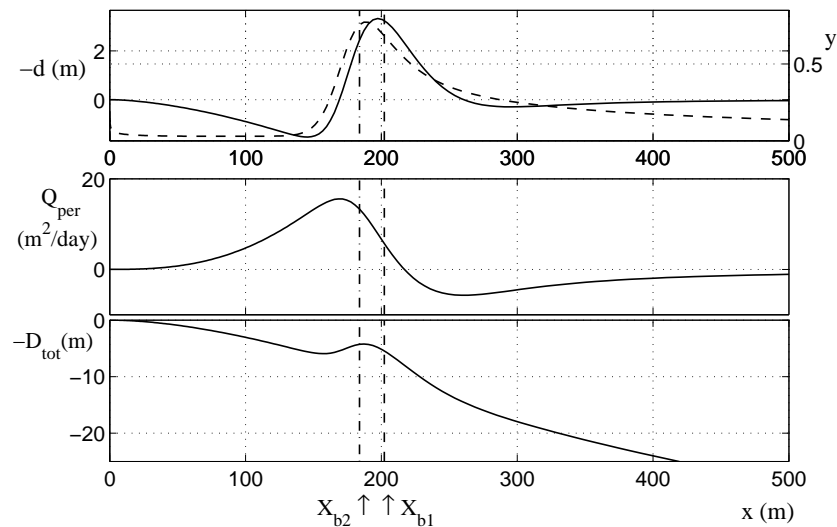
Figure A.1: Example of mode 1 with a dimensional growth time of 40 days, obtained solving the equations in a semi-infinite domain ($b = 1$). Computations have been done using $y_c/\gamma_c = 1.2$, $s_0 = 0.11$, $p = 1$ and $A = 1.33$. The corresponding equilibrium profile is a relatively 'planar beach'. The horizontal axis corresponds to the cross-shore position, $x$. All quantities shown are dimensional, computed using $H_{off} = 1m$. The vertical dashed line is the 'effective break-point', $X_{b1}$, and the vertical point-dashed line is another characteristic point of the equilibrium profiles, $X_{b2}$. The amplitude of the perturbations is arbitrary as it can not be determined by a linear stability analysis. Top: The solid line is the perturbation in water depth, $-d$, and the dashed line is the perturbation in the relative wave height, $y$. Middle: The solid line corresponds to the linear cross-shore sediment transport ($Q_{per} > 0$ means offshore transport). Bottom: The solid line is the resultant topography, equal to minus the total water depth, $-D_{tot} = -D_{eq} - d$.

'effective break-point' of the equilibrium profile, $x = X_{b1}$ (for instance see Fig. A.1, where $X_{b1}$ is the vertical dashed line). These bottom perturbations are always associated with positive perturbations of the relative wave height along all the domain, $y > 0$. Two of the modes, named 1 and 3 respectively, come from eigensolutions that have real eigenvalues and eigenfunctions, so that these bars do not migrate at the linear regime (which describes the initial formation of the features). There are two main differences between these two modes: the shape inside the surf zone and their growth rate. Mode 2 has a more complicated dynamics and will be described later on.

Figure A.1 shows an example of the mode with the largest growth rate (mode 1) that is found using a realistic set of parameter values (see section 3.2.3). In this mode, the sand is moved to the break-point from both the surf and the shoaling zones. This can be seen in the water depth perturbation, $d$, and in the linear sediment flux, $Q_{per}$. The non-dimensional growth rate of this example is $\omega_r = 0.13$, giving a dimensional e-folding growth time of $T_g = \omega_r^{-1} T_m = 40$ days (this is obtained using $y_c = 0.6$ in the expression for $T_m$ shown in table 3.2.1). All the quantities shown in this appendix have been made dimensional using
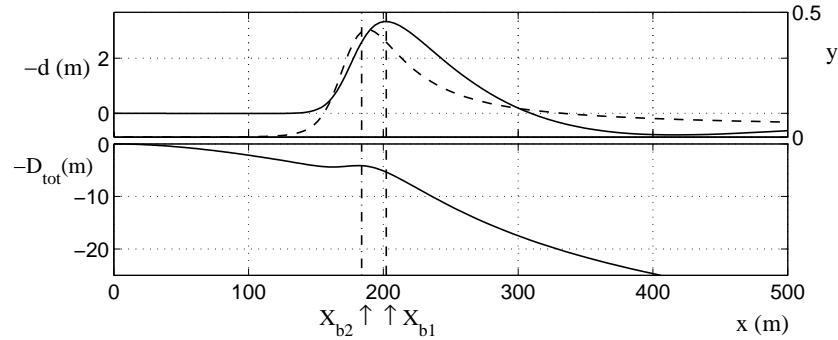
Figure A.2: Example of mode 3 with a dimensional growth time of 5 years, obtained solving the equations in a semi-infinite domain ($b = 1$). Computations have been done using the values $y_c/\gamma_c = 1.2$, $s_0 = 0.11$, $p = 1$ and $A = 1.33$. See the caption of Fig. A.1 and the text for more explanations. Top: The solid line is the perturbation in water depth, $-d$ and the dashed line is the perturbation in the relative wave height, $y$. Middle: The solid line corresponds to the linear cross-shore sediment transport ($Q_{per} > 0$ means offshore transport). Bottom: The solid line is the resultant topography, equal to minus the total water depth, $-D_{tot} = -D_{eq} - d$.

$H_{off} = 1m$. Mode 3, which has a smaller growth rate, is shown in Fig. A.2 (this example of bar is formed from the same equilibrium profile as mode1). In this case, the sand is only moved from the shoaling zone to the break-point. This bar has an associated growth rate of $\omega_r = 0.0026$ that leads to a dimensional growth time of some 5 years. Notice that in any linear stability analysis, both the amplitude and the sign of the growing perturbations are arbitrary ($\mathcal{A}$ in Eqns. (4.2.15) and (4.2.16)). Here, we have chosen the sign so as to show that this instability mechanism is capable of generating break-point bars. The same solution can describe the formation of a trough just by switching from one sign to the other. The dimensional value chosen for the amplitude allows to produce a realistic aspect of the final topography that would result from the addition of the equilibrium plus the perturbation in the graphs. Predicting the final amplitude of the solutions (with its sign) needs a non-linear analysis.

Finally, mode 2 is computed from two complex conjugate eigensolutions that emerge from the analysis, which have non-zero real and imaginary parts of both the eigenfunctions and the eigenvalues. Due to these imaginary quantities, mode 2 not only grows but also oscillates between two states with a certain period. The shape of the first state is very similar to the shape of mode 1 and the second state exactly corresponds to the negative value of the first state. Physically, this could be interpreted as two sand waves migrating in opposite directions (a sort of standing topographic pattern). The dimensional period of oscillation can be defined from its frequency, that is to say the imaginary part of the corresponding eigenvalue, $T_v = T_m \, 2\pi/\omega_i$. The non-dimensional growth rate and frequency of mode 2 (for the parameter values used in the other two examples shown above) are $\omega_r = 0.094$ and $\omega_i = 0.17$, respectively. So its dimensional growth time is $T_g = 50$ days and its period of oscillation, $T_v = 200$ days.

The shape and dynamics of the three described solutions seem physically realistic for the moment. However, there are at least three of their properties that deserve further attention. Firstly, the physical validity of mode 2 is doubtful due to its oscillations, which do not seem to have been observed in natural break-point bars. Secondly, the relative wave height linked to these three solutions is significantly different from zero along all the shoaling zone, even in the most seaward part of the domain, when $d$ is already negligible (see Fig. A.1). The perturbation $y$ decreases very slowly towards zero in the offshore direction compared with $d$. In fact, the value of $y$ at the last point inside the domain is quite large, of order $y_{N-1} = O(10^{-3})$ (while $d_{N-1} = O(10^{-12})$). This is strange taking into account that the boundary condition set is $y_N = y(\infty) = 0$. And thirdly, the three solutions are linked to a very large perturbation of the wave height, $H_{per}$. From $H = Y D$, one can find the expression, $H_{per} = y D_{eq} + d Y_{eq}$. An example of the value of $H_{per}$ at the 'effective break-point' ($x = X_{b1}$) for the first mode can be roughly evaluated from Fig. A.1. Imagine that we have a small perturbation of the topography that is $d = 0.5m$ height at $x = X_{b1}$ (the amplitude used in Fig. A.1 is 6 times larger because we wanted to show a noticeable bar in the final topography). Then, the corresponding perturbation on the relative wave height becomes $y(X_{b1}) \simeq 0.1$. The values for the equilibrium variables are $D_{eq}(X_{b1}) \simeq 8.6m$ and $Y_{eq}(X_{b1}) \simeq 0.3$. The result for the perturbation in the wave height becomes $H_{per}(X_{b1}) \simeq 1m$. Therefore, a bar of $0.5m$ would induce an increase in the wave height of $1m$, which is dramatically large. A possible interpretation of this property can be that the instability is linked to some ressonance of the hydrodynamical equation. Anyway, these three properties of the solutions call their physical validity into question. A deeper investigation of the physics behind their growth is needed, paying special attention to the behaviour of the hydrodynamical equation.

More insight into the physics behind the existence of these modes can be gained from a deeper study of the different terms of the linear wave transformation equation (Eq. 4.2.2). Figure A.3 contains the cross-shore distribution of the different terms of this equation corresponding to $d$ and $y$ of mode 1. The top graph shows the perturbation in the topography of mode 1 and the corresponding perturbation of the relative wave height (exactly the same as the top graph of Fig. A.1). The dotted line in this graph shows a different perturbation of the relative wave height that will be described later on. The graph in the middle shows the perturbations of the energy dissipation term in solid line, of the shoaling term in dashed line and of the energy flux in dotted line. All of them are taken from the linear wave transformation computed using the variables $(d, y)$ and a semi-infinite domain ($b = 1$). The dissipation term, $Dis$, corresponds to the two last terms in Eq. (4.2.2) and the shoaling term, $Sho$, corresponds to the two first terms in the same equation. The expression used for the wave energy flux at first order, $Flux = \mathcal{F}_w^{(1)}$, has been shown in Eq. (4.2.18). As can be seen in Fig. A.3 (dotted line in the middle graph), the perturbation of the wave energy flux corresponding is significantly large in the shoaling zone and, in fact, it does not vanish far offshore. This can explain the fact that the $H_{per}$ linked to this solution is so large, but in turn this is a very undesirable property of these solutions. Since we are interested in the 'self-organized behaviour' of the nearshore, any perturbation of the equilibrium variables must vanish far offshore. The reason is that in our model there is not reflection of wave energy at the shoreline, so that it makes no sense that a process occurring inside the nearshore induces an input of wave energy far offshore. Therefore, these three solutions do not match the physical motivation of our mathematical approach and have been rejected.

The reason why there is this spurious input of wave energy at first order can be understood by looking at the expression for the perturbation of the energy flux shown in Eq. (4.2.18). The boundary conditions imposed to the linear variables far offshore ($d(\infty) = 0$ and $y(\infty) = 0$) should in principle forbid any input of energy at first order. Unluckily enough, the first term in Eq. (4.2.18) turns out be very ill-conditioned. As we have already said, the perturbation of the relative wave height of the three growing solutions do not converge to 0 fast enough in the offshore direction. This is dramaticly coupled with the fact that the equilibrium water depth, $D_{eq}$, becomes extremely large far offshore (as explained in section 3.4), so that the first term in Eq. (4.2.18) becomes significantly different from 0. As an example, we show the non-dimensional value obtained for this term at the last point inside the domain $x_{N-1}$ corresponding to the mode 1 shown in Fig. A.1. The non-dimensional equilibrium water depth is very large $D_{eqN-1} = O(10^3)$, the corresponding relative wave height is small $Y_{eqN-1} = O(10^{-3})$ and the perturbation in the relative wave height is $y_{N-1} = O(10^{-3})$. Thus, the final value for $\mathcal{F}_w^{(1)}{}_{N-1} = O(10)$. This value for the perturbation of the energy flux is dramaticly large given the fact that $y$ and specially $d$ are small at that point. The exact boundary conditions imposed far offshore should forbid the entrance of wave energy, but they turn out to be not enough restrictive from a numerical point of view. The numerical zero obtained for the first order wave energy flux, $Flux$, is not small enough and the corresponding eigensolutions can not be considered as 'physical valid growing modes'.

Imposing a (small enough) zero wave energy flux at the offshore boundary is therefore essential and it can be done in our method by means of using a finite domain up to a certain $x = x_{off}$ (found with $b < 1$), instead of the semi-infinite one (found with $b = 1$). The boundary condition applied there, $y(x_{off}) = 0$, becomes restrictive enough to avoid the spurious input of wave energy. Another possibility to solve this discovered shortcoming of the model is to maintain the semi-infinite domain but changing the variables used from $(d, y)$ to $(d, H_{per})$. The offshore boundary condition applied to the perturbation of the wave height, $H_{per}(\infty) = 0$, turns out to be more restrictive than the same condition applied to the perturbation of the relative wave height, $y(\infty) = 0$. While the latter allows for the spurious input of wave energy, the former forbids it even when using a semi-infinte domain. In fact, the two approaches overcome the shortcoming of the model and give exactly the same final results. The model configuration leading to the spurious input of wave energy (so using $(d, y)$ as variables and $b = 1$) is called *'ill-posed problem'* from now on, while the *'well-posed problem'* refers to using either the variables $(d, H_{per})$ or a finite domain, $b < 1$. In section 4.4.1 we present the results found using the original variables $d$ and $y$ but with the finite domain obtained with $b \sim 0.8 - 0.9$. This is the solution finally chosen in the rest of that chapter because it is more coherent with our 'self-organization approach' and the idea of studying the nearshore area. In the rest of this appendix, however, we present some results of the 'well-posed problem' that are obtained if we write the problem in terms of $d$ and $H_{per}$ and keeping the semi-infinite domain given by $b = 1$.

The 'well-posed linear wave transformation equation' obtained for these new variables ($D$ and $H_{rms}$) can be solved over the topography corresponding to mode 1 (found using the variables $D$ and $Y$). Remember that this type of analysis is called 'FOT problem'. The results can be seen in the bottom graph of Fig. A.3, which shows exactly the same quantities as the middle graph of the same figure but now obtained with the 'well-posed equation'. As can be seen, the perturbation of the energy flux is now vanishing in the offshore direction. The cross-shore distribution of the other two terms also change dramaticly. For instance, the
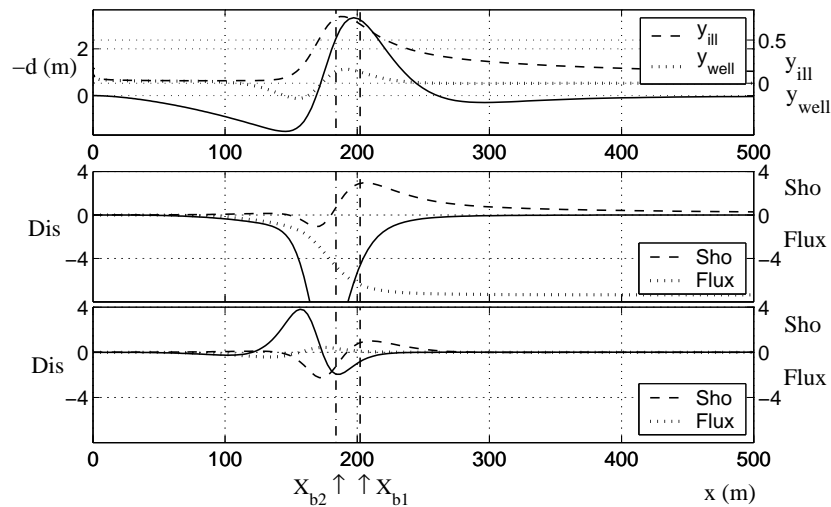
Figure A.3: Detailed study of the hydrodynamical terms coupled to the topography of the mode 1, shown in Fig. A.1. More information can be found in the caption of Fig. A.1. Top: The solid line is the perturbation in water depth, $-d$, the dashed line is the perturbation in the relative wave height corresponding to the 'ill-posed problem', $y_{ill}$, and the dotted line stands for the relative wave height corresponding to the 'well-posed problem', $y_{well}$. Middle: Cross-shore distribution of the dissipation and shoaling terms of the wave transformation equation (Eq. 4.2.2) and the corresponding linear wave energy flux in the 'ill-posed problem' (using the variables $(d, y)$ and a semi-infinite domain, $b = 1$). The solid line shows the dissipation term induced by the perturbations (corresponding to the two last terms in Eq. (4.2.2)). $Dis < 0$ means a decrease in wave energy with respect to the equilibrium situation, due to more breaking. The dashed line is the shoaling term (corresponding to the two first terms in the right hand side of the same equation). $Sho > 0$ means an increase in wave energy due to more shoaling. Finally, the dotted line is the dimensional linear wave energy flux, $Flux = \mathcal{F}_w^{(1)}$ (described by Eq. (4.2.18)). Its real value has been multiplied by a factor $10^{-2}$ in order to display it in the same axis as $Sho$. $Flux < 0$ means onshore direction of wave propagation. As can be seen, this latter quantity is not vanishing at the offshore boundary, which is a very undesirable property of these solutions. Bottom: Cross-shore distribution of the dissipation and shoaling terms of the linear wave transformation equation and the linear wave energy flux in the 'well-posed problem' (using the new variables $(d, H_{per})$ and a semi-infinite domain, $b = 1$). The legend is the same of the graph in middle. As can be seen, the linear energy flux is now vanishing in the offshore boundary.

cross-shore average of the perturbation of the energy dissipation of the 'ill-posed problem' is different from zero (see the solid line in the middle graph of Fig. A.3). This is due to the fact that the spurious input of wave energy form the offshore boundary has to be dissipated along the domain. On the contrary, the energy dissipation term of the 'well-posed problem' has an average that is approximately zero (see the solid line in the bottom graph of Fig. A.3). However, the most important difference found when solving the 'well-posed problem' refers

to the obtained perturbation for the relative wave height. This quantity is shown in the dotted line of the top graph of Fig. A.3 ($y_{well}$). As it can be seen, the magnitude of the $y_{well}$ is four times smaller than the one of $y_{ill}$ and it becomes negative in the inner surf zone (defined as $x < X_{b2}$). It turns out that this new $y_{well}$ inhibits the growth of the underlying topography. The result is that mode 1 is not obtained as an eigensolution of the 'well-posed problem'. The same behaviour is found for mode 3 shown in Fig. A.2 and also for mode 2. They do not emerge as solutions of the eigenproblem solved with a finite domain. An interpretation for all this is given in sections 4.3 and 4.4.3.

# Appendix B

# A simple analytical model for the 'Dirac $\delta$ instability'

A simple model that can be solved analytically has been formulated in order to better understand the behaviour of the cross-shore model for the generation of shore-parallel bars presented in chapter 4. A cross-shore transport formula that displays a similar convergence/divergence pattern than the transport used in that chapter (Eq. 3.2.3) has been chosen,

$$q(x,t) = c(x)\, h(x,t) - a\, \frac{\partial h(x,t)}{\partial x} \quad , \qquad x \,\epsilon\, (-1,1) \quad . \tag{B.1}$$

The parameter $a$ is again a kind of downslope 'morphodynamical diffusivity' and the function $c(x)$ is equal to $c(x) = 2\, b\, (1 - \Theta(x))$, with $\Theta(x)$ being the Heaviside function, so that

$$c(x) = \begin{cases} 2b & \text{for} \quad -1 < x < 0 \\ -2b & \text{for} \quad 0 > x > 1 \end{cases} \quad . \tag{B.2}$$

This function is positive along the negative part of the cross-shore domain ($x < 0$) and it is negative along the positive domain.

Introducing the formula given by Eq. (B.1) in a bed evolution equation for the perturbation of the bottom, $h(x,t)$,

$$\frac{\partial h}{\partial t} + \frac{\partial q}{\partial x} = 0 \quad , \qquad x \,\epsilon\, (-1,1) \quad , \tag{B.3}$$

gives

$$\frac{\partial h}{\partial t} + c(x)\frac{\partial h}{\partial x} = a\, \frac{\partial^2 h}{\partial x^2} \quad , \qquad x \,\epsilon\, (-1,1) \quad . \tag{B.4}$$

This is again a boundary value problem, to which we impose the following boundary conditions

$$h(1,t) = 0 \quad , \qquad h(-1,t) = 0 \quad , \tag{B.5}$$

together with an initial condition, $h(x,0)$, when necessary.

## B.1    Solution for two limiting cases

First, the solution in the two limiting situations will be given. When $b \to 0$, the following diffusion equation is obtained (boundary value problem),

$$\frac{\partial h}{\partial t} = a \, \frac{\partial^2 h}{\partial x^2} \quad . \tag{B.6}$$

Two families of solutions verify this equation for the boundary conditions given,

$$
\begin{aligned}
h_m^c(x,t) &= A_c \, e^{\sigma_m^c t} \, \cos(\kappa_m^c x) \quad , \\
h_m^s(x,t) &= A_s \, e^{\sigma_m^s t} \, \sin(\kappa_m^s x) \quad .
\end{aligned}
\tag{B.7}
$$

These are the diffusive 'normal modes' of the dynamical system and due to their shape are called *'cosinus and sinus family'*, respectively. The wave numbers, $\kappa$, are given by

$$\kappa_m^c = \frac{2m+1}{2} \, \pi \quad , \qquad \kappa_m^s = m\pi \quad , \tag{B.8}$$

where the mode numbers are $m = 0, 1, 2, 3, ....$ The growth rates, $\sigma$, are

$$\sigma_m^c = -\frac{a \left( (2m+1) \, \pi \right)^2}{4} \quad , \qquad \sigma_m^s = -a \, (m\pi)^2 \quad , \tag{B.9}$$

being always negative. They depend on the diffusivity coefficient, $a$, and on the mode number $m$.

When $a \to 0$, the following two propagation equations are obtained (initial value problem),

$$
\begin{cases}
\frac{\partial h}{\partial t} + 2b \frac{\partial h}{\partial x} = 0 & \text{for} \quad -1 < x < 0 \\
\frac{\partial h}{\partial t} - 2b \frac{\partial h}{\partial x} = 0 & \text{for} \quad 0 > x > 1
\end{cases}
\quad . \tag{B.10}
$$

The generic solution of this set of propagation equations is found by separation of variables and reads

$$
h(x,t) =
\begin{cases}
f(x - 2\,b\,t) & \text{for} \quad -1 < x < 0 \\
f(x + 2\,b\,t) & \text{for} \quad 0 > x > 1
\end{cases}
\quad , \tag{B.11}
$$

which implies that given a certain initial function, $h(x,0)$, it will migrate mantaining the same shape. The function $c(x)$ in Eq. (B.4) turns out to give the migration celerity of a perturbation $h(x,0)$. As this celerity is positive for $x < 0$, a bump located in this area, $h(x,t) > 0$, would migrate to the positive direction with a celerity $2\,b$. For $x > 0$, the celerity is negative so that a bump would migrate to the negative direction. This imitates the behaviour found in the cross-shore model used in chapter 4. The time evolution of two different initial conditions are now analysed in more detail. We choose $h_1^c(x,0) = 2 \, \cos(\pi x/2)$ and $h_1^s(x,0) = 2 \, \sin(\pi x)$, which correspond to the first 'normal modes' of the 'cosinus and sinus families' respectively (the solution given by Eq. (B.7) found with the diffusion equation, $b = 0$).

The evolution in time of these two initial conditions are plotted in Fig. B.1. The second initial condition ($h_1^s(x,0) = 2 \, \sin(\pi x)$, which is the first 'normal mode' of the 'sinus familiy of solutions', ) can be interpreted as a trough at $x < 0$ and a bar at $x > 0$. Its subsequent
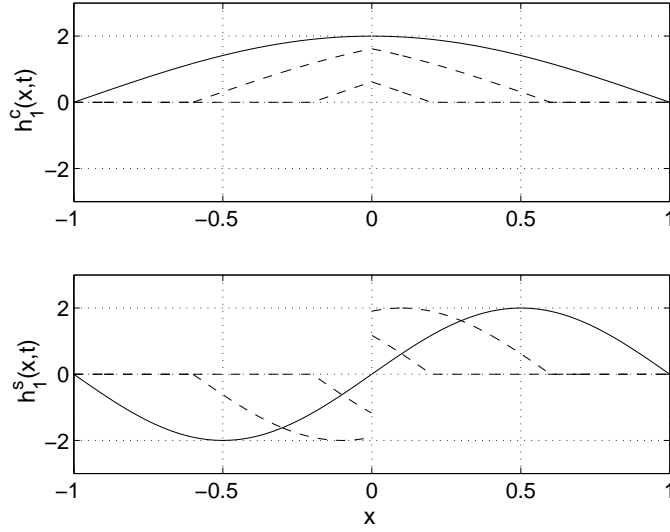
Figure B.1: Temporal evolution given by Eq. (B.10) of two initial conditions that are a solution of the diffusion Eq. (B.6). The specific values of the parameters are $a = 0$ and $b = 1$. The horizontal axis os the cross-shore direction. All the variables are non-dimensional. Top: Temporal evolution of the initial condition given by the first mode of the 'cosinus familiy of solutions', $h_1^c(x, 0) = 2 \cos(\pi x/2)$. The solid line is the initial state and the two dashed lines are the subsequent evolution after certain time steps. Bottom: Temporal evolution of the initial condition given by the first mode of the 'sinus familiy of solutions', $h_1^s(x, 0) = 2 \sin(\pi x)$.

evolution can be described as a migration of the trough to the positive direction and a migration of the bar to the left (see Fig. B.1, bottom). When $t = t_F = 1/(2\,b)$, the solution is $h_1^s(x, t_F) = 0$ in all the domain. An easy physical interpretation is that the sand arriving to $x = 0$ from the bar on the right feeds the trough at $x < 0$. The transport pattern can not be continuous due to the formulation taken, which is essentially discontinuous for $b = 0$. The first initial condition ($h_1^c(x, 0) = 2 \cos(\pi x/2)$, which is the first 'normal mode' of the 'cosinus familiy of solutions', ) can be interpreted as a bar filling all the domain with a maximum at $x = 0$. The evolution can then be described as an erosion of the bar. The corresponding physical explanation is less simple. The initial bar seems to migrate to $x = 0$ from both sides so that at $t = t_F = 1/(2\,b)$ the solution seems to be $h_1^c(x, t_F) = 0$. The strange behaviour is that the sand disappears when it arrives to $x = 0$, so that it does not seem to be conserved. The answer to this apparent paradox arises when considering a global transport equation instead of the local one (Eq. B.10). The simple transport formula is proportional to the Heaviside function ($\Theta(x)$, see Eqns. (B.1) and (B.2)), which should then be derived also with respect to $x$ for computing Eq. (B.10). This would give an additional contribution proportional to the Dirac $\delta$ function. The Dirac $\delta$ like problems can be treated through an integral analysis. The integral version of Eq. (B.10) over a small interval $(-\epsilon, \epsilon)$ around $x = 0$ gives

$$\frac{\partial}{\partial t} \int_{-\epsilon}^{\epsilon} h(x, t)\, dx + \int_{-\epsilon}^{\epsilon} \frac{\partial q(x, t)}{\partial x}\, dx = 0 \quad . \tag{B.12}$$

Imagine that $2\epsilon$ is small enough to consider that the solution inside the small interval can be kept constant in $x$ and equal to the solution outside the interval, $h(x,t) = h(0,t) = h(\epsilon,t)$. This would give the following solution for the first initial condition $h_1^c(x,0) = \cos(\pi x/2)$ at $x = 0$,

$$\frac{\partial h_1^c(0,t)}{\partial t} = \frac{b}{\epsilon}(h_1^c(\epsilon,t) - h_1^c(-\epsilon,t)) = \frac{2b}{\epsilon} \cos\left(\frac{\pi}{2}(\epsilon + 2bt)\right) \quad , \tag{B.13}$$

Thus, the solution for the amplitude of the perturbation inside the interval $(-\epsilon, \epsilon)$ is

$$h_1^c(0,t) = \frac{2}{\pi\epsilon} \sin\left(\frac{\pi}{2}(\epsilon + 2\,b\,t)\right) \quad , \tag{B.14}$$

which have been simplified due to the fact that $\epsilon$ is small. After $t = t_F = (1 - \epsilon)/(2\,b)$ all the sand is inside the interval $(-\epsilon, \epsilon)$ and the amplitude of the solution there has become

$$h_1^c(0,t_F) = \frac{2}{\pi\epsilon} \quad . \tag{B.15}$$

Therefore, the sand arriving to the interval is accumulated there. When taking the limit of $\epsilon \to 0$, the amplitude of the solution at $x = 0$ becomes $h_1^c(0,t_F) \to \infty$. This indicates that the solution is the typical type of *'point actions'* that can be described mathematically with a Dirac $\delta$ function. The value of the integrals in Eq. (B.12) are the a measure of the strength of the *'sudden excitation'* induced by this 'Dirac $\delta$ instability'.

## B.2    Solution for the complete problem

Finally, the complete boundary value problem given by Eq. (B.4) is solved. We seek for solutions satisfying the boundary conditions (Eq. B.5), together with continuity of the function and the derivative at $x = 0$. A separation of variables can be done,

$$h(x,t) = e^{\sigma t}\,e^{\kappa x} \quad , \tag{B.16}$$

with

$$\kappa = \frac{\pm 1 \pm \sqrt{1 + \sigma\frac{a'}{b}}}{a'} \quad . \tag{B.17}$$

where an *'effective diffusivity'*, $a' = a/b$, is defined and used from now on. Imposing the four boundary conditions given at the beginning of the appendix, the following equation is reached,

$$p\sinh\left(\frac{2\,p}{a'}\right) + \cosh\left(\frac{2\,p}{a'}\right) = 1 \quad , \tag{B.18}$$

where $p = \sqrt{1 + \sigma a'}$. It is demonstrated from Eq. (B.18) that $p$ must be a complex number with zero real part, which means that $\sigma < -b/a'$ (all the solutions have negative growth rates). Replacing $2\,p/a' = i\,\omega$ in Eq. (B.18) leads to

$$1 - \cos(\omega) = \left(\frac{-\omega\,a'}{2}\right) \sin(\omega) \quad , \tag{B.19}$$
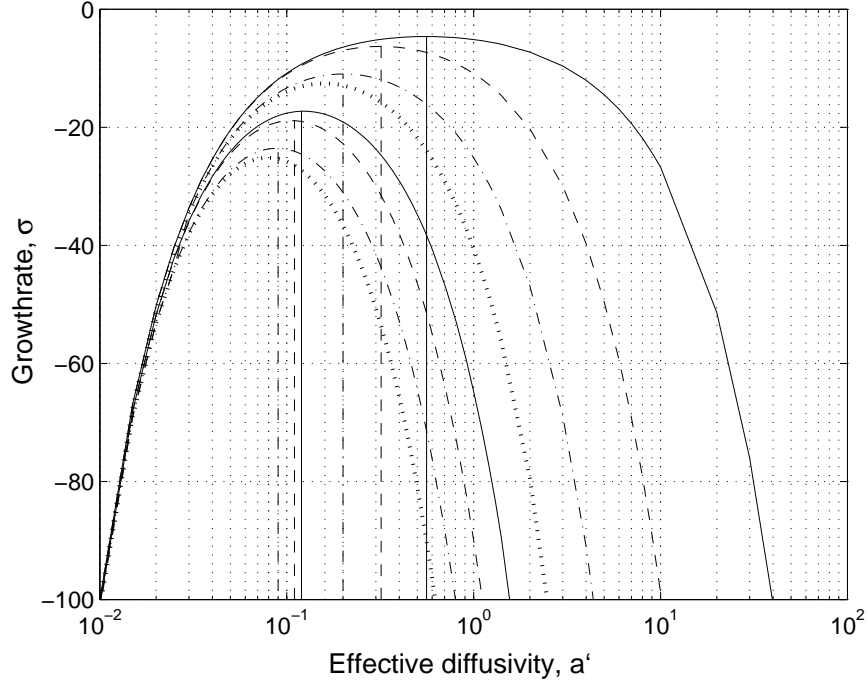
which can be solved with standard numerical techniques.

Figure B.2: Growth rate, $\sigma$, as a function of the 'effective diffusivity' parameter, $a'$, for the first eight 'normal modes' of the complete problem. The first solid line, which reaches the largest value at $a'_M = 0.56$, corresponds to the growth rate of the first mode of the 'cosinus family', $\sigma_1^c$. The first dashed line, which reaches the largest value at $a'_M = 0.32$, corresponds to the growth rate of the first mode of the 'sinus family', $\sigma_1^s$. The first dot-dashed line, which reaches the largest value at $a'_M = 0.20$, corresponds to the growth rate of the second mode of the 'cosinus family', $\sigma_2^c$, and so on.

A first set of solutions of Eq. (B.19) is given by $\omega_m^s = 2\pi(m + 1)$ with $m = 1, 2, 3, ....$ The other set of solutions, $\omega_n^c$, are not analytical and must be found numerically. Then the result for the different growth rates and wave numbers can be computed, giving

$$\sigma = -b\left(\frac{1}{a'} + \frac{a'\,\omega^2}{4}\right) \quad , \quad \kappa = \pm\frac{1}{a'} \pm \frac{i\,\omega}{2} \quad . \tag{B.20}$$

The celerity parameter, $b$, can be chosen to set the time scale so that it will be taken equal to 1 from now on. The 'effective diffusivity', $a'$, turns out to be the main dynamical parameter. Figure B.2 shows the growth rates as a function of the 'effective diffusivity' for the first eight 'normal modes' of the complete problem.
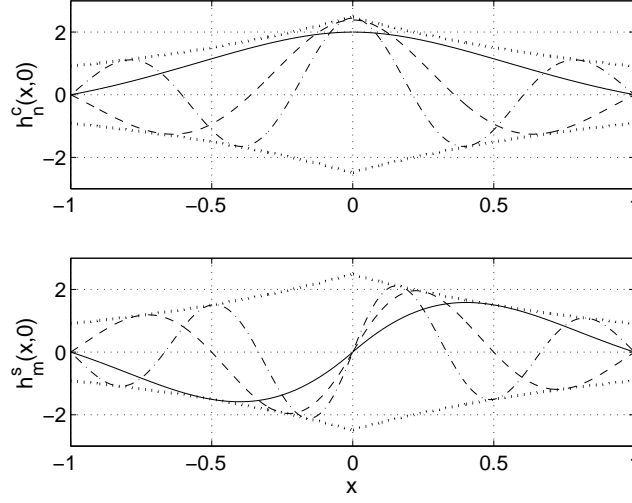
Figure B.3: Results for the perturbations obtained for $a' = 1$. The solutions are plotted setting the value for the arbitrary constant $\mathcal{A}$ in Eqns. (B.21) and (B.22) so that the amplitude of the first mode is equal to 2 at $x = 0$. The evolution of both perturbations is simply an exponential decay in time with the corresponding rate $\sigma$. The exponential decay in $x$ given by $e^{\pm \frac{x}{a'}}$, which clearly shapes the solution, is shown in both graphs with a dotted line. Top: Three first modes of the 'cosinus familiy of solutions', $h_n^c(x, 0)$, given by Eq. (B.22). The solid line is the first mode ($n = 1$), the dashed line is the second mode ($n = 2$) and the dot-dashed line is the third mode ($n = 3$). Bottom: Three first modes of the 'sinus family of solutions', $h_m^s(x, 0)$ ($m = 1, 2, 3$), given by Eq. (B.21).

The solution for the perturbation satisfying Eq. (B.4) and the four boundary conditions, corresponding to $\omega_m^s = 2\pi(m + 1)$, is given by

$$h_m^s(x,t) = \begin{cases} 2\,\mathcal{A}\,e^{\sigma_m^s t}\,e^{\frac{x}{a'}}\sin(m\pi x) \,, & \text{for } -1 < x < 0 \\ 2\,\mathcal{A}\,e^{\sigma_m^s t}\,e^{-\frac{x}{a'}}\sin(m\pi x) \,, & \text{for } 0 > x > 1 \end{cases} \tag{B.21}$$

where $\sigma_m^s = -b\left(\frac{1}{a'} + a'(m\pi)^2\right)$. This solution is clearly related with the 'sinus family of solutions' of the diffusion equation (see Eq. B.7). The solution for the perturbation corresponding to the numerical $\omega_n^c$, is given by

$$h_n^c(x,t) = \begin{cases} A\,e^{\sigma_n^c t}\,e^{\frac{x}{a'}}\left[e^{i\omega_n^c \frac{x}{2}} - e^{-i\omega_n^c \frac{x+2}{2}}\right] \,, & \text{for } -1 < x < 0 \\ A\,e^{\sigma_n^c t}\,e^{-\frac{x}{a'}}\left[e^{-i\omega_n^c \frac{x}{2}} - e^{i\omega_n^c \frac{x+2}{2}}\right] \,, & \text{for } 0 > x > 1 \end{cases} \tag{B.22}$$

where $\sigma_n^c = -b\left(\frac{1}{a'} - \frac{a'\,\omega_n^{c\,2}}{4}\right)$. Surprisingly enough, this solution turns out to be related with the 'cosinus family of solutions' of the diffusion equation. Figure B.3 shows the results for the perturbations given in Eqns. (B.21) and (B.22) for $a' = 1$. The solutions are plotted setting the value for the arbitrary $\mathcal{A}$ in these equations so that the amplitude of the first
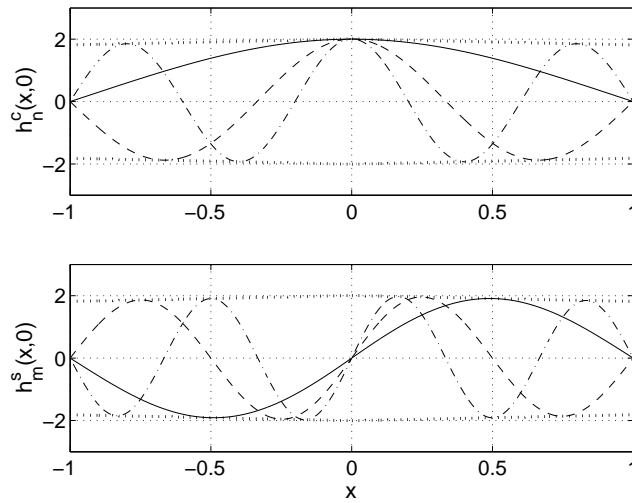
Figure B.4: Results for the perturbations obtained for $a' = 10$. The graph description is the same as in Fig. B.3. Top: Three first modes of the 'cosinus familiy of solutions', $h_n^c(x, 0)$ ($n = 1, 2, 3$), given by Eq. (B.22). Bottom: Three first modes of the 'sinus family of solutions', $h_m^s(x, 0)$ ($m = 1, 2, 3$), given by Eq. (B.21).
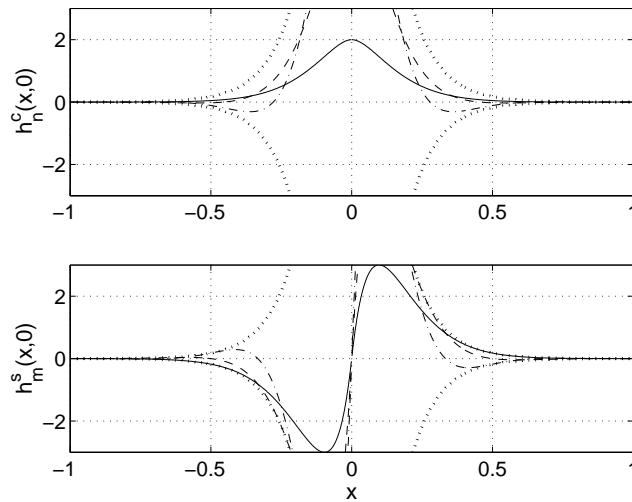


Figure B.5: Results for the perturbations obtained for $a' = 0.1$. The graph description is the same as in Fig. B.3. Again, the arbitrary constant $\mathcal{A}$ in Eq. (B.21) and (B.22) is set so that the first mode have an amplitude of 2 at $x = 0$. The other modes for this $a'$ have quite larger amplitudes so they are not seen well in the graphs. Top: Three first modes of the 'cosinus familiy of solutions', $h_n^c(x, 0)$ ($n = 1, 2, 3$), given by Eq. (B.22). Bottom: Three first modes of the 'sinus family of solutions', $h_m^s(x, 0)$ ($m = 1, 2, 3$), given by Eq. (B.21).

Figure B.6: Results for the perturbations obtained for $a' = 0.01$. The graph description is the same as in Fig. B.5. Top: Three first modes of the 'cosinus familiy of solutions', $h_n^c(x, 0)$ ($n = 1, 2, 3$), given by Eq. (B.22). Bottom: Three first modes of the 'sinus family of solutions', $h_m^s(x, 0)$ ($m = 1, 2, 3$), given by Eq. (B.21).
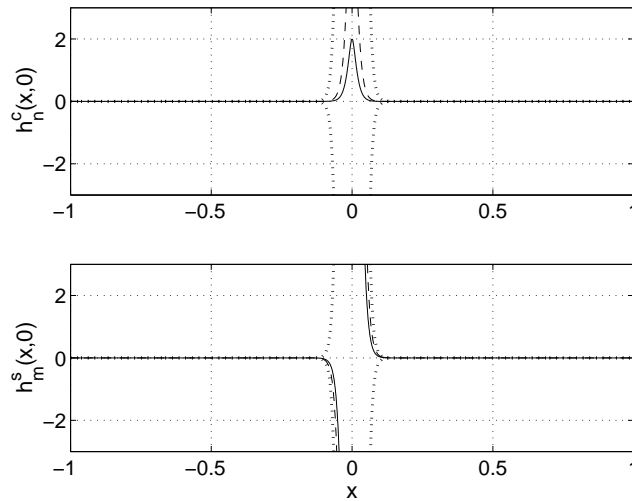
mode is equal to 2 at $x = 0$. Their evolution in time is simply described by an exponential decay following the corresponding rate, $\sigma$.

The interpretation of these results is not straightforward. In the limit of $a' >> 1$, the results clearly correspond to the diffusive modes described by Eqns. (B.7), (B.8) and (B.9), the growth rates increasing when the diffusivity decreases. The result for the perturbations in case of $a' = 10$ is shown in Fig. B.4. The 'cosinus and sinus families' are cleary recognisable in the top and bottom graphs, respectively. This is due to the fact that the exponential decay in $x$ given by $e^{(\pm x/a')}$ (shown in the graphs with a dotted line), which clearly shapes the solution, is quite similar to 1 in the domain $(-1, 1)$ for $a' = 10$.

In the other limit, $a' << 1$, the behaviour is quite odd. As it can be seen in Fig. B.2 far each mode, the growth rates increase when the 'effective diffusivity' decreases until they reach a certain negative maximum (different for each mode). Then the growth rates start to decrease again. So for $a' << 1$, the solution becomes more stable when de diffusivity decreases! An explanation for this strange property, very similar to the behaviour found in the linear stability solutions of chapter 4, is found when looking to the shape of the perturbations for this range of small $a'$. Figures B.5, B.6 and B.7 show the result for the perturbations in case of $a' = 0.1, 0.01, 0.001$, respectively. The arbitrary constant $\mathcal{A}$ in Eqns. (B.21) and (B.22) is again set so that the first modes have an amplitude of 2 at $x = 0$. The other modes have quite larger amplitudes so they are not well seen in the graphs. As $a'$ decreases, the spatial shape given by $e^{(\pm x/a')}$ bounds the solution to a region closer to $x = 0$. The result is that the solution tends to a kind of Dirac $\delta$ function as $a' \to 0$ (as can be clearly seen in Fig. B.7 for the first mode of the 'cosinus solution' in case of $a' = 0.001$).
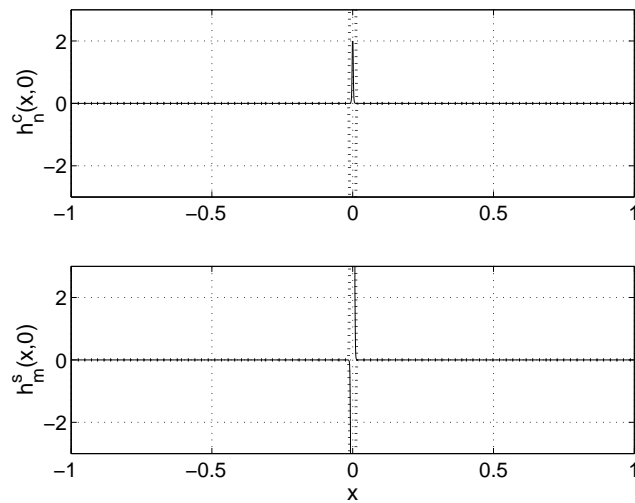
Figure B.7: Results for the perturbations obtained for $a' = 0.001$. The graph description is the same as in Fig. B.5. Top: Three first modes of the 'cosinus familiy of solutions', $h_n^c(x, 0)$ ($n = 1, 2, 3$), given by Eq. (B.22). Bottom: Three first modes of the 'sinus family of solutions', $h_m^s(x, 0)$ ($m = 1, 2, 3$), given by Eq. (B.21).

This is in complete agreement with the solution obtained for $a' = 0$. Therefore, we are again dealing with a 'Dirac $\delta$ instability', as it has happened in chapter 4. The interpretation done for the behaviour of the corresponding growth rates is that the diffusion term in Eq. (B.10) becomes very strong when the solutions tend to the infinite slopes that characterizes the Dirac $\delta$ function. This makes them become more and more stable as $a' \to 0$.

# Appendix C

# Equations allowing for a 'variable breaking line' in the model for the growth of oblique bars

The linearised equations presented in section 5.4 describe the dynamics of the system in case of a fixed breaking line, defined as $x = X_b$. However, the perturbations in water depth due to the growing patterns result in a displacement of the breaking line position ($x = X_b + \Delta X_b$). This is because waves tend to break in a more seaward position ($\Delta X_b > 0$) if there is a growing shoal close to the equilibrium breaking line and the contrary occurs ($\Delta X_b < 0$) if there is a deepening trough around there (see a scheme in Fig. C.1). At first sight, this would seem to be an infinitesimal disturbance localised in an infinitesimal region, hence being a second order effect. This is actually not true and a first order contribution occurs, which has to be accounted for in the linearised dynamical problem. The final used linear governing equations, which deal with a 'variable breaking line', consist not only of the differential Eqns. (5.4.2)-(5.4.5), but also of the two integro-differential equations that are derived in the present appendix.

Due to the 'saturated surf zone assumption' (see section 5.2.1), the position of the breaking line in equilibrium conditions is defined by $\gamma_b D(x = X_b) = H_b$, where $D(x = X_b)$ and $H_b$ are the water depth and wave height at the equilibrium breaking line. When a small perturbation in the water depth is introduced, the position of the breaking line changes to $x = X_b + \Delta X_b$ in such a way that the wave height at this new position is still equal to $H_b$ (see Fig. C.1). Therefore, the following expression is reached

$$H_b = \gamma_b D (x = X_b + \Delta X_b) =$$
$$= \gamma_b \left( D(X_b) + \frac{dD_0(X_b)}{dx} \left( \eta(X_b, y, t) - h(X_b, y, t) \right) \Delta X_b \right) \quad , \tag{C.1}$$

where we have applied a Taylor expansion of the water depth around the equilibrium breaking line position. From Eq. (C.1) and using again the assumption $H_b = \gamma_b D(X_b)$, an expression for the displacement of the breaking line ($\Delta X_b$) due to the perturbations in the water
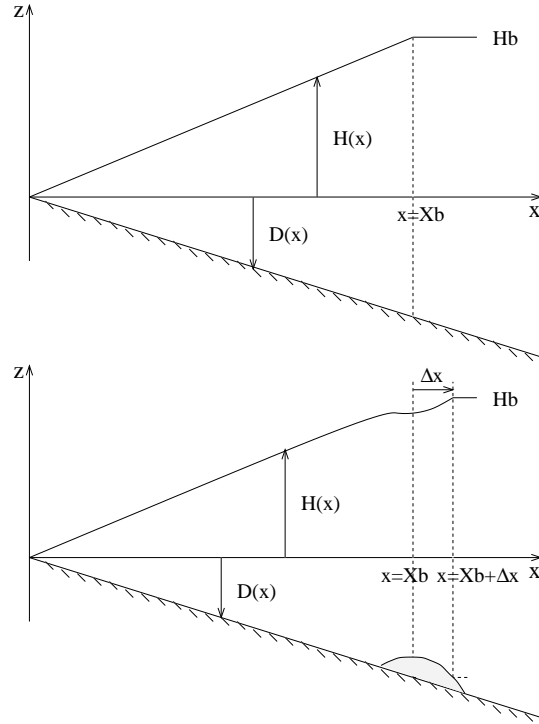
Figure C.1: Scheme showing the displacement of the breaking line position due to the growth of a shoal ($x = X_b + \Delta X_b$). The perturbation in water depth due to the growing shoal results in a displacement of the breaking line position because waves tend to break in a more seaward position ($\Delta X_b > 0$) if there is a growing shoal close to the equilibrium breaking position. The contrary would occur ($\Delta X_b < 0$) if there was a deepening trough close to the equilibrium breaking line. Left: Idealised equilibrium state. Right: Situation reached after superimposing an arbitrary bump, showing the seaward displacement of the breaking line.

depth can be found. This displacement depends on time and on the alongshore coordinate, following the growing perturbation, and reads

$$\Delta X_b(y, t) = -\frac{\eta(X_b, y, t) - h(X_b, y, t)}{dD_0(X_b)/dx} \quad . \tag{C.2}$$

From Eq. (5.2.2), the momentum balance equations up to first order can computed both inside and outside the surf zone, taking into account that there are no gradients in the radiation stress tensor outside the surf zone, by assumption (see section 5.2.1). Remember that the breaking line position at first order becomes $x = X_b + \Delta X_b$, whereas its position at zero order is $x = X_b$. By subtracting the zero order equations from the first order equations, we obtain a new system of linearised equations. This computation can be made either in case $\Delta X_b > 0$ or in the opposite situation. The linearised equations presented in section 5.4 have been obtained with a very similar computation but using a fixed breaking line position

equal to $x = X_b$ also at first order. The new set of linear equations are then similar to Eqns. (5.4.2) and (5.4.3) but with an important difference: now there are two zero order terms, called $F_x^{bl}$ and $F_y^{bl}$, that are not cancelled and read

$$
F_x^{bl} = \begin{cases} \text{if } \Delta X_b > 0 & \begin{cases} -\frac{3\,g\,\gamma^2}{8}\frac{\partial D_0}{\partial x} &, \quad X_b < x < X_b + \Delta X_b \\ 0 &, \quad \text{otherwise} \end{cases} \\[3em] \text{if } \Delta X_b < 0 & \begin{cases} +\frac{3\,g\,\gamma^2}{8}\frac{\partial D_0}{\partial x} &, \quad X_b + \Delta X_b < x < X_b \\ 0 &, \quad \text{otherwise} \end{cases} \end{cases} \tag{C.3}
$$

$$
F_y^{bl} = \begin{cases} \text{if } \Delta X_b > 0 & \begin{cases} +\frac{5\,\gamma_b^2\,\sin(\theta_b)}{16}\sqrt{\frac{D_o}{D_{ob}}}\frac{\partial D_o}{\partial x} &, \quad X_b < x < X_b + \Delta X_b \\ 0 &, \quad \text{otherwise} \end{cases} \\[3em] \text{if } \Delta X_b < 0 & \begin{cases} -\frac{5\,\gamma_b^2\,\sin(\theta_b)}{16}\sqrt{\frac{D_o}{D_{ob}}}\frac{\partial D_o}{\partial x} &, \quad X_b + \Delta X_b < x < X_b \\ 0 &, \quad \text{otherwise} \end{cases} \end{cases} \tag{C.4}
$$

Assume now that the perturbations $u$, $v$, $\eta$, $h$ and $\Delta X_b$ are of the order of $\epsilon \ll 1$. Imagine that we divided by $\epsilon$ the two linearised Eqns. (5.4.2) and (5.4.3) (after adding to them the to new zero order terms given by Eqns. (C.3) and (C.4)). If we then took the limit $\epsilon \to 0$, all the terms would be of first order except for $(F_x^{bl}, F_y^{bl})/\epsilon$, which would tend to $\infty$ but only in an infinitesimal interval of a width of the order of $\Delta X_b \sim \epsilon$. This is a Dirac $\delta$ like problem, where an excitation is exerted at a certain point of the domain, $x = X_b$. The idealised unit impulse function, $\delta(x - X_b)$, has the following property when combined with a continuous and bounded function such as $\vec{F}^{bl}(x)$,

$$
\int_0^\infty \delta(x - X_b)\vec{F}^{bl}(x)\,dx = \vec{F}^{bl}(X_b) \quad . \tag{C.5}
$$

The solution procedure is then the following one. The differential Eqns. (5.4.2) and (5.4.3) are solved separately in the intervals $(0, X_b)$ and $(X_b, \infty)$, with the restriction that the integral of the equations over the whole interval $(0, \infty)$ must vanish. This poses two integro-differential equations, where Eqns. (C.3) and (C.4) and the integral expression in Eq. (C.5) are used,

$$
-i\,\omega\,\epsilon\int_0^\infty u\,dx = -\int_0^\infty i\,\kappa\,V\,u\,dx - \int_0^\infty \frac{2\,r\,\gamma_b}{\pi\,F}\frac{u}{\sqrt{D_o}} + \left(1 + \frac{3}{8}\gamma_b^2\right)\eta|_{x=0} - \tag{C.6}
$$
$$
- \frac{3\,\gamma_b^2}{8\,F^2}h|_{x=0} + \frac{i\,\kappa\,5\,\gamma_b^2\,\sin(\theta_b)}{16}\int_0^{X_b}\sqrt{\frac{D_o}{D_{ob}}}\left(\eta - \frac{h}{F^2}\right)dx + \int_0^\infty \vartheta_x\,dx
$$

$$-i\,\omega\,\epsilon \int_0^\infty v\,dx = -\int_0^\infty \left( i\,\kappa\,\eta + i\,\kappa\,V\,v + \frac{dV}{dx}\,u \right) dx - \int_0^\infty \frac{r\,\gamma_b}{\pi\,F}\,\frac{v}{\sqrt{D_o}}\,dx +$$

$$+ \int_0^\infty \frac{r\,\gamma_b\,V}{2\,\pi\,F}\,\frac{(F^2\,\eta - h)}{D_o^{3/2}}\,dx + \frac{\gamma_b^2}{8} \int_0^{X_b} \Bigg( -i\,\kappa +$$

$$+ \frac{5\,\sin(\theta_b)}{4}\sqrt{\frac{1}{D_o\,D_{ob}}}\,\frac{dD_o}{dx} \Bigg)\left( \eta - \frac{h}{F^2} \right) dx + \tag{C.7}$$

$$+ \frac{5\,\gamma_b^2\,\sin(\theta_b)}{16} \left( \int_0^{X_b} \sqrt{\frac{D_o}{D_{ob}}}\left( \frac{d\eta}{dx} - \frac{1}{F^2}\,\frac{dh}{dx} \right) dx - \right.$$

$$\left. - \left( \eta|_{x=X_b} - \frac{h|_{x=X_b}}{F^2} \right) \right) + \int_0^\infty \vartheta_y\,dx \quad ,$$

where $\vec{\vartheta}$ includes the linearised turbulence terms defined in Eqns. (5.4.6) and (5.4.7) (section 5.4). These are the final integro-differential equations used, where we have made use of the expression for the breaking line displacement (Eq. C.2).

The numerical procedure to add these two new equations to the model described in section 5.4 is as follows. The expansions of the linear variables in Chebyschev-like basis (see Eq. 4.2.5) are again used in the two integro-differential equations written above (Eqns. C.6 and C.7, obtaining a discrete version of these two equations for the coefficients of the expansion). Then, the two linearised Eqns. (5.4.2) and (5.4.3) that had to be in principle applied to the collocation point closest to the breaking line are replaced by the discrete version of the two integro-differential equations. See section 4.2.2 for the definition of the collocation points and a general description of the numerical procedure used in this model.

# Appendix D

# Linear stability results for the growth of alongshore rhythmic patterns in case of normal wave incidence

In order to understand the results in case of small wave incidence angle described in section 5.5.4, it is convenient to recall the solution found in case of normal wave incidence that were presented by Falqués *et al.* (2000). As it happens in case of slightly oblique waves, instability was found only in case of 'wave-dominated beaches' ($m$=1) and a 'wave stirring function' increasing quadratically with the water depth ($\alpha \sim D^2$). The 'crescentic pattern' solution that was described in Falqués *et al.* (2000) was stationary. However, there is no physical reason why migrating patterns could not emerge. In fact, in other problems of fluid mechanics where there is no preferred direction along a coordinate axis, instability modes that migrate along this axis can exist. An example can be found in case of thermal convection for binary mixtures between two horizontal planes at different temperatures: any horizontal direction is preferred and, however, migrating convection cells can form from instability modes (Knobloch & Moore, 1988). Of course, this type of solutions emerge in pairs, one migrating in one direction, the other migrating in the opposite direction.

Further studies with the model for normal wave incidence used in Falqués *et al.* (2000) have demonstrated that, in addition to that stationary solution, alongshore migrating solutions may also exist. A systematic study of them is beyond the scope of the present thesis, which is devoted to oblique wave incidence. However, a short description of these patterns is given in this appendix in order to favour the interpretation of the behaviour of the system for small incidence angle. These 'migrating crescentic patterns' found for normal wave incidence also occur in pairs, each one migrating with the same celerity but in opposite directions. The solution that moves in the positive (negative) y-axis direction will be referred to as mode B (A) because of its similarity with mode B1 (A1) in case of small wave incidence angle. The 'non-migrating crescentic pattern' will be referred to as mode C.
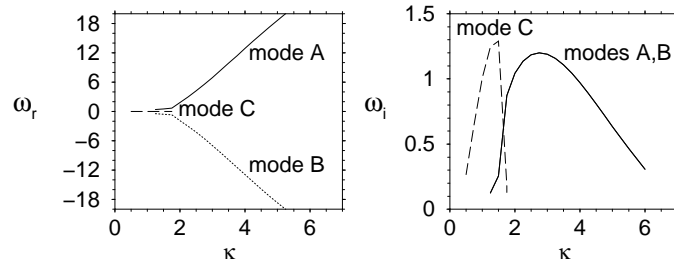
Figure D.1: Dispersion line and growth rate curve for $m = 1$ and $\alpha \sim D^2$ in case of normal wave incidence, $\theta_b = 0^o$, and a particular set of beach and wave parameters. All the variables are non-dimensional.

Figure D.1 shows the growth rate and dispersion curves in case of $m = 1$, $\alpha \sim D^2$ and $\theta = 0^o$ for a particular set of beach and wave parameters. The three solutions A, B and C are shown. Modes A and B have the same growth rates and their maximum wave number is about $\kappa_M \simeq 3.5$, very similar to the result found in case of small wave incidence angle ($\kappa_M \simeq 4$, see Fig. 5.5.14). Mode C does not migrate, $w_{rM} = 0$ and has a wave number smaller than the one of modes A and B. In this particular case, mode C has a dominant wave number about $\kappa_M \simeq 1.5$ (see Fig. D.1). Thus, it is clear than the two 'migrating crescentic patterns' found for slightly oblique waves (modes A1 and B1) correspond to the modes A and B of exactly normal wave incidence. An interesting finding is that the 'non-migrating pattern' (mode C) has not been recovered in case of small incidence angle. This is certainly due to the symmetry-breaking produced by the small obliqueness of wave incidence and has an important consequence for morphodynamical instabilities in case of exact normal wave incidence since some of the solutions might be physically unrealistic.

Figure D.2 show the non-dimensional topography and current perturbations of the two 'migrating crescentic patterns'. As it can be seen, both modes have a series of main shoals and troughs out of the surf zone and smaller ones alternating inside the surf zone. In this respect, they are similar to the stationary solution presented in Falqués *et al.* (2000). However, it becomes apparent that modes A and B show some distortion associated to the direction of migration, the outer shoals being sharper at the side of the propagation direction and more rounded on the other hand (and similarly for the troughs). The inner shoals are weaker, elongated and oblique with respect to the coastline: those of mode A being 'down-current oriented', those of mode B being 'up-current oriented'. A mirror reflection with respect to a cross-shore section maps A into B and vice-versa. This is in agreement with the theory of Hopf bifurcation for migrating solutions in other problems of fluid dynamics (Knobloch, 1996).

Striking enough, the direction of migration is fully consistent with the circulation pattern. Indeed, according to the bottom evolution equation (Eq. 5.6.2) in case of $m = 1$ with $\alpha$ constant beyond the breaking line, an offshore flow out of the surf zone produces accretion. Sure enough, for the stationary solution, C, and out of the surf zone, an offshore flow is found over the shoals and an onshore flow over the troughs. A similar current circulation

is found for mode A (B) but somewhat shifted in the direction of the negative (positive) y axis. The maximum accretion is no longer centered over the shoals but somewhat down or up along the coast. This shift is the reason for the migration of the solutions A and B in the negative and positive $y$ directions respectively.



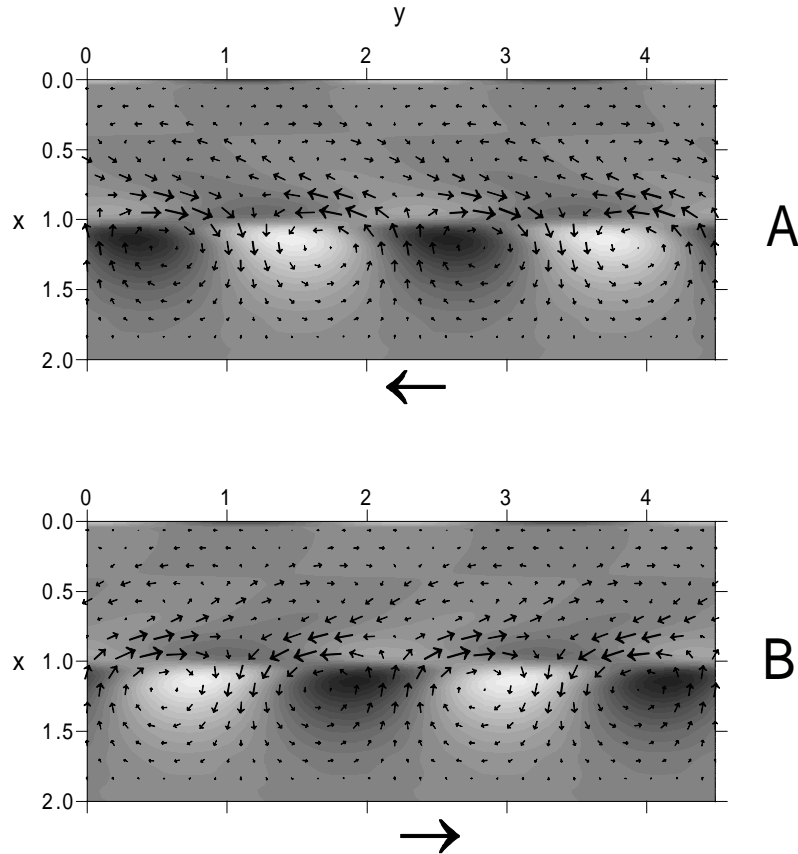Figure D.2: Example of a 'migrating crescentic pattern' in case of normal wave incidence. Non-dimensional topography and current perturbations corresponding to the maximum wave number of modes A (top) and B (bottom) for $m = 1$, $\alpha(x) \sim D^2$ and $\theta_b = 0^o$. These eigensolutions correspond to the instability curves displayed in Fig. D.1. The graph description is the same as in Fig. 5.5.2.

# Bibliography

AAGAARD, T. 1991 Multiple-bar morphodynamics and its relation to low-frequency edge waves. *J. Coastal Res.* **7**, 801–813.

AAGAARD, T., NIELSEN, J. & GREENWOOD, B. 1998 Suspended sediment transport and nearshore bar formation on a shallow intermediate-state beach. *Marine Geol.* **148**, 203–225.

ALLEN, J. R. L. 1984 *Sedimentary Structures*. Elsevier.

AMES, W. F. 1977 *Numerical Methods for Partial Differential Equations*. Orlando, U.S.A.: Academic Press.

ASHTON, A., MURRAY, A. B. & ARNAULT, O. 2001 Formation of coastline features by large-scale instabilities induced by high-angle waves. *Nature* **414**, 296–300.

BAGNOLD, R. A. 1963 Mechanics of marine sedimentation. In *The Sea* (ed. M. Hill), pp. 507–528. New York, U.S.A.: Wiley–Interscience.

BAILARD, J. A. 1981 An energetics total load sediment transport model for a plane sloping beach. *J. Geophys. Res.* **86** (C11), 10938–10954.

BAILARD, J. A. & INMAN, D. L. 1981 An energetics bedload model for a plane sloping beach: local transport. *J. Geophys. Res.* **86** (C3), 2035–2043.

BAKKER, W. T. 1968 A mathematical theory about sand waves and its application on the Dutch Wadden Isle of Vlieland. *Shore and Beach* **36** (2), 4–14.

BARCILON, A. I. & LAU, J. P. 1973 A model for formation of transverse bars. *J. Geophys. Res* **78** (15), 2656–2664.

BATTJES, J. A. 1975 Modeling of turbulence in the surfzone. In *Symp. on Modeling Techniques*, pp. 1050–1061.

BATTJES, J. A. & JANSSEN, J. P. F. M. 1978 Energy loss and set-up due to breaking of random waves. In *Coastal Eng. 1978* (ed. B. L. Edge), pp. 1993–2004. Am. Soc. of Civ. Eng.

BATTJES, J. A., SOBEY, R. J. & STIVE, M. J. F. 1990 Nearshore circulation. In *The Sea: Ocean Engineering Science,* vol. 9, pp. 469–493. John Wiley & Sons, Inc.

BAUER, B. & GREENWOOD, B. 1990 Modification of a linear bar-trough system by a standing edge wave. *Mar. Geol* **92**, 177–204.

BAYRAM, A., LARSON, M., MILLER, H. C. & KRAUS, N. C. 2001 Cross-shore distribution of longshore sediment transport: comparison between predictive formulas and field measurements. *Coastal Eng.* **44** (2), 79–99.

BIRKEMEIER, W. A. & HOLLAND, K. T. 2001 The corps of engineers' Field Research Facility: more than two decades of coastal research. *Shore & Beach* **69** (1), 3–12.

BLONDEAUX, P. 1990 Sand ripples under sea waves. Part 1. Ripple formation. *J. Fluid Mech.* **218**, 1–17.

BLONDEAUX, P. & SEMINARA, G. 1985 A unified bar-bend theory of river meanders. *J. Fluid Mech.* **157**, 449–470.

BOCZAR-KARAKIEWICZ, B., BONA, J. L. & COHEN, D. L. 1987 Interaction of shallow-water waves and bottom topography. In *Dynamical Problems in Continuum Physics,* vol. 4 (ed. J. Bona), pp. 131–176. Springer.

BOWEN, A. J. 1980 Simple models of nearshore sedimentation: Beach profiles and longshore bars. In *The Coastline of Canada* (ed. S. B. McCann), pp. 1–11 (Paper 80–10). Otawa, Canada: Geological Survey of Canada.

BOWEN, A. J. & INMAN, D. L. 1971 Edge waves and crescentic bars. *J. Geophys. Res.* **76**, 8662–8671.

BRÖKER, I., ROELVINK, J. A., SOUTHGATE, H., PECHON, P., NICHOLSON, J. & HAMM, L. 1992 Intercomparison of coastal profile models. In *Coastal Engineering 1992*, pp. 2108–2121. Reston, Va.: Am. Soc. of Civ. Eng.

BRUUN, P. 1954 Migrating sand waves or sand humps, with special reference to investigations carried out on the Danish North Sea Coast. In *Coastal Eng. 1954*, pp. 269–295. Grenoble, France: Am. Soc. of Civ. Eng.

CABALLERIA, M. 2000 Self-organization in the nearshore: shear waves, transverse and crescentic bars. PhD thesis, Appl. Physics Dept., Univ. Politècnica de Catalunya, Barcelona, Spain.

CABALLERIA, M., COCO, G. & FALQUÉS., A. 2003 Crescentic patterns and self-organization processes on barred beaches. In *Coastal Sediments 2003*. Am. Soc. of Civ. Eng., in press.

CABALLERIA, M., COCO, G., FALQUÉS, A. & HUNTLEY, D. A. 2002 Self-organization mechanisms for the formation of nearshore crescentic and transverse sand bars. *J. Fluid Mech.* **465**, 379–410.

CALVETE, D. 1999 Morphological stability models: Shoreface-connected sand ridges. PhD thesis, Appl. Physics Dept., Univ. Politècnica de Catalunya, Barcelona, Spain.

CALVETE, D. & DE SWART, H. E. 2003 Analysis of the long-term behaviour of shoreface-connected sand ridges: a nonlinear model study. *J. Geophys. Res.* **108** (C5), doi:10.1029/2001JC001091.

CALVETE, D., DODD, N. & FALQUÉS, A. 2003 Morphological development of nearshore bed-forms. In *Coastal Engineering 2002* (ed. J. M. Smith), , vol. 3, pp. 3321–3332. Singapure: World Scientific.

CALVETE, D., FALQUÉS, A., DE SWART, H. E. & WALGREEN, M. 2001 Modelling the formation of shoreface-connected sand ridges on storm-dominated inner shelves. *J. Fluid Mech.* **441**, 169–193.

CAMENEN, B. & LARROUDE, P. 1999 Nearshore and transport modelling: application to Trucvert Beach. In *Proc. 1$^{st}$ IAHR Symposium on River, Coastal and Estuarine Morphodynamics,* vol. 2, pp. 31–40. Italy.

CANUTO, C., HUSSAINI, M. Y., QUARTERONI, A. & ZANG, T. A. 1988 *Spectral Methods in Fluid Dynamics*. New York, U.S.A.: Springer–Verlag.

CHAPPEL, J. & ELIOT, I. G. 1979 Surf-beach dynamics in time and space - an Australian case study, and elements of a predictive model. *Mar. Geol.* **32**, 231–250.

CHRISTENSEN, E., DEIGAARD, R. & FREDSOE, J. 1994 Sea bed stability on a long straight coast. In *Coastal Eng. 1994,* vol. 4 (ed. B. L. Edge), pp. 1865–1879. New York, U.S.A.: Am. Soc. of Civ. Eng.

COCO, G., HUNTLEY, D. A. & O'HARE, T. J. 2000 Investigation of a self-organization model for beach cusp formation and development. *J. Geophys. Res.* **105** (C9), 21991–22002.

COLOMBINI, M., SEMINARA, G. & TUBINO, M. 1987 Finite–amplitude alternate bars. *J. Fluid Mech.* **181**, 213–232.

DALLY, W. R. 1987 Longshore bar formation - Surf beat or undertow? In *Coastal Sediments 1987*, pp. 71–86. Am. Soc. of Civ. Eng.

DAMGAARD, J., DODD, N., HALL, L. & CHESHER, T. 2002 Morphodynamic modelling of rip channel growth. *Coastal Eng.* **45**, 199–221.

DEAN, R. G. 1977 Equilibrium beach profiles: U.S. Atlantic and Gulf coasts. *Tech. Rep..* Delaware Univ., U.S.A.

DEAN, R. G. 1991 Equilibrium beach profiles: characteristics and application. *J. Coastal Res.* **7** (1), 53–84.

DEAN, R. G., SRINIVAS, R. & PARCHURE, T. M. 1992 Bar generation mechanisms. In *Coastal Engineering 1992*, pp. 2001–2014. Reston, Va.: Am. Soc. of Civ. Eng.

DEIGAARD, R. 1997 Comparison between a detailed sediment transport model and an energetics based formula. In *Coastal Dynamics 1997* (ed. E. B. Thornton), pp. 217–226. Reston, Va.: Am. Soc. of Civ. Eng.

DEIGAARD, R., DROONEN, N., FREDSOE, J., JENSEN, J. H. & JORGESEN, M. P. 1999 A morphological stability analysis for a long straight barred coast. *Coastal Eng.* **36**, 171–195.

DODD, N., BLONDEAUX, P., CALVETE, D., DE SWART, H. E., FALQUÉS, A., HULSCHER, S. J. M. H., ROZYNSKI, G. & VITTORI, G. 2002 The use of stability methods in understanding the morphodynamical behavior of coastal systems. *J. Coastal Res.* In press.

DODD, N., OLTMAN-SHAY, J. & THORNTON, E. B. 1992 Shear instabilities in the longshore current: a comparison of observation and theory. *J. Phys. Oceanogr.* **22** (1), 62–82.

DYHR-NIELSEN, M. & SORENSEN, T. 1970 Sand transport phenomena on coasts with bars. In *Coastal Eng. 1970*, pp. 855–866. New York, U.S.A: Am. Soc. of Civ. Eng.

ENGELUND, F. & FREDSOE, J. 1982 Sediment ripples and dunes. *Ann. Rev. Fluid Mechanics* **14**, 13–37.

EVANS, O. F. 1938 The classification and origin of beach cusps. *J. Geology* **46**, 615–627.

EVANS, O. F. 1939 Mass transportation of sediments on subaqueous terraces. *J. Geology* **47**, 325–334.

FALQUÉS, A. 1989 Formación de topografía rítmica en el Delta del Ebro. *Revista de Geofísica* **45** (2), 143–156.

FALQUÉS, A. 1991 A note on the Barcilon and Lau model for transverse bars. *Revista de Geofísica* **47**, 191–195.

FALQUÉS, A. 2003 On the diffusivity in coastline dynamics. *Geophys. Res. Lett.* In press.

FALQUÉS, A. & CALVETE, D. 2003 Shoreline sand waves and 1D coastal modelling. In *Coastal Sediments 2003*. Am. Soc. of Civ. Eng., in press.

FALQUÉS, A., COCO, G. & HUNTLEY, D. A. 2000 A mechanism for the generation of wave-driven rhythmic patterns in the surf zone. *J. Geophys. Res.* **105** (C10), 24071–24088.

FALQUÉS, A. & IRANZO, V. 1994 Numerical simulation of vorticity waves in the nearshore. *J.Geophys.Res.* **99** (C1), 825–841.

FALQUÉS, A., MONTOTO, A. & IRANZO, V. 1996 Bed-flow instability of the longshore current. *Cont. Shelf Res.* **16** (15), 1927–1964.

FALQUÉS, A., RIBAS, F., MONTOTO, A. & LARROUDE, P. 1999 Nearshore oblique bars. Modelling versus observations at the Truc Vert Beach. In *Proc. 1st IAHR symposium on River, Coastal and Estuarine Morphodynamics,* vol. 1, pp. 207–216.

FREDSOE, J. & DEIGAARD, R. 1992 *Mechanics of Coastal Sediment Transport*, 1st edn. Singapore: World Scientific.

GALLAGHER, E., ELGAR, S. & GUZA, R. T. 1998 Observations of sand bar evolution on a natural beach. *J. Geophys. Res.* **103** (C2), 3203–3215.

GOLDSMITH, V., BOWMAN, D. & KILEY, K. 1982 Sequential stage development of crescentic bars: Hahoterim beach, Southeastern Mediterranean. *J. Sediment. Petrol.* **52**, 233–249.

GOTTLIEB, D. & ORSZAG, S. D. 1977 *Numerical Analysis of Spectrals Methods: Theory and Applications*. Society for Industrial and Applied Mathematics.

GUILCHER, A., GODARD, A. & VISSEAUX, E. 1952 Les cretes et sillons obliques de l'estran des Landes de Gascogne. *Comite d'Oceanogr. et d'Etudes des Cotes Bull.* **4** (4), 151–157.

GUILLEN, J., STIVE, M. J. F. & CAPOBIANCO, M. 1999 Shoreline evolution of the Holland Coast on a decadal scale. *Earth Surf. Process. Landforms* **24**, 517–536.

Guza, R. T. & Bowen, A. 1975 The resonant instabilities of long waves obliquely incident on a beach. *J. Geophys. Res.* **80**, 4529–4534.

Hino, M. 1974 Theory on formation of rip-current and cuspidal coast. In *Coastal Eng. 1974*, pp. 901–919. New York, U.S.A.: Am. Soc. of Civ. Eng.

Hoefel, F. & Elgar, S. 2003 Wave-induced Sediment Transport and Sandbar Migration. *Science* **299**, 1885–1887.

Holman, R. A. & Bowen, A. J. 1982 Bars, bumps, and holes: models for the generation of complex beach topography. *J. Geophys. Res.* **87** (C1), 457–468.

Holman, R. A. & Sallenger, A. H. 1993 Sand bar generation: A discussion of the Duck experiment series. *J. Coastal Res.,* Special Issue **15**, 76–92.

Horikawa, K. 1988 *Nearshore Dynamics and Coastal Processes*. Tokio: University of Tokio Press.

Hulscher, S. J. M. H. 1996 Tidal-induced large-scale regular bed form patterns in a three-dimensional shallow water model. *J. Geophys. Res.* **101** (C9), 20727–20744.

Hulscher, S. J. M. H., de Swart, H. E. & de Vriend, H. J. 1993 The generation of offshore tidal sand banks and sand waves. *Cont. Shelf Res.* **13** (11), 1183–1204.

Hulscher, S. J. M. H., Falqués, A., Ribas, F. & Plant, N. G. 2001 Asymptotic behaviour of a coupled waveheigth-depth model near the coastline. In *Proc. 2ⁿᵈ IAHR Symposium on River, Coastal and Estuarine Morphodynamics* (ed. S. Ikeda), pp. 345–354. Obihiro, Japan.

Hunter, R. E., Clifton, H. E. & Phillips, R. L. 1979 Depositional processes, sedimentary structures, and predicted vertical sequences in barred nearshore systems, Southern Oregon coast. *J. Sediment. Petrol.* **49** (3), 711–726.

Huthnance, J. M. 1982 On one mechanism forming linear sand banks. *Estuarine Coastal Shelf Sci.* **14**, 79–99.

Inman, D. L., Elwany, M. H. S., Khafagy, A. A. & Golik, A. 1992 Nile delta profiles and migrating sand blankets. In *Coastal Eng. 1992* (ed. B. L. Edge), pp. 3273–3284. Reston, Va.: Am. Soc. of Civ. Eng.

Inman, D. L. & Guza, R. T. 1982 The origin of swash cusps on beaches. *Mar. Geol.* **49**, 133–148.

Kajima, R., Shimizu, T., Maruyama, K. & Saito, S. 1982 Experiments on beach profile change with a large wave flume. In *Coastal Eng. 1982*, pp. 1385–1404. New York, U.S.A.: Am. Soc. of Civ. Eng.

King, C. A. M. & Williams, W. W. 1949 The formation and movement of sand bars by wave action. *Geogr. J.* **113**, 70–85.

Kit, E. & Pelinovski, E. 1998 Dynamical models for cross-shore transport and equilibrium bottom profiles. *J. Waterway, Port, Coastal and Ocean Eng.* **124** (3), 138–146.

Knobloch, E. 1996 Symmetry and instability in rotating hydrodynamic and magneto hydrodynamic flows. *Physics of Fluids* **8** (6), 1446–1454.

KNOBLOCH, E. & MOORE, D. R. 1988 Linear stability of experimental Soret convection. *Phys. Review A* **37** (3), 860–870.

KOMAR, P. D. 1998 *Beach Processes and Sedimentation*, 2nd edn. Prentice Hall.

KONICKI, K. M. & HOLMAN, R. A. 2000 The statistics and kinematics of transverse bars on an open coast. *Mar. Geol.* **169**, 69–101.

KROON, A. 1994 Sediment transport and morphodynamics of the beach and nearshore zone near Egmond. PhD thesis, Utrecht Univ., Utrecht, The Netherlands.

KUENEN, P. H. 1948 The formation of beach cusps. *J. Geology* **56**, 34–40.

LAFON, V., DUPUIS, H., HOWA, H. & FROIDEFOND, J. M. 2002 Determining ridge and runnel longshore migration rate using spot imagery. *Oceanologica Acta* **25**, 149–158.

LARSON, M. 1988 Quantification of beach profile change. *Tech. Rep.* 1008. Institute of science and technology, Lund University, Lund, Sweden.

LIPPMANN, T. C. & HOLMAN, R. A. 1989 Quantification of sand bar morphology: a video technique based on wave dissipation. *J. Geophys. Res.* **94** (C1), 995–1011.

LIPPMANN, T. C. & HOLMAN, R. A. 1990 The spatial and temporal variability of sand bar morphology. *J. Geophys. Res.* **95** (C7), 11575–11590.

LIPPMANN, T. C., HOLMAN, R. A. & HATHAWAY, K. K. 1990 Episodic, non-stationary behavior of a two sand bar system at Duck, NC, USA. *J. Coastal Res.* **15**, 49–75.

LONGUET-HIGGINS, M. S. 1952 On the statistical distribution of the heights of sea waves. *J. Marine Res.* **XI** (3), 245–266.

LONGUET-HIGGINS, M. S. 1970 Longshore currents generated by obliquely incident sea waves. *J. Geophys. Res* **75** (33), 6778–6801.

LOPEZ, J. M. & MARQUÉS, F. 2000 Quasiperiodic response to parametric excitations. In *Numerical Methods for Bifurcation Problems and Large-Scale Dynamical Systems* (ed. E. Doebel & L. S. Tuckerman), pp. 209–227. Springer.

MARQUÉS, F. & LOPEZ, J. M. 2000 Spatial and temporal resonances in a periodically forced hydrodynamic system. *Physica D* **136**, 340–352.

MASSELINK, G. & BLACK, K. P. 1995 Magnitude and cross-shore distribution of bed return flow measured on natural beaches. *Coastal Eng.* **25**, 165–190.

MEI, C. C. 1985 Resonant reflection of surface water waves by periodic sandbars. *J. Fluid Mech.* **152**, 315–335.

MEI, C. C. 1989 *The Applied Dynamics of Ocean Surface Waves*. Singapore: World Scientific.

MICHEL, D. & HOWA, H. L. 1999 Short-term morphodynamic response of a ridge and runnel system on a mesotidal sandy beach. *J. Coastal Res.* **15** (2), 428–437.

NIEDERODA, A. W. & TANNER, W. F. 1970 Preliminary study on transverse bars. *Mar. Geol.* **9**, 41–62.

PATTIARATCHI, C. & COLLINS, M. 1987 Mechanisms for linear sandbank formation and maintenance in relation to dynamical oceanographic observations. *Prog. Oceanog.* **19**, 117–156.

PEDLOSKY, J. 1987 *Geophysical Fluid Dynamics*. Berlin: Springer–Verlag.

PETERS, K., NEWE, J. & OUMERACI, H. 2001 Characterization of sediment transport. In *Coastal Dynamics 2001* (ed. H. Hanson & M. Larson), pp. 293–302. Reston, Va.: Am. Soc. of Civ. Eng.

PHILLIPS, O. M. 1977 *The Dynamics of the Upper Ocean*. Cambridge: Cambridge University Press.

PLANT, N. G., FREILICH, M. H. & HOLMAN, R. A. 2001*a* Role of morphologic feedback in surf zone sandbar response. *J. Geophys. Res.* **106** (C1), 973–989.

PLANT, N. G., HOLMAN, R. A., FREILICH, M. H. & BIRKEMEIER, W. A. 1999 A simple model for interannual sandbar behavior. *J. Geophys. Res.* **104** (C7), 15755–15776.

PLANT, N. G., RUESSINK, B. G. & WIJNBERG, K. M. 2001*b* Morphologic properties derived from a simple cross-shore sediment transport model. *J. Geophys. Res.* **106** (C1), 945–962.

RAUBENHEIMER, B., GUZA, R. T. & ELGAR, S. 1996 Wave transformation across the inner surf zone. *J. Geophys. Res.* **101** (C10), 25589–25597.

RENIERS, A. J. H. M., ROELVINK, J. A. & THORNTON, E. B. 2003 Morphodynamic modeling of an embayed beach under wave group forcing. *J.Geophys.Res.* Submitted.

RIBAS, F., FALQUÉS, A., HULSCHER, S. J. M. H. & PLANT, N. G. 2003*a* Dynamics and stability of cross-shore beach profiles. *J. Geophys. Res.* In preparation.

RIBAS, F., FALQUÉS, A. & MONTOTO, A. 2000*a* Normal mode analysis of the surf zone morphodynamics. In *Coastal Eng. 2000* (ed. B. L. Edge), pp. 3229–3242. Reston, Va.: Am. Soc. of Civ. Eng.

RIBAS, F., FALQUÉS, A. & MONTOTO, A. 2003*b* Nearshore oblique sand bars. *J. Geophys. Res.* **108** (C4), 3119, doi:10.1029/2001JC000985.

RIBAS, F., FALQUÉS, A., PLANT, N. G. & HULSCHER, S. J. M. H. 2001 Self-organization in surf zone morphodynamics: alongshore uniform instabilities. In *Coastal Dynamics 2001* (ed. H. Hanson & M. Larson), pp. 1068–1077. Reston, Va.: Am. Soc. of Civ. Eng.

RIBAS, F., MONTOTO, A. & FALQUÉS, A. 2000*b* Sensitivity of rhythmic oblique bar generation to wave-driven turbulence in the surf zone. In *Proc. $8^{th}$ European Turbulence Conf.: Advances in turbulence*, pp. 375–378.

ROELVINK, J. A. & BROKER, I. 1993 Cross-shore profile models. *Coastal Eng.* **21**, 163–191.

ROELVINK, J. A. & STIVE, M. J. F. 1989 Bar-generating cross-shore flow mechanisms on a beach. *J. Geophys. Res.* **94** (C4), 4785–4800.

RUESSINK, B. G., HOUWMAN, K. T. & HOEKSTRA, P. 1999 Medium-term frequency distributions of cross-shore suspended sediment transport rates in water depth of 3 to 9 m. *Coastal Eng.* **38**, 25–46.

RUESSINK, B. G. & KROON, A. 1994 The behavior of a multiple bar system in the nearshore zone of Terschelling, The Netherlands, 1965-1993. *Mar. Geol.* **21**, 187–197.

RUESSINK, B. G. & TERWINDT, J. H. J. 2000 The behaviour of nearshore bars on the time scale of years: a conceptual model. *Mar. Geol.* **163**, 289–302.

RUESSINK, B. G., VAN ENCKEVORT, I. M. J., KINGSTON, K. S. & DAVIDSON, M. A. 2000 Analysis of observed two- and three-dimensional nearshore bar behaviour. *Mar. Geol.* **169**, 161–183.

RUSSELL, R. J. & MCINTIRE, W. G. 1965 Beach cusps. *Geol. Soc. Am. Bull.* **76**, 307–320.

SCHAFFER, H. A. 1994 Edge waves forced by short-wave groups. *J. Fluid Mech.* **259**, 125–148.

SCHIELEN, R. R., DOELMAN, A. & DE SWART, H. E. 1993 On the dynamics of free bars in straight channels. *J. Fluid Mech.* **252**, 325–356.

SEMINARA, G. 1995 Invitation to river morphology. In *Nonlinear Dynamics and Pattern Formation in the Natural Environment* (ed. A. Doelman & A. van Harten), pp. 269–294. Reading, Mass.: Addison-Wesley-Longman.

SHORT, A. D. 1975 Multiple offshore bars and standing waves. *J. Geophys. Res.* **80** (3838), 3840.

SHORT, A. D. 1994 Coastal photograph. *J. Coastal Res.* **10** (1), 250.

SHORT, A. D. 1999 *Handbook of Beach and Shoreface Morphodynamics*. Chichester: Wiley.

SLEATH, J. F. A. 1984 *Sea Bed Mechanics*. Wiley.

SONU, C. J. 1968 Collective movement of sediment in littoral environment. In *Coastal Eng. 1968*, pp. 373–400. Am. Soc. of Civ. Eng., New York, U.S.A.

SOULSBY, R. 1997 *Dynamics of Marine Sands*. Thomas Telford Publications.

STIVE, M. J. F. 1986 A model for cross-shore sediment transport. In *Coastal Eng. 1986* (ed. B. L. Edge), pp. 1550–1564. Am. Soc. of Civ. Eng.

STIVE, M. J. F. & RENIERS, A. J. H. M. 2003 Sandbars in motion. *Science* **299**, 1855–1856.

TAPIA, I. M. 2003 Cross-shore sediment transport processes on natural beaches and their relation to sandbar migration patterns. PhD thesis, Plymouth Univ., Plymouth, U.K.

THEVENOT, M. M. & KRAUS, N. C. 1995 Longshore sandwaves at Southampton Beach, New York: observations and numerical simulation of their movement. *Mar. Geology* **126**, 249–269.

THORNTON, B. & GUZA, R. T. 1983 Transformation of wave height distribution. *J. Geophys. Res.* **88** (10), 5925–5938.

THORNTON, B. & HUMISTON, R. T. 1996 Bar/trough generation on a natural beach. *J. Geophys. Res.* **101** (C5), 12097–12110.

TROWBRIDGE, J. H. 1995 A mechanism for the formation and maintenance of shore-oblique sand ridges on storm-dominated shelves. *J. Geophys. Res.* **100** (C8), 16071–16086.

VAN ENCKEVORT, I. M. J. 2001 Daily to yearly nearshore bar behaviour. PhD thesis, Netherlands Geographical Studies, Utrecht Univ., Utrecht, The Netherlands.

VAN RIJN, L. C. 1993 *Principles of Sediment Transport in Rivers, Estuaries and Coastal Seas*. Amsterdam, The Netherlands: Aqua Publications.

VERHAGEN, H. J. 1989 Sand waves along the dutch coast. *Coastal Eng.* **13**, 129–147.

VITTORI, G. & BLONDEAUX, P. 1990 Sand ripples under sea waves. Part 2. Finite amplitude development. *J. Fluid Mech.* **218**, 19–39.

VITTORI, G., DE SWART, H. E. & BLONDEAUX, P. 1999 Crescentic bedforms in the nearshore region. *J. Fluid Mech.* **381**, 271–303.

WERNER, B. T. & FINK, T. M. 1993 Beach cusps as self-organized patterns. *Science* **260**, 968–971.

WIJNBERG, K. M. & KROON, A. 2002 Barred beaches. *Geomorphology* **48**, 103–120.

WIJNBERG, K. M. & TERWINDT, J. H. J. 1995 Extracting decadal morphological behavior from high–resolution, long-term bathymetric surveys along the Holland coast using eigenfunction analysis. *Mar. Geol.* **126**, 301–330.

WINANT, C. D., INMAN, D. L. & NORDSTROM, C. E. 1975 Description of seasonal beach changes using empirical eigenfunctions. *J. Geophys. Res.* **80** (15), 1979–1986.

WRIGHT, L. D., CHAPPELL, J., THOM, B. G., BRADSHAW, M. P. & COWELL, P. J. 1979 Morphodynamics of reflective and dissipative beach and inshore systems, Southeastern Australia. *Mar. Geol.* **32**, 105–140.

WRIGHT, L. D. & SHORT, A. D. 1984 Morphodynamic variability of surf zones and beaches: a synthesis. *Mar. Geol.* **56**, 93–118.

YOYOKI, H., LARSON, M. & HANSON, H. 2002 Rhythmic features along Sylt Island, Germany. *Tech. Rep.*. Water Resources Engineering, Lund Univ., Lund, Sweden.

YU, J. & MEI, C. C. 2000 Formation of sand bars under surface waves. *J. Fluid. Mech.* **416**, 315–348.

# Summary of the thesis

In spite of the complex behaviour in space and time of the surf zone dynamics, relatively regular morphological patterns dominate quite often the beach topography at length and time scales well above those of incident waves. Well known examples are giant beach cusps, shore-parallel bars, crescentic longshore bars and shore-attached transverse/oblique bar systems. Their regularity indicates that the large scale complex dynamics of the surf zone as a whole can be understood in terms of simple physical mechanisms, at least in some circumstances. Remarkably, after decades of research, no model has been widely accepted to explain the origin and migration of these intriguing large-scale morphological patterns. Understanding the behaviour of nearshore sand bars is not only challenging from a scientific point of view but also very interesting for testing sediment transport formulations with engineering purposes.

The main goal of this thesis is to investigate theoretically some physical processes that can be responsible for the shape of equilibrium profiles and the origin and dynamics of nearshore sand bars (in particular, shore-parallel bars and alongshore rhythmic systems of oblique bars are studied). This may fill some of the existing gaps of our current knowledge about these topographic features. The main working hypothesis is that these bars stem from 'free instabilities' of the morphodynamical system. A stability analysis is performed for each type of bar system, starting from a steady equilibrium configuration of the beach without the pattern. A small topographic perturbation is then assumed and its effects on the hydrodynamics and on the sediment transport are investigated. If the transport pattern reinforces the topographic perturbation, a 'positive feedback' occurs between the topography and the flow. This results in what is called a 'free instability' of the system or a 'self-organization process'. It can provide an explanation for the emergence of morphological patterns not associated to any previous regular template in the hydrodynamics.

The first model is focused on describing the shape of equilibrium beach profiles and the growth and migration of shore-parallel bars, assuming alongshore uniformity. A wave transformation equation, describing the shoaling and breaking processes of normally incident random waves, is coupled with an innovatory cross-shore sediment transport formula containing three terms: an onshore contribution due to non-linear wave properties, an offshore contribution due to undertow currents and a term accounting for the downslope gravitational effect. These three latter processes are the basis of the so-called 'breakpoint-bar interaction', which has been claimed to be an explanation for the formation of shore-parallel bars. In chapter 3 of the present thesis, this model is used to predict equilibrium beach profiles, which resemble natural non-barred beaches. In case of very dissipative conditions (storm weather and fine sediment), profiles consist of a gently sloping terraced surf zone

and a concave-up shoaling zone. For less dissipative conditions, the entire profile gradually becomes more planar with similar surf zone and shoaling zone slopes.

Chapter 4 presents a complete stability analysis of such equilibrium profiles with respect to arbitrary cross-shore perturbations. The aim is not only finding the range of parameter values leading to stable equilibrium profiles, but also testing whether shore-parallel bars can stem as free instabilities of the system. Results demonstrate that the equilibrium profiles are always stable, both in the linear and in the non-linear regimes. Therefore, the terraced non-barred profiles seem to be a strong attractor of this dynamical system and more attention should be paid to their frequent occurrence on natural beaches. The results of the linear stability analysis indicate that a 'Dirac delta instability' tries to emerge at the effective break-point of the equilibrium profiles. However, its growth is always inhibited by the downslope transport that is induced by the inherent infinite slopes. The non-linear temporal evolutions subsequently performed also tend to final states that correspond to the equilibrium non-barred profiles. Even starting from initial states moderately far from equilibrium and allowing for a potential shoreline migration, this idealised version of the 'breakpoint-bar interaction' is only able to reproduce the formation of terraces. Therefore, verifying quantitatively that this interaction can be responsible for the growth of natural shore-parallel bars still remains as an important open question in the nearshore sciences.

Finally, the second model presented in chapter 5 aims at reproducing the formation of alongshore rhythmic systems of oblique sand bars, starting from the same equilibrium non-barred profiles but now allowing for alongshore non-uniformities. The potential coupling between the time- and depth-averaged hydrodynamics and the evolving rhythmic topography is examined in case of oblique wave incidence. The used classical sediment transport law is proportional to a power of the depth-averaged current and contains some influence of the waves. In this case, it is shown that 'positive feedback' can occur and the different studied underlying physical mechanisms lead to the initial growth of several types of oblique bars. Results mainly depend on the sediment transport conditions and the wave incidence angle. In qualitative agreement with available field observations, for moderately large incidence angles and transport dominated by the mean currents, the emerging bars are 'oriented down-current'. This means that their offshore end is shifted down-stream of the equilibrium longshore current with respect to their shore attachment. Their orientation is very oblique, that is to say that the bars are nearly shore-parallel. The wave lengths are of the order of several times the surf zone width. In the opposite situation, when mean currents are weak compared with wave orbital motions, either 'up-current oriented bars' or 'crescentic/down-current oriented bars' can occur. This depends on the wave incidence angle and on the influence of infragravity waves into the transport. In both cases, the wave lengths are similar to the surf zone width. The e-folding growth times of all these patterns range from a few hours to a few days and they migrate down-flow with velocities that can be up to some few meters per day. The conditions favouring the generation of these rhythmic bar systems are steady waves and intermediate beach states, in between the fully dissipative and the fully reflective situations.

# Resum de la tesi

La zona de rompents de les platges està governada per una gran quantitat de processos complexes altament no lineals i a diverses escales de longitud i de temps. Tot i això, algunes vegades s'hi poden trobar estructures morfològiques regulars, com ara punts cuspidals, barres de sorra uniformes en la direcció longitudinal, barres crescèntiques i sistemes rítmics de barres obliqües. La seva regularitat indica que la dinàmica complexa de la zona de rompents a gran escala pot ser explicable en termes de mecanismes físics simples en certes circumstàncies. L'origen i les propietats dinàmiques d'aquestes curioses estructures morfològiques encara són un problema obert, tot i que la comunitat científica hi està interessada des de fa dècades. En particular, descriure el comportament de les barres de sorra a la zona de rompents és interessant tant des d'un punt de vista científic, com per a contrastar les fórmules de transport de sediment que s'utilitzen actualment en enginyeria de costes.

L'objectiu principal d'aquesta tesi és l'estudi teòric d'alguns mecanismes físics que podrien ser responsables de la forma dels perfils d'equilibri de les platges i de l'origen i la dinàmica de les barres de sorra a la zona de rompents (en concret, les barres longitudinals i els sistemes rítmics de barres obliqües). Es pretén així omplir alguns dels buits de coneixement actuals sobre aquestes formes topogràfiques. La principal hipòtesi de treball és que els dos tipus de barres es poden formar per 'processos d'auto-organització'. El procediment consisteix en realitzar una anàlisi d'estabilitat per a cada tipus de barra, seguint els passos següents. Primerament es busca un estat d'equilibri rellevant del sistema sense les formes morfològiques. Aleshores s'afegeix una pertorbació a la topografia i s'estudien els efectes que produeix en la hidrodinàmica i en el transport de sediment. Si el transport resultant reforça la pertorbació inicial, s'obté una reacció de 'retro-alimentació positiva' i les barres creixen. Això és el que s'anomena un 'procés d'auto-organització' del sistema o un 'mecanisme d'inestabilitat' i podria ser una explicació de l'aparició d'aquestes estructures morfològiques complexes, sense estar associades a cap patró regular previ en la hidrodinàmica.

El primer model teòric que es presenta en aquesta tesi s'ha construit per a descriure la forma dels perfils d'equilibri i la formació i migració de barres longitudinals, assumint uniformitat en la direcció longitudinal. El model està basat en una equació d'evolució de l'onatge acoblada a una innovadora fórmula pel transport de sediment transversal. La primera equació descriu la transformació i posterior ruptura d'onades d'alçada aleatòria i incidència perpendicular. La fórmula pel transport conté tres termes sumats: el transport cap a la costa a causa de les propietats no lineals de les onades, el transport cap al mar produït pels corrents de retorn i el transport gravitacional pendent avall. Aquests tres processos són la base d'un mecanisme físic d''interacció entre la barra i el punt de ruptura', que podria ser l'explicació pel creixement de barres longitudinals de sorra. Al capítol 3 de

la tesi es descriuen els resultats d'aquest model quan s'imposen condicions d'equilibri. Els perfils que s'obtenen són similars als de les platges naturals i consisteixen en una terrassa plana i amb poc pendent dins la zona de rompents i una part còncava més inclinada més enllà del punt de ruptura. Quan el sediment és gruixut i les onades incidents són de freqüència baixa (situació típica de platges reflectives), els perfils tenen força pendent i una zona de rompents estreta. Quan la sorra és més fina i les onades són d'alta freqüència (platges més dissipatives), la zona de rompents és molt més ampla i plana i el pendent és menor.

Al capítol 4 es presenta una anàlisi complerta de l'estabilitat d'aquests perfils d'equilibri respecte pertorbacions uniformes longitudinalment. Els dos objectius principals són trobar el rang de paràmetres en el qual els estats d'equilibri són estables i posar a prova la hipòtesi de si les barres longitudinals poden aparèixer com a inestabilitats del sistema. Els resultats demostrenque tots els perfils d'equilibri obtinguts són estables, tant en el règim lineal com en el no lineal. Per tant, les platges amb terrassa semblen ser forts atractors dinàmics del sistema i caldria estudiar amb més atenció la seva freqüent presència a les platges naturals. Els resultats del model lineal indiquen que una 'inestabilitat de tipus delta de Dirac' podria sorgir a prop del punt de ruptura, però el seu creixement queda sempre inhibit pel transport gravitacional produït pels forts pendents associats. Les evolucions temporals no lineals realitzades posteriorment també tendeixen a estats finals que corresponen als perfils d'equilibri sense barres. Fins i tot començant des d'estats inicials força allunyats de l'equilibri i permetent una possible migració de la línia de costa, aquesta versió idealitzada del mecanisme d'"interacció entre la barra i el punt de ruptura' només ha permès descriure platges amb terrassa. Per tant, verificar quantitativament que el creixement de barres longitudinals pot ser degut a aquest mecanisme encara és un important problema obert de la física del litoral.

Finalment, el segon model presentat al capítol 5 intenta reproduir la formació de sistemes rítmics de barres obliqües, partint dels mateixos perfils d'equilibri sense barres però ara permetent l'aparició d'inestabilitats no uniformes en la direcció longitudinal. El possible acoblament entre les estructures hidrodinàmiques en el pla horitzontal i la topografia emergent s'examina pel cas d'incidència obliqua de l'onatge. S'utilitza una fórmula clàssica de transport de sediment proporcional a diferents potències del corrent mitjà i amb una certa influència de les onades. En aquest cas, es demostra que pot existir 'retro-alimentació positiva' i que els diferents mecanismes físics descrits poden explicar el creixement inicial de diversos tipus de sistemes rítmics com els que s'observen en les platges naturals. Els resultats depenen principalment del tipus de transport de sediment dominant i de l'angle d'incidència de les onades. En el cas d'angles d'incidència relativament grans i transport dominat pels corrents mitjans, s'obtenen 'barres orientades a favor del corrent'. Això significa que el costat de mar de les barres està desplaçat corrent avall respecte el costat de terra. La orientació és molt obliqüa, o sigui que les barres són gairebé paral·leles a la línia de costa. La seva longitud d'ona és de diverses vegades l'amplada de la zona de rompents. En cas contrari, quan els corrents mitjans són febles comparats amb la velocitat orbital de les onades, poden créixer 'barres orientades a contra-corrent' o bé 'barres crescèntiques orientades a favor del corrent', depenent de l'angle d'incidència i de la influència de les ones infragravitatòries en el transport. En tots dos casos, l'espaiat és de l'ordre de l'amplada de la zona de rompents. El temps típic de creixement oscil·la entre diverses hores i un parell de dies i les barres migren a favor del corrent amb velocitats fins a desenes de metres per dia. Les condicions que afavoreixen la formació d'aquests sistemes rítmics de barres són onatge regular i estats morfodinàmics intermitjos (situacions ni molt dissipatives ni molt reflexives).

# Agraïments

*'El lema de la il·lustració és doncs: Sapere aude!*
*Tingues la valentia d'utilitzar la teva pròpia raó!'*

De *Resposta a la pregunta: Què és la il·lustració?*,
Immanuel Kant

El lema *'Sapere aude!'* és especialment aplicable a l'evolució que tot doctorant ha de sofrir en el seu procés de formació. Durant aquests anys d'estudi i d'elaboració de la tesi he hagut de recórrer un llarg camí en aquest sentit, i no només en el camp de la recerca sinó també (i gosaria dir, principalment) en el terreny personal. En aquesta travessa he tingut la sort d'estar acompanyada de persones fantàstiques que, a part de col·laborar en la meva formació com a persona, li han donat sentit a aquest caminar. I per això vull expressar el meu apreci i agraïment...

... a l'Albert, per ser el principal responsable que aquesta tesi existeixi, pel seu entusiasme per la ciència i pel seu suport incondicional al meu treball. És remarcable el fet que, tot i el poc temps de què disposa, sempre sigui accessible i pacient amb tots els que treballem amb ell, encomanant el seu optimisme desbordant. Com a petit exemple, transcric una sàvia frase que em va escriure damunt del manuscrit de tesi mentre el corregia (cap al final del capíol 4) i que em va fer riure una bona estona: *'Al cap i a la fi, tothom sap que els millors bars són els que tenen terrassa!'*.

... als companys del grup de recerca dels *morfos* pel seu companyerisme indiscutible, sempre intentant fer més fàcil el camí dels altres: a l'Amadeu perquè la seva tesi és la llavor de totes les altres i per haver-la escrit d'una manera amena i amable, al Miquel i al Daniel per ser dos referents molt importants per mi, tant per la seva manera de treballar com per les seves respectives tesis, i a la Iolanda perquè a part de ser una companya imprescindible de despatx i de congressos, és una germana que escolta i explica i un exemple de lluita (vull donar-li les gràcies especialment per la seva part de culpa en les darreres aventures viscudes a Nicaragua i tot el que això significa). L'arribada del *morfo* més recent, el Roland, amb una bona dosi de curiositat i d'alegria, ha sigut una alenada d'aire fresc pel grup.

... als altres precaris i precàries del Departament de Física Aplicada de la UPC: el David, l'Àlex, l'Andreea, els gueros, tots els *complex*, l'Eloi, la Pilar, el Ricard i més recentment, la Verónica i l'Hadrian, perquè aquests anys no haurien sigut el mateix sense tots els cafès, les sobretaules, els sopars i les *fistukis*. Alguns d'ells han sigut (i espero que continuaran essent) molt més que companys de feina. Un reconeixement molt especial pel David, per haver sigut el meu padrí de doctorat, estant sempre disposat a respondre infinites preguntes sobre Unix, L^ATEX, Fortran i mètodes numèrics, i perquè les nostres llargues discussions sobre política, sobre el funcionament de la universitat i sobretot, sobre la vida, m'han ajudat molt a créixer.

... a la resta de membres del Departament per les facilitats rebudes i pel tracte amable, especialment als companys i companyes del grup de fluids, i a la Sílvia, la Rosa, l'Amador, el Josep, el Joan Ramon, el Fernando, el Javi, l'Àngel i l'Esther, per la seva competència i bona voluntat, que han sigut essencials en molts moments.

One of the duties of a PhD candidate is to collaborate with foreigner researchers, which I have fulfilled with great pleasure. I made two research stays abroad, one at the University of Twente, in The Netherlands, and another at the Naval Research Laboratory, in U.S.A. I want to thank Suzanne Hulscher and Nathaniel Plant for the perfect organization of these stays, for all the subsequent years of fruitful collaboration and for their teachings about how to present and sell scientific results. Their optimism and faith on my research projects have been essential stones in the building of this thesis. I also appreciate the hospitality of all the people I met in these institutions. The economic support of both the University of Twente and the Naval Research Laboratory during these stays is gratefully acknowledged, together with the staff at the Field Research Facility in Duck, U.S.A., for their tireless efforts that provided the bathymetric profiles and wave conditions cited in this thesis.

I feel very lucky for all the interesting and funny people I have met during these years. Giovanni Coco has appeared and disappeared often in my way, always leaving a wonderful flavour of happiness and passion for his profession and for the Jazz music. I highly appreciate the interest that Huib de Swart has always shown for my work. His professional way of doing research has been an important reference for me. I also thank the kindness and hospitality of his whole group at the University of Utrecht, The Netherlands. The research presented in this thesis has been carried out in the framework of two European projects, the SASME and the HUMOR. Apart from acknowledging the financial support received from the European commission, I am grateful for all the meetings and discussions with the other involved researchers. I have specially appreciated the conversations with Aart Kroon, Miguel Losada and Nick Dodd.

I attended two research courses: the *10<sup>th</sup> National Summer School on Geophysical and Environmental Fluid Dynamics* at the Cambridge University, U.K., and the *International Summer Course on Hydro- and Morphodynamics of Coastal Seas* in Renesse, The Netherlands. I want to thank the organizers and professors of both courses for their enthusiastic way of teaching and for encouraging (and forcing!) the students to communicate and collaborate, both in a scientific and in a human sense. The last two years, three Dutch students developed part of their career at our university: Nicolette, Saskia and Danielle. Meeting them has been a never-ending source of inspiration and new ideas.

També vull agrair al Ministerio de Ciencia y Tecnología el finançament dels diversos projectes del nostre grup i a la Generalitat de Catalunya la beca de recerca que ha fet possible aquesta tesi. No obstant, voldria deixar constància del meu desacord en la política científica que estan aplicant aquestes dues institucions, per la poca inversió i la mala distribució dels recursos. En especial, l'actual sistema de finançament en forma de beques dels investigadors en formació és el responsable de la precarietat laboral en què han de desenvolupar la seva professió. Aquest col·lectiu, que és la base dels projectes de recerca del nostre país, realitza una tasca professional que hauria d'estar regulada mitjançant contractes laborals amb totes les prestacions socials.

Darrera d'aquesta tesi hi ha moltes hores passades en solitud davant de les equacions i de l'ordinador. I és poc probable que hagués sobreviscut a totes les preguntes, dubtes i pors, si no fos per les fonts de vida que sovint m'han rescatat de la ciència i m'han ajudat a posar els peus sobre la terra. M'agradaria deixar una petita (i segurament incomplerta) mostra d'amistat i agraïment...

... als companys i companyes de *D-Recerca* i de *Precarios*, per la seva fe en la possibilitat de millorar la societat i per totes les hores i energies invertides en intentar-ho. Gràcies especialment al Xavi i l'Eduard, per ser els pares de tota la moguda, i a la Teresa, l'Ana, l'Elisenda, l'Hèctor, l'Òscar, el Miquel, la Maria, l'Ignasi, la Mar, la Pastora, el Toni, la Cristina i la Marta, per ser els millors companys de trifulgues polítiques.

... als *fisikets*, per ser els companys de carrera més divertits, fent amens fins i tot els moments més durs d'estudi. Gràcies especialment al Carles i al Sergio, per totes les estones i alegries compartides.

... als cantaires de la coral Cantiga, per les inoblidables hores passades entre assaigs i concerts. Gràcies especialment a la Claudia, al Joan, al Carles i a l'Alfredo, per haver esdevingut essencials en la meva vida, i al Pep, per la seva dedicació apassionada a la feina i per ser un dels culpables del despertar de la meva sensibilitat musical.

... a les directores i directors de la coral infantil El Virolet, pel seu entusiasme i energia, que esquitxa als qui els envolten i per ser un exemple remarcable de feina ben feta sense esperar res a canvi. Un reconeixement molt especial per la Clara, la Marta i el Pablo, que han sigut els meus mestres en aquest terreny.

... al Jordi i a la Lala, no només per ser uns grans mestres i continuar vetllant per mantenir desperta la sensibilitat de tants alumnes i ex-alumnes, sinó sobretot, per ser la seva vida un referent inqüestionable per tots nosaltres.

... al Xavi, per ajudar-me a despertar de l'endormiscament dogmàtic i per tantes hores de felicitat compartida.

... als organitzadors de Contrabaix, per haver lluitat contra tots els vents per poder oferir a la nostra ciutat concerts de gran qualitat musical i humana.

... al Ferran, per ser el pare d'aquest cicle de concerts i haver elaborat la tapa de la tesi, però sobretot, per la seva encomanadissa passió per la vida i perquè en els darrers mesos ha esdevingut un compatriota indispensable, ajudant-me a reconstruir un edifici vital que estava en runes.

... a les *mestraleres*, per ser les millors companyes de viatge i per voler compartir la seva manera especial de veure i de viure. Gràcies especialment a la Marta i a la Carme, per estar sempre a prop, a la Cristina i a la Noemí, per haver-se llegit i corregit una part del manuscrit de tesi i per ser unes fonts inesgotables de crítica constructiva, a la Sara, per donar-se als altres d'una manera tan natural, i a la Caterina, per haver mantingut el pis en condicions durant els mesos més durs d'enclaustrament, per ser la millor germana i per la seva passió i alegria incombustibles.

... a la meva família, perquè són, a la vegada, un pilar vital i uns grans mestres, i per estar genuïnament interessats en la meva feina. Gràcies a tots els Prats, per ser exemples d'amor i d'integritat, a la familia Riba, per ser referents intel·lectuals indispensables, a la iaia Teresina, pel seu exemple de força i dignitat, i al Bernat i a la Roser, per la seva natural alegria.

... i als meus pares, per la seva paciència i suport incondicional i per l'empremta que han deixat en mi, de la que em sento molt orgullosa.

Barcelona, a 3 de Gener del 2004